Simulation of Cavitation Using Compressible Flow Solvers

Nikolaos Kyriazis

Thesis submitted for the fulfilment of the requirements for the Degree of Doctor of Philosophy

School of Mathematics, Computer Science & Engineering
Department of Mechanical Engineering & Aeronautics
September 2018

In the memory of my best friend Dimitris Kazakos, who left life so early.

Contents

List of Figures

List of Tables

Acknowledgements

First of all, I would like to thank Prof. Manolis Gavaises for giving me the opportunity to join his research group, for trusting me with this specific topic and for urging me to publish and present my work. Secondly, I would like to express my gratitude to Dr. Phoevos Koukouvinis and to Dr. Ioannis Karathanassis for the fruitful collaboration, their advice and the endless discussions, scientific or not, all these years.

I would also like to thank my colleagues Akis Stavropoulos-Vasilakis, Kostas Kolovos and Thodoris Lyras for their cooperation and the times we spend in the office discussing about OpenFOAM. Special thanks should be given to Nikos Chatziarsenis for his administrative help and to Amalia Petrova for her efforts to improve my presentation skills:) During my PhD at City, I had the pleasure to meet and work with people from all over the world, therefore I would like to thank Dr. Ilias Malgarinos and Dr. Hesam Jadidbonab for the time they spent with me analyzing droplet impact cases, as well as Milad Heidari Koochi, Georgia Nykteri, Andreas Papoutsakis, Homa Naseri, Mithun Murali Girija, Carlos Rodriguez, Alvaro Vidal and Max Brunhart for the days we spent in the office.

I am grateful to my parents, Sotiria Varlami and Thanasis Kyriazis for the emotional and financial support in the early years of my career, my sister Eleftheria Kyriazi and my girlfriend Aggeliki Giannoula for encouraging me to pursuit my dreams. Equally important was the support from my good friends and specifically from Giorgos Kanellis, with whom we had several "brainstorming meetings" and the support from Stathis Zogakis, Christos Zoumpos, Danae Mpalatsouka, Giorgos Lazaridis, Kostas Leloudas, Charis Vlogiaris, Tasos Toulitsis. Finally, I acknowledge the European Union's H2020 programme CaFE for funding this research.

Nikos Kyriazis, London Sept 2018

Declaration

I hereby declare that the contents of this dissertation are original and have not been submitted in whole or in part for consideration for any other degree or qualification in this, or any other university. This dissertation is my own work, except where specific reference is made to a joint effort in the text and Acknowledgements accordingly.

I grant powers of discretion to the University Librarian to allow the thesis to be copied in whole or in part without further reference to me. This permission covers only single copies made for study purposes, subject to normal conditions of acknowledgement.

Nikos Kyriazis, London Sept 2018

Abstract

An explicit density-based solver suitable for multiphase flows has been developed and implemented in OpenFOAM. Phase change is predicted through the density variation under the HEM assumption and different thermodynamic models that have been utilized, starting from barotropic EoS to more complicated ones that include real fluid thermodynamics (Helmholtz EoS). In the latter, a tabulated data technique has been followed aiming to reduce he computational cost; the value of each thermodynamic quantity within each thermodynamic element is approximated by a finite element interpolation. Apart from the liquid and vapour phases, the non-condensable gas is modelled by adding a transport equation for the gas mass fraction (2-phase model). Finite volume discretization is employed in conjunction with high order Runge-Kutta methods for time integration. A Mach number consistent numerical flux, based on approximate Riemann solvers, is proposed and renders the solver suitable for low subsonic flows of the liquid regime, up to highly supersonic flow conditions noticed in the vapour phase. The validity of the developed models has been assessed against the exact solution of the Riemann problem, experimental data, other numerical tools and parametric studies.

Different multiphase flow simulations have been performed, from fundamental studies of bubble dynamics and droplet impacts on a solid surface to industrial applications such as Diesel injectors, needle-free devices and nozzles in cryogenic flows. Concerning the real fluid thermodynamics model, n-Dodecane bubble dynamics simulations in the proximity of a wall have been performed. The effect of the initial conditions and the different thermodynamic models utilized was investigated. The methodology has been also applied to cryogenic flows inside converging-diverging nozzles and demonstrated satisfactory agreement with prior experimental studies. The 2-phase solver was employed for modelling the wave dynamics and the cavitation regime inside a droplet which impacts a solid surface. Finally, the influence of the initial bubble pressure and the meniscus geometry on the developed jet velocity of a needle-free device is studied.

Present contribution

The developed multiphase solver has the following attributes:

- **Real fluid thermodynamics modelling:** The Helmoltz energy EoS has been employed and a unified methodology is presented, suitable for both subcritical and supercritical regimes. The Helmholtz energy EoS has been utilized only in a few works, however here its applicability is extended to different materials, either for cavitating or flashing flows. For the latter, simulations using the Helmholtz EoS have not been reported.

- **Tabulated data technique:** Instead of solving the Helmhotz EoS at each time step, it is computationally more efficient to have stored in advance its solution in a 2-D table (thermodynamic mesh). Compared to previous tabulated data approaches, an unstructued thermodynamic mesh, refined around the saturation curve has been employed and a static linked-list algorithm has been developed for efficient data mining.

- **Gas effect has been included:** Apart from the liquid and vapour phases, the non-condensable gas has been also modelled in a newly developed 2-phase solver in OF. A thermodynamic closure has been provided, depending on the EoS used for each phase. More specifically, up to author's best knowledge, the Tait EoS combined with 2 isentropic relations for liquid-vapour-gas mixture of section 2.2.1, and section 2.3.2 have not been developed in the past.

- **Mach consistent numerical flux:** The hybrid numerical flux which is proposed here, has been implemented in OF and tested for several cases. The new flux is a combination of approximate Riemann solvers and previously proposed flux functions. It enables the use of the density based solver even for flow regimes with Mach number in the order of $\mathcal{O}(10^{-2})$ and its behaviour has been tested for 2 material interfaces.

- **Model cavitation during droplet impact:** The phase-change between the liquid and the vapour inside the droplet volume has been simulated for first time, whereas the surrounding air is modelled by a transport equation.
- **2-phase simulation of liquid jets:** The compressibility effects, as well as the liquid-vapour mixture and the liquid-gas jet interface due to shock wave focusing have been modelled, which has not been previously reported in the literature.

Symbols and abbreviations

Latin symbols

a	molar Helmholtz energy (J)
a^0	ideal gas contribution to the Helmholtz energy (J)
a^r	residual Helmholtz energy, responsible for the influence of Intermolecular forces (J)
B	liquid bulk modulus (Pa)
C	speed of sound parameter $(Pa \cdot kg/m^3)$
C_N	Cavitation number $(-)$
C_p	specific heat at constant pressure $(J/(kg \cdot K))$
C_v	specific heat at constant volume $(J/(kg \cdot K))$
c	speed of sound (m/s)
e	internal energy (J/kg)
e_{l0}	internal energy at reference temperature T_0 (J/kg)
E	total energy (J/kg)
$\mathbf{F}_k$	k-direction inviscid (convective) flux vector
$\mathbf{F}_k^V$	k-direction viscous flux vector
Fr	Froude number $(-)$
L_v	latent heat $(J/(kg \cdot K))$
M	Mach number $(-)$
N_{nm}	finite element nodal shape function of node n, evaluated at node m $(-)$
$\mathbf{n}$	normal surface vector $(-)$
p	pressure (Pa)
n	Tait equation parameter, $n \sim 7.15$ for weakly compressible liquids $(-)$
p	pressure (Pa)
Pr	Prandtl number $(-)$
p_{sat}	saturation pressure (Pa)
p_c	critical pressure (Pa)

R	specific gas constant $(J/(kg \cdot K))$
Re	Reynolds number $(-)$
$\mathbf{S}$	geometric source vector for spherical coordinates
s	geometric source term, unity for cylindrical symmetry and two for spherical symmetry
St	Strouhal number $(-)$
T	temperature (K)
$\mathbf{U}$	conservative variable vector
u_x	velocity in the x-direction (m/s)
u_y	velocity in the y-direction (m/s)
u_z	velocity in the z-direction, for either cartesian or spherical coordinates (m/s)
u_r	velocity in the r-direction, for spherical coordinates (m/s)
We	Weber number $(-)$
Y_i	mass fraction of the i component $(-)$

Subscripts

c	critical condition
g	gas
l	liquid
m	mixture of liquid and liquid-vapour
r	triple point
sat	saturation condition
v	vapour

Greek symbols

α_i	local volume fraction of the i component $(-)$
α^0	dimensionless ideal gas contribution to the Helmholtz energy $(-)$
α^r	dimensionless residual Helmholtz energy, responsible for the influence of Intermolecular forces $(-)$
β_i	volume fraction of the i component $(-)$
γ	ratio of specific heats $(-)$
λ	thermal conductivity $(W/(m \cdot K))$
μ	dynamic viscosity, 0.001 for water at $20°C$ $(Pa \cdot s)$
ν	kinematic viscosity (m^2/s)

ρ	density (kg/m^3)
ρ_c	critical density (kg/m^3)
τ_{ij}	viscous stress tensor, ij component (Pa)
σ	surface tension, 0.072 for water (N/m)

Abbreviations

CFD	Computational Fluid Dynamics
EoS	Equation of State
FE(M)	Finite Element (Method)
FV(M)	Finite Volume (Method)
GDI	Gasoline Direct Injection
HEM	Homogeneous Equilibrium Mixture
HLLC	Harten-Lax-van Leer-Contact
IBM	Immersed Boundary Method
IC	Internal combustion
LBM	Lattice Boltzmann Method
LES	Large Eddy Simulation
LOX	Liquid Oxygen
LSM	Level Set Method
MAC	Marker and Cell
MPI	Message Passing Interface
NS	Navier-Stokes
OF	OpenFOAM
RK(M)	Runge-Kutta (Method)
VOF	Volume Of Fluid

Chapter 1

Introduction

1.1 Motivation

Cavitating flows occur in a wide range of applications, some of the most important are in automotive industry (injection systems in IC engines), in naval engineering (propellers), in energy industry (turbines and pumps) and in the biomedical sector (lithotripsy, drug delivery). While in some cases cavitation may act beneficially, such as in lithotripsy, in the majority of the applications it has an adverse effect, either reduced efficiency, noise or even erosion damage of the machine.

Modelling the multiphase flow in many applications necessitates complex thermodynamic EoS in order to accurately capture the flow field under extreme pressure or temperature conditions. One typical example is Diesel injection systems, where there is the tendency to rise the injection pressure up to 3000 bar from 2000 bar [1], aiming to design more efficient IC engines and to comply with environmental friendly EU legislations [2, 3]. Such injection pressures result in high velocity fields (above 500 m/s) in the narrow passages of the injector, which may lead to cavitation [4]. The main consequences of cavitation formation are reduced injection volumetric efficiency and material erosion [5]. Moreover, the fuel density variation in the injector can be around 10% which can dramatically change the fuel properties [6]. On the other hand, the benefit of cavitation is the increased spray cone angle, which offers improved air-fuel mixing [7]. Therefore, there is the need of a compressible flow solver with incorporated real fluid thermodynamics.

Complex thermodynamic modelling is also required in flashing phenomena for cryogenic fuels in space applications. Similar to diesel injectors, there is a

trend in rocket engines towards higher chamber pressures which will result in a higher specific impulse for the engine [8], but may cause the liquid pressure to go beyond the critical pressure [8]. Due to its high specific impulse, oxygen is preferred compared to other fuels in such applications. Aiming to minimize the fuel tank structure in the rocket, oxygen is stored in liquid form (LOX) at cryogenic conditions [9]. For instance, LOX is used in the Ariane 5 and in the future Arianne 5ME upper stage engines [10]. Experimental studies are scarce due to the cryogenic flow conditions, which pose serious questions about the accuracy and reliability of the results [10], while numerical works necessitate real fluid thermodynamics [11, 12] and there is again little information in the literature regarding LOX simulations [12].

Although the temperature effects are not dominant in microfluidics and needle-free injection systems, the complexity of the latter lies in the three phase flow (liquid-vapour-air) and its jetting effects. In particular, the aim is to generate a liquid jet strong enough to punch a hole into the skin through erosion and fracture and to deliver the medicine/vaccine into the tissue, without damaging the skin and the drug molecule [13, 14]. A determining factor for a successful design is the possibility of splash back. If the volumetric rate of the hole formation is less than the volumetric rate of the jet impinging the skin, backflow is noticed [15, 13]. This splashing back of the liquid from the skin onto the nozzle was responsible for subject-to-subject contamination of hepatitis B virus [16, 17, 15]. Consequently, an algorithm appropriate to handle such phenomena and a numerical investigation of the 3-phase flow inside the needleless injection devices has to be performed in order to examine if the above criteria are satisfied.

The distinctive feature of multiphase flows is the great variation in the speed of sound among the different phases, from 1 m/s for the vapour up to 1400 m/s for the liquid regime. This variation in the speed of sound results in totally different flow conditions, from subsonic ($M \sim 10^{-2}$) up to highly supersonic ($M \sim 10^3$ or even higher [18]). This is an obstacle either in pressure-based or in density-based solvers. In the former, the condition number of the system is very large, causing convergence problems, while in the latter, slow convergence and dispersion in low Mach number flows is noticed [19, 20, 21]. A unified treatment for all Mach number flows is necessary, so as to obtain smooth and accurate solutions [22, 23, 24, 25].

The motivation of the present work lies in understanding and investigating

multiphase flows from a numerical point of view. It can be concluded from the above that a numerical approach with high order EoS is necessary in order to describe the change in the fluid properties under extreme conditions, as well as the capability to model three phase flows. A CFD tool which offers a unified treatment for the above problems has been developed.

1.2 State of the art

In this section, the algorithms used in the literature to model the physical problems of section 1.1 are described [26, 27, 28]. The most important numerical methods for modelling two-phase flows and their classification are shown in Fig. 1.1. In the present work, algorithms for HEM, with or without temperature effects have been developed, as well as mass transfer models (diffuse-interface approach). For the three-phase solver developed in OF, the HEM approach is extended by a homogeneous transport equation (VOF-like method) for the non-condensable gas.

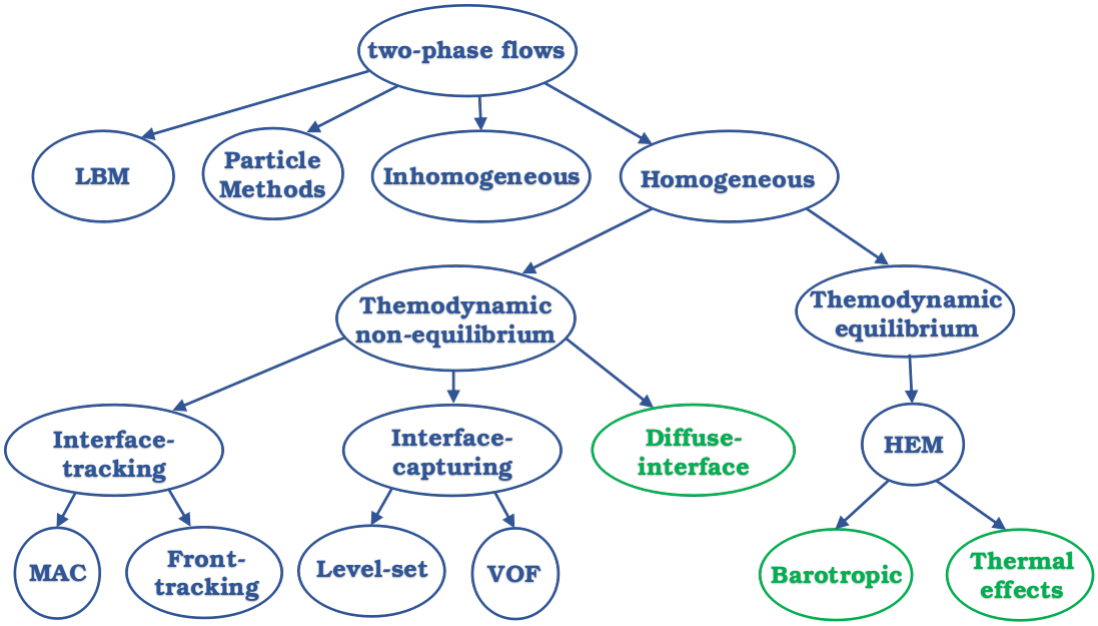

Figure 1.1: Classification of the numerical methods for two-phase flows. The developed methods are in green.

In general, the numerical methods for two-phase flows are classified into conventional mesh methods and mesh-free approaches. The former are further categorized into inhomogeneous (two-fluid or generally N-fluid for N phases) and homogeneous (one-fluid) methods, while the latter are split into LBM [29] and

Particle methods, SPH [30] being the most significant among them.

Concerning the family of SPH methods, they were originally developed for astrophysical problems in 1977 by Lucy, Gingold and Monaghan [31, 32]. However 15 years later, SPH was extended to free surface flows by Monaghan [33] and has been widely used for interfacial flows ever since [34, 35]. Vila [36] introduced the mathematical framework of the SPH-ALE, so as to overcome the drawbacks of the standard SPH method. In follow-up studies, Marongiu et al. [37, 38, 39, 40] applied the method in the free surface flow of Pelton turbines and later on, they implemented the method for GPU processors [41, 42]. Traditionally, SPH methods can easily handle material deformation, without the need of mesh deformation techniques and they offer solutions free of dissipation. However, they suffer from some serious drawbacks. Due to the arbitrary distribution of the particles in the numerical domain, the order of the spatial accuracy is not straightforward and can vary within the domain. Consequently, in areas with insufficient population of particles or non-uniformly distributed particles, spatial accuracy is downgraded.

In multi-component models (inhomogeneous methods) there is no mechanical equilibrium between the phases (non zero slipping velocity), so each phase is characterized by its own pressure and velocity field. Phase-change is predicted by a transport equation for the vapour volume fraction with mass transfer terms in the RHS (non-homogeneous PDE). Although this approach is more realistic, it has some serious disadvantages in practice, such as the large computational cost (N continuity, momentum and energy equations are solved for N phases) and that it is problem dependent, due to the appropriate closure and interface relations needed for each phase. The added value of multi-component models was demonstrated by Wallis [43] and later on, a 2-fluid model was employed by Baer and Nunziatio [44] for detonation waves in granular explosives. Saurel and Abgrall [45] modified the two-fluid model and extended its applicability for multi-phase compressible flows.

On the other hand, in homogeneous methods there is mechanical equilibrium (1 pressure and 1 velocity field) and both phases behave as a mixture. This approach is further classified depending on whether or not thermodynamic equilibrium is satisfied. Thermodynamic non equilibrium methods are categorized into interface-tracking, interface-capturing and diffuse interface methods (mass transfer models).

In the interface tracking methods, the moving boundary (interface) is explicitly described by the computational mesh (interface nodes) and often its movement is predefined, for example by the velocity vector. The location of the inner mesh nodes however, is not prescribed and several techniques are used in order to maintain good mesh quality, such as the elastic mesh update method. Some of the most widely used interface tracking methods are the MAC technique, front-tracking methods, the volume-tracking approach and IBM.

The oldest approach for modelling two-phase flows is the MAC method, where marker particles were used to identify the different fluid regions on a stationary grid [46, 47] and was used later on by Plesset and Chapman for bubble collapse simulations [48].

In front tracking methods, which have been originally developed by Glimm et al. [49] and in a follow-up study by Unverdi and Tryggvason [50], the interface is explicitly described by the computational grid. The most famous package for front tracking methods is FrontTier, which was originally developed by Glimm et al. [51]. Du et al. [52] proposed significant improvements to the FronTier toolkit regarding topological bifurcations and they assessed the performance of the front-tracking methodology compared to LSM and VOF. In general, front tracking methods offer high accuracy in resolving the interface between the two phases. Their main advantage is that they allow for smear-free interfaces and they can be applied to complex geometries while they allow for large deformations of the surface to be simulated. They cannot capture large topological changes though, for example the formation of cavity inside a liquid metal droplet [53]. Another drawback is their complexity, since the interface grid must be dynamically reconstructed, either adding or removing nodes in areas of stretched or compressed cells, respectively [50].

The immersed boundary method was originally developed by Peskin [54] for fluid- structure interaction applications, but has been also used for representing the interface between two phases on Cartesian grids [55]. In IBM, Eulerian and Lagrangian variables are employed, the former on a fixed Cartesian mesh and the latter on a curvilinear mesh which is able to move freely through the Cartesian mesh. While their implementation is relatively easy, by adding for example a source term in the NS equations, the solid or the interface motion is not accurately described.

In the interface-capturing methods the interface is implicitly reconstructed

by a field variable. Subcategories of the interface-capturing method are the discontinuous and the continuous approach. The most popular continuous approach is the level-set method [56, 57], where the interface is described as the zero level-set of some auxiliary function ϕ. Volume of fluid (VOF) [58] is the most representative discontinuous interface-capturing method, where the main idea is to calculate the vapour volume fraction which defines the interface as a step function.

The volume of fluid (VOF) scheme, introduced by Hirt and Nichols [58] and later Youngs [59] proposed a 3-D volume tracking algorithm (see also [60]). Aniszewski et al. [61] made a comparative study among different VOF methodologies. Based on the innovative works of [58, 59], the Piece-wise linear Interface Calculation (PLIC) aprroach [62, 63], the Weighted Linear Interface Calculation (WLIC) method, which was introduced by Yokoi [64] and independently by Marek et al. [65], and the Tangent of Hyperbola for Interface Capturing (THINC) interface reconstruction scheme, which was described by Xiao et al. [66] (more recent works are [67, 68]), have been developed. More recently, Shukla et al. [69] solved the multi-component compressible flow equations with an interface compression technique aiming to capture the thickness of the interface within a few cells. Although the VOF method was originally developed and has been mainly used for incompressible flows, it has been also extended to compressible fluids[70, 71, 72, 73, 69, 67]. Nowadays, geometric VOF methods with arbitrary unstructured meshes have become popular and have been implemented in the open source CFD toolbox OpenFOAM [74, 75]. Apart from OpenFOAM, Gerris, an open source incompressible VOF solver with adaptive mesh refinement capabilities, was originally developed by Popinet [76] and has been used in either droplet or bubble simulations [77].

While admittedly the discussed interface-capturing methodologies can provide a sharp interface, the concept of "interface capturing" is questionable when pressures reach close to the critical point, since liquid and vapour densities become similar and surface tension diminishes, preventing a clear distinction between the two phases. Another challenge for interface capturing methods is that they are numerically expensive and they cannot be used for capturing thousands or millions of bubbles in a real case simulations.

In mass transfer models (diffuse-interface approach), a transport equation for the volume (or mass) fraction of the vapour with source terms to model phase-

change is incorporated in the NS system of equations. The different regions share the same velocity, pressure and temperature, however the mass transfer phenomena are time dependent and not instantaneous, while the mass transfer rate and the nucleation points are finite (non-equilibrium). The main drawback of this approach is that the mass transfer source terms are empirical and case dependent, and thus tuning is necessary. It has to be clarified here that mass transfer terms are also added in VOF and LSM in order to model phase-change, however they are considered as three distinct methodologies, since VOF and LSM are characterized by sharp interface. Mass transfer models are based on kinetic theory of gases, such as the Hertz-Knudsen equation [78, 77] or they adopt condensation and vaporisation terms, such as the models suggested by Zwart-Gerber-Belamri (ZGB) [79, 80], Merkle et al. [81] and Schnerr-Sauer [82]. In the latter models, where condensation and evaporation terms are used, cavitation is described with respect to the growth and collapse process of vapour bubbles. Starting from nuclei, bubbles grow or collapse, depending on the flow conditions (pressure and temperature).

Overcoming the limitation of the previous methods, in HEM the two-phase regime is in thermodynamic and mechanical equilibrium, so the two phases share the same velocity, pressure and temperature. Although this assumption may not be valid in metastable thermodynamic states, the model is accurate enough for medium and large scale simulations of cavitating flows (see for example [83], where 120 million cells have been used for a bubble cluster collapse). In HEM thermodynamic equilibrium is achieved instantaneously, as infinite nucleation points and infinite mass transfer rate are assumed. Phase-change is predicted here through the variation of density from the corresponding Equation of State (EoS), without solving any transport equation for the volume vapour fraction and thus, no empirical parameters and tuning are needed. Despite the limitation of not explicitly defining the bubble interface, such models are still widely used due to simplicity; this limitation has been proved not to be important, since the bubble interface can be estimated by the density variation when using a reasonable amount of cells. Since the bubble interface or the liquid-vapour interface in general may be somewhat diffuse, surface tension is commonly neglected. In any case the effect of this assumption is minor, due to the minor role of the surface tension at the stage of bubble collapse, which is mainly governed by inertia.

HEM models have been used for several applications, either macroscopic or

microscopic ones and they can be either barotropic (pressure depends only on the density) or they can include temperature effects. Delannoy and Kuevy [84] proposed a barotropic law from which the phase change is predicted; different barotropic models have been also applied, such as [85, 86]. Barotropic models have been employed in several studies, due to their simplicity, such as [87, 88, 89]. On the other hand, HEM with temperature effects has been employed by Saurel et al. [90] for studying cavitation in an underwater projectile, by Schmidt, Sezal, Adams et al. for hydrofoil [91, 83] and bubble cluster simulations [83] or for modelling the flow in injection nozzles [92, 23]. In the largest scale simulation to author's best knowledge, Rossinelli et al. [93] used a single fluid model and simulated the collapse of a bubble cluster of $15,000$ bubbles discretized with 13 trillion grid points; the liquid was modelled as stiffened gas and the vapour as ideal gas. Concerning works with real fluid thermodynamics, the interested reader is addressed to the work of Dumbser [94] for cavitating flows around hydrofoils and to the work of the author [95] for single bubble collapse. In the above works, density based solvers were utilized in order to model the hyperbolic nature of the equations and to capture expansion and shock waves which were formed.

1.3 Literature review

In this section, a literature review of most of the cases simulated in Chapters 3 and 4 is given, including both fundamental studies (bubble dynamics and droplet impacts) and industrial applications (Diesel injectors, cryogenic flow in nozzles and the needle-free injection device).

1.3.1 Bubble dynamics

Many studies deal with the dynamics of vapour bubbles, both computationally and experimentally, due to the implications they have in a number of physical conditions and technological applications. Up to now, different approaches have been proposed for simulating bubble collapse dynamics, such as potential flow solvers with dynamic boundary conditions on the bubble surface, homogeneous mixture models and interface tracking/capturing methods.

Methodologies based on potential flow solvers have been among the first employed to simulate the collapse of bubbles. For example, Plesset and Chapman

[48] were the first to study cavitation bubble collapse close to a solid surface. A potential flow solver was used for the liquid phase and a Marker-and-Cell technique was developed for tracking the bubble interface. A similar flow solver was employed by Zhang et al. [96, 97] but a Boundary Element Method was incorporated for predicting the shape of the bubble and the pressure profile on the wall. In an extension of the BEM method, Wang [98] employed a combination of compressible and incompressible potential flow for the simulation of a bubble collapse in the vicinity of a wall, aiming to describe the energy loss due to pressure waves radiated during the bubble collapse. The advantage of the BEM methodology is that only the bubble interface is discretized and resolved, transforming the 3D problem to a 2D one. However, mesh handling is problematic when topological changes of the bubble interface have to be taken into consideration, e.g. during bubble jet formation or impact on walls. For that reason, Chahine [99] used a coupling between an incompressible BEM potential flow solver and a multiphase compressible flow solver based on the Euler equations for simulating the growth and collapse of a bubble in the vicinity of (deformable) walls. Each solution strategy was employed at different stages of the bubble development; for the violent growth and collapse of the simulated bubble the compressible multiphase approach was used, whereas the BEM method was employed at intermediate stages where flow velocities are small.

Concerning bubble dynamics modelled under the HEM approach, Adams and Schmidt [83] simulated the collapse of a bubble cluster consisting of 125 bubbles with a 120 million cell grid. Another work by the same group [91], emphasized on the detection of the shock formation and propagation in three dimensional cloud cavitation on hydrofoils; HEM models have been also used for Diesel injector simulations [23], microchannels [87] and for estimating erosion [100] among others. Since the temperature variation of the liquid can be negligible in some cases, the energy equation can be omitted and thus, barotropic cavitation models have been successfully employed for the prediction of cavitation either on macroscopic (e.g. hydrofoils [101], venturi [102], high pressure throttle flows [103]), or single bubble collapses [89].

Overcoming the limitation of the previous methods, front tracking methods have been utilised for modelling bubble dynamics, since they offer higher accuracy in resolving the exact bubble shape. Hawker and Ventikos [104, 105] used a marker to track the liquid-gas interface in the FrontTier code; the computational

mesh was divided into two regions, with different EoS applied for each phase. In a similar study, Popinet and Zaleski [106, 107] employed a finite volume formulation with a fixed grid and a front-tracking approach; free surface boundary conditions were imposed for simulating bubble flows near solid boundaries and cubic splines were used for the surface representation. In addition, Pan et al. [108] computationally studied a bubble transport in a microchannel by utilizing a front-tracking approach in connection with an IBM methodology for the moving boundaries.

Interface capturing schemes based on the VOF methodology have been also employed to the simulation of cavitation bubbles. For example, Li et al. [109] investigated the bubble collapse near a conical rigid boundary, formulating an extension to the classical Rayleigh collapse time, incorporating the wall stand-off distance and the cone angle. Koukouvinis et al. [110, 111] investigated the effect of asymmetries (e.g. pressure gradient and free surfaces) affecting the bubble collapse, using the VOF technique, and demonstrating jetting effects and bubble shape at collapse stages. Hu et al. [112] developed a conservative interface method based on the level set technique for solving compressible multiphase flows, maintaining a sharp liquid-gas interface. The methodology was tested in fundamental shock tube cases, bubble-shock wave interactions and underwater explosions. In connection to the previous work, Lauer et al. [113] used a LSM for bubble dynamics, including non-equilibrium thermodynamic effects and finite mass transfer based on the Hertz-Knudsen relation, while exploring the effect of the wall distance on the bubble shape during collapse (see also [114]).

In two-phase models that utilise interface capturing methods, the common assumption is to prescribe a finite mass transfer rate across the bubble interface, describing the evaporation and condensation processes. On the other hand, in single-phase models (HEM), mass transfer is assumed to be infinite. More specifically, in barotropic models, pressure is only a function of density and thus, temperature effects are omitted.

The homogeneous equilibrium model (HEM) approach is followed, where each thermodynamic property can be expressed as a function of density and internal energy. While in the previous studies, thermal effects were typically ignored or were considered utilising simplified EoS, the present work contributes towards a better understanding of the thermodynamics of collapsing bubbles. The thermodynamic closure used for the bubble dynamics simulations of section 3.3 is based

on the Helmholtz energy EoS from NIST Refprop databases [115], which can provide thermodynamic properties at subcritical and supercritical conditions in a consistent framework. By using the Helmholtz EoS, a complex thermodynamic model is incorporated in the finite volume solver, while the tabulated data algorithm is proved to be more efficient than using iterative calculation methods for finding the thermodynamic properties at each time step. Following the methodology of Dumbser et al. [94], tabulated EoS are employed in the present explicit density-based algorithm; the low Mach number problem is tackled by the hybrid flux model of Schmidt et al. [23]. To the author's best knowledge, this is the first work implementing the Mach consistent numerical flux in connection with real fluid properties for n-Dodecane, demonstrating heating effects in bubble collapse cases; the only relevant work is that of Dumbser et al. [94], who focused instead on water/vapour behaviour in benchmark (e.g. shock tube, explosion/implosion, forward step) and macroscopic (e.g. hydrofoil) cases. Furthermore, the strong pressurization and heating leads to the formation of supercritical fluid in the vicinity of the bubble collapse, which has not been reported before.

1.3.2 Diesel Injectors

From bubble dynamic studies of section 1.3.1, a rough estimation of the pressure peaks and potential material erosion at conditions realised in micro-orifice flow passages can be obtained. A more detailed insight can be acquired by performing larger scale simulations of industrial interest, such as Diesel injectors.

Sezal et al. have followed a compressible approach for simulating the flow inside a Diesel injector and predicted cavitation; the collapse pressure peaks that were noticed, can be used as indicators of erosion [92, 116, 117]. Salvador et al. have worked in different aspects of Diesel injectors, starting from validation cases [118] and expanded into the effect of geometrical features on the hydraulic performance of the injectors (see also the work of Molina et al. [119]) and LES simulations in OpenFOAM [120].

Concerning works with needle movement, Koukouvinis et al. [3] performed compressible LES studies for estimating the flow inside a Diesel injector (see also [121, 2] from the same research group). The transient effects due to the needle movement have been also taken into account in [122, 123, 124, 125]. Significant contribution in the field of mesh motion in pistons and GDI injectors has been also made by Montorfano, Piscaglia et al. [126, 127, 128, 129]; they implemented

a parallel algorithm for layer addition-removal in OF and performed LES studies. In a follow-up work, Wu et al. [130] expanded the idea of Dynamic Length-Scale Resolution Model (DLRM), which includes an adaptive rescaling procedure for turbulent length and time scales in a simplified square-piston engine. Compared to LES, where the mean length scales of unresolved turbulence are proportional to the local grid spacing, the turbulent length scale here is calculated based on statistical turbulence models. The length and time scales which have been modelled, are now filtered in order to suppress their influence on the flow field. The functional form of the filter is derived by comparison between the modelled and the resolved scales [131]. Apart from the layer addition-removal technique, Örley [132] et al. employed the IBM for modelling the needle motion and took into account the vapour and gas phases as well.

In the present work, a Diesel injector simulation has been performed in OF by utilising a density based solver with a Mach number consistent numerical flux. A two-step barotropic EoS, the Tait equation for the liquid and a isentropic-resembling relation for the liquid-vapour mixture has been used. Compared to past studies in OF (see for example [128, 129]), the compressibility effects have been considered in the present study. The only exception is in [120], where compressible simulations were performed in the standard pressure based OF solver (cavitatingFoam). Simulation of a Diesel injector with real fluid thermodynamics at high operating pressures was not feasible, since the operating conditions exceed the applicability range of Helmholtz EoS. The applicability range of Helmholtz EoS cannot be extended due to scarce experimental data needed for calibration.

1.3.3 Rocket propulsion systems

The Helmholtz EoS and the tabulated data technique are applicable to any material, as long as experimental data exist to calibrate the EoS. Thus, the same methodology can be expanded to cryogenic simulations of LOx, where real fuel thermodynamic modelling is needed as well.

There are only a few research facilities conducting experiments at cryogenic flow conditions, such as the Lewis Research Center of NASA and the Mascotte test facility of Onera [133]. In the former, Hendricks, Simoneau and Barrows [134, 135] acquired experimental data for cryogenic fluids (Nitrogen, Methane, Hydrogen and Oxygen) in four different converging-diverging nozzle geometries. Nevertheless, there is a lack in the literature concerning cryogenic studies due to

the extreme conditions that the experimental facilities must achieve. This poses difficulties in validating and calibrating the computational models developed by several researchers.

Two-fluid models have been widely used in predicting flashing flows and they were originally introduced by Wallis in 1980 [43]. Maksic and Mewes [136] simulated flashing in converging-diverging nozzles by adding a transport equation for the bubble number density (4-equation model) to the continuity, momentum and energy equations. More recently, Liao and Lucas [137] performed a flashing flow simulation in a 3-D converging-diverging nozzle for water by utilising a two-fluid model with $k-\omega$ SST turbulence model. The 5-equation model they used consisted of two continuity equations, 2 momentum equations and 1 energy equation. Switching to more complex approaches, a 6-equation model (continuity, momentum and enthalpy equations for each phase separately) has been employed by Marsh and O' Mahony [138] in Ansys Fluent for flashing flows and by Mimouni et al. in NEPTUNE_CFD [139] for boiling flows, where Janet et al. [140] utilised a 7-equation model and they considered nucleation during flashing flow in converging-diverging nozzles. In the latter, a bubble number transport equation was added in the system of 6 equations. Meng and Yang [141] developed a numerical framework for n species, by employing one continuity, one momentum, one energy and n transport equations. The algorithm was incorporated into a preconditioning scheme for solving fluid flows at all speeds. Supercritical LOx injection has been investigated numerically with reference to swirl atomisers suitable for rocket engines [142, 143] using the Soave-Redlich-Kwong (SRK) EoS.

Concerning one-fluid models, the Homogeneous Relaxation Model (HRM), which considers non-equilibrium vapour generation, was originally introduced by Bilicki and Kestin [144] and later on by Downar-Zapolski et al. [145] for 1-D flows. Schmidt et al. [146] expanded the HRM to 2-D problems in order to study thermal non-equilibrium and two-phase flows with flash-boiling (see also [147]). In another approach, Travis et al. [12] utilised the Helmholtz EoS for isentropic cryogenic flows of hydrogen, methane, nitrogen and oxygen. They introduced a non-equilibrium parameter in order to correlate the liquid and vapour temperatures and they validated their findings against the NASA tabulated data [134, 135]. Regarding mass-transfer models, Karathanassis et al. [148] assessed their performance in a comparative study among Hertz-Knudsen [77], ZGB [80], HRM [146] and HEM [28] models for various nozzle geometrical configurations.

Apart from Eulerian approaches, hybrid methods have been used. For instance, Ramcke et al. [149] used an Euler-Lagrange method for simulating LOX and gaseous Methane. Schmehl and Steelant [150] performed a numerical investigation of Oxidizer Preflow in an Upper-Stage Rocket Engine with a hybrid method, which is basically a combination of the Euler-Euler approach and the Euler-Lagrange method. More recently, Gaillard et al. [9] modelled the cryogenic injection in rocket engines in CEDRE software, by coupling a diffuse interface approach (4-equation model) in a LES context (CHARME solver) with an Eulerian kinetic model (SPIREE solver).

In the previous works, simplified EoS were utilised or significant assumptions were made ignoring temperature effects, e.g. adiabatic flow conditions. In some other works, high order EoS such as the SRK EoS were employed [142, 143], which in general requires a smaller number of experimental data points for fitting the EoS parameters compared to Helmholtz EoS. However, SRK EoS is considered to be less accurate than the Helmholtz EoS, which is independently calibrated for each material. The aim of the present work is to employ a higher order and more realistic EoS suitable for cryogenic flows. Therefore, the cryogenic flow in a converging- diverging nozzle is modelled by utilizing the Helmholtz EoS, which provides real fluid thermodynamics closure to the solved equations. The tabulated data algorithm for the Helmholtz EoS has been incorporated in an explicit single-phase solver in OF under the HEM approach; the use of HEM is justified by the retrograde behavior of Oxygen [151, 152]. In addition, the methodology is applicable to different flow conditions, either subcritical or supercritical and therefore offers a unified treatment.

1.3.4 Droplet impacts

Droplets impacting onto solid or liquid surfaces are of significance not only in engineering applications [153, 154, 155], but also in many other fields, such as oceanography [153], food science [156] or even forensics [154]. Engineering applications where droplet impacts play a key role are low pressure steam turbines, aircraft components which are subject to material erosion or ink-jet printing, where thin coating is placed on the paper [157]. The steam in the turbine engine operating at low pressure conditions is prone to condensation and thus, water droplets are formed. These droplets travel with the flow and can impact the blade with high speeds (over 200 m/s) [158, 155]. Under those conditions, cavitation

may form inside the droplet due to the pressure waves developing within the droplet's volume. As a result, consecutive impacts can lead to erosion damage, not only because of the impact pressure, but also due to the pressure increase after the collapse of the cavitation bubble.

Numerous fundamental studies of droplet impacts address the complex phenomena taking place, such as the interaction of shock and expansion waves, jet starting from the free surface, cavitation and possible erosion. These include analytical, experimental and computational works for a wide variety of impact velocities and droplet diameters.

Heymann [159] and Lesser [160] were the first who provided analytic solutions of liquid droplet impact onto a solid surface. Heymann [159] performed a quasi-steady state 2-D analysis of the dynamics of impact between a compressible liquid droplet and a rigid surface. However, this analysis is only valid for the initial stages of the impact, during which the shock is attached to the solid surface, so the jetting in the contact edge cannot be predicted. Later on, Lesser [160] expanded this work and took into account the elasticity of the surface while he also gave an analytic solution of the 3-D droplet impact problem. Regarding experimental studies, Field et al. [161] studied the main mechanisms during the droplet impact and documented that the edge pressures depend on the impact velocity and the angle between the liquid and the solid surfaces (see also [162]). Later on, Field et al. [163] presented high-speed images of impacted liquids using several different techniques. By adding gelatine in the water, they produced 2-D drops between two transparent plates and the impact was modelled by a projected third plate. This case has been utilised as a means of validation in the present study since it elucidates the wave dynamics and the cavity formation after impact.

Complex numerical simulations based on the solution of the Navier-Stokes equations have also been performed, as they can in principle provide more detailed insight to the phenomenon. Both Lagrangian (interface tracking) and Eulerian (interface capturing) approaches, or even a combination of the two have been performed for simulation of liquid droplet impact onto solid surfaces.

The Lagrangian approach has been widely used for simulating the droplet-gas interface and the splash of a liquid droplet onto a flat plate was originally modelled by Harlow and Shannon [164]; they used a marker-and-cell (MAC) finite difference algorithm ignoring surface tension and viscosity. In the subsequent

studies of Tsurutani et al. [165] and Hatta et al. [166], a MAC technique was used but this time surface tension and viscosity were taken into account (see also [167]). The main drawback of MAC methods lies in the fact that they cannot easily predict large topological changes which take place at later times of the droplet impact and therefore, more advanced methods have been developed. Some other researchers employed the finite element method (FEM) for discretizing the relevant differential equations [168, 169, 170, 171]. A deforming triangular grid was utilized in order to capture the interface between the liquid and the gas in the above studies, whereas in [169], the mesh was adapting to the flow field. For instance, Fukai et al. [168] investigated the effect of impact velocity, droplet diameter, surface tension and material properties on the hydrodynamics of the droplet impingement by developing a FEM for the incompressible flow equations. The hyperbolic character of the equations was obtained by the artificial compressibility method. These methods traditionally cannot handle problems with strong mesh deformation, where most likely degenerate cells occur.

Several studies have considered the effect of surface tension on the droplet deformation. For instance, Davidson [172] adopted the boundary integral method (BIM) for predicting the spreading of an inviscid droplet impact. Furthermore, Harvie et al. [173] simulated droplet impacts on hot surfaces; they employed an implicit pressure-based algorithm for the incompressible Navier-Stokes equations. The interface of the droplet is captured by the VOF model which is coupled with an 1-D algorithm for the flow in the viscous vapour layer and the heat transfer within the solid, liquid and vapour phases (vapour layer model). VOF methodologies for tracking the free surface of droplets which impact a solid surface have been also developed by Pasandideh-Fard et al. [174], Rieber and Frohn [175], Bussmann et al. [176], Pasandideh-Fard et al. [177] and later on by Malgarinos et al. [178]. In order to have a more accurate reconstruction of the interface, Guo et al. [179] invoked the moment of fluid (MOF) method to investigate droplet impingement and splashing on dry and wet surfaces. In the MOF method, which is an extension of the VOF model, the centroid of each material is integrated along with the volume fraction for each material.

Concerning compressibility effects, which were omitted in the previous studies, a front tracking solution procedure was invoked by Haller et al. [180] for high-speed impact of small size droplets. A rectangular finite difference Eulerian grid and a moving lower dimension Lagrangian one to track the location

of the wave fronts have been utilized (see also [169]). In another compressible approach, Sanada et al. [181] used the multicomponent Euler equations to model high-speed droplet impact. They developed a third-order WENO scheme with an HLLC Riemann solver and the time advancement was achieved by a third-order TVD Runge-Kutta. More recently, Niu and Wang [182] developed a compressible two-fluid model for the Euler equations and they proposed an approximated linearized Riemann solver for the liquid-gas interface. Surface tension was neglected due to high We number, as well as in the above high-speed droplet impacts. Furthermore, they showed that higher impact speed results in higher impact pressure and possible damage in the solid surface.

A compressible approach has been only considered in a small part of the aforementioned literature, whereas in the present study, the compressibility effects during droplet impact which lead to cavitation formation are studied. To author's best knowledge, this is the first time that cavitation is considered in a droplet impact simulation and three phases are modelled; the only exception is the work of Niu et al. [182], where cavitation zones have been identified but without actually simulating the phase-change process. Furthermore, parametric studies with varying impact velocity and simulations with the absence or presence of gas between the droplet and the solid surface provide estimates of the vapour generated and the pressure loading in the surface.

1.3.5 Needle-free injection

Needle-free injection systems (NFIS) have gained popularity and are widely used nowadays instead of the invasive drug delivery systems, since they offer several benefits, such as effectiveness in mass immunization programmes, avoiding at the same time infectious diseases such as HIV and hepatitis. Compared to conventional needle injection systems, NFIS can inject not only liquid drugs and vaccines, but also in solid particle form [14] and they ensure faster drug delivery. Based on the type of load, NFIS can be classified as: powder injections, liquid injections and depot (projectile) injections [13, 14]. Concerning the actuation mechanism, spring and compressed gas are the most common power sources among commercial needle-free injection systems.

In the present study, the liquid injection is simulated where the jet is created due to the expansion of a laser-induced bubble [183]. Such laser powered systems are not yet available for clinical use and were originally designed by Yoh et al.

[184, 185, 186, 187]. The expansion of the high pressure bubble results in the creation of a shock wave travelling inside the liquid, which is later reflected by the walls. When the superposition of the waves reaches the liquid-gas interface, a liquid jet is formed in the nozzle which impacts on the skin surface [17, 185, 188]. The objective is to generate a liquid jet strong enough to punch a hole into the skin through erosion and fracture and to deliver the medicine/vaccine in to the tissues, without damaging the skin and the drug molecule [13, 14]. After that, the depth of the hole is increased due to further impingement of the jet and the mechanism is the same for all liquid injections. If the volumetric rate of the hole formation is less than the volumetric rate of the jet impinging the skin, backflow is noticed [15, 13], which was responsible for subject-to-subject contamination of hepatitis B virus [16, 17, 15] in the past. Once the jet impacts on the skin, the flow decelerates but it continues to travel through the hole, until it reaches a point where the velocity is no longer sufficient to puncture the hole (stagnation point). Because of the dispersion of the jet when it impacts the stagnation point, the hole takes a spherical-like shape [15, 17].

Several works regarding theoretical, experimental and numerical works on liquid jets formed by a shock wave have been performed. Apart from fundamental studies, there are applications in medicine (NFIS), or even in military (shape-charges).

Among the first theoretical studies on axisymmetric jets produced by a gas bubble is the work of Longuet-Higgins [189]. Since such jets are inertia driven in their initial stage, he modelled them by a Dirichlet hyperboloid, neglecting surface tension and gravity (see also [190]). In a similar work, Antkowiak et al. [191] examined the role of the free-surface geometry on the evolution of the jet, when a tube filled with liquid falls under gravity, by deriving an analytical expression for the velocity field. Furthermore, Katz [192] modelled the aspherical collapse of a bubble and predicted the shape and the velocity of the jet, whereas Sun et al. [193], studied theoretically and experimentally the growth and the collapse of a vapour bubble inside a micro-tube and they demonstrated the role of the thermal effects.

Leighton et al. [194, 195, 196, 197] studied theoretically and experimentally the collapse of a conical gas bubble at the end of a tube filled with liquid. This work was later extended by Symons [198], who derived an equation of motion for the liquid displacement. Bergmann et al. [199] denoted the importance of the

inward radial flow in the strength and formation of the jet on the free surface. A pressurised air filled tube inside a container filled with water was used in their apparatus. After a sudden release of the pressure in the tube, a singularity is formed on the interface. Tagawa et al. [200] produced thin supersonic micro-jets by vaporisation of liquid in an open capillary. They examined how several parameters such as the contact angle, the distance between the laser focus and the free surface and the diameter of the capillary affect the jet velocity (see also [201, 202]). Later, Hayasaka et al. [183] investigated the effect of the shock wave on the jet velocity and on the cavitation onset. They demonstrated that the jet velocity depends on the pressure impulse of the shock wave and that the probability of cavitation onset depends only on the peak pressure of the shock wave (see also [203]). In a similar device, Avila et al. [204] demonstrated the creation of two different jets, due to the expansion and the collapse of a hemispherical vapour bubble and they reported the potential of such devices in biomedical applications such as NFIS (see also [205]). Finally, Kiyama et al. [206] studied the formation of jet on the gas-liquid interface in a test tube which is induced by gravitational acceleration and hits the rigid floor and they manifested three different types of jet (normal, splashing, cavitating).

Concerning numerical studies, Ory et al. [207] studied the growth and the collapse of a vapour bubble in a narrow tube by employing the incompressible Navier-Stokes equations without phase-change (see also [208]). Free surface and surface tension were modelled using the marker-chain technique, where the free surface was described by massless particles (markers). In a similar work, López-Villa et al. [209] simulated the formation of a gaseous bubble inside a tube by a constant gas flow rate and compared their findings against experimental data. By changing the shape of the surrounding walls from cylindrical to conical, they demonstrated that the shape and the volume of the bubbles was also affected. Duchemin et al. [210] simulated a bubble burst at a free surface of liquid and the jet formation with a droplet at its tip. The marker-chain technique has been used there as well for taking into account the free surface and surface tension. In order to satisfy the boundary condition of zero tangential stress on the free surface, a least-square approach has been utilized (see also [211]). Turangan et al. [212] employed a free-Lagrangian method (FLM) for the compressible Euler equations in order to simulate the jetting collapse of air bubbles in the water. They performed simulations for a shock-induced collapse of an initially stable

bubble with applications in lithotripsy, as well as for a bubble collapse due to pressure difference between the liquid and the gas (see also [213]). In a follow-up study, Turangan et al. [214] studied shock-induced collapse and its interaction with elastic-plastic material. Finally, Peters et al. [215] simulated cavitating microjets by using a boundary integral code. They also elucidated the effect of several parameters on the jet velocity magnitude and they compared their results with the experimental findings of Tagawa et al. [200].

In the above numerical works, the compressibility effects were neglected, apart from [212]. On the contrary, the compressible Navier-Stokes equations have been modelled in the present study aiming to capture the waves created by the compressed gas and its reflection at the meniscus. To author's best knowledge, either the gas phase (air) or the vapour phase were neglected and phase change has not been modelled in past studies. In the present work, a two-phase solver able to model the liquid jet (water), the gas (air) and the cavitation regime in the nozzle (vapour), has been employed. Although the penetration into the human skin is not modelled, erosion and fracture of the skin is estimated based on the velocity of liquid jet. While in previous studies efforts to correlate the dependence of the jet velocity on the contact angle have been made [215, 200], in the present work different meniscus geometries have been investigated in order to study how the diameter and the velocity magnitude of the jet are affected.

1.4 Non dimensional numbers and cavitation regimes

The following non dimensional numbers are characteristic of the flows examined in the present work. The cavitation number C_N characterizes the potential of the flow to cavitate:

$$C_N = \frac{p_\infty - p_{sat}}{1/2\rho U^2}. \tag{1.1}$$

When $C_N < C_{NI}$, where C_{NI} is the value of C_N corresponding to cavitation inception, cavitation usually becomes increasingly developed [216]. The Froude number Fr indicates the influence of the gravity in the fluid flow:

$$Fr = \frac{U}{\sqrt{gL}}. \tag{1.2}$$

The Mach number M is a measurement of the compressibility:

$$M = \frac{U}{c}. \tag{1.3}$$

The Prandtl number Pr is defined as the ratio of momentum diffusivity to thermal diffusivity:

$$Pr = \frac{C_p \mu}{\lambda}. \tag{1.4}$$

The Reynolds number Re is the ratio of the inertial forces to the viscous forces:

$$Re = \frac{\rho U L}{\mu}. \tag{1.5}$$

The Strouhal number St is used for describing oscillating flows:

$$St = \frac{fL}{U}, \tag{1.6}$$

L here is the cavity length and f is the shedding frequency. The Weber number We measures the fluid's inertia compared to its surface tension:

$$We = \frac{\rho_l U^2 L}{\sigma}. \tag{1.7}$$

In the above relations, L is the characteristic length of the flow, U is the fluid velocity magnitude, p_∞ is the free stream pressure and $g = 9.81\, m/s^2$ is the gravitational acceleration.

Depending on the flow conditions and the geometry, different cavitation patterns can be noticed [216, 117]:

- **Bubble cavitation:** Bubbles in low pressure regions due to the nuclei of the liquid. These bubbles are travelling with the flow field and disappear in higher pressure regions.

- **Sheet cavitation:** A vapour region near the leading edge due to low pressure. It can be found in propeller blades and hydrofoils.

- **Cloud cavitation:** Many vapour bubbles forming a large vapour structure which is detached from the surface and it is travelling with the flow field.

- **Vortex cavitation:** Vortex structures in regions of low pressure can cause cavitation. It is usually found at the tip of lifting devices.

- **Supercavitation:** Large region of vapour structure surrounding the body. It can be noticed in applications with low cavitation numbers.
- **Shear cavitation:** In regions of high shear vorticity, coherent structures are formed, for example in wakes, jets or hydrofoils at high angle of attack.

1.5 Objective

The aim of the present work is to develop a numerical tool in order to predict cavitation in industrial multiphase flow applications. The main objectives are summarised:

- To develop an accurate in space and time FV method for cavitating flows in OF.
- Incorporate in the CFD solver real fluid thermodynamics, by employing high order EoS (Helmholtz).
- Provide thermodynamic closure and develop a two-phase model for liquid, vapour and gas phases.
- Implement a Mach number consistent numerical flux to handle the transition from incompressible to highly compressible flow regions.
- Perform verification and validation of the numerical scheme. The algorithm will be verified against exact solutions and validation will be performed by comparing with experimental results for several cases.
- Simulate cases of industrial interest in several different engineering fields, such as automotive (injector nozzles) or biomedical (needle-free devices).

1.6 Outline

A short outline of the following chapters is given. In Chapter 2 the numerical method is described, including the governing equations, the HEM approach, the EoS used and their derived thermodynamic closure, as well as the space and time discretization, as they have been implemented in OF. In Chapter 3 benchmark cases and fundamental studies are presented, as a mean of validation for the

developed algorithms. In Chapter 4 industrial applications and macroscale simulations are demonstrated, whereas in Chapter 5 the most important conclusions are drawn and future work is proposed. Finally, in Appendix several additional topics are discussed, such as the derivation of exact solutions for the Riemann problem, the temperature difference during an isentropic compression etc.

Chapter 2

Numerical Method

The solver described in this chapter is based on the explicit density-based OF [217] solver which is called rhoCentralFoam. RhoCentralFoam is a single phase solver using the Tadmor-Kurganov flux and ideal gas assumption. The EoS described in sections 2.2 and 2.3, the space discretization schemes of section 2.6 and the RK time advancement of section 2.7 have been implemented on this modified solver aiming to model 2 or 3 phases. A contribution of this work is the thermodynamic closure which has been derived and it is presented in 2.2.3 for the liquid-vapour mixture, in 2.2.1 for the liquid-vapour-gas mixture and in 2.3.2 for the liquid-gas mixture. In addition, the capability of simulating low Mach number flows with Mach number consistent numerical fluxes is elucidated in Fig. 2.8, whereas in Fig. 2.9 the suitability of the proposed hybrid flux for 2-phase simulations is demonstrated.

2.1 Governing Equations

Without loss of the generality, the three dimensional compressible Navier-Stokes equations with a transport equation for the gas mass fraction in conservative form are considered:

$$\frac{\partial \mathbf{U}}{\partial t} + \frac{\partial \mathbf{F}_k(\mathbf{U})}{\partial x_k} = \frac{\partial \mathbf{F}_k^V(\mathbf{U}, \nabla \mathbf{U})}{\partial x_k}, \quad in \quad \Omega, \tag{2.1}$$

where $k = 1, 2, 3$ denotes the x, y, z directions. The following initial and boundary conditions are used for the PDE system:

$$\mathbf{U}(\mathbf{x}, 0) = \mathbf{U}_0(\mathbf{x}), \quad in \quad \Omega, \tag{2.2}$$

$$\mathbf{U} = \mathbf{U}_D, \quad on \quad \partial\Omega_D, \tag{2.3}$$

$$\frac{\partial \mathbf{U}}{\partial \mathbf{n}} = \mathbf{U}_N, \quad on \quad \partial\Omega_N, \tag{2.4}$$

where $\mathbf{U} = \begin{bmatrix} \rho & \rho Y_g & \rho u_1 & \rho u_2 & \rho u_3 & \rho E \end{bmatrix}^T$ is the conservative solution vector, ρ is the mixture density, ρY_g is the gas mass fraction and $\rho\mathbf{u}$ is the mixture momentum. The convective flux tensor $\bar{\bar{\mathbf{F}}}$ can be analysed into x, y and z components: $\bar{\bar{\mathbf{F}}} = \begin{bmatrix} \mathbf{F}_1 & \mathbf{F}_2 & \mathbf{F}_3 \end{bmatrix}$, where:

$$\mathbf{F_1} = \begin{bmatrix} \rho u_1 \\ \rho Y_g u_1 \\ \rho u_1^2 + p \\ \rho u_1 u_2 \\ \rho u_1 u_3 \\ (\rho E + p) u_1 \end{bmatrix}, \quad \mathbf{F_2} = \begin{bmatrix} \rho u_2 \\ \rho Y_g u_2 \\ \rho u_2 u_1 \\ \rho u_2^2 + p \\ \rho u_2 u_3 \\ (\rho E + p) u_2 \end{bmatrix}, \quad \mathbf{F_3} = \begin{bmatrix} \rho u_3 \\ \rho Y_g u_3 \\ \rho u_3 u_1 \\ \rho u_3 u_2 \\ \rho u_3^2 + p \\ (\rho E + p) u_3 \end{bmatrix} \tag{2.5}$$

Similarly, the viscous flux tensor $\bar{\bar{\mathbf{F}}}^V$ can be analysed into x, y and z components: $\bar{\bar{\mathbf{F}}}^V = \begin{bmatrix} \mathbf{F}_1^V & \mathbf{F}_2^V & \mathbf{F}_3^V \end{bmatrix}$, where:

$$\mathbf{F_1^V} = \begin{bmatrix} 0 \\ 0 \\ \tau_{11} \\ \tau_{12} \\ \tau_{13} \\ u_k \tau_{1k} + q_1 \end{bmatrix}, \quad \mathbf{F_2^V} = \begin{bmatrix} 0 \\ 0 \\ \tau_{21} \\ \tau_{22} \\ \tau_{23} \\ u_k \tau_{2k} + q_2 \end{bmatrix}, \quad \mathbf{F_3^V} = \begin{bmatrix} 0 \\ 0 \\ \tau_{31} \\ \tau_{32} \\ \tau_{33} \\ u_k \tau_{3k} + q_3 \end{bmatrix}, \quad k = 1, 2, 3 \tag{2.6}$$

For Newtonian fluids the viscous stress tensor is given by the relation:

$$\tau_{ij} = \mu \left(\frac{\partial u_i}{\partial x_j} + \frac{\partial u_j}{\partial x_i} - \frac{2}{3} \frac{\partial u_k}{\partial x_k} \delta_{ij} \right), \quad i, j, k = 1, 2, 3. \tag{2.7}$$

Rewriting the viscous stress tensor of Eq. 2.7 in vector form:

$$\bar{\bar{\boldsymbol{\tau}}} = \mu\nabla\mathbf{U} + \mu(\nabla\mathbf{U})^T - \frac{2}{3}\mu\nabla\cdot\mathbf{U}\mathbf{I} = \mu\nabla\mathbf{U} + \mu\left((\nabla\mathbf{U})^T - \frac{2}{3}\mathrm{tr}(\nabla\mathbf{U})^T\mathbf{I}\right), \quad (2.8)$$

since $\nabla\cdot\mathbf{a} = \mathrm{tr}(\nabla\mathbf{a}) = \mathrm{tr}(\nabla\mathbf{a})^T$. The second part of Eq. 2.8 is the deviatoric part of matrix $\nabla\mathbf{U}$ multiplied by the factor 2 in the trace, since by definition, the deviatoric part of a matrix $\mathbf{A}$ is: $dev(\mathbf{A}) = \mathbf{A} - \frac{1}{3}\mathrm{tr}(\mathbf{A})\mathbf{I}$. The viscous term in the momentum equations takes the form of Eq. 2.8 in the OF implementation and it is discretized according to section 2.6.

The $\bar{\bar{\boldsymbol{\tau}}}\cdot\mathbf{u}$ term is the energy by viscous dissipation and the $\mathbf{q}$ term is the energy by conduction. The heat flux vector $\mathbf{q}$ is modelled by following Fourier's law: $\mathbf{q} = -\lambda\nabla T$, where λ is the thermal conductivity. This term is neglected in the simulations, it is stated here for completeness.

2.1.1 RANS equations

The mean values of the flow quantities have been calculated for turbulent flows, following Reynolds and Favre averaging of the NS equations [218]. According to that, a turbulent flow quantity $A(x, y, z, t)$ can be decomposed into a mean value (overbar) and a fluctuating part (prime):

$$A = \overline{A} + A' \quad (2.9)$$

The mean value is the time-averaged quantity of A:

$$\overline{A} = \frac{1}{\Delta t}\int_{t_0}^{t_0+\Delta t} A dt \quad (2.10)$$

For compressible flow, a density-weighted time average is used (Favre averaging):

$$A = \widetilde{A} + A'' \quad (2.11)$$

and now the density-weighted average of quantity A is:

$$\widetilde{A} = \frac{\overline{\rho A}}{\overline{\rho}} = \frac{1}{\overline{\rho}\Delta t}\int_{t_0}^{t_0+\Delta t} \rho A dt \quad (2.12)$$

and the mean of density weighted fluctuation is $\overline{\rho A''} = 0$. Note that $\overline{A'} = 0$ but $\overline{A''} \neq 0$, since by expanding the first equality of Eq. 2.12: $\widetilde{A} = \overline{A} + \frac{\overline{\rho' A'}}{\overline{\rho}}$, and

hence $A'' = A' - \frac{\overline{\rho' A'}}{\overline{\rho}}$. Applying the time average procedure on the compressible NS equations, Eq. 2.1 is reformed for the mean conservative variables. The stress tensor is now the sum of the viscous stress tensor and the Reynolds stress tensor (Boussinesq approximation [218]):

$$\tau_{ij} = (\mu + \mu_t)\left(\frac{\partial \widetilde{u}_i}{\partial x_j} + \frac{\partial \widetilde{u}_j}{\partial x_i} - \frac{2}{3}\frac{\partial \widetilde{u}_n}{\partial x_n}\delta_{ij}\right) - \frac{2}{3}\rho k \delta_{ij}, \quad i,j,n = 1,2,3. \tag{2.13}$$

where μ_t is the eddy viscosity and k is the turbulent kinetic energy. The heat flux in the viscous term is now redefined as: $\mathbf{q} = -(\lambda + \lambda_t)\nabla T$, where λ_t is the turbulent thermal conductivity: $\lambda_t = \frac{\mu_t C_p}{Pr_t}$. The turbulent kinetic energy in Eq. 2.13 can be neglected, since it is relatively small compared to mean flow enthalpy and the turbulent Prandtl number Pr_t is usually $\sim$0.9. The $k-\epsilon$ RNG and $k-\omega$ turbulence models have been utilised and modified following Reboud's correction [219]. After solving the PDEs for the turbulent kinetic energy k and the turbulent dissipation ϵ, the eddy viscosity μ_t is calculated from the following formula:

$$\mu_t = f(\rho) C_\mu k^2/\epsilon, \tag{2.14}$$

where $C_\mu = 0.085$. Reboud replaced ρ with $f(\rho)$ in the above eddy viscosity relation, aiming to reduce the eddy viscosity noticed in unphysically steady cavities by introducing the limiter:

$$f(\rho) = \rho_{sat,v} + \left(\frac{\rho_{sat,v} - \rho}{\rho_{sat,v} - \rho_{sat,l}}\right)^n (\rho_{sat,l} - \rho_{sat,v}), \quad n >> 1, \tag{2.15}$$

This modification has been also extended to other turbulence models with the same limiting function. Depending on the thermodynamic model, the corresponding simplifications are made. For example, in the barotropic solver the energy equation is omitted, whereas the mass transport equation is not solved in the single phase solver with phase change etc. Likewise for the laminar and the eddy viscosity, both of them are omitted in inviscid flows and the latter is omitted in laminar simulations. In cylindrical coordinates the NS equations (Eq. 2.1) are transformed to the ones described in Appendix A.

2.2 HEM

In HEM, all phases are in thermodynamic and mechanical equilibrium, in other words they share the same temperature and pressure (mixture). Thermodynamic equilibrium is achieved instantaneously, as infinite nucleation points and infinite mass transfer rate are assumed. In addition, the phase change between the liquid and the vapour is predicted through the variation in the density from the corresponding EoS. The gas, whenever modelled is non-condensable, therefore there is no phase change between the gas and the liquid. So, if the two phases are pure liquid (l) and a liquid-vapour mixture (v), the corresponding properties are:

$$\rho = (1-\alpha_v)\rho_{sat,l} + \alpha_v\rho_{sat,v} \tag{2.16}$$

$$\rho e = (1-\alpha_v)e_{sat,l}\rho_{sat,l} + \alpha_v e_{sat,v}\rho_{sat,v} \tag{2.17}$$

$$\rho h = (1-\alpha_v)h_{sat,l}\rho_{sat,l} + \alpha_v h_{sat,v}\rho_{sat,v} \tag{2.18}$$

$$\rho s = (1-\alpha_v)s_{sat,l}\rho_{sat,l} + \alpha_v s_{sat,v}\rho_{sat,v} \tag{2.19}$$

In the above relations, α_v denotes the vapour volume fraction and $\alpha_v + \alpha_l = 1$. The viscosity of the mixture is calculated by the weighted average of the liquid and vapour viscosities:

$$\mu = (1-\alpha_v)\mu_{sat,l} + \alpha_v\mu_{sat,v} \tag{2.20}$$

and the mixture speed of sound is determined by using the Wallis speed of sound formula [220] (except from the liquid-vapour mixture of 2.2.1):

$$\frac{1}{\rho c^2} = \frac{\alpha_l}{\rho_{sat,l}c^2_{sat,l}} + \frac{\alpha_v}{\rho_{sat,v}c^2_{sat,v}} \tag{2.21}$$

Expanding the HEM approach to 3 phases, which in the present study are pure liquid (l), liquid-vapour mixture (m) and non-condensable gas (g), Eq. 2.16-2.19 take an equivalent form, for example the 3-phase mixture density is:

$$\rho = (1-\beta_g)[\ (1-\alpha_v)\rho_{sat,l} + \alpha_v\rho_{sat,v}] + \beta_g\rho_g \rightarrow \rho = \beta_{lm}\rho_{lm} + \beta_g\rho_g, \tag{2.22}$$

where β_g is the gas volume fraction and $\beta_g + \beta_{lm} = 1$. The same applies for the rest quantities [221]. The density of the i component ($i = l, m, g$) can be found

from:

$$\rho_i = \frac{m_i}{V_i} = \frac{Y_i m}{\beta_i V} = \frac{Y_i}{\beta_i}\rho, \tag{2.23}$$

where β is the volume fraction of the i component and it is defined as:

$$\beta_i = \frac{V_i}{V}, \quad \sum_i \beta_i = 1, \tag{2.24}$$

and Y_i is the mass fraction of the i component, defined as:

$$Y_i = \frac{m_i}{m}, \quad \sum_i Y_i = 1. \tag{2.25}$$

The gas mass fraction is calculated from the transport equation (2^{nd} relation in Eq. 2.1) and the local vapour volume fraction can be calculated from the formula:

$$\alpha_v = \begin{cases} 0, & \rho \geq \rho_{l,sat} \\ \beta_{lm}\dfrac{\rho_{l,sat} - \rho_{lm}}{\rho_{l,sat} - \rho_{v,sat}}, & \rho < \rho_{l,sat} \end{cases} \tag{2.26}$$

The Wallis formula in order to find the speed of sound between the mixture (lm) and the gas (g) can be expressed as:

$$\frac{1}{\rho c^2} = \frac{\beta_{lm}}{\rho_{lm} c_{lm}^2} + \frac{\beta_g}{\rho_g c_g^2}, \tag{2.27}$$

where the speeds of sound c_{lm} and c_g depend on the EoS used for each phase and will be explained in detail in 2.2.1 and 2.3. Wallis formula is used for most of the thermodynamic models, unless otherwise stated (see 2.3.1).

2.2.1 Barotropic approach

The barotropic approach is the most simplified EoS among HEM, since there is no temperature effect (no energy equation is solved) and the saturation properties have been calculated assuming constant temperature T. Below the EoS for 2 phase and 3 phase mixtures are described.

Liquid-vapour mixture

For the 2 phase mixture, the modified Tait EoS for the liquid part and an isentropic-resembling relation [87] for the mixture have been used:

$$p(\rho) = \begin{cases} B\left[\left(\dfrac{\rho}{\rho_{sat,l}}\right)^n - 1\right] + p_{sat}, & \rho \geq \rho_{sat,l} \\ p_{sat} + C\left(\dfrac{1}{\rho_{sat,l}} - \dfrac{1}{\rho}\right), & \rho < \rho_{sat,l} \end{cases} \tag{2.28}$$

The speed of sound is calculated by differentiating the pressure with respect to density $c^2 = \dfrac{\partial p}{\partial \rho}$:

$$c(\rho) = \begin{cases} \sqrt{Bn\dfrac{\rho^{n-1}}{\rho^n_{sat,l}}}, & \rho \geq \rho_{sat,l} \\ \sqrt{\dfrac{C}{\rho^2}}, & \rho < \rho_{sat,l} \end{cases} \tag{2.29}$$

Compared to Eq. 2.28, which is continuous at $\rho = \rho_{sat,l}$, Eq. 2.29 is not continuous. After solving the continuity and momentum equations, Eq. 2.28 is used for calculating the pressure with respect to density only, where the saturation properties have been calculated at temperature $300\,K$. Although this method is robust, it lacks in predicting the temperature effects.

Liquid-vapour-gas mixture, linear EoS

Here the single fluid model for the liquid and mixture is extended by a transport equation for the non-condensable gas. A linear barotropic model has been utilized for the liquid and mixture. The density ρ_{lm} of the latter is:

$$\rho_{lm} = \rho_{l,sat} + \frac{1}{c^2}(p - p_{sat}), \quad c = \begin{cases} c_l, & p \geq p_{sat} \\ c_m, & p < p_{sat} \end{cases} \tag{2.30}$$

The gas phase, has been modelled by an isothermal ideal gas EoS and thus, the gas density is given by:

$$\rho_g = \frac{p}{R_g T_{ref}}, \tag{2.31}$$

where the reference temperature is $T_{ref} = 293.15\,K$ and the specific gas constant is $R_g = 287.06\,J/(kg\,K)$. The barotropic approach is followed in cases where the temperature difference is negligible (see Appendix C).

Differentiating isentropically Eq. (2.30) with respect to density, constant speed of sound for the liquid and mixture is found for water: $c_l = 1482.35\,m/s$ and $c_m = 1\,m/s$, following Brennen [220] and Örley et al. [88]. For the ideal gas,

the speed of sound is calculated from:

$$c_g = \sqrt{R_g T_{ref}}, \tag{2.32}$$

In the three phase mixture, the speed of sound between lm and g phases is determined by the Wallis speed of sound [216, 220]:

$$\frac{1}{\rho c^2} = \frac{1-\beta_g}{\rho_{lm} c_{lm}^2} + \frac{\beta_g}{\rho_g c_g^2}, \tag{2.33}$$

After solving the continuity equation, the transport equation for the gas mass fraction follows, then the pressure equation is solved accompanied by the momentum equation. In order to calculate the pressure of the mixture, a closed form equation of state describing the co-existence of three phases is employed from Eq. (2.22):

$$\rho = \beta_{lm}\Big[\rho_{l,sat} + \frac{1}{c^2}(p - p_{sat})\Big] + \beta_g \frac{p}{R_g T_{ref}}, \tag{2.34}$$

replacing the volume fraction β_g from Eq. (2.23) and eliminating β_{lm} by using Eq. (2.25) and Eq. (2.31), a quadratic equation for the pressure is derived:

$$\mathcal{A}p^2 + \mathcal{B}p + \mathcal{C} = 0, \tag{2.35}$$

where

$$\mathcal{A} = \frac{1}{c^2}, \tag{2.36}$$

$$\mathcal{B} = \rho(Y_g - 1) + \rho_{l,sat} - \frac{p}{c^2} - \frac{Y_g \rho R_g T_{ref}}{c^2}, \tag{2.37}$$

$$\mathcal{C} = Y_g \rho R_g T_{ref}\left(\frac{p_{sat}}{c^2} - \rho_{l,sat}\right). \tag{2.38}$$

In the case of two real solutions $p_1, p_2 \in \mathbb{R}$, the largest root of Eq. (2.35) is kept. The speed of sound in Eq. (2.36), (2.37) and (2.38) is set to either c_l or c_m, depending on the pressure at the previous time step for identifying the liquid or mixture regions. Therefore, Eq. (2.35) is solved iteratively, in case the computed pressure does not fulfil the original assumption. In practice, the algorithm is repeated for no more than three iterations.

Liquid-vapour-gas mixture, Tait-isentropic EoS

However, if the linear relation is replaced with the modified Tait equation and the isentropic-like relation of Eq. 2.28, there is no exact solution for the pressure and it has to be iteratively solved. Solving Eq. 2.28 for density:

$$\rho_{lm} = \begin{cases} \rho_{sat,l}\left(\dfrac{p - p_{sat}}{B} + 1\right)^{1/n}, & p \geq p_{sat} \\ \left(\dfrac{1}{\rho_{sat,l}} - \dfrac{p - p_{sat}}{C}\right)^{-1}, & p < p_{sat} \end{cases} \tag{2.39}$$

whereas the gas density here is given by the isentropic gas EoS:

$$\rho_g = \left(\frac{p}{C_2}\right)^{1/\gamma} \tag{2.40}$$

The gas phase is predicted by the homogeneous transport equation for the gas mass fraction. The density of the mixture can be found from Eq. 2.23, 2.24:

$$\frac{\rho Y_g}{\rho_g} + \frac{\rho Y_{lm}}{\rho_{lm}} = 1 \rightarrow \rho = \frac{\rho_g \rho_{lm}}{Y_g \rho_{lm} + Y_{lm} \rho_g} \tag{2.41}$$

A closed form for the pressure is derived by replacing Eq. 2.39 and 2.40 into Eq. 2.41:

$$\mathcal{F}(p) = \rho Y_g \rho_{lm}(p) + \rho Y_{lm} \rho_g(p) - \rho_g(p) \rho_{lm}(p) \tag{2.42}$$

The derived Eq. 2.42 is non-linear and has no apparent exact solution. Thus, the pressure is iteratively found by using the Newton-Raphson method of Eq. 2.43 and then the density and the volume fraction for each phase are calculated. It has to be mentioned here that only the solutions when $\mathcal{F}'(p) < 0$ are of interest.

$$p^{k+1} = p^k - \frac{\mathcal{F}(p)}{\mathcal{F}'(p)} \tag{2.43}$$

The pressure within the Newton-Raphson iterations is relaxed and limited to a minimum value p_{min}:

$$p^{k+1} = max\Big(p_{min}, p^{k+1} rlx + p^k (1 - rlx)\Big) \tag{2.44}$$

Here the superscript k denotes the Newton-Raphson iterations within the time step loop from time n to $n+1$ and rlx is a relaxation coefficient. So after solving the continuity and the mass transport equations, the pressure equation 2.42 is

iteratively solved until a convergence criterion is satisfied ($|\mathcal{F}(p)| \leq 10^{-6}$).

2.2.2 HEM with temperature effects (Liquid-vapour mixture)

The second thermodynamic model which has been utilized, is a more sophisticated extension of the previous barotropic model, since the saturation properties depend on temperature [28, 222]. In this case, the modified Tait equation is used for the liquid, the ideal gas EoS for the vapour and the Wallis formula for the speed of sound in the mixture regime. This model is based on the assumption that the latent heat is constant and it is calculated based on the initial temperature $T_0 = 300K$, which is valid only for a small variation of the temperature. Moreover, it cannot predict transcritical to supercritical transitions. The pressure is given by the following three-step equation as a function of density and temperature:

$$p(\rho, T) = \begin{cases} B\left[\left(\dfrac{\rho}{\rho_{sat,l}(T)}\right)^n - 1\right] + p_{sat}(T), & \rho \geq \rho_{sat,l}(T) \\ p_{sat}(T), & \rho_{sat,v}(T) < \rho < \rho_{sat,l}(T) \\ \rho RT, & \rho < \rho_{sat,v}(T) \end{cases} \tag{2.45}$$

and the internal energy is given by the following equation:

$$e(T) = \begin{cases} C_{v,l}(T - T_0) + e_{l0}, & \rho \geq \rho_{sat,l}(T) \\ \dfrac{\alpha\rho_{sat,v}(T)e_{vap}(T) + (1-\alpha)\rho_{sat,l}(T)e_{liq}(T)}{\rho}, & \rho_{sat,v}(T) < \rho < \rho_{sat,l}(T) \\ C_{v,v}(T - T_0) + L_v(T_0) + e_{l0}, & \rho < \rho_{sat,v}(T) \end{cases} \tag{2.46}$$

where e_{vap} and e_{liq} stand for the internal energy of the liquid and vapour from the first and the third step respectively. After calculating the solution vector and thus the total energy is known, the Newton-Raphson method has been employed for the following function in order to calculate the temperature:

$$\mathcal{F}(T) = e(T) - E(T) + \frac{1}{2}(u^2 + v^2) = 0 \tag{2.47}$$

Once the Newton-Raphson algorithm has converged, the pressure and the volume fraction are calculated and then the algorithm advances to the next time step.

The saturation properties have to be calculated for each Newton-Raphson iteration, since they depend on the temperature and they are given by the following formulas:

$$ln\left(\frac{p_{sat}(T)}{p_c}\right) = \frac{T_c}{T}\sum_{i=1}^{7} a_i \theta^{\hat{a_i}}, \tag{2.48}$$

$$\frac{\rho_{sat,l}(T)}{\rho_c} = \sum_{i=1}^{7} b_i \theta^{\hat{b_i}}, \tag{2.49}$$

$$ln\left(\frac{\rho_{sat,v}(T)}{\rho_c}\right) = \sum_{i=1}^{7} c_i \theta^{\hat{c_i}}, \tag{2.50}$$

where $\theta = T/T_c$. The coefficients $\hat{a_i}, \hat{b_i}, \hat{c_i}$ for n-Dodecane are given in Table 2.1 for $\rho_c = 226.55\, kg/m^3$, $p_c = 1817000\, Pa$, $\gamma = 1.03$. It must be mentioned here that the previous equations are valid as long as the temperature is within the range: $T \in [T_r, T_c]$, where r, c subscripts denote the triple point and the critical point respectively. Therefore, the applicability range for n-Dodecane is: $T \in [T_r = 273.15, T_c = 658.1]\, K$.

Table 2.1: Coefficients in Eq. 2.48, 2.49, 2.50 for n-Dodecane. The coefficients are calculated in order to give the same saturation conditions as the Helmholtz energy EoS.

Index	a_i	$\hat{a_i}$	b_i	$\hat{b_i}$	c_i	$\hat{c_i}$
1	−0.03359	0	1.37610	0	−0.39275	0
2	−8.54218	1	11.88513	1	−19.73929	1
3	3.20579	3	−69.63935	2	78.72869	2
4	11.27780	4	297.58733	3	−361.4296	3
5	7.66350	5	−717.4947	4	779.84876	4
6	−7.09773	6	888.91121	5	−899.4366	5
7	−0.03359	0	−438.5464	6	331.66738	6

In conclusion, this method is efficient but not so robust as the barotropic model and it suffers from limitations in the temperature range, compared to the Helmholtz EoS, which will be presented next (see also section 2.4 where the different thermodynamic models are compared).

2.2.3 Helmholtz energy EoS for liquid-vapour mixture

The derivation of the thermodynamic properties from the Helmholtz energy is described in this section. It has to be clarified here that this methodology is applicable for any material, assuming that there are experimental data to calibrate

the aforementioned energy equation. The EoS for calculating the thermodynamic properties of a material can be expressed using the Helmholtz energy, having as independent variables the density and the temperature [115]:

$$a(\rho, T) = a^0(\rho, T) + a^r(\rho, T) \tag{2.51}$$

the above in dimensionless form becomes:

$$\frac{a(\rho, T)}{RT} = \alpha^0(\delta, \tau) + \alpha^r(\delta, \tau), \tag{2.52}$$

where $\delta = \rho/\rho_c$, $\tau = T_c/T$. The dimensionless Helmholtz energy contribution of the ideal gas can be written in the form:

$$\alpha^0 = a_1 + a_2\tau + ln\delta + (c_0 - 1)ln\tau + \sum_{k=1}^{5} c_k ln\left[1 - exp\left(-\frac{u_k\tau}{T_c}\right)\right], \tag{2.53}$$

where a_1, a_2 are arbitrary values set by the reference state. The residual Helmholtz energy can take a complicated form depending on the material. For instance, the residual Helmholtz energy for the n-Dodecane is written in the following non-dimensional form [115]:

$$\begin{aligned}\alpha^r = {} & n_1\delta\tau^{0.32} + n_2\delta\tau^{1.23} + n_3\delta\tau^{1.5} + n_4\delta^2\tau^{1.4} + n_5\delta^3\tau^{0.07} + n_6\delta^7\tau^{0.8} + n_7\delta^2\tau^{2.16}e^{-\delta} \\ & + n_8\delta^5\tau^{1.1}e^{-\delta} + n_9\delta\tau^{4.1}e^{-\delta^2} + n_{10}\delta^4\tau^{5.6}e^{-\delta^2} + n_{11}\delta^3\tau^{14.5}e^{-\delta^3} + n_{12}\delta^4\tau^{12.0}e^{-\delta^3}.\end{aligned} \tag{2.54}$$

Equations similar to 2.52 can be manipulated in order to obtain all thermodynamic properties, like pressure, internal energy, enthalpy, entropy and speed of sound as a function of density and temperature. The interested reader is addressed to [115] for all the necessary manipulations needed and the coefficients of Eq. 2.54 for n-Dodecane. Saturation conditions are identified by using the Maxwell criterion. i.e. the pressure for which the Gibbs energy of the liquid and the vapour phases are equal. Upon identifying the saturation pressure as a function of temperature, the saturation dome may be identified; within the saturation dome fluid properties are determined by using the mixture assumption based on volume fraction α (Eq. 2.16-2.21).

The aforementioned procedure can be performed on the fly, during code execution. However, in practice it requires root finding of non-linear equations, since both Helmholtz equation and all the properties derived from it, are naturally expressed as a function of density ρ and temperature T, whereas the flow solver

calculates density ρ and internal energy e. In other words, at each time step the conservative variables $(\rho, \rho E)$ must be transformed to ρ, T and then they can be used to derive pressure and speed of sound for the next calculation step. This can be achieved by using for example the Newton-Raphson method, however it is very time consuming and inefficient.

Tabulated data technique

Instead of solving the Helmholtz EoS for each time step (using the Newton-Raphson method or similar), a similar technique as the one employed by Dumbser et al. [94] has been employed. In the present work, an unstructured thermodynamic table has been used (instead of the Cartesian used in [94]), which has been constructed prior to the simulations, containing all the thermodynamic properties derived from the Helmholtz EoS. This way, the mismatch in the variables needed as input in the Helmholtz EoS (ρ, T) and the ones calculated from the NS equations $(\rho, \rho E)$ is handled by numerical inversion. In other words, based on $(\rho, \rho E)$ the rest thermodynamic properties are calculated. Static linked lists have been used in order to split the thermodynamic table into smaller groups of data and search only the group that has the desired values within its range. The resulting algorithm is much more efficient than the on-the-fly calculation of the Helmholtz EoS, by almost one order of magnitude of the computational time.

The unstructured thermodynamic table for each material is built by selecting an appropriate range for the density and the internal energy: $\rho_{min} \leq \rho \leq \rho_{max}$ and $e_{min} \leq e \leq e_{max}$ that define a 2-D table $\Sigma = [\rho_{min}, \rho_{max}] \times [e_{min}, e_{max}]$, which should enclose the expected conditions for each simulation. The thermodynamic table Σ, which has been created for each material, is discretized with quadrilateral elements, in an unstructured way. For example, an unstructured grid of approximately $40,000$ elements has been created for n-Dodecane (Fig. 2.1) and similarly for Oxygen O_2 (Fig. 2.2). The grids has been refined around the saturation curve in order to accurately capture the large variation of the thermodynamic properties in this area (e.g. for speed of sound or internal energy). Indicatively for the n-Dodecane and Oxygen, 3-D phase diagrams derived from the Helmholtz energy EoS are shown in Fig. 2.3 and 2.4 respectively, expressing pressure, internal energy and speed of sound as a function of density and temperature.

During the algorithm execution, after calculating the conservative vector in

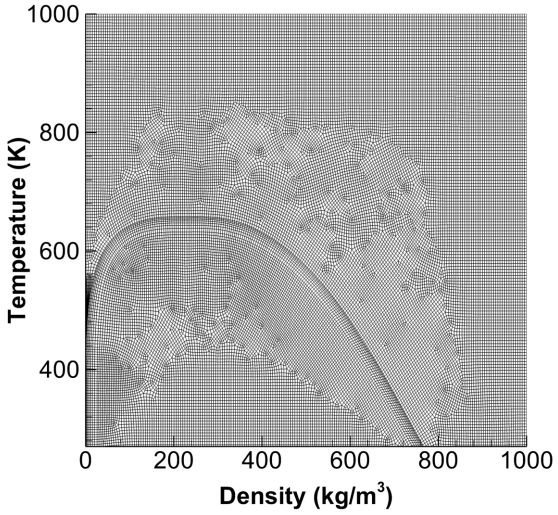

Figure 2.1: Unstructured thermodynamic grid of approximately 40,000 finite elements for n-Dodecane, refined around the saturation curve in order to capture the rapid change in the thermodynamic properties.

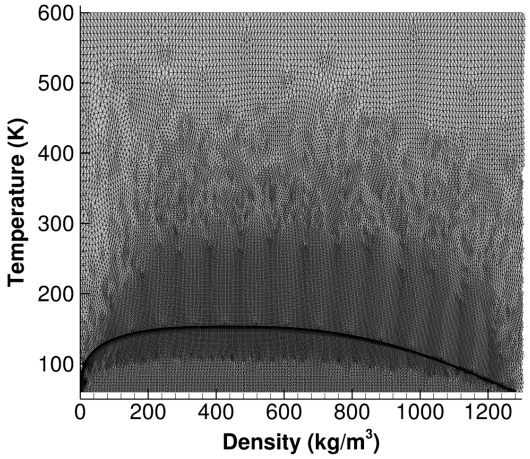

Figure 2.2: Unstructured thermodynamic grid of approximately 34,000 finite elements for Oxygen, refined around the saturation curve in order to capture the rapid change in the thermodynamic properties.

the time loop, and hence the density and the internal energy are known, the element of the thermodynamic grid in which each cell of the computational domain belongs may be determined, by employing a static linked-list algorithm. Then using a FE bilinear interpolation, any thermodynamic property ϕ in the space Σ can be approximated as:

$$\phi(\rho, e) = \sum_{n}^{nodes} N_n(\rho, e) b_n, \tag{2.55}$$

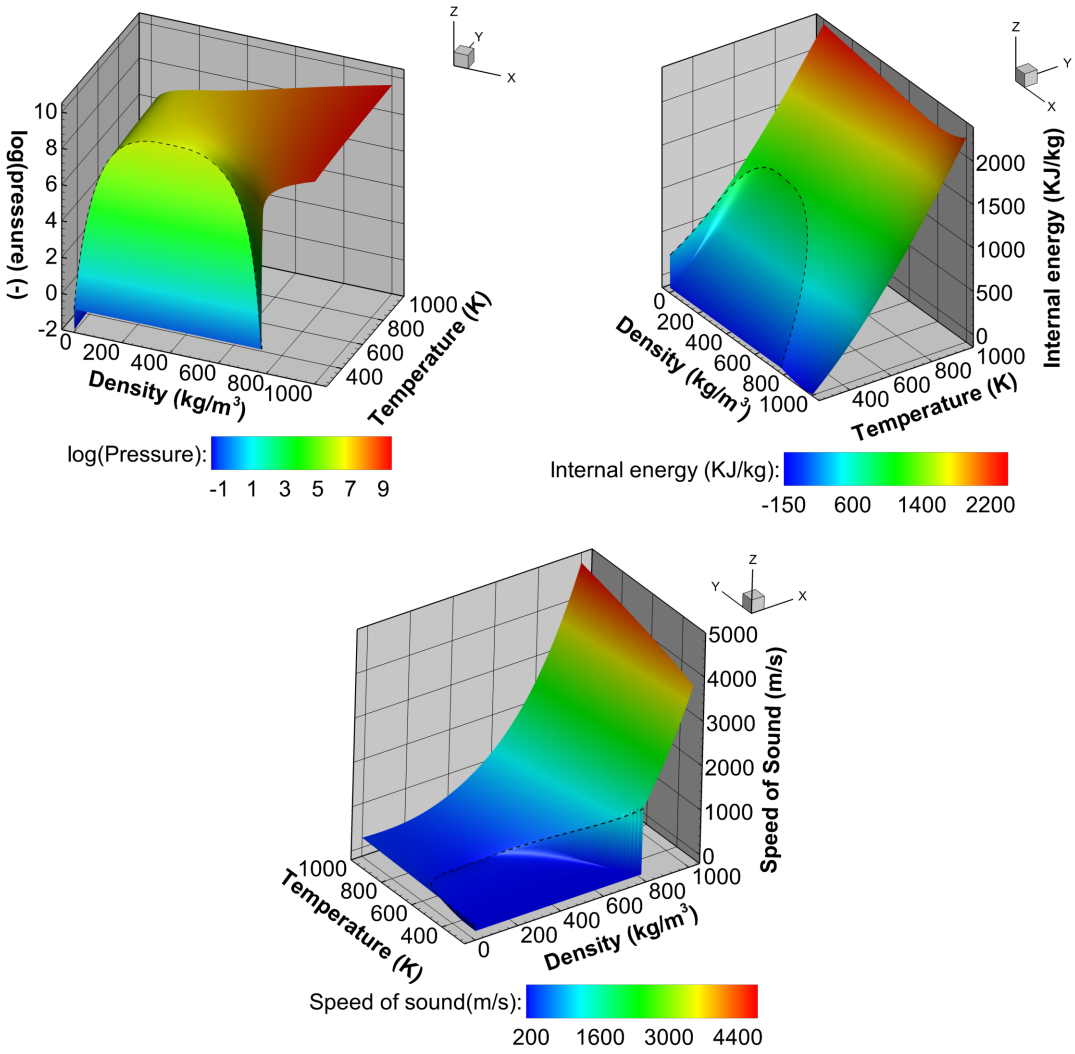

Figure 2.3: Three dimensional phase diagrams for n-Dodecane, where the dashed line is the saturation line. The properties have been derived from the Helmholtz EoS.

where ϕ can be either pressure, temperature and speed of sound, which are needed for the flux calculation (see section 2.6), or any other property such as enthalpy, entropy needed during the post-processing stage. The unknown coefficients of ϕ are notated by b and N is the shape function of node n:

$$N_n(\rho, e) = 1 + (e - e_n) + (\rho - \rho_n) + (e - e_n)(\rho - \rho_n). \tag{2.56}$$

The b coefficients of property ϕ for each element are calculated by solving the following equation:

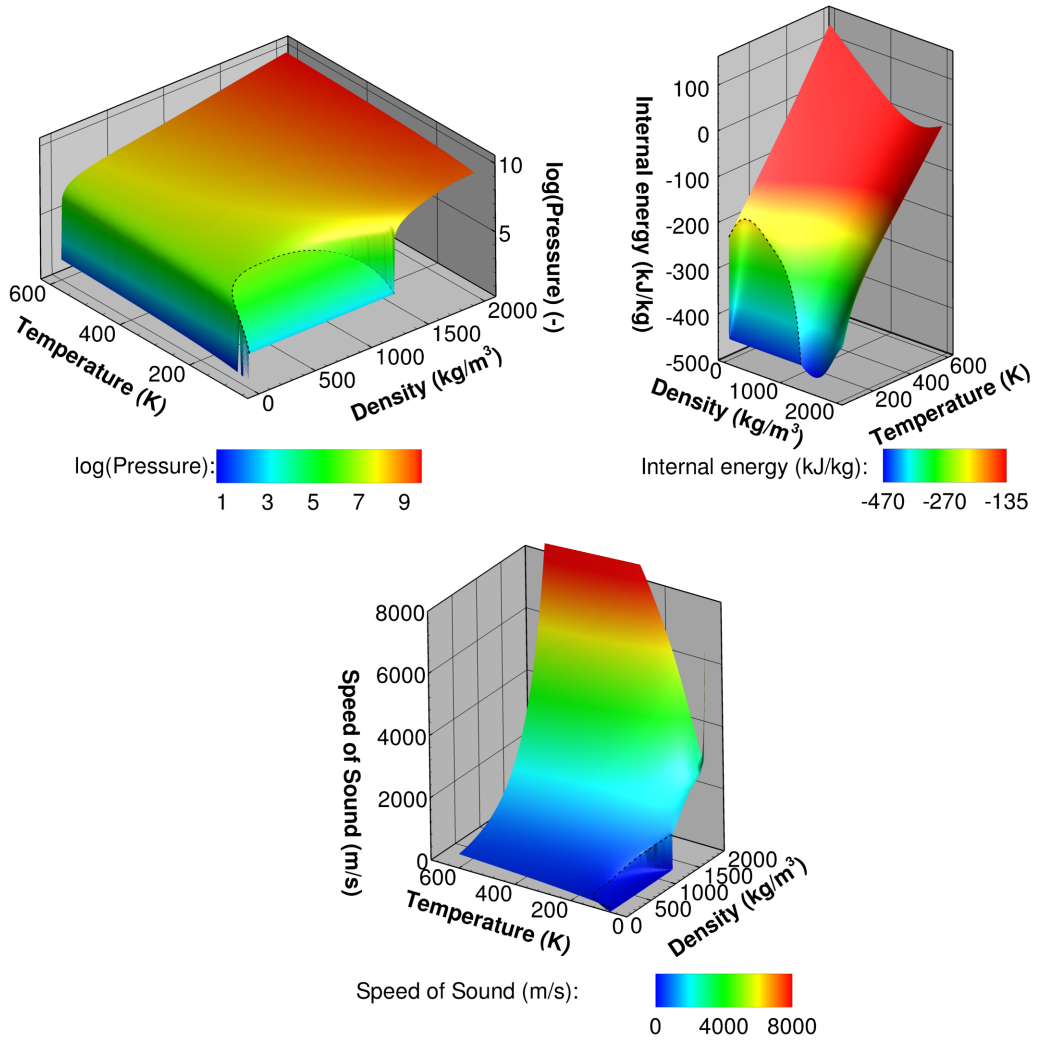

Figure 2.4: Three dimensional phase diagrams for Oxygen, where the dashed line is the saturation line. The properties have been derived from the Helmholtz EoS.

$$[\mathbf{N}]\mathbf{b} = \boldsymbol{\phi} \rightarrow \begin{bmatrix} N_{11} & N_{12} & N_{13} & N_{14} \\ N_{21} & N_{22} & N_{23} & N_{24} \\ N_{31} & N_{32} & N_{33} & N_{34} \\ N_{41} & N_{42} & N_{43} & N_{44} \end{bmatrix} \begin{bmatrix} b_1 \\ b_2 \\ b_3 \\ b_4 \end{bmatrix} = \begin{bmatrix} \phi_1 \\ \phi_2 \\ \phi_3 \\ \phi_4 \end{bmatrix}, \tag{2.57}$$

where ϕ_i are the values of the property at the nodes of the quadrilateral element (known from the thermodynamic table) and N_{mn} is the shape function of node n evaluated at node m:

$$N_{mn} = 1 + (e_m - e_n) + (\rho_m - \rho_n) + (e_m - e_n)(\rho_m - \rho_n). \tag{2.58}$$

The most efficient way to find the coefficient $\mathbf{b}$, is to calculate in advance and store the inverse of the mass matrix $[\mathbf{N}]$ for all elements before time advancement begins. That way, the coefficients $\mathbf{b}$ for each thermodynamic property ϕ can be found:

$$\mathbf{b} = [\mathbf{N}]^{-1}\boldsymbol{\phi} \tag{2.59}$$

After finding the conservative vector within the time loop, each thermodynamic property ϕ can be approximated from Eq. 2.55.

2.3 Liquid-gas flows without phase change

In this section, the EoS with temperature effects for 2-phase flows of liquid and gas are described. The transport equation for the gas is homogeneous and thus, no phase change is predicted.

2.3.1 Stiffened gas-ideal gas

The liquid density from the stiffened gas EoS is given by:

$$\rho_l = \frac{p + p_\infty}{(\gamma_l - 1)C_{vl}T}, \tag{2.60}$$

and the gas density using the ideal gas EoS is:

$$\rho_g = \frac{p}{R_g T}, \tag{2.61}$$

which is similar to Eq. 2.31, but now the temperature is not constant. The density of the mixture can be found from Eq. 2.23, 2.24:

$$\frac{\rho Y_g}{\rho_g} + \frac{\rho Y_l}{\rho_l} = 1 \rightarrow \rho = \frac{\rho_g \rho_l}{Y_g \rho_l + Y_l \rho_g} \tag{2.62}$$

Replacing Eq. 2.60 and 2.61 into Eq. 2.62, a quadratic EoS for the pressure with respect to temperature and density is derived:

$$\mathcal{A}p^2 + \mathcal{B}p + \mathcal{C} = 0, \tag{2.63}$$

where

$$\mathcal{A} = \frac{-1}{R_g(\gamma_l - 1)C_{vl}T^2}, \tag{2.64}$$

$$\mathcal{B} = \frac{\rho Y_l}{R_g T} + \frac{\rho Y_g}{(\gamma_l - 1) C_{vl} T} + \frac{p_\infty}{R_g (\gamma_l - 1) C_{vl} T^2}, \tag{2.65}$$

$$\mathcal{C} = \frac{\rho Y_g p_\infty}{(\gamma_l - 1) C_{vl} T}. \tag{2.66}$$

In the case of two real solutions $p_1, p_2 \in \mathbb{R}$, the largest root is kept. The internal energy of the liquid, based on the stiffened gas EoS can be derived from:

$$de_l = C_{vl} dT + \left[T \left(\frac{\partial p}{\partial T} \right)_v - p \right] dv, \quad dv_l = -\frac{1}{\rho_l^2} d\rho_l. \tag{2.67}$$

Using Eq. 2.60, Eq. 2.67 becomes:

$$de_l = C_{vl} dT - \frac{p_\infty}{\rho_l^2} d\rho_l \tag{2.68}$$

and after integration:

$$e_l = C_{vl} T + \frac{p_\infty}{\rho_l} \rightarrow e_l = \frac{p + \gamma_l p_\infty}{(\gamma_l - 1)\rho_l}, \tag{2.69}$$

which are the two expressions of internal energy for stiffened gas with respect to temperature and pressure respectively. Similarly, the internal energy of the gas is given by the following relation, assuming it is ideal:

$$e_g = C_{vg} T. \tag{2.70}$$

The internal energy of the mixture is calculated by the weighted average of the two phases:

$$e = e_g Y_g + e_l Y_l, \tag{2.71}$$

replacing the internal energy of the liquid and the gas from Eq. 2.69, 2.70 into Eq. 2.71 and using Eq. 2.60 the equation for the internal energy in terms of pressure, temperature and mass fraction is derived:

$$T = \frac{e}{C_{vg} Y_g + C_{vl} Y_l + \frac{Y_l (\gamma_l - 1) C_{vl} p_\infty}{p + p_\infty}} \tag{2.72}$$

So after solving the NS equations accompanied by the transport equation for the gas mass fraction, and thus, the internal energy is known, the pressure and temperature equations 2.63, 2.72 are iteratively solved. The temperature is calculated based on an initial pressure guess and then the pressure is calculated

from the quadratic equation. This algorithm is repeated until a convergence criterion is satisfied, which in this case is a tolerance between the initial and the final pressure. The speed of sound of the mixture based on the Gibbs energy is:

$$c = \sqrt{\frac{f_1 T}{f_0 - \frac{f_1}{f_{pm}}}}, \tag{2.73}$$

where f_0, f_1 and f_{pm} are given by:

$$f_0 = 1 - \frac{Y_l \rho (\gamma_l - 1) T p_\infty C_{vl}}{(p + p_\infty)^2}, \tag{2.74}$$

$$f_1 = R_g Y_g + Y_l (\gamma_l - 1) C_{vl} \frac{p}{p + p_\infty}, \tag{2.75}$$

$$f_{pm} = Y_g C_{pg} + Y_l C_{pl} \tag{2.76}$$

2.3.2 Tait-ideal gas

A similar approach is followed here, but now instead of the stiffened gas EoS, Tait EoS has been utilised for the liquid. The density of the liquid is given from the first step of Eq. 2.28:

$$\rho_l = \rho_{sat,l} \left(\frac{p - p_{sat}}{B} + 1 \right)^{1/n}, \tag{2.77}$$

whereas the gas density is given from Eq. 2.61 and the expression for the mixture density is Eq. 2.62. After replacing the density expression for each phase in the latter, the closed form of the pressure equation is derived:

$$\rho Y_g \rho_{sat,l} \left(\frac{p - p_{sat}}{B} + 1 \right)^{1/n} + \rho Y_l \frac{p}{R_g T} = \rho_{sat,l} \frac{p}{R_g T} \left(\frac{p - p_{sat}}{B} + 1 \right)^{1/n} \tag{2.78}$$

The above equations is solved iteratively with Newton-Raphson method by defining the pressure function $\mathcal{F}(p)$ and its derivative $\mathcal{F}'(p)$:

$$\mathcal{F}(p) = \rho Y_g \rho_{sat,l} \left(\frac{p - p_{sat}}{B} + 1 \right)^{1/n} + \rho Y_l \frac{p}{R_g T} - \rho_{sat,l} \frac{p}{R_g T} \left(\frac{p - p_{sat}}{B} + 1 \right)^{1/n}, \tag{2.79}$$

$$\mathcal{F}'(p) = \Bigg[- p\rho_{sat,l}\left(\frac{p-p_{sat}}{B}+1\right)^{1/n-1} - Bn\rho_{sat,l}\left(\frac{p-p_{sat}}{B}+1\right)^{1/n} + Bn\rho Y_l + \rho_{sat,l}R_g\rho Y_g T\left(\frac{p-p_{sat}}{B}+1\right)^{1/n-1}\Bigg] \Bigg/ \left(BnTR_g\right) \tag{2.80}$$

Similar to section 2.3.1, starting from Eq. 2.67 and making use of Eq. 2.77, the internal energy of the liquid is given by:

$$e_l = C_{vl}(T-T_{ref}) + \frac{1}{(n-1)\rho_{sat,l}}\left(\frac{p-p_{sat}}{B}+1\right)^{-1/n}\Bigg[(n-1)p_{sat}\left(\frac{p-p_{sat}}{B}+1\right)^{1/n} - (n-1)p_{sat} + Bn - B + B\left(\frac{p-p_{sat}}{B}+1\right) - Bn\left(\frac{p-p_{sat}}{B}+1\right)^{1/n}\Bigg] \tag{2.81}$$

and in a short form:

$$e_l = C_{vl}(T-T_{ref}) + \mathcal{D}(p), \tag{2.82}$$

where

$$\mathcal{D}(p) = \frac{1}{(n-1)\rho_{sat,l}}\left(\frac{p-p_{sat}}{B}+1\right)^{-1/n}\Bigg[(n-1)p_{sat}\left(\frac{p-p_{sat}}{B}+1\right)^{1/n} - (n-1)p_{sat} + Bn - B + B\left(\frac{p-p_{sat}}{B}+1\right) - Bn\left(\frac{p-p_{sat}}{B}+1\right)^{1/n}\Bigg]. \tag{2.83}$$

Similarly, the internal energy of the gas, assuming it is ideal:

$$e_g = C_{vg}(T-T_{ref}) + L_{v0}. \tag{2.84}$$

The temperature equation is derived by Eq. 2.71 by using Eq. 2.82, 2.83, 2.84:

$$T = \frac{\rho e - \rho Y_g L_{v0} - \rho Y_l \mathcal{D}(p)}{\rho Y_g C_{vg} + \rho Y_l C_{vl}} + T_{ref}. \tag{2.85}$$

After solving the NS and the transport equations and thus, the internal energy is known, the pressure and temperature equations 2.78, 2.85 are iteratively solved. The temperature is calculated based on an initial guess for the pressure and then the pressure is calculated from the quadratic equation. This algorithm is repeated until a convergence criterion is satisfied, which in this case is a tolerance between the initial and the final pressure.

2.4 Evaluation of the different EoS

The thermodynamic models presented in 2.2, 2.3 are compared against the NIST database [223] in this section, where n-Dodecane was selected as the working liquid. In Fig. 2.5 the pressure and the speed of sound for the different utilized EoS suitable for modelling phase-change are plotted. The stiffened gas EoS is not suitable for modelling cavitation as the saturated liquid density is significantly different from the physical saturation value [28]. If the parameters of [224] are used in the stiffened gas EoS for dodecane, negative pressures are obtained for reasonable densities at the liquid state. And vice versa, in order for the density, pressure and speed of sound to match the experimental data, non-physical values for the specific heat at constant pressure must be used [28].

Fig. 2.5 can be utilized as a preliminary validation of the Helmholtz EoS implementation, since the Helmholtz curve appears to be in good agreement with the NIST database. The formulation of subsection 2.2.2 is not so accurate compared to the Helmholtz EoS at large pressures and temperatures, although it considers temperature effects (see Fig. 2.5). This is due to the fact that the latent heat is constant regardless the temperature variation and because the second term in the RHS of Eq. 2.81 is not taken into account. In practice, convergence problems in the Newton-Raphson method have been noticed when there is significant temperature or pressure increase. The barotropic models of subsection 2.2.1 are less accurate in high pressures and a large deviation in the speed of sound between such models and the Helmholtz EoS is noticed in the mixture regime. More specifically, in the Tait-isentropic vapour approach, the speed of sound is estimated by the second step of Eq. 2.29, which is the derivative of the isentropic relation, instead of using the Wallis formula or similar. Among the four models, the less accurate is the linear EoS utilized for simulating liquid-vapour-gas mixtures, where the speed of sound is a step function and large deviation between the linear EoS and NIST at high pressures has been noticed.

2.5 Mass transfer models

Although this work focuses mostly on HEM, mass transfer models have been developed for future use. In order to model phase-change, condensation and evaporation source terms are added in the previously homogeneous transport

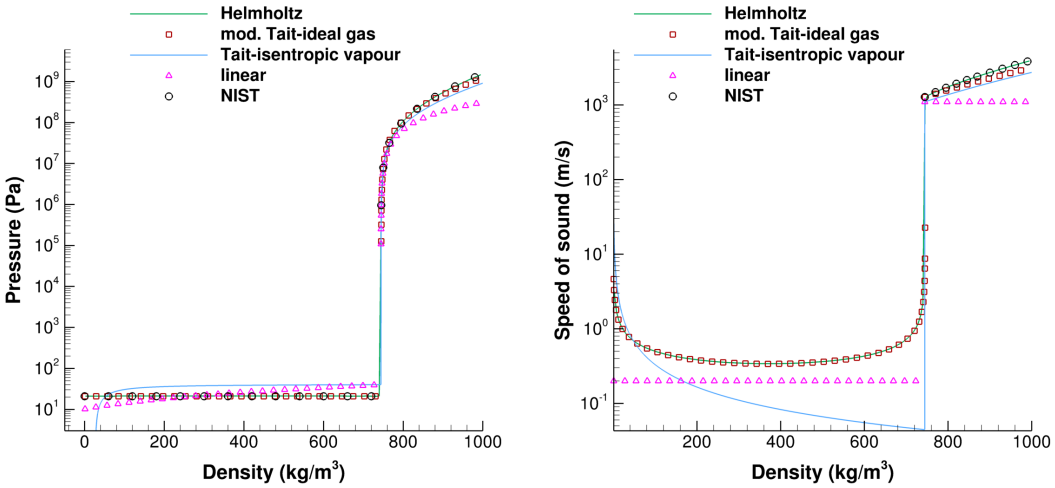

Figure 2.5: Pressure (left) and speed of sound (right) of n-Dodecane with respect to density for the thermodynamic models presented in 2.2, 2.3. The solid green line is the Helmholtz EoS (2.2.3), the squares denote the modified Tait-ideal gas EoS which consider temperature effects (2.2.2), the solid blue line is the barotropic approach by employing the Tait-isentropic vapour EoS, whereas the triangulars represent the linear EoS for the liquid-vapour mixture which is also barotropic (the first and the second subsections in 2.2.1 respectively). Finally, the circles represent the NIST database [223].

equation for the gas mass fraction of section 2.3. Therefore, the liquid now becomes vapour and vice versa through the transport equation and not through the variation of the density as it was predicted by the EoS in section 2.2. The Zwart-Gerber-Belamri (ZGB) [80] and the Schnerr and Sauer [82] models have been implemented in OF.

Concerning the ZGB model, the evaporation and condensation terms are respectively:

$$R_e = F_{vap}\frac{3\alpha_{nuc}\alpha_l\rho_v}{R_B}\sqrt{\frac{2}{3}\frac{p_{sat}-p}{\rho_l}}, \quad p \leq p_{sat} \tag{2.86}$$

$$R_c = F_{cond}\frac{3\alpha_v\rho_v}{R_B}\sqrt{\frac{2}{3}\frac{p-p_{sat}}{\rho_l}}, \quad p \geq p_{sat} \tag{2.87}$$

where $R_B = 10^{-6}\,m$ is the bubble radius, $\alpha_{nuc} = 5 \cdot 10^{-4}$ is the nucleation site volume fraction, $F_{vap} = 50$ and $F_{cond} = 0.001$ are the evaporation and condensation coefficients respectively. Regarding the Schnerr and Sauer model the terms are as follows:

$$R_e = \frac{\rho_v\rho_l}{\rho}\alpha_v\alpha_l\frac{3}{R_B}\sqrt{\frac{2}{3}\frac{p_{sat}-p}{\rho_l}}, \quad p \leq p_{sat} \tag{2.88}$$

$$R_c = \frac{\rho_v \rho_l}{\rho} \alpha_v \alpha_l \frac{3}{R_B} \sqrt{\frac{2}{3} \frac{p - p_{sat}}{\rho_l}}, \quad p \geq p_{sat} \tag{2.89}$$

2.6 FV discretization

The Navier-Stokes equations (Eq. 2.1) can be also expressed in an integral form, let $\Omega \in \mathbb{R}^3$ be a physical domain and $S = \partial\Omega \in \mathbb{R}^2$ its boundary:

$$\int_\Omega \frac{\partial \mathbf{U}}{\partial t} d\Omega + \int_\Omega \nabla \cdot \bar{\bar{\mathbf{F}}}(\mathbf{U}) d\Omega = \int_\Omega \nabla \cdot \bar{\bar{\mathbf{F}}}^V(\mathbf{U}) d\Omega. \tag{2.90}$$

Applying Gauss theorem:

$$\int_\Omega \frac{\partial \mathbf{U}}{\partial t} d\Omega + \int_S \bar{\bar{\mathbf{F}}}(\mathbf{U}) \cdot \mathbf{n} dS = \int_S \bar{\bar{\mathbf{F}}}^V(\mathbf{U}) \cdot \mathbf{n} dS, \tag{2.91}$$

where $\mathbf{n}$ is the unit normal vector on S, pointing out of the control volume. Now let Ω_h be a collection of N disjoint cells (or finite volumes) $V_i, i \in N$ that partition Ω: $\Omega_h = \bigcup_{i \in N} V_i$, where $N \subset \mathbb{Z}^+$ is the number of cells. The boundary of the control volume V_i is ∂V_i, which in 3-D is the sum of its surrounding faces $A_{ij}, j \in M$: $\partial V_i = \sum_{j=1}^{M} A_{ij}$, where $M \subset \mathbb{Z}^+$ is the number of the local boundary faces that the cell i has. The boundary ∂V_i can be an external boundary $\partial V_i^B \coloneqq \partial V_i : S \cap \partial V_i \neq \varnothing$, or an interior boundary $\partial V_i^{int} \coloneqq \partial V_i : S \cap \partial V_i = \varnothing$. In case of an interior boundary, the finite volume V_i is neighbour with a finite volume V_m and share a common face: $A_{ij} = \partial V_i \cap \partial V_m$, where $i, m \in N$ and $j \in M$ (see Fig. 2.6). Considering Eq. 2.91 for each control volume V_i, the weak form of the NS equations is derived:

$$\int_{V_i} \frac{\partial \mathbf{U}}{\partial t} d V_i + \int_{\partial V_i} \bar{\bar{\mathbf{F}}}(\mathbf{U}) \cdot \mathbf{n} d\partial V_i = \int_{\partial V_i} \bar{\bar{\mathbf{F}}}^V(\mathbf{U}) \cdot \mathbf{n} d\partial V_i. \tag{2.92}$$

The control volume average $\bar{\mathbf{U}}_i$ of $\mathbf{U}_i$ is:

$$\bar{\mathbf{U}}_i(t) = \frac{1}{|V_i|} \int_{V_i} \mathbf{U}(x, y, z, t) d V_i, \tag{2.93}$$

where $|V_i|$ is the volume of cell i. The discrete form of Eq. 2.92 is:

$$\frac{\partial \bar{\mathbf{U}}_i}{\partial t} + \frac{1}{|V_i|} \sum_{j=1}^{M} \int_{A_{ij}} \bar{\bar{\mathbf{F}}}(\mathbf{U}) \cdot \mathbf{n}_{ij} dA_{ij} = \frac{1}{|V_i|} \sum_{j=1}^{M} \int_{A_{ij}} \bar{\bar{\mathbf{F}}}^V(\mathbf{U}) \cdot \mathbf{n}_{ij} dA_{ij}. \tag{2.94}$$

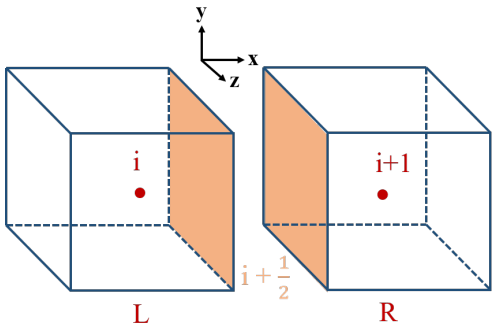

Figure 2.6: Two neighbour finite volumes i (left) and $i+1$ (right), as well as their common interface $\partial V_i \cap \partial V_{i+1}$ (orange).

2.6.1 Numerical flux

As it can be seen in the previous sub-section from Eq. (2.32) and (2.30), the speed of sound can vary from $1\,m/s$ in the mixture regime, up to $1482.35\,m/s$ in the liquid region, whereas in the gaseous phase the speed of sound is $290\,m/s$. Due to this large variation in the speed of sound, the Mach number in three phase flows can range from 10^{-2} up to 10^{2} or even higher [18]. This is an obstacle in density-based solvers, since they are prone to slow convergence and dispersion in low Mach number flows [19, 20, 21]. Therefore, proper flux functions suitable for all-Mach number flows have been developed and incorporated in density based solvers, for instance in [22, 23], or in some more recent studies [24, 25]. In order to handle the low Mach number problem, a hybrid numerical flux, suitable for multiphase flows of 2 materials, is proposed here.

Mach consistent numerical flux

Schmidt et al. [23] proposed a Mach consistent numerical flux (MC) for cavitating flows, based on the HLLC and AUSM [22] fluxes. The behaviour of the MC flux is evaluated against the HLL flux in Fig. 2.7 and against the Tadmor-Kurganov central scheme [225] in Fig. 2.8. Given the benefits of the MC flux, it has been implemented in OF and used for cavitating flows. In Fig. 2.7 the Riemann problem in the computational domain $x \in [-50, 50]$ with initial conditions: $\rho_L = 1000\,kg/m^3$, $u_L = 0\,m/s$, $\rho_R = 1\,kg/m^3$, $u_R = 500\,m/s$ is examined at time $0.01\,s$. The computational solutions with the HLL and the MC fluxes are compared against the exact solution. The solution obtained by the MC flux is closer than the HLL one to the exact solution, while the latter fails to capture the pressure right of the liquid region. In Fig. 2.8 the pressure contours

for inviscid flow around cylinder at $M = 0.01$ and $p_\infty = 150\,bar$ are shown by utilizing the standard rhoCentralFoam and the barotropicFoam solvers. In the former, the central scheme of Tadmor-Kurganov for ideal gas was used, whereas in the latter, the MC solver with the Tait equation was employed. The standard density based solver gives an incorrect and oscillatory solution. The MC solver however, provides a smooth and symmetric solution even for low Mach numbers.

The inviscid numerical flux in the k direction at the $i+1/2$ interface (see Fig. 2.6) is:

$$\mathbf{F}_k^{i+1/2} = \rho^{L/R} u_k^\star \begin{bmatrix} 1 \\ Y_g^{L/R} \\ u_1^{L/R} \\ u_2^{L/R} \\ u_3^{L/R} \\ E^{L/R} \end{bmatrix} + p^\star \begin{bmatrix} 0 \\ 0 \\ \delta_{1k} \\ \delta_{2k} \\ \delta_{3k} \\ u_k^\star \end{bmatrix}, \tag{2.95}$$

where the interface velocity $u_k^\star$, pressure $p^\star$ and speed of sound $c^\star$ are approximated by:

$$u_k^\star = \frac{1}{\rho^L + \rho^R}\left(\rho^L u_k^L + \rho^R u_k^R + \frac{p^L - p^R}{c^\star}\right), \tag{2.96}$$

$$p^\star = \frac{p_L + p_R}{2}, \tag{2.97}$$

$$c^\star = max(c_L, c_R), \tag{2.98}$$

The superscript L/R denotes that the value considered depends on the sign of $u_k^\star$; if $u_k^\star > 0$, the left cell value is considered and vice versa.

Hybrid numerical flux

Although the MC numerical flux gives accurate and smooth solutions for 1 material problems, overshoots were noticed when a 2 phase solver was employed (2 material problem), see Fig. 2.9. In Fig. 2.9 the Riemann problem for the linear EoS (Eq. 2.34) in the computational domain $x \in [-0.5, 0.5]$ with initial conditions: $\rho_L = 998.2\,kg/m^3$, $u_L = 0\,m/s$, $Y_g = 0$, $\rho_R = 0.017\,kg/m^3$, $u_R = 0\,m/s$, $Y_g = 1$ is examined at time $0.1\,\mu s$. An overshoot in the velocity is noticed when the MC flux is employed, while the MC solver seems incapable of capturing the

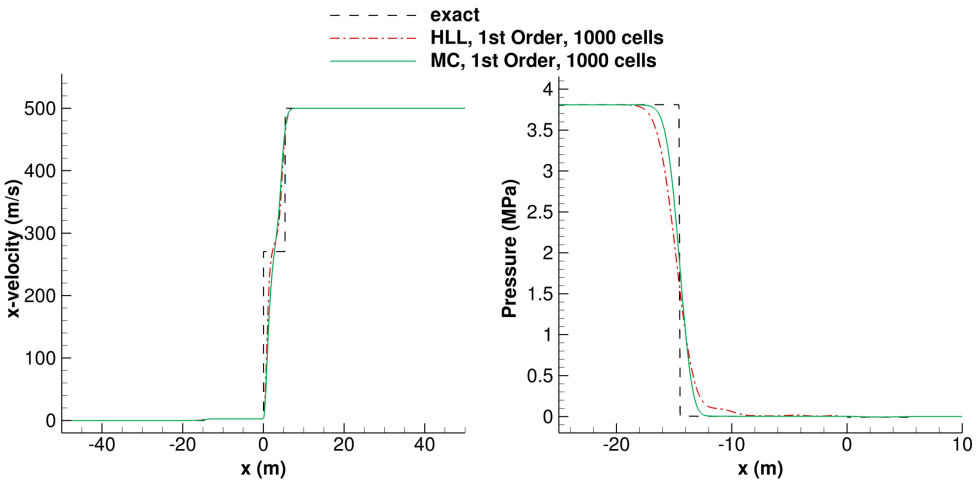

Figure 2.7: Comparison between HLLC and the Mach consistent (MC) numerical fluxes for the 1 material Riemann problem at time $t = 0.01\,s$; x-velocity on the left and pressure on the right.

correct pressure pattern. For that purpose, a hybrid numerical flux has been developed and implemented in OF [226].

The aforementioned flux is based on the Primitive Variable Riemann Solver (PVRS) [227] and the Mach consistent numerical flux of Schmidt et al. [23]. That way, an efficient and robust solver is developed, by utilizing an approximated Riemann solver, instead of the exact one. At the same time, the numerical scheme is suitable for subsonic up to supersonic flow conditions. The inviscid numerical flux in the k direction at the $i+1/2$ interface takes the following form:

$$\mathbf{F}_k^{i+1/2} = \rho^{L/R} u_k^\star \begin{bmatrix} 1 \\ Y_g^{L/R} \\ u_1^{L/R} \\ u_2^{L/R} \\ u_3^{L/R} \\ E^{L/R} \end{bmatrix} + p^\star \begin{bmatrix} 0 \\ 0 \\ \delta_{1k} \\ \delta_{2k} \\ \delta_{3k} \\ u_k^\star \end{bmatrix}, \tag{2.99}$$

where the interface velocity $u_k^\star$ is approximated by:

$$u_k^\star = \frac{1}{C^L + C^R}\left[C^L u_k^L + C^R u_k^R + (p^L - p^R)\right], \tag{2.100}$$

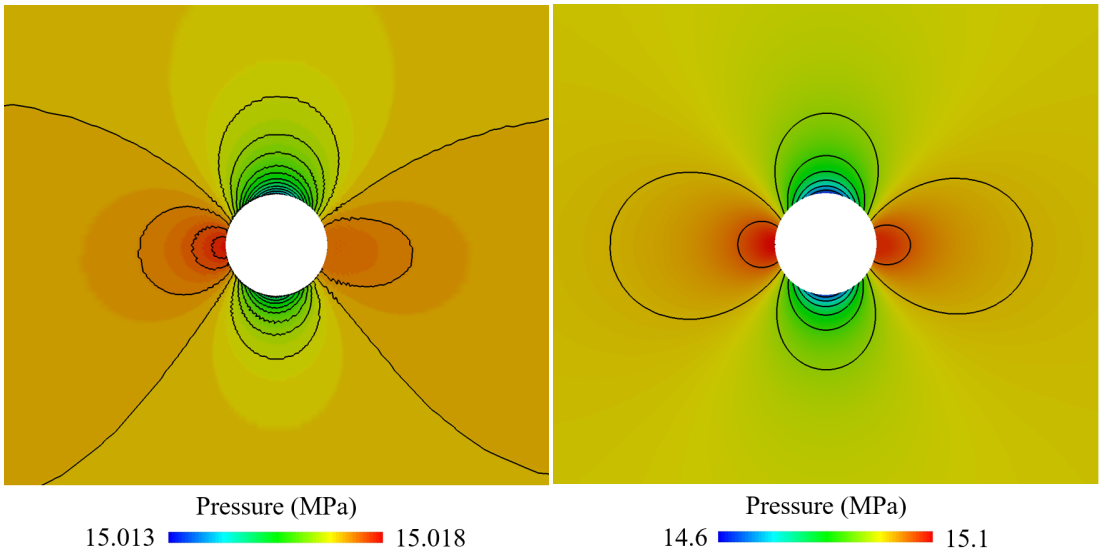

Figure 2.8: Pressure contours for inviscid flow around cylinder at $M = 0.01$; comparison between rhoCentralFoam (left) and barotropicFoam (right) solvers.

and C is the acoustic impedance $C = \rho c$. The interface pressure $p^\star$ is:

$$p^\star = (1 - \beta)p^{\star,incr} + \beta p^{\star,comp}. \tag{2.101}$$

In Eq. (2.101), the interface pressure is the sum of the incompressible and the compressible parts, where the incompressible contribution is:

$$p^{\star,incr} = \frac{C^L p^R + C^R p^L}{C^L + C^R}, \tag{2.102}$$

and the compressible contribution is:

$$p^{\star,comp} = \frac{C^L p^R + C^R p^L + C^R C^L (u_k^L - u_k^R)}{C^L + C^R} \tag{2.103}$$

Depending on the Mach number, the contribution of the incompressible or the compressible part in Eq. (2.101) is more dominant and the weighted term β is :

$$\beta = 1 - e^{-aM}, \tag{2.104}$$

where the Mach number M is defined as:

$$M = max\Big(\frac{|\mathbf{u}^L|}{c^L}, \frac{|\mathbf{u}^R|}{c^R}\Big). \tag{2.105}$$

The blending coefficient is $\alpha \sim (10, 100)$. For incompressible single phase flow,

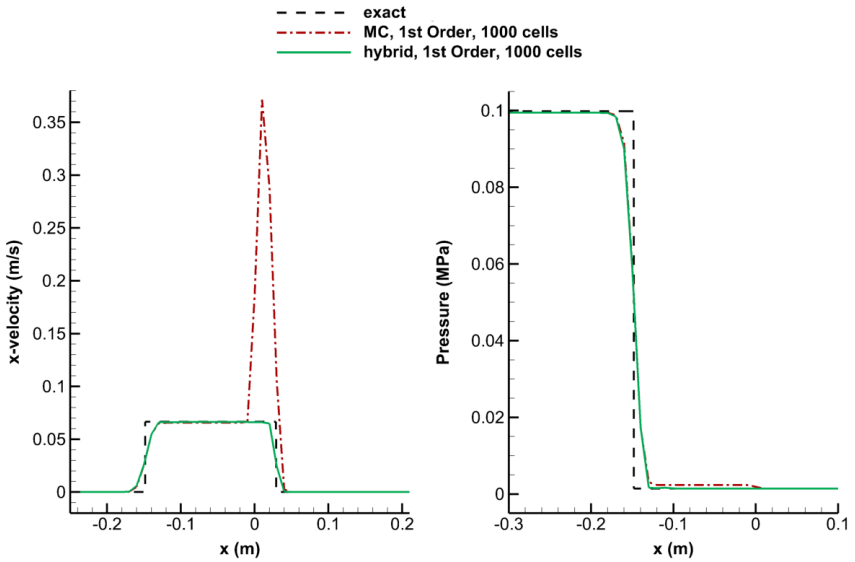

Figure 2.9: Comparison between the MC and the Hybrid numerical fluxes for the 2 material Riemann problem at time $t = 0.01\,s$; x-velocity on the left and pressure on the right.

Eq. (2.102) is taking the form of $\frac{1}{2}(p_L + p_R)$ since $C^L = C^R$. However, for two-phase flows, Eq. (2.102) is much closer to the exact solution. Regarding spatial accuracy, linear interpolation (2nd order spatial accuracy) with van Leer reconstruction has been used [228].

2.7 Time discretization

For simulating unsteady flows, where often an oscillating flow pattern appears, such as vortex shedding, higher order of time accuracy is required. This is achieved by implementing RK schemes in the flow solver. Let rewriting the NS equations 2.1 as an initial value problem which is defined by the following differential equation and its initial condition:

$$\frac{\partial \mathbf{U}}{\partial t} = \mathbf{R}(t, \mathbf{U}), \quad \mathbf{U}(\mathbf{t_0}) = \mathbf{U_0} \tag{2.106}$$

Here $\mathbf{R}$ denotes the inviscid and the viscous terms of the NS equations.

A low storage, four stage Runge-Kutta method, 2^{nd} order in time has been employed. The numerical solution of this differential equation is given by the following steps, where the coefficients have been chosen in order to improve

stability [229]:

$$\mathbf{U^1} = \mathbf{U^n} + 0.11\mathbf{R}(\mathbf{U^n}), \tag{2.107}$$

$$\mathbf{U^2} = \mathbf{U^n} + 0.2766\mathbf{R}(\mathbf{U^1}), \tag{2.108}$$

$$\mathbf{U^3} = \mathbf{U^n} + 0.5\mathbf{R}(\mathbf{U^2}), \tag{2.109}$$

$$\mathbf{U^{n+1}} = \mathbf{U^n} + \mathbf{R}(\mathbf{U^3}) \tag{2.110}$$

For calculating the solution vector at an intermediate stage, only the solution vector of the previous stage is required and when advancing to the next time-step, only the solution vector at times n and $n+1$ are stored. A four stage RK, with 4^{th} order of temporal accuracy [227] has been also used and implemented in OF:

$$\mathbf{k^1} = \mathbf{R}(t^n, \mathbf{U^n}), \tag{2.111}$$

$$\mathbf{k^2} = \mathbf{R}(t^n + \frac{\Delta t}{2}, \mathbf{U^n} + \frac{\Delta t}{2}\mathbf{k^1}), \tag{2.112}$$

$$\mathbf{k^3} = \mathbf{R}(t^n + \frac{\Delta t}{2}, \mathbf{U^n} + \frac{\Delta t}{2}\mathbf{k^2}), \tag{2.113}$$

$$\mathbf{k^4} = \mathbf{R}(t^n + \Delta t, \mathbf{U^n} + \Delta t\mathbf{k^3}), \tag{2.114}$$

$$\mathbf{U^{n+1}} = \mathbf{U^n} + \Delta t\Big[\frac{\mathbf{k_1}}{6} + \frac{\mathbf{k_2}}{3} + \frac{\mathbf{k_3}}{3} + \frac{\mathbf{k_4}}{6}\Big] \tag{2.115}$$

Here the solutions at all the intermediate stages are required to be stored in order to advance from time n to time $n+1$. However, the advantage is that 4^{th} order of temporal accuracy is achieved with only 4 intermediate stages.

Chapter 3

Results: Fundamental Studies

In this chapter, validation of the numerical method is performed for the Riemann problem and the Rayleigh bubble collapse. Then, fundamental cases are examined, such as bubble dynamics, flow in a converging-diverging nozzle, the flow around a hydrofoil, bubble-shock wave interaction and droplet impact simulations. More specifically, the advantages of the numerical flux compared to a conventional one are demonstrated in Fig. 3.5, where a dispersion-free solution is obtained. In addition, the vapour n-Dodecane bubble collapse alongside with the cryogenic flow in a converging-diverging nozzle demonstrate the applicability of the solver to different materials and phenomena, either cavitation or flashing. Concerning the collapse of vapour n-Dodecane bubbles, parametric studies at conditions realised in micro-orifice flow passages have been performed. The liquid temperature and pressure changes on the wall are estimated as a function of the surrounding liquid pressure, the initial bubble radius and the location of the wall from the center of the initial bubble, giving an insight into fuel pyrolysis and erosion damage. Finally, in the droplet impact simulations, the compressibility effects have been considered and the cavitation formation inside the droplet has been modelled at We numbers greater than 10^5, which has not been simulated in the past, up to author's best knowledge.

3.1 Riemann problem

The Riemann problem is an Initial Value Probelm (IVP) with a discontinuity at x_0 [227]:

$$\mathbf{U}(x, t=0) = \begin{cases} \mathbf{U}_L(x), & x < x_0 \\ \mathbf{U}_R(x), & x \geq x_0 \end{cases} \tag{3.1}$$

For validating the developed numerical schemes, the 1-D Euler Riemann problem is considered next, with two different constant states on the left ($\mathbf{U}_L$) and right ($\mathbf{U}_R$). Validation for the different EoS implemented in OF and the different materials, such as water, n-Dodecane and LOX has been performed.

3.1.1 Barotropic model, liquid-vapour mixture

The first Riemann problem examined is for the single phase algorithm by employing the Tait EoS for the liquid and the isentropic gas EoS for the liquid-vapour mixture. The shock tube problem is studied in the domain $x \in [-50, 50]$ with initial conditions for the left state: $\rho_L = 1000\,kg/m^3$, $u_L = 0\,m/s$ and for the right state: $\rho_R = 1\,kg/m^3$, $u_R = 500\,m/s$; the corresponding pressure based on Eq. 2.28 is $p_L = 3.809\,MPa$ and $p_R = 890.45\,Pa$ respectively. Wave transmissive boundary conditions have been used for the left and the right sides of the shock tube, that is $\mathbf{U}_{n+1}(x = L) = \mathbf{U}_n(x = L)$ and $\mathbf{U}_{n+1}(x = 0) = \mathbf{U}_n(x = 0)$. Comparison between the exact and the numerical solution is shown in Fig. 3.1 at time $t = 0.01\,s$ for first order of spatial accuracy with 2000, 5000 and 10000 equally spaced cells in the x direction. The numerical solution converges to the exact solution as the cell resolution increases.

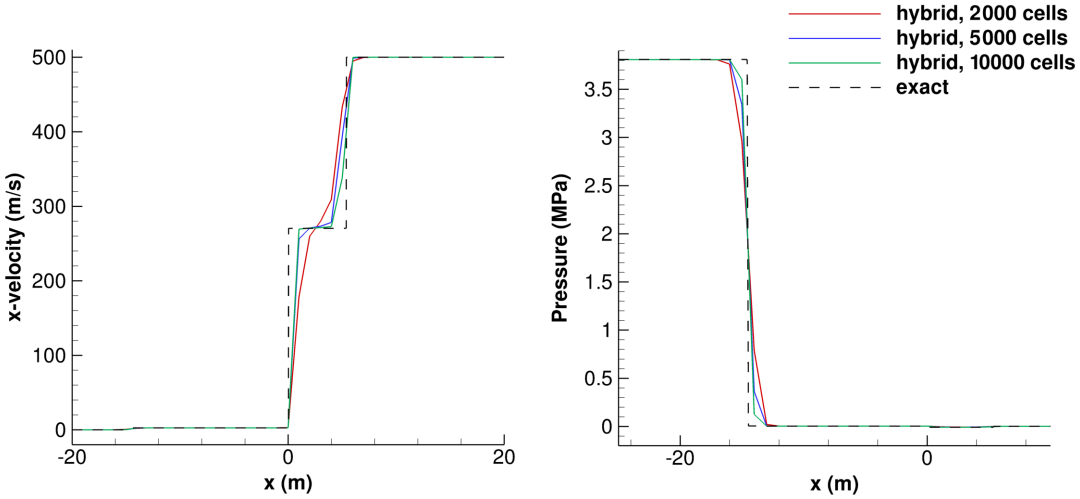

Figure 3.1: Verification of the one-phase solver for the Riemann problem. Comparison of the x-velocity (left) and pressure (right) between the exact and the numerical solution at time $t = 0.01\,s$. First order accuracy in space with 2000, 5000 and 10000 cells has been used.

3.1.2 Barotropic model, liquid-gas mixture (linear EoS)

The Riemann problem for the 2-phase algorithm is examined in the computational domain $x \in [-0.5, 0.5]$ with initial conditions for the left state: $\rho_L = 998.2\,kg/m^3$, $u_L = 0\,m/s$, $Y_g = 0$ and for the right state: $\rho_R = 0.017\,kg/m^3$, $u_R = 0\,m/s$, $Y_g = 1$. The boundary conditions on the right and the left sides were set as wave transmissive. Comparison between the exact and the numerical solution is shown in Fig. 3.2 at time $t = 0.1\,\mu s$, where second order of spatial accuracy with 500 equally spaced cells in the x direction was used for obtaining the numerical solution. A close-up view in order to compare first and second order in space schemes with resolution either 500 or 1000 equally spaced cells in the x direction is shown in Fig. 3.3. In Fig. 3.2, the exact solution of the Riemann problem and the computed one are in satisfactory agreement and the wave pattern has been correctly captured. As it was expected in Fig. 3.3, the 2nd order solutions in space are free of numerical diffusion, which is dominant in the 1st order schemes. In addition, the computed solution is getting closer to the exact by increasing the mesh resolution and the numerical diffusion is eliminated. No dispersion is noticed at the boundary interface (between the gas and the liquid), which is the case when using convectional schemes such as HLLC or similar. The exact solution of the Riemann problem is not trivial for multi-material cases and it has been derived in the Appendix B.2.

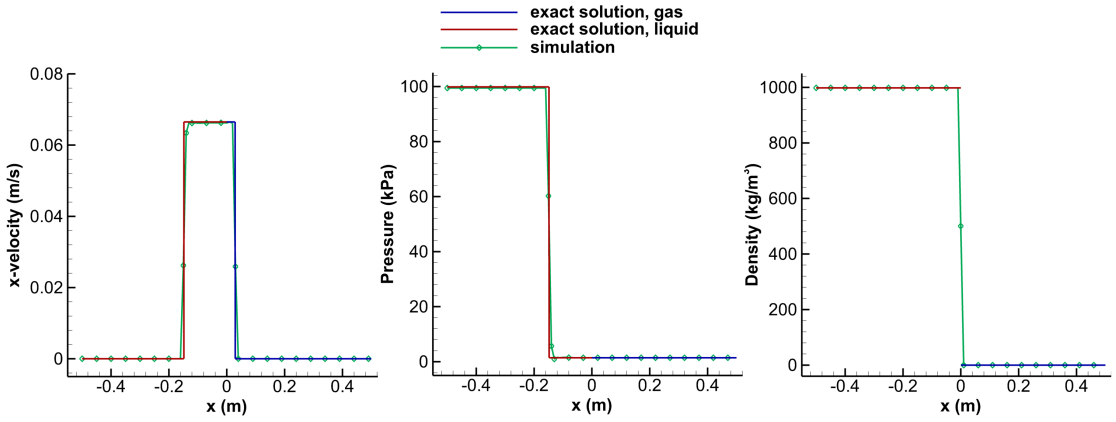

Figure 3.2: Verification of the two-phase solver for the Riemann problem. Comparison of the x-velocity (left), pressure (middle) and density (right) between the exact and the numerical solution at time $t = 0.1\,\mu s$. Second order accuracy in space with 500 cells has been used.

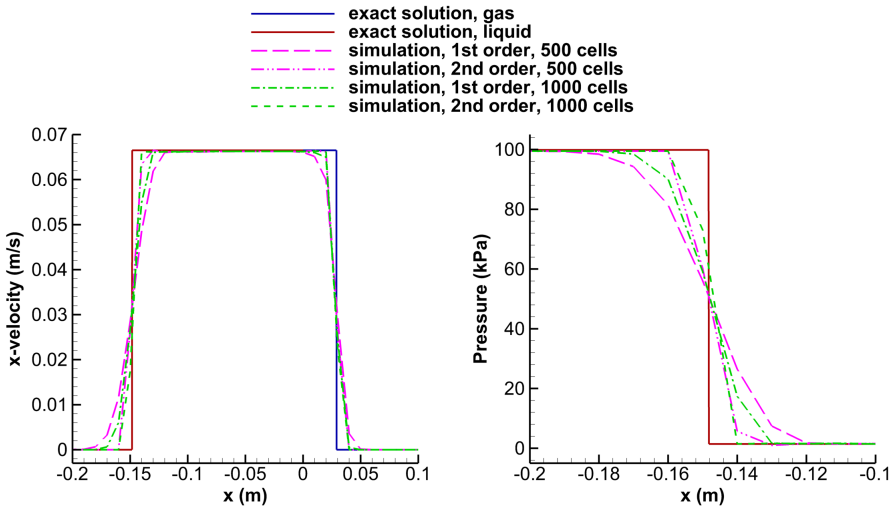

Figure 3.3: Close-up view of the Riemann problem. Comparison of the x-velocity (left) and pressure (right) between the exact and the numerical solution at time $t = 0.1\,\mu s$. First and second order spatial accuracy schemes with resolution of 500 and 1000 cells have been used.

3.1.3 Helmholtz EoS, liquid-vapour mixture

N-Dodecane

The Riemann problem for the Helmhotz EoS is examined in the computational domain $x \in [-2, 2]$ with initial conditions for the left state $\rho_L = 752.5\,kg/m^3$, $T_L = 289\,K$ and for the right state $\rho_R = 717.5\,kg/m^3$, $T_R = 350\,K$. Comparison between the exact and the numerical solution is shown in Fig. 3.4 at time $t = 0.5\,\mu s$. First order of spatial accuracy with 800 equally spaced cells in the x direction was used. Wave transmissive boundary conditions have been used for the left and the right side of the shock tube. As it can be seen in Fig. 3.4, the exact solution of the Riemann problem and the computed one are in satisfactory agreement and the wave pattern has been correctly captured. The exact solution of the Riemann problem is not trivial for an arbitrary EoS and it has been derived in Appendix B.1.

LOX

Since the tabulated data algorithm has been used for cryogenic applications as well, it has been validated for such conditions. The Riemann problem in the computational domain with initial conditions for the left state: $\rho_L = 965.8\,kg/m^3$, $T_L = 208.9\,K$, $u_L = 0\,m/s$ and for the right state: $\rho_R = 417.6\,kg/m^3$, $T_R = 111\,K$, $u_R = 0\,m/s$ is examined. The numerical solution is compared with the

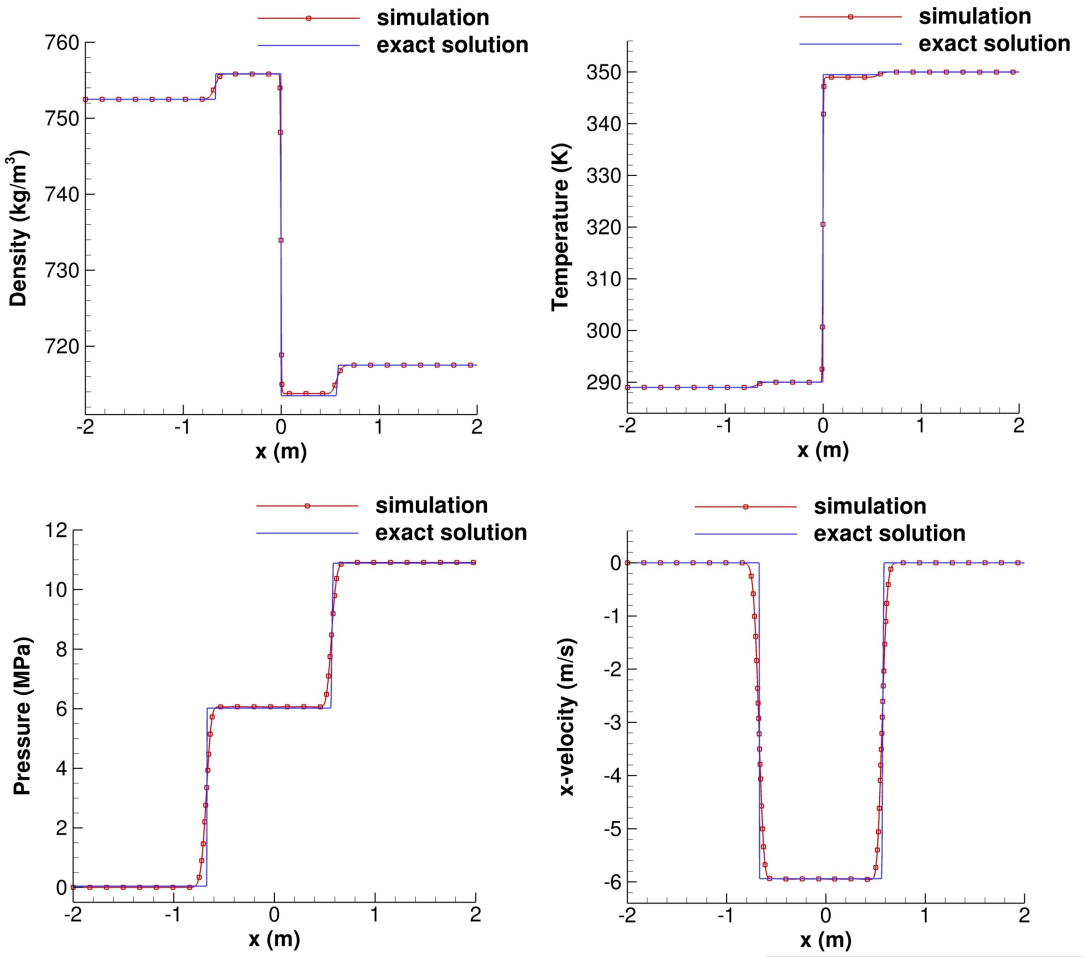

Figure 3.4: Validation of the solver for the Riemann problem (n-Dodecane). Comparison of the density (upper left), temperature (upper right), pressure (lower left) and x-velocity (lower right) between the exact and the numerical solution.

solution from an 1-D FV solver which has been validated against the exact solution at time $1\,ms$ (Fig. 3.5). First order of spatial accuracy with 1000 equally spaced cells in the x-direction has been used in both solvers. Wave transmissive boundary conditions have been employed for the left and the right side of the shock tube.

As it can be seen in Fig. 3.5, the two solutions are in satisfactory agreement and the correct wave pattern has been successfully captured: a left moving expansion wave on the left, a right moving contact discontinuity in the middle and a right moving shock wave on the right. It has to be mentioned here that although the same amount of computational cells and the same spatial accuracy is used in both solvers, the traditional HLLC solver gives a dispersive solution at the location of the right moving wave at $x = 0.2\,m$. This is a good demonstration

of the capabilities of the Mach consistent numerical flux, which gives smooth and accurate solutions.

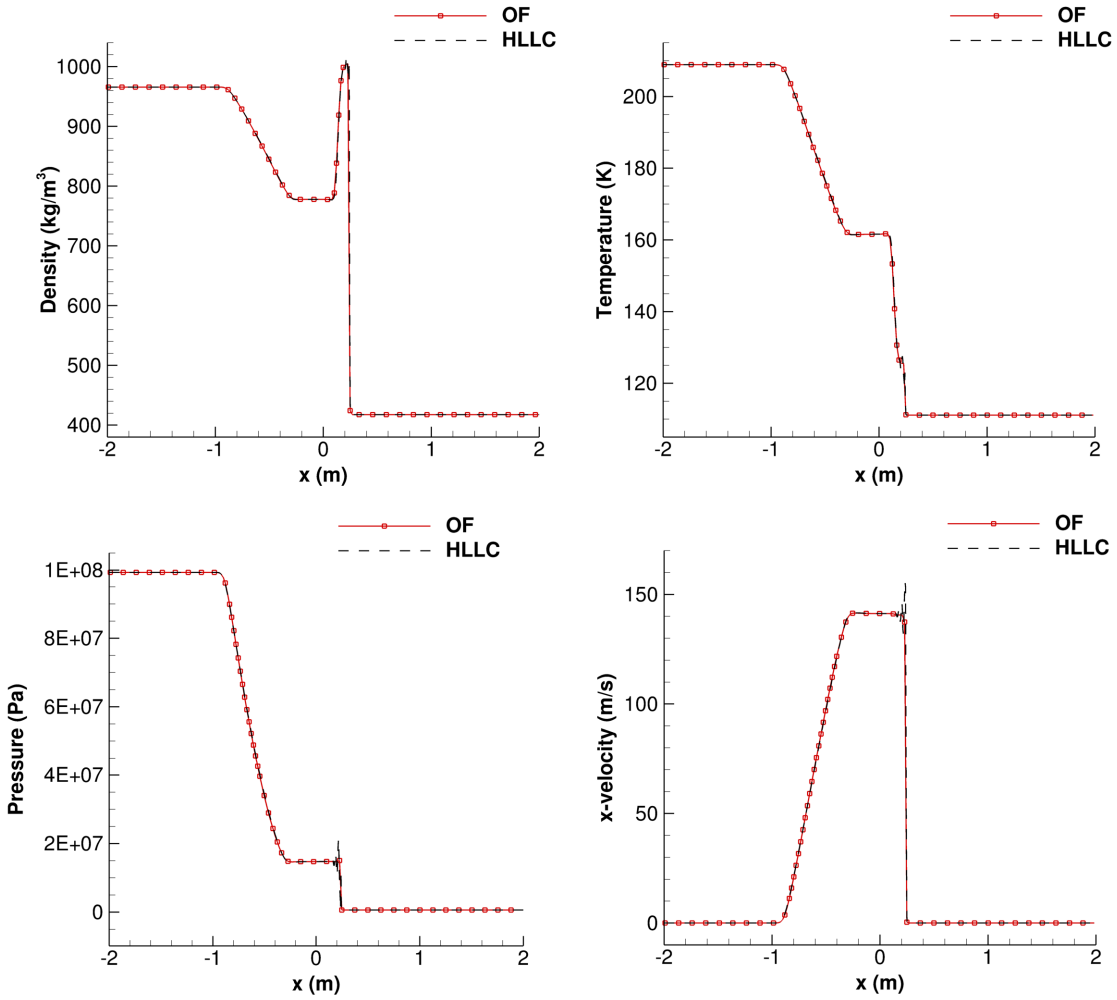

Figure 3.5: Validation of the solver for the Riemann problem (LOx). Comparison of the density (upper left), temperature (upper right), pressure (lower left) and x-velocity (lower right) between the numerical solution and the one from an 1-D FV solver.

3.1.4 HEM with temperature effects

Pure liquid flow

A shock tube configuration for pure liquid flow is examined in the computational domain $x \in [0, 1]$ with initial conditions for the left state ($x < 0$): $p_L = 10^8\, Pa$, $u_L = 0\, m/s$ and for the right state ($x \geq 0$): $p_R = 10^4\, Pa$, $u_R = 0\, m/s$. First order spatial accuracy with 1000 equally spaced cells was used and wave transmissive boundary conditions were utilised for both sides. Based on the initial

configuration, a left running expansion wave, a right running contact discontinuity and a right running shock wave are formed and travel inside the domain. Comparison with Koop's solution [28] at $t = 90\,\mu s$ is shown in Fig. 3.6; the present solution appears to be in satisfactory agreement with Koop's.

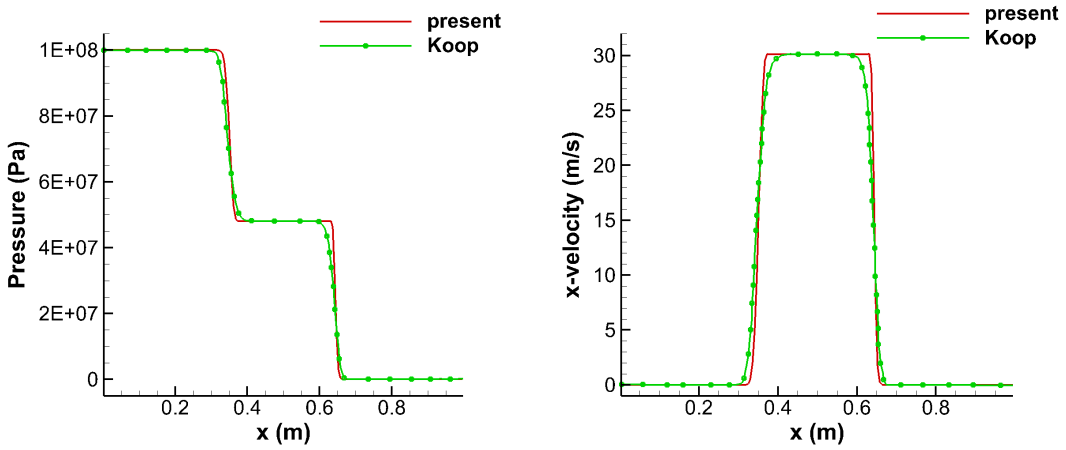

Figure 3.6: Validation of the HEM with temperature EoS for the Riemann problem (pure water): comparison of the pressure (left) and the x-velocity (right) between the present (red) and Koop's solution [28] (green).

Liquid-vapour mixture

A shock tube configuration for the liquid-vapour mixture is examined next in the computational domain $x \in [0, 1]$ with initial conditions for the left state ($x < 0$): $p_L = 0.9 \cdot 10^5\, Pa$, $u_L = -10\, m/s$ and for the right state ($x \geq 0$): $p_R = 0.9 \cdot 10^5\, Pa$, $u_R = 10\, m/s$. First order spatial accuracy with 1000 equally spaced cells was used and wave transmissive boundary conditions were utilised for both sides. Due to the opposite moving states, 2 expansion waves, one right and one left running are formed and evaporation takes place. Comparison with Koop's solution [28] at $t = 90\,\mu s$ is shown in Fig. 3.7; the two solutions are in satisfactory agreement.

3.2 Rayleigh bubble collapse (Helmholtz EoS)

The second test case examined is the Rayleigh bubble collapse, where a vapour sphere of radius $R_0 = 400\,\mu m$ is under compression owing to the higher pressure of the surrounding liquid. The bubble collapse velocity is given by Franc and Michel [216]:

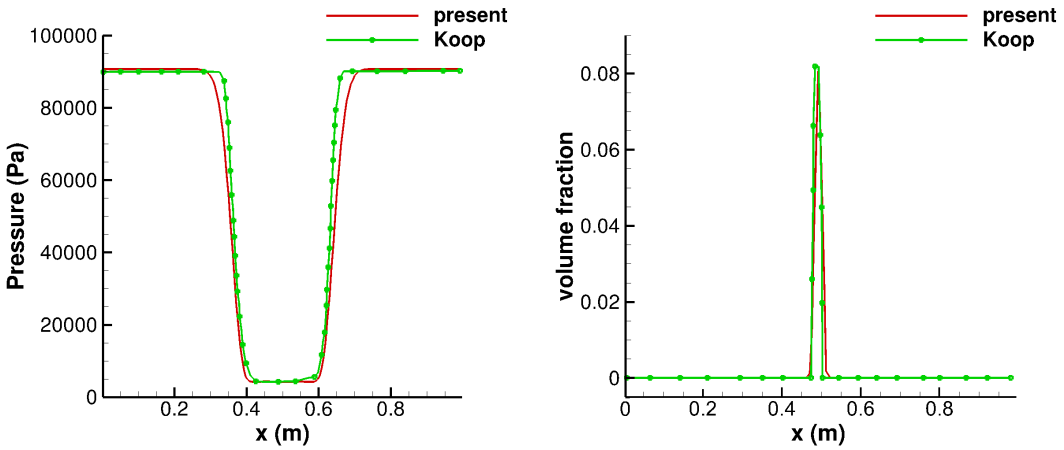

Figure 3.7: Validation of the HEM with temperature EoS for the Riemann problem (liquid-vapour mixture): comparison of the pressure (left) and the vapour volume fraction (right) between the present (red) and Koop's solution [28] (green).

$$\frac{dR}{dt} = -\sqrt{\frac{2}{3}\frac{p_\infty - p_v}{\rho_l}\left[\left(\frac{R_0}{R}\right)^3 - 1\right]}, \tag{3.2}$$

and the characteristic Rayleigh time τ of the bubble is:

$$\tau = 0.915 R_0 \sqrt{\frac{\rho_l}{p_\infty - p_v}}, \tag{3.3}$$

Here, the vapour pressure is $p_v = 19.64\,Pa$, the liquid density is $\rho_l = 744.36\,kg/m^3$ and the far-field pressure is $p_\infty = 0.1\,MPa$. An 1-D solver was employed for this simulation, taking advantage of the spherical symmetry (see A). The total computational domain is 20 times the size of the initial vapour radius in order to minimize the interference of the boundaries. The mesh is refined in the bubble region, where 1000 equally spaced cells have been used and a stretching ratio of 1.05 with 150 cells has been used outside the bubble. Wave transmissive boundary condition has been used on the far-field right side and symmetry condition was selected for the left side. Comparison with the semi-analytical solution gives satisfactory results (see Fig. 3.8), since the current methodology is able to predict the correct curve of the bubble radius with respect to time. In Fig. 3.8, the radius has been divided by the initial radius R_0 and the time has been non-dimensionalized by the Rayleigh time which is $\tau = 31.5\,\mu s$ for the current configuration.

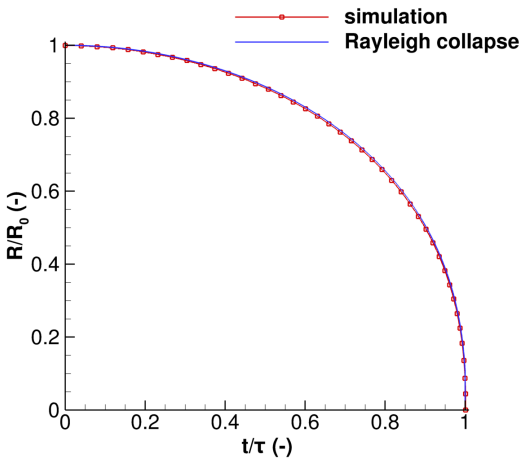

Figure 3.8: Comparison between the Rayleigh collapse solution and the numerical one. The bubble radius and the time are expressed in non-dimensional form, in reference to the initial radius R_0 and Rayleigh collapse time τ respectively.

3.3 N-Dodecane bubble dynamics (Helmholtz EoS)

After validating the method for the Riemann problem of section 3.1.3 and for the Rayleigh bubble collapse of section 3.2, the collapse of a vaporous n-Dodecane bubble at different configurations is simulated by utilising the tabulated data algorithm presented in section 2.2.3. The viscosity and surface tension are neglected in the present simulations, since bubble growth and collapse are inertial phenomena [96]. The $2-D$ Euler equations in the rz cylindrical coordinates with a geometric source term in order to take into account cylindrical symmetry [227] have been employed (see Appendix A).

The initial configuration is the same as the cases examined in [113, 89]. The radius of the bubble is $R = 400\,\mu m$ and its centre has been placed at distance $d = 416$, 140 and $-140\,\mu m$ from the horizontal wall (x-axis) on the axis of symmetry (y-axis), as it can be seen in Fig. 3.9. The properties of the liquid n-Dodecane surrounding the bubble are $p_l = 12.144\,MPa$, $T_l \approx 300\,K$ and the vapour bubble properties are $p_v = 19.64\,Pa$, $T_v \approx 300\,K$. The computational domain is 20 times the bubble radius and 200 equally spaced cells were used for describing the initial radius of the bubble. After distance $2.5R$ from the origin, the mesh is coarsened with ratio 1.05 in both directions. Zero gradient boundary condition has been used for the right and the upper side, slip wall for the lower side, whereas for the y-axis of symmetry, the normal velocity component is zero.

3.3.1 Numerical investigation

In Fig. 3.10, 3.11, 3.12 there are two columns of images. In the first column the pressure field is shown on the left and the velocity field on the right. Similarly, in the second column the temperature field is shown on the left and numerical Schlieren is depicted on the right. In all images, iso-lines of density $380\,kg/m^3$ are shown as well. In Fig. 3.13, 3.14, 3.15 wall pressure (left) and wall temperature (right) combined with the density iso-surface of $380\,kg/m^3$ are shown. The units are in SI or their submultiples and multiples of the SI units. The simulation time indicated in the next Figures is non-dimensional and it is divided by the Rayleigh collapse time $\tau = 2.88\,\mu s$.

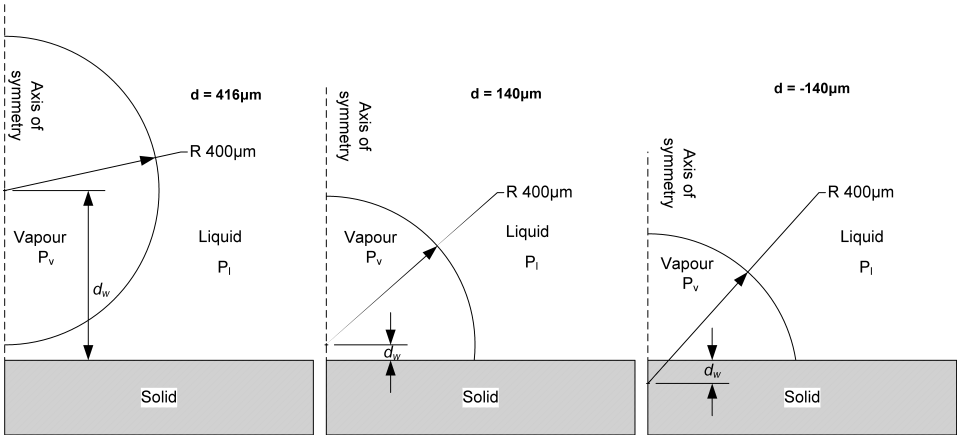

Figure 3.9: Initial bubble configurations: the bubble centre is placed at $d = 416\,\mu m$, $d = 140\,\mu m$ and $d = -140\,\mu m$ from the origin of the axes.

In all three configurations, there is slow shrinking of the bubble initially, until the jet is formed and after that the bubble is collapsing rapidly. Of course, the direction of the jet depends on the configuration, as it will be explained below. In Fig. 3.10 the evolution of the bubble collapse is shown for the configuration where its initial centre is placed at $d = 416\,\mu m$ from the x-axis. At the beginning of the collapse, a rarefaction wave expands from the bubble. The interaction of the rarefaction wave with the wall causes local depressurisation and vaporisation in the vicinity of the wall [89]. As the collapse proceeds, the bubble shape departs from spherical, due to the interaction with the wall boundary (x-axis). A micro-jet is formed on the top of the bubble and the heart-like-shape is noticed, which is in accordance with previous results reported [113, 89]. In addition, the propagating pressure wave after collapse is shown at time 1.18 in Fig. 3.10. There is a significant rise in the temperature of the liquid, up to $1000\,K$, after

the collapse of the bubble, due to vapour condensation and liquid compression, while there is a significant drop in the temperature above the bubble, to $273\,K$, due to the large acceleration of the flow which causes a reduction in the internal energy. We highlight here, that the critical point for n-Dodecane is $T_c \sim 658\,K$ and $p_c \sim 18\,bar$; this implies that in areas of collapse the fluid may transition to supercritical state. In Fig. 3.11 instances of the bubble having initially its centre at $d = 140\,\mu m$ from the x-axis are shown. Again, a non-symmetric shape for the bubble and a micro-jet are created. A torus which is attached to the wall is formed and it collapses creating a pressure wave. In both cases, that is for $d = 416\,\mu m$ and $d = 140\,\mu m$, the jet's and the bubble collapse direction are towards the wall. In this specific case, a secondary jet is created when the primary jet, which is normal to the wall, is deflected at the wall and interacts with the remaining ring ($t = 1.09$ in Fig. 3.11). In Fig. 3.12 snapshots of the bubble having its centre in the lowest position ($d = -140\,\mu m$) are demonstrated. In comparison with the two previous positions, the shape of the bubble looks like a pin and the collapse direction is tangential to the wall. The jet which is formed is towards to the axis of symmetry, which was not the case in the previous positions. A propagating pressure wave at $t = 0.77$ is shown in Fig. 3.12.

Focusing on the iso-surfaces of Fig. 3.13, 3.14, 3.15, the different collapse pattern is clearly visible. The justification for the collapse shape is related to the local angle between the liquid-vapour interface and the wall, at the closest point or point of contact to the wall; this has been discussed in more detail in [89], but the main mechanism will be briefly discussed here as well. When the local angle is below 90°, the flow in the vicinity of the wall tends to detach, reducing the pressure and preventing further acceleration of the collapse, thus near wall velocities are small and the collapse is mainly directed in the form of a micro-jet towards the wall on the axis-of-symmetry. On the other hand, when the local angle is higher than 90° the flow tends to move towards the wall, leading to pressurization and further acceleration of the collapse (see Fig. 3.16-3.18 where the velocity vectors are illustrated). These effects underline the influence of boundary presence and pressure gradients to the bubble collapse, as demonstrated also in experimental [230, 231] and numerical work [48, 105, 113]. In Fig. 3.16, 3.17, 3.18 the velocity vectors are shown and the supercritical cells ($T_c = 658.1\,K$, $p_c = 1.817\,MPa$) are coloured in black, whereas the vapour (white) and liquid (grey) regions are distinguished by a red iso-line of density

$380\,kg/m^3$.

3.3.2 Effect of thermodynamic models

A more thorough study of the collapse times for the previous configurations which are compared against different thermodynamic models is shown next, such as the barotropic model of section 2.2.1, the HEM with temperature effects of section 2.2.2 and the Helmholtz EoS of section 2.2.3. The model parameters and the initial conditions have been chosen accordingly to match the conditions of the Helmholtz EoS bubble collapse, for consistency reasons. The initial configuration of the barotropic model of section 2.2.1 is as follows: $B = 125.956\,MPa$, $p_{sat} = 40\,Pa$, $\rho_{sat} = 744.29\,kg/m^3$, $C = 1100\,Pa \cdot kg/m^3$ and $n = 7.15$. The initial density of the liquid was set to $\rho_l = 753.91\,kg/m^3$ and the density in the bubble was set to $\rho_l = 74.0\,kg/m^3$. For the HEM model with temperature effects of section 2.2.2, the initial density of the liquid was set to $\rho_l = 752.3\,kg/m^3$, whereas the density in the bubble was $\rho_l = 3.95\,kg/m^3$ and the initial temperature was $T_0 = 300\,K$. In addition, $B = 168.638\,MPa$, $n = 7.15$, $R = 48.9\,J/(kg \cdot K)$, $C_{vl} = 1823\,J/(kg \cdot K)$, $C_{vv} = 1593.3\,J/(kg \cdot K)$, $L_v = 345739.0\,J/(kg \cdot K)$ and $e_{l0} = 9450\,J/kg$ have been set. In Fig. 3.19, vapour volume fraction (left) with respect to time is shown for the three different thermodynamic models. The collapse time of the bubbles is reasonable and comparable to the Rayleigh collapse time, as well as proportional to the initial volume of the vapour which exists in the bubble. It is obvious that the barotropic model predicts slightly earlier collapse time for all three positions of the bubble, because the pressure is expressed only as a function of the density, and the temperature effect is not taken into account. The other two models considering the temperature effects, predict the same collapse time and their curves coincide for all three positions of the bubble. However, for the highest position after the collapse, rebound is noticed for all three models but for the Helmholtz EoS the rebound is more dominant. This rebound in Fig. 3.19 is caused due to the conservation of angular momentum; even if the solver employed is based on the Euler equations, the asymmetric bubble collapse near the wall induces vorticity (it is evident in Fig. 3.16 at $t =$ 1.13, 1.15, 1.18). This vorticity causes centrifugal force, which prevents the total collapse and disappearance of the bubble, at least until vorticity is dissipated by numerical diffusion. For more information on the rebound of cavitating vortices the interested reader is addressed to [216] (see also [107]). In addition, if the

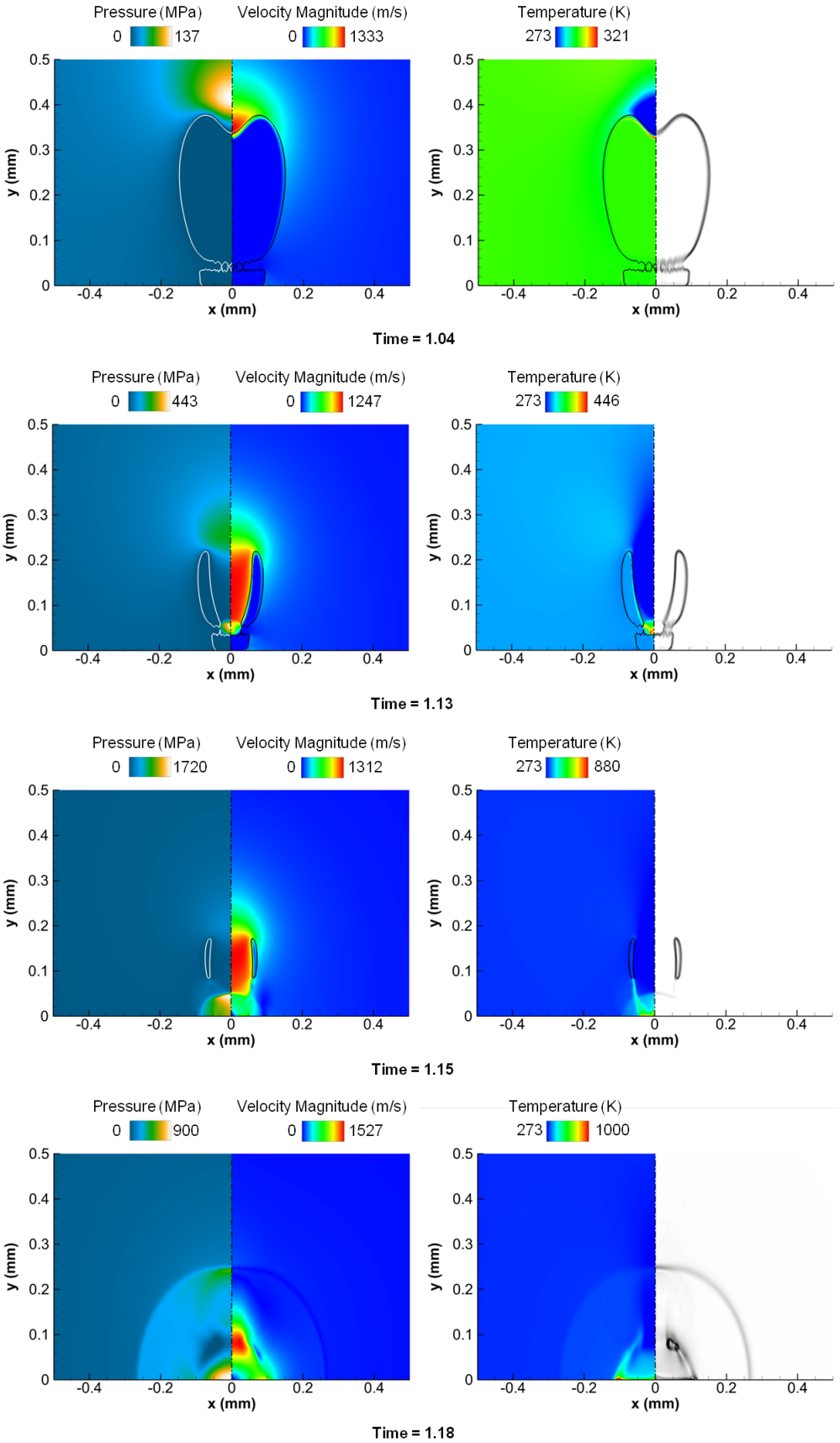

Figure 3.10: Contour field instances during vapour bubble collapse for $d = 416\,\mu m$. Time has been non-dimensionalized with $\tau = 2.88\,\mu s$.

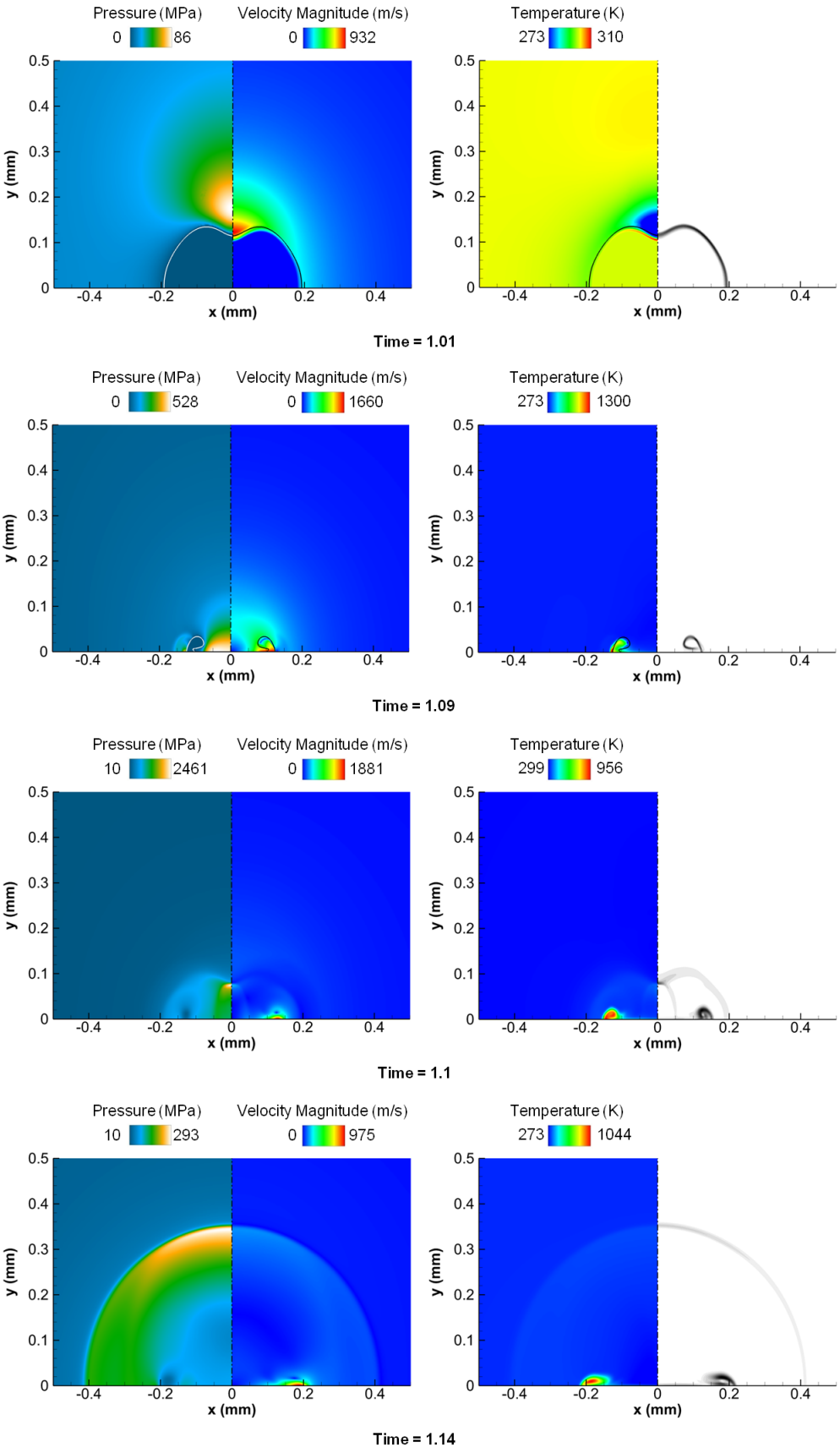

Figure 3.11: Contour field instances during vapour bubble collapse for $d = 140\,\mu m$. Time has been non-dimensionalized with $\tau = 2.88\,\mu s$.

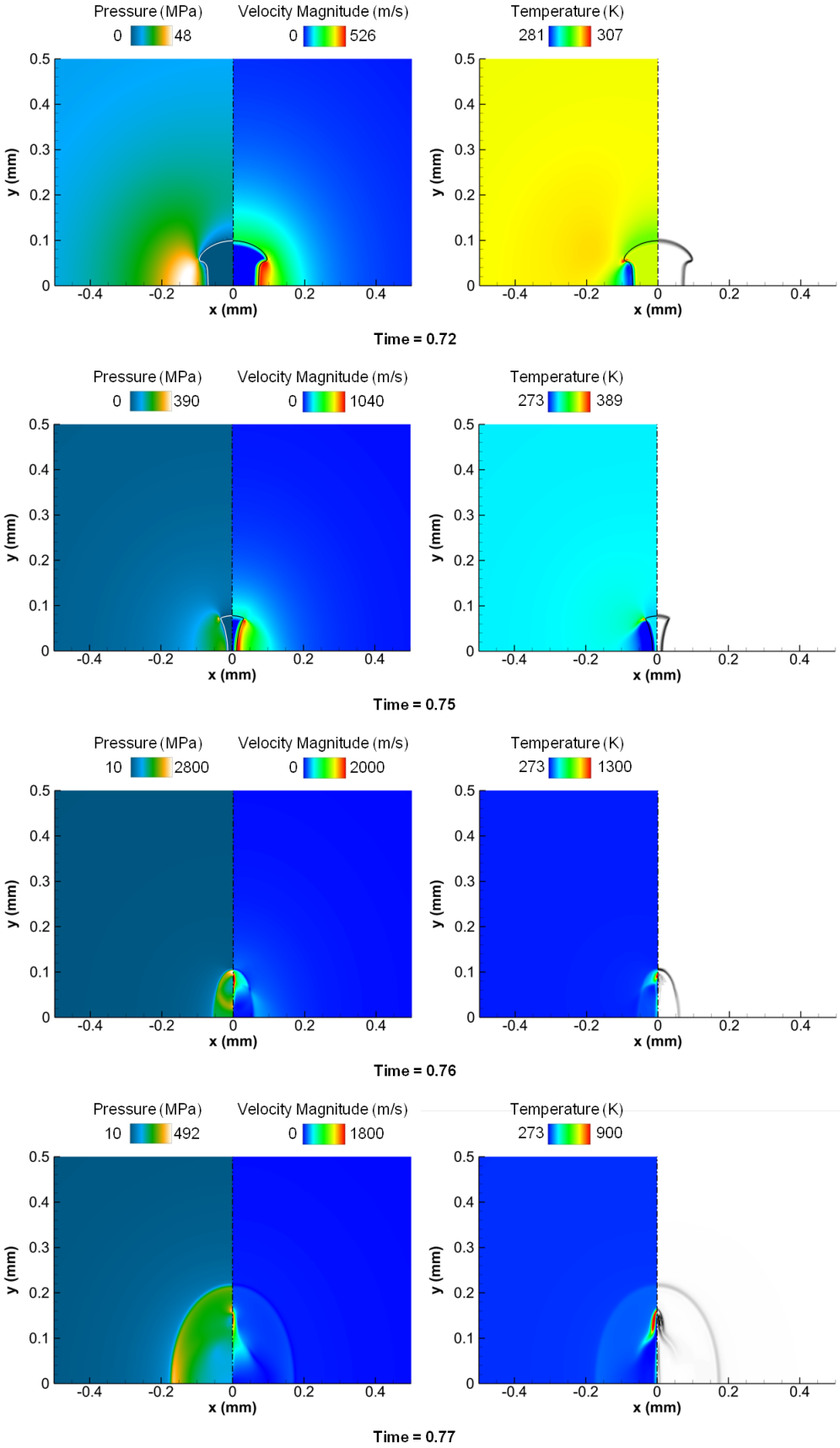

Figure 3.12: Contour field instances during vapour bubble collapse for $d = -140\,\mu m$. Time has been non-dimensionalized with $\tau = 2.88\,\mu s$.

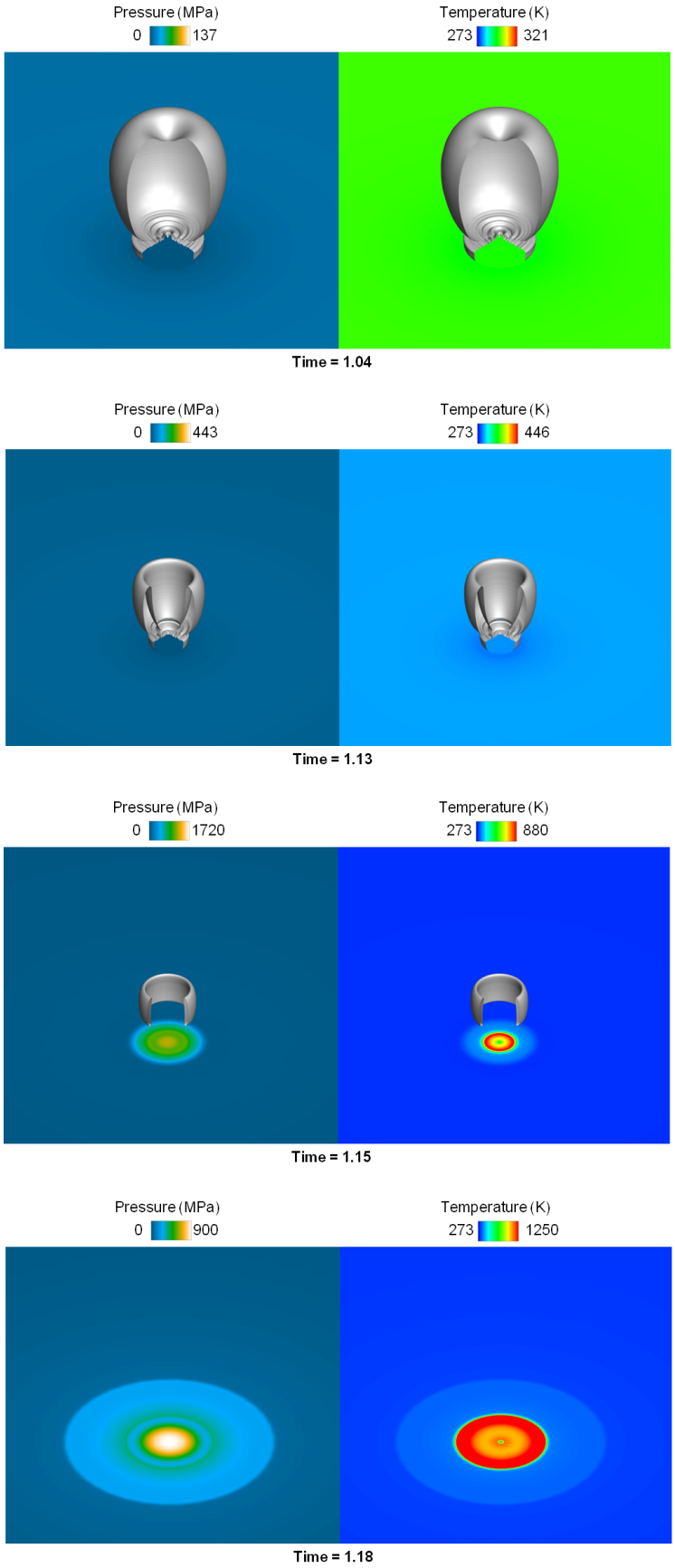

Figure 3.13: Wall pressure and temperature contours combined with bubble isosurface of $\rho = 380\,kg/m^3$ for $d = 416\,\mu m$. Time has been non-dimensionalized with $\tau = 2.88\,\mu s$.

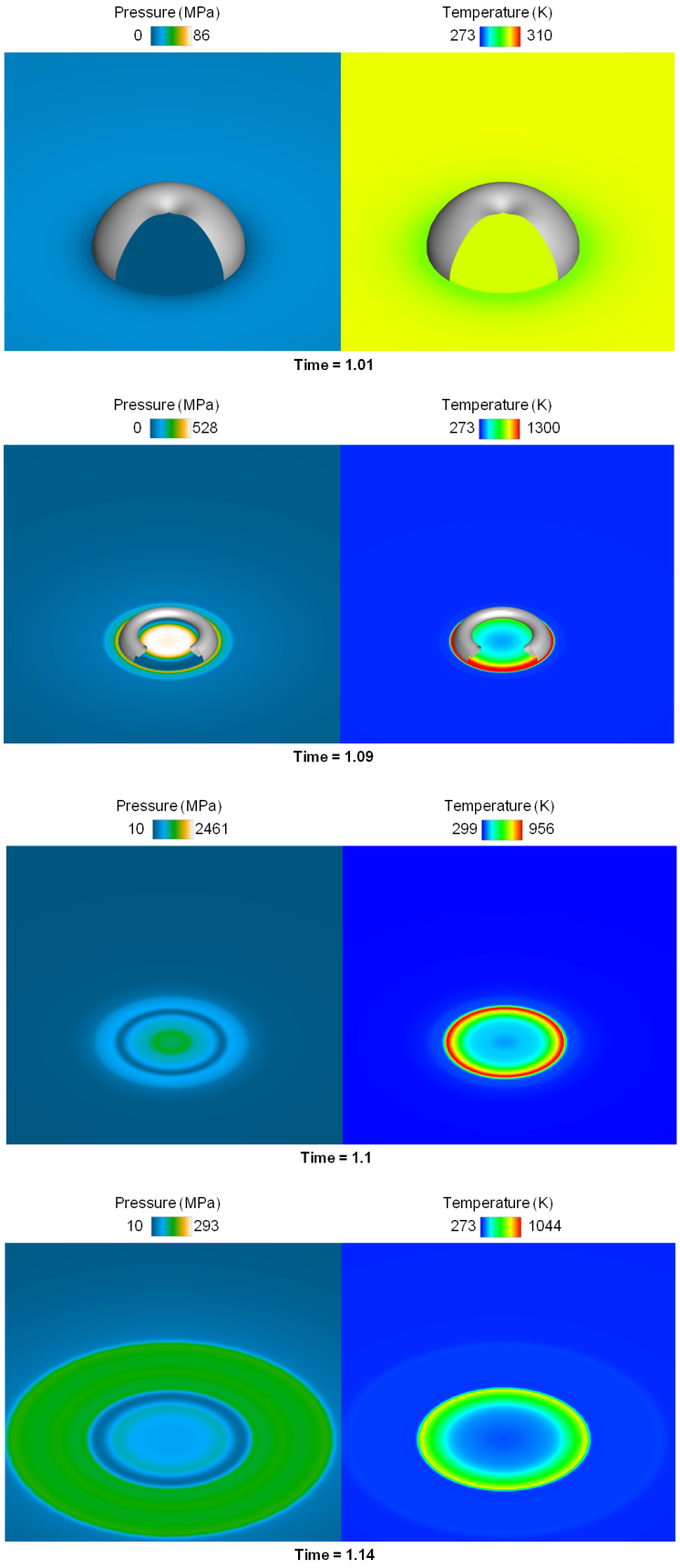

Figure 3.14: Wall pressure and temperature contours combined with bubble iso-surface of $\rho = 380\,kg/m^3$ for $d = 140\,\mu m$. Time has been non-dimensionalized with $\tau = 2.88\,\mu s$.

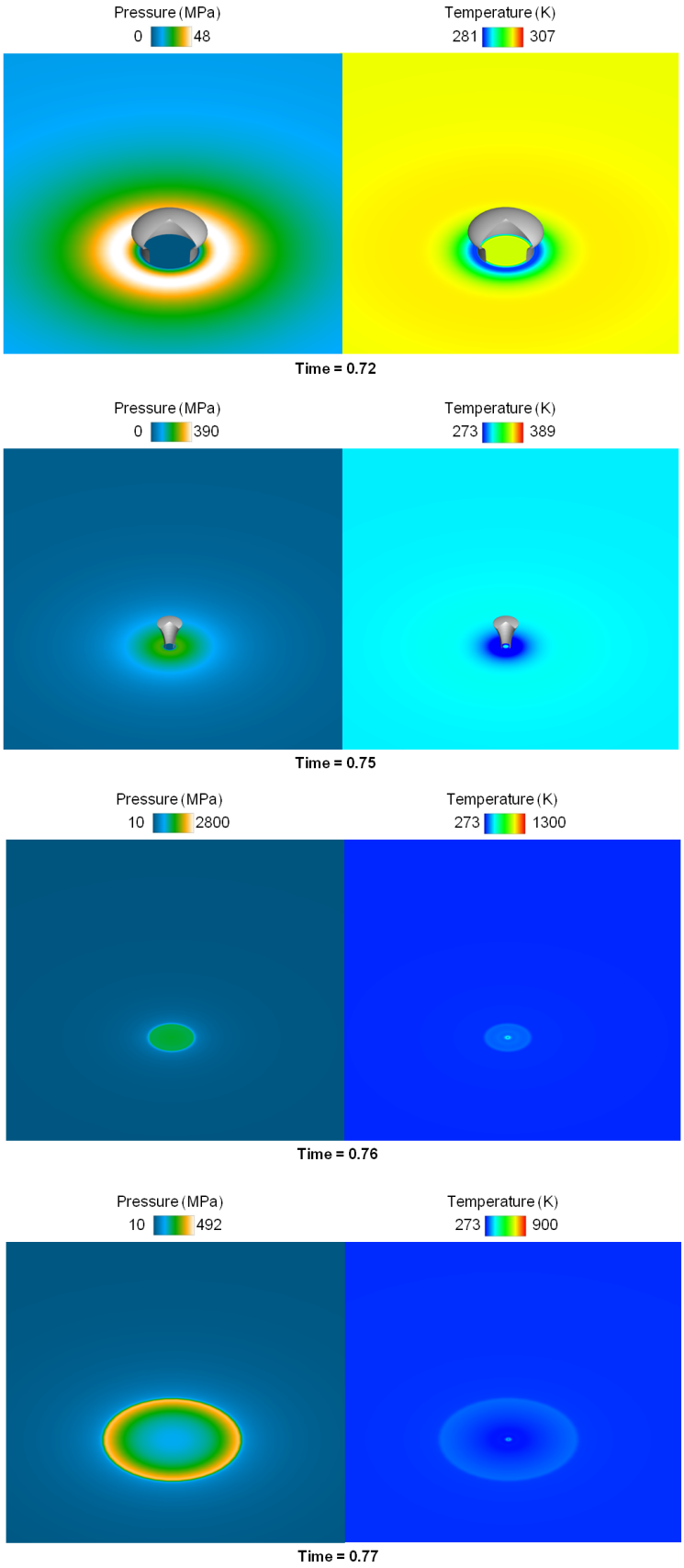

Figure 3.15: Wall pressure and temperature contours combined with bubble isosurface of $\rho = 380\,kg/m^3$ for $d = -140\,\mu m$. Time has been non-dimensionalized with $\tau = 2.88\,\mu s$.

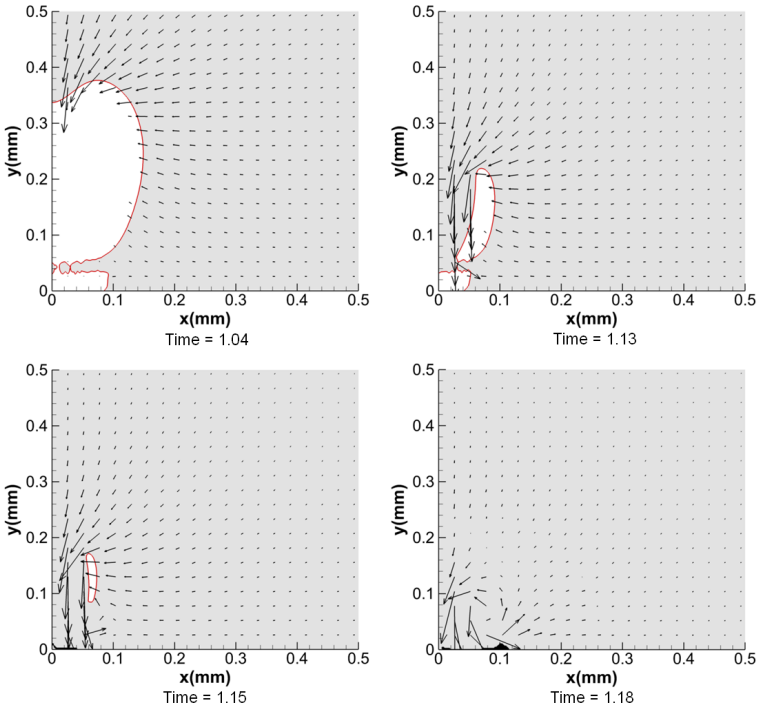

Figure 3.16: Depiction of the supercritical (black), vapour (white) and liquid (grey) regions, combined with velocity vectors for $d = 416\,\mu m$. Time has been non-dimensionalized with $\tau = 2.88\,\mu s$.

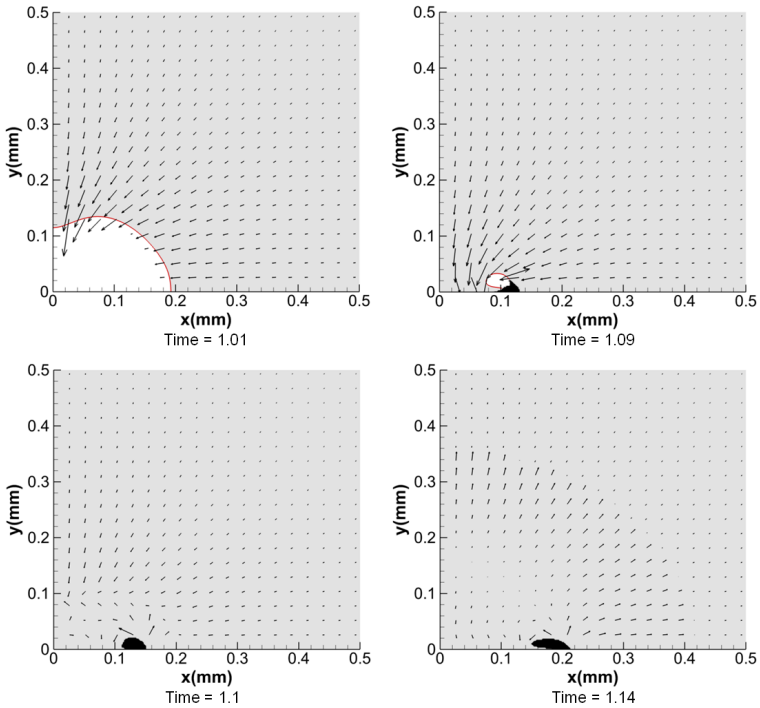

Figure 3.17: Depiction of the supercritical (black), vapour (white) and liquid (grey) regions, combined with velocity vectors for $d = 140\,\mu m$. Time has been non-dimensionalized with $\tau = 2.88\,\mu s$.

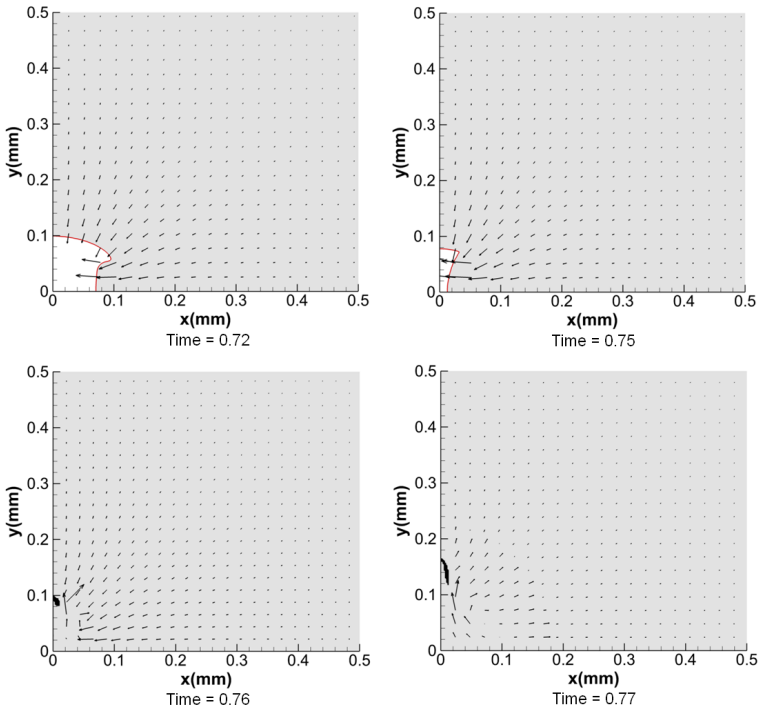

Figure 3.18: Depiction of the supercritical (black), vapour (white) and liquid (grey) regions, combined with velocity vectors for $d = -140\,\mu m$. Time has been non-dimensionalized with $\tau = 2.88\,\mu s$.

EoS is expressed as a function of density and internal energy, baroclinic torque is predicted, due to the misalignment of pressure and density gradient vectors and as a result, more vorticity is generated [232]. This is the case for the Helmholtz EoS, where the rebound is more dominant than the barotropic model. The HEM with temperature effects is weakly dependent on the temperature and thus, the rebound is the same as the barotropic model.

In Fig. 3.19 (right) the maximum wall pressure is shown with respect to time, which is due to the impact of the jet to the wall. It can be noticed that all models predict similar patterns for each position of the bubble, and the wall pressure can even be of the order of $10^{10}\,Pa$ for the lowest position of the bubble, as it has also been shown by Koukouvinis et al. [89]. The maximum wall pressure is predicted slightly earlier in the barotropic model, as a result of the earlier collapse time which was also noticed in this model. This pressure increase which is due to the re-entrant jet and the shock wave after the collapse of the bubble, can lead to erosion damage of materials.

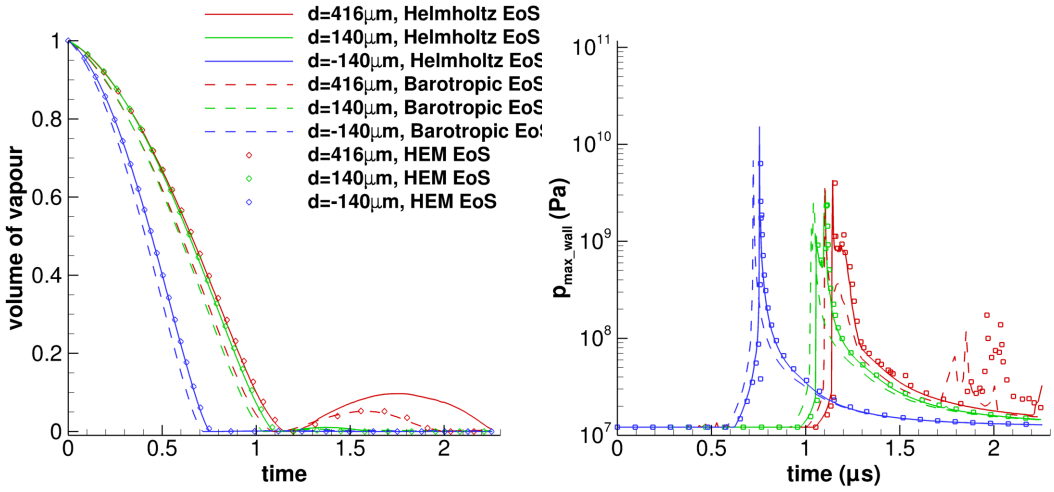

Figure 3.19: Vapour volume fraction of the bubble and maximum wall pressure with respect to time. Time has been non-dimensionalized with $\tau = 2.88\,\mu s$.

3.3.3 Effect of initial conditions

In this subsection, parametric studies of vaporous bubble collapse in the proximity of a wall have been performed, aiming to investigate how the distance between the bubble center and the wall, the surrounding liquid pressure and the initial bubble radius affect the maximum pressure and temperature on the wall. The examined cases are summarized in Table 3.1.

Table 3.1: Numbering, wall distance divided by the bubble radius d_w/R, bubble radius R, liquid pressure p_l, initial temperature of both phases T and Rayleigh collapse time τ of the simulated bubble dynamics cases.

No	d_w/R	$R\ (\mu m)$	$p_l\ (bar)$	$T\ (K)$	$\tau\ (s)$
1	1.5	1	10	400	$2.37 \cdot 10^{-8}$
2	1.5	10	10	400	$2.37 \cdot 10^{-7}$
3	1.5	1	100	400	$7.55 \cdot 10^{-9}$
4	1.5	10	100	400	$7.55 \cdot 10^{-8}$
5	0	1	10	400	$2.37 \cdot 10^{-8}$
6	0	10	10	400	$2.37 \cdot 10^{-7}$
7	0	1	100	400	$7.55 \cdot 10^{-9}$
8	0	10	100	400	$7.55 \cdot 10^{-8}$
9	−0.5	1	10	400	$2.37 \cdot 10^{-8}$
10	−0.5	10	10	400	$2.37 \cdot 10^{-7}$
11	−0.5	1	100	400	$7.55 \cdot 10^{-9}$
12	−0.5	10	100	400	$7.55 \cdot 10^{-8}$

In Fig. 3.20 the volume of vapour (top left), the maximum wall pressure (top right) and the maximum wall temperature (bottom middle) are shown with respect to time. Regarding Fig. 3.20, the collapse time is proportional to the initial volume of the vapour for each bubble. A rebound is noticed for *cases 1-4*, however it is weaker than the one noticed in section 3.3.1, due to the larger distance between the wall and the center of the bubble. The early pressure peaks at $t < 0.5$ for *cases 1, 2* and at $t < 0.8$ for cases *3, 4* (Fig. 3.20) are because of the collapse of a vapour region below the bubble which was originally created by a rarefaction wave (see also [95]). A pressure and temperature peak (total maximum) due to the bubble collapse is noticed in Fig. 3.20 at $t \sim 1$ for *cases 1-8* and at $t \sim 0.7$ for *cases 9-12*. However, at *cases 1-4* are noticed the lowest wall pressures and the lowest wall temperatures because most of the energy is transformed into kinetic and as a consequence the pressure increase is not as significant as in the rest cases; the same applies for the temperature. On the contrary, at *cases 5-8* the maximum wall pressures and the maximum wall temperatures are noticed due to the maximum compression that the bubble undergoes during its collapse. After the collapse of the bubble ($t > 1.5$), additional pressure peaks are noticed for *cases 1-4*, because of the collapse of the regenerated vapour regions (rebound). For all three figures the curves among the cases with different initial radius but the same surrounding pressure and the same distance d_w coincide as it was expected, given the fact that the time has been non-dimensionalized with τ. Although the vapour volume is higher in bubbles with larger initial radius, the

non-dimensional distance d_w is the same and thus, the actual distance between the center of the bubble and the wall is higher. Proportionally, it has the same effect as a vaporous bubble with smaller initial radius placed at smaller actual distance from the wall surface.

In Fig. 3.21 the evolution of the bubble iso-surface ($\alpha_v = 0.5$) for *case 1* is shown. Compared to Fig. 3.10 and 3.13, the bubble shape is much more symmetrical due the longer distance between the bubble center and the solid surface; the heart-shape is only noticed at the later stages of the collapse ($t = 1.06, 1.08$), which was much more evident in Fig. 3.10 and 3.13. Up to non-dimensional time $t = 1.03$, a slow shrinking of the bubble is noticed, while afterwards until $t = 1.08$ the bubble experiences a rapid collapse due to the high velocity jet. A rebound is noticed after $t = 1.22$ owning to the EoS and the influence of the wall (see also section 3.3.2 and [95]).

3.3.4 Conclusions

The pressure increase due to the re-entrant jet and the shock wave after the collapse can potentially lead to erosion damage of materials. Furthermore, the maximum temperatures noticed on the wall which are actually the maximum temperatures of the liquid, are high enough during cavitation collapse that they can induce pyrolysis of Diesel fuel and contribute to deposit formation.

During the grid independence study, higher maximum pressure and temperature for the finer mesh have been noticed. This is reasonable in a way that more scales can be captured with the finer mesh. For example, if the vapour bubble size is smaller than the cell size, then it cannot be captured with the coarse mesh and neither can the collapse. Similar observations have been made by Adams and Schmidt [83]. Furthermore, the collapse time was the same, regardless the resolution of the mesh that has been used.

The system-cpu time required for each thermodynamic model is compared for simulating the bubble collapse case until time $6.5\,\mu s$. The user-cpu time for the Helmholtz model is almost 3.7 times the HEM time, whereas the barotropic simulations are computationally the most efficient, as the execution time is almost 52 times smaller than the HEM time. The main reason for the increased cpu-time of the HEM model is the iterative calculation of the temperature using Newton-Raphson method, which necessitates complex expressions, especially in the mixture regime. The energy equation, which is not solved in the barotropic

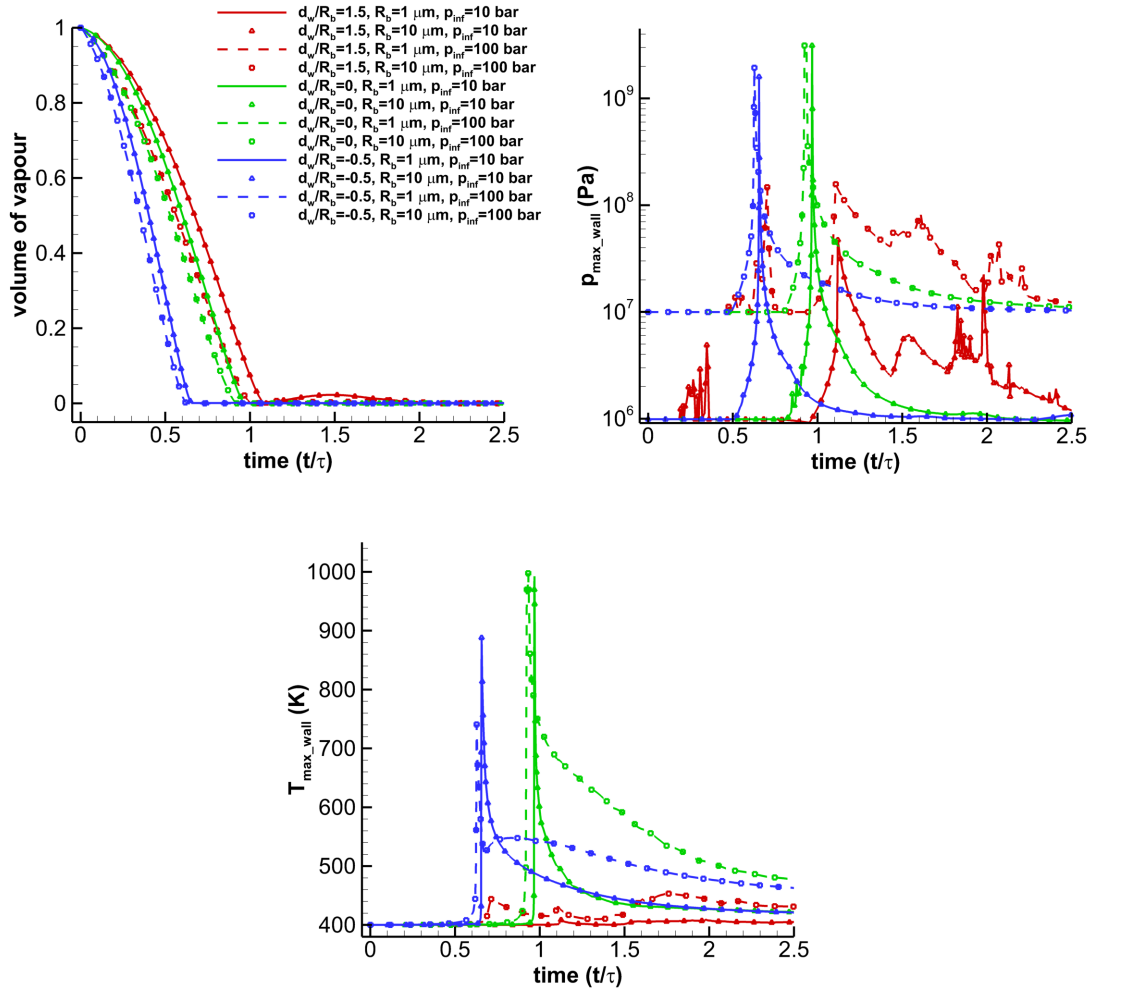

Figure 3.20: Vapour volume fraction of the bubble, maximum wall pressure and maximum wall temperature with respect to time for the configurations given in Table 3.1. Time has been non-dimensionalized with τ.

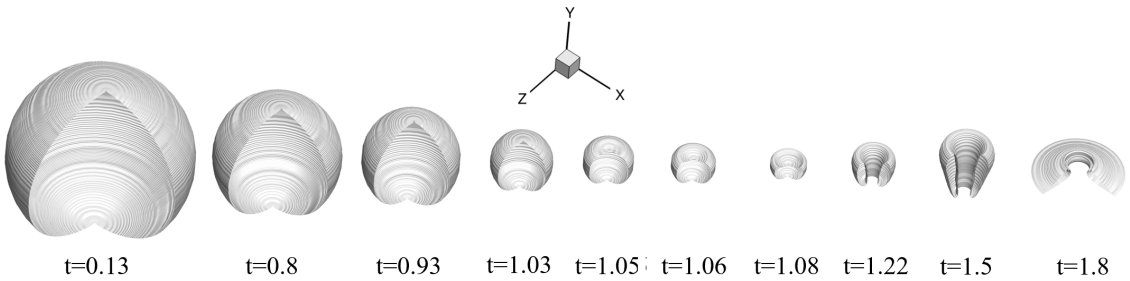

Figure 3.21: Bubble collapse evolution for *case 1*; iso-surfaces of vapour volume fraction $\alpha_v = 0.5$. Time has been non-dimensionalized with τ.

model, doesn't affect the computational cost of the HEM with temperature effects.

Although no gas phase is included in the current model and thus the heating in the inner of the bubble cannot be predicted, real fluid thermodynamics

are incorporated in the algorithm, with the potential of predicting supercritical transitions. The barotropic model is robust and can be used as a reference, but temperature effects are ignored. The HEM with simplified thermodynamics, is only applicable for a small range of temperatures. On the other hand, Helmholtz EoS is applicable for a wider range, as long as experimental data exist to calibrate the equation (regarding the applicability range of the bubble dynamics simulations, see Appendix E). For instance, in some cases during the vapour bubble collapse, local conditions may exceed the applicability range of the equation for the selected material. In such cases, the Helmholtz EoS was applied to derive thermodynamic properties beyond the calibration limits. Even though there is no guarantee that the calibration of the Helmholtz equation is valid in this regime, the derived properties have been checked for consistency (e.g. increasing density as pressure increases, for given temperature) and were found to behave in a reasonable manner, i.e. no inflexion or stationary points were found, indicating a monotonic behaviour of the property functions. Although the trend of all thermodynamic models employed is similar, supercritical transitions are only possible to capture using the Helmholtz (or equivalent cubic/high order EoS, such as Peng-Robinson, see Lacaze et al. [233]), showing the importance of accurate thermodynamic modelling.

3.4 2-D axisymmetric nozzle (Helmholtz EoS)

In order to expand the tabulated data methodology to cryogenic flow applications, inviscid flow of LOX inside a symmetrical converging-diverging nozzle is examined. The circular cross-section S is variable with the length x: $S(x) = 0.01x^2 + 0.01$, $x \in [-2, 2]\, m$. The inlet conditions are $\rho_{in} = 817.07\, kg/m^3$, $T_{in} \approx 143\, K$, which will lead to an inlet pressure $p_{in} = 5387100\, Pa$, whereas in the outlet condition, only the pressure is specified, $p_{out} = 1634699.75\, Pa$. A structured grid of approximately 5200 cells has been created for a 5° wedge, where the length size is $\Delta x \approx 1\, cm$, equally spaced in the x-direction and $\Delta y \approx 4.3\, mm$, equally spaced in the y-direction (Δy changes in the x direction, as the radius of the nozzle decreases or increases).

As it can be seen in Fig. 3.22, the obtained numerical solution and the reference solution from a pseudo 1-D FV solver coincide for all the plotted quantities. Due to subsonic flow conditions in the entrance, flow accelerates in the converg-

ing part. In the diverging part, flow continues to accelerate ($M > 1$), resulting in further depressurization and beginning of vaporization. The supersonic region in this configuration is extended all the way down until the exit and no shock wave is noticed.

3.5 Cavitating flow around NACA 0015 (barotropic model)

The cavitating flow around NACA 0015 hydrofoil is simulated next. The cavitation sheet formation and the shedding of the vapour cloud are predicted in a periodic pattern by employing the single phase barotropic model of section 2.2.1.

A 2-D NACA 0015 hydrofoil at 6° angle of attack with chord length $c = 0.13\,m$ was utilised and the computational grid which was created, consists of $16.8k$ finite volumes. The hydrofoil curve is discretized by 160 cells, equally divided between the upper and the lower sides; the leading and trailing edges are refined with stretching ratio of $1.3 \cdot 10^{-4}\,m$ (the computational domain is shown in Fig. 3.23). In the inflow, the free-stream velocity is set to be $u_\infty = 12\,m/s$ and a zero gradient condition was selected for the pressure. The free-stream pressure is $p_\infty = 10^5\,Pa$, which is specified in the outlet. The hydrofoil surface is treated as no-slip wall. First order interpolation was used initially and then, second order interpolation with van Leer flux limiter was utilized. The time-step is controlled by the CFL number, whose value was selected to be 0.9.

In Fig. 3.24 the 4 latest cavitation cycles of the generated vapour volume fraction are shown. The flow field has an oscillatory behaviour and it can be described as periodic. The order of the reconstruction and the mesh resolution strongly affect the cavitation frequency f and consequently the St number [234, 116, 28]. For instance, Sauer [234] reported a frequency of $f = 11\,Hz$, whereas in the work of Schnerr et al. [116] the frequency was calculated to be $f = 9\,Hz$ for both first order coarse and second order finer grids. Koop [28] reported $f = 19.9\,Hz$ ($St = 0.21$) when 100 cells where used for the airfoil, whereas when the NACA geometry was described by 400 cells, a frequency of $f = 40.9\,Hz$ ($St = 0.44$) was calculated. In the present study, the St number was calculated to be about $St = 0.52$, based on the cavitation frequency of $f = 48\,Hz$.

In Fig. 3.25, 3.26, 3.27 contour fields for the pressure, the vapour volume fraction and the velocity magnitude within a cavitation cycle are shown respec-

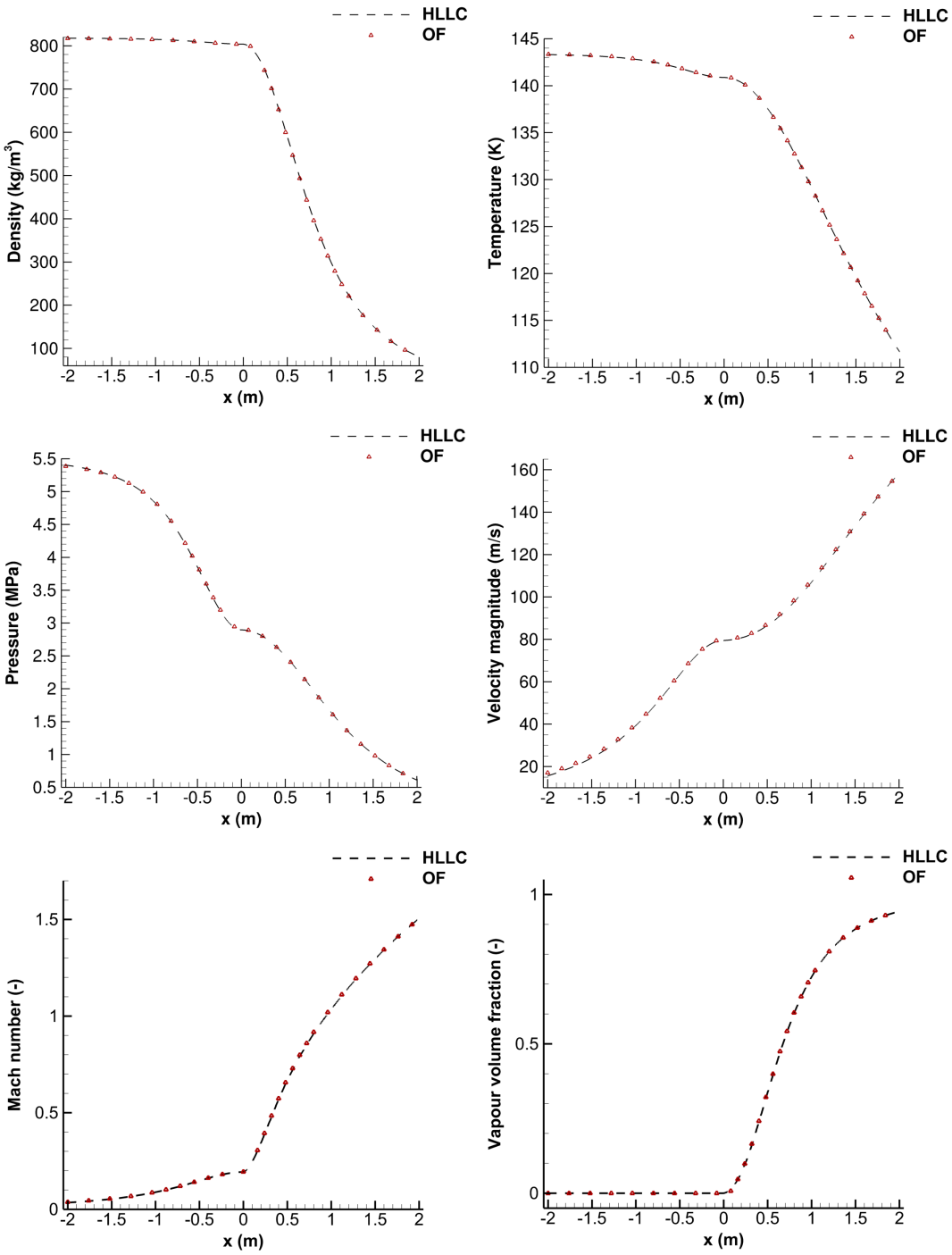

Figure 3.22: Validation for the converging-diverging nozzle case: comparison of the density (upper left), temperature (upper right), pressure (middle left), velocity magnitude (middle right), Mach number (lower left) and vapour volume fraction (lower right) between the OF solver (OF) and a pseudo-1D FV solver (HLLC).

tively. The corresponding times for each frame number of Fig. 3.25 are shown in Table 3.2. The first and the last frames, *frame 1* and *frame 8* demonstrate the periodic pattern, as *frame 1* is from the previous period. In *frame 2* the sheet

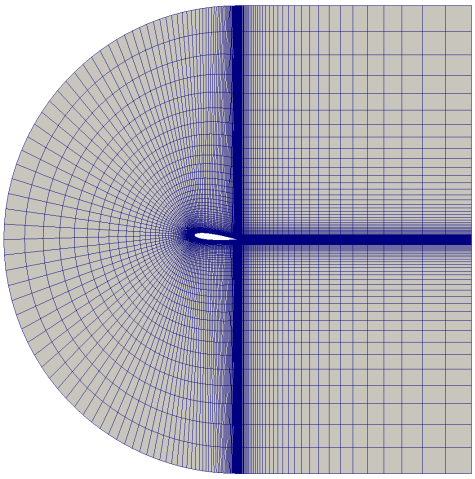

Figure 3.23: Computational grid of 16.8k cells around NACA 0015 hydrofoil.

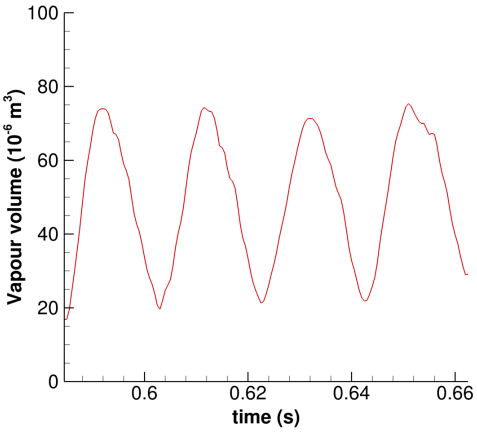

Figure 3.24: Plot of the generated vapour volume fraction of the NACA 0015 hydrofoil with respect to time for 4 cavitation cycles.

cavity starts to grow at the leading edge of the hydrofoil. Another vapour region from the previous shedding cycle has convected and it is in the middle of the chord. In *frame 3* the sheet cavity has increased and there is a re-entrant flow noticed (see Fig. 3.27 in the middle of the chord on *frame 3*), while the shed vapour region has travelled towards the trailing edge and it starts to collapse on *frame 4*. In the next frame (*frame 5*), the shed vapour region has collapsed, the sheet cavity has reached its maximum length and the shedding is about to begin. While the shed vapour region collapses in the trailing edge, a pressure peak is noticed in *frame 6*. In *frame 6* part of the sheet cavity has collapsed and it is decomposed into smaller vapour regions, which produce a shock wave as they collapse. Three different shock waves at the leading edge of the hydrofoil are shown in *frame 7* of Fig. 3.25 as a result of the collapse of different vapour

regions which were originally part of the sheet cavity.

Table 3.2: Frame number and the corresponding time for the NACA 0015 hydrofoil simulation.

Frame No	t (s)
1	0.6020
2	0.6070
3	0.6090
4	0.6125
5	0.6150
6	0.6185
7	0.6225
8	0.6230

3.6 Bubble-shock wave interaction (Stiffened-ideal gas)

The two-phase solver of section 2.3.1 is utilized to model a gaseous bubble-shock wave interaction. Such phenomena are noticed in lithotripsy (see selectively [235, 236, 237, 238]) or for drug delivery purposes. Similar to the vaporous bubble collapse of section 3.3, the phenomenon is inertia driven and thus, the compressible Euler equations are solved.

A wedge of 5° is used by taking advantage of the problem axial symmetry. A gaseous bubble of initial radius $R_0 = 400\,\mu m$ at atmospheric conditions ($p_g = 0.1\,MPa$, $T_g = 300\,K$, $Y_g = 1$) is surrounded by water at the same pressure and temperature ($p_l = 0.1\,MPa$, $T_l = 300\,K$, $Y_l = 0$). The bubble center is on the y-axis, at $y = 416\,\mu m$ above the solid surface. On the upper side, water at higher pressure ($p_s = 6\,MPa$, $T_s = 300\,K$, $Y_s = 0$) is set as boundary condition (see Fig. 3.28). The computational domain is extended up to 20 times the bubble radius; 150 equally spaced cells were used for describing the initial radius of the bubble. After distance $2.5R_0$ from the origin, the mesh is coarsened with ratio 1.05 in both directions. Zero gradient boundary condition has been used for the right side, slip wall for the lower side, pressure inlet for the upper side and wedge for the 2 front and back sides.

In Fig. 3.29 a temperature slice is shown on the left accompanied with the bubble iso-surface ($Y_g = 0.5$) which is coloured by the velocity magnitude. Furthermore, in Fig. 3.30, 3.31 contours of the magnitude of the density gradient

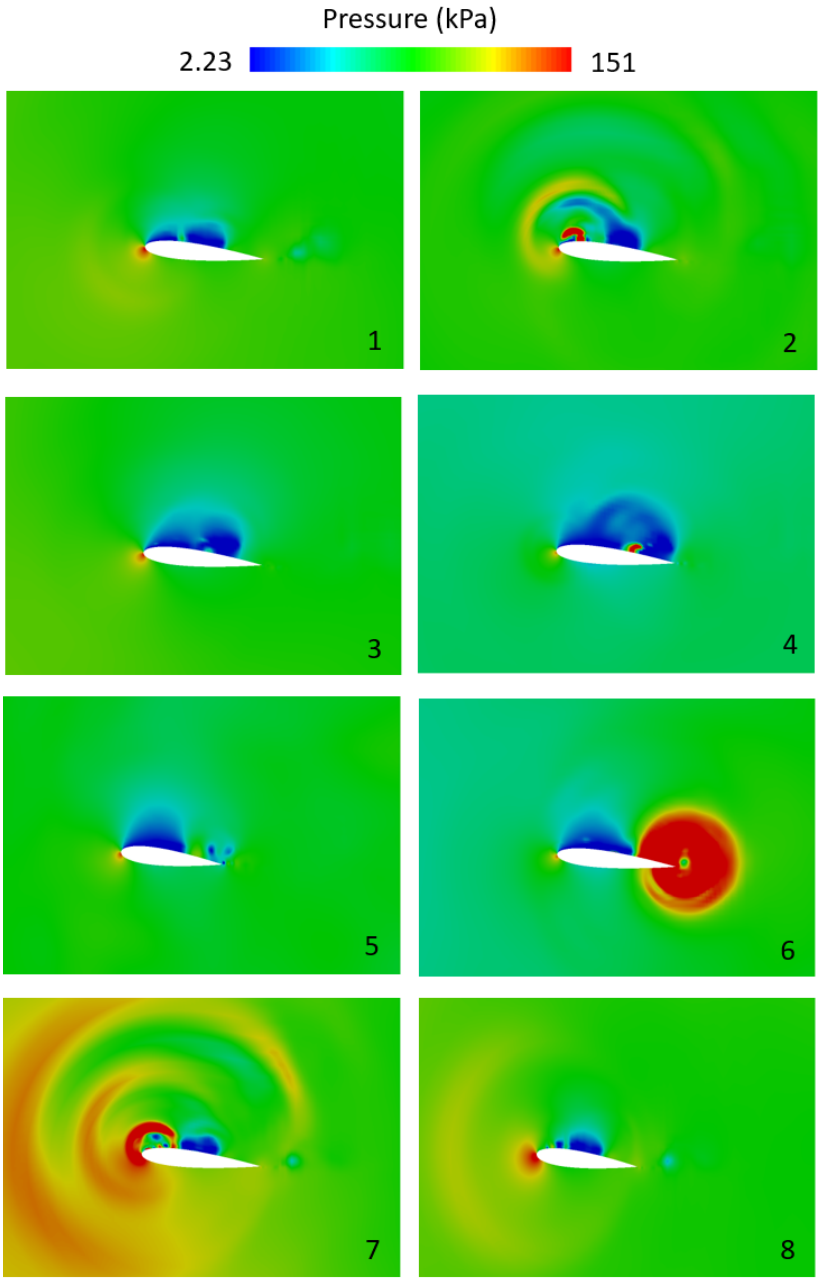

Figure 3.25: Instances of the pressure contours for the NACA 0015 hydrofoil.

are shown on the left slice, combined with the bubble-liquid interface in red ($Y = 0.5$), whereas on the right slice the pressure contours are depicted accompanied with the bubble-liquid interface in white ($Y = 0.5$).

It can be observed that the bubble collapse pattern is similar to the bubble evolution at the highest position of section 3.3.1, as in both of them the distance between the center of the bubble and the solid boundary is the same. However, the bubble collapse in section 3.3.1 is driven by the pressure difference between the vaporous bubble and the surrounding liquid, in contrast to this section where

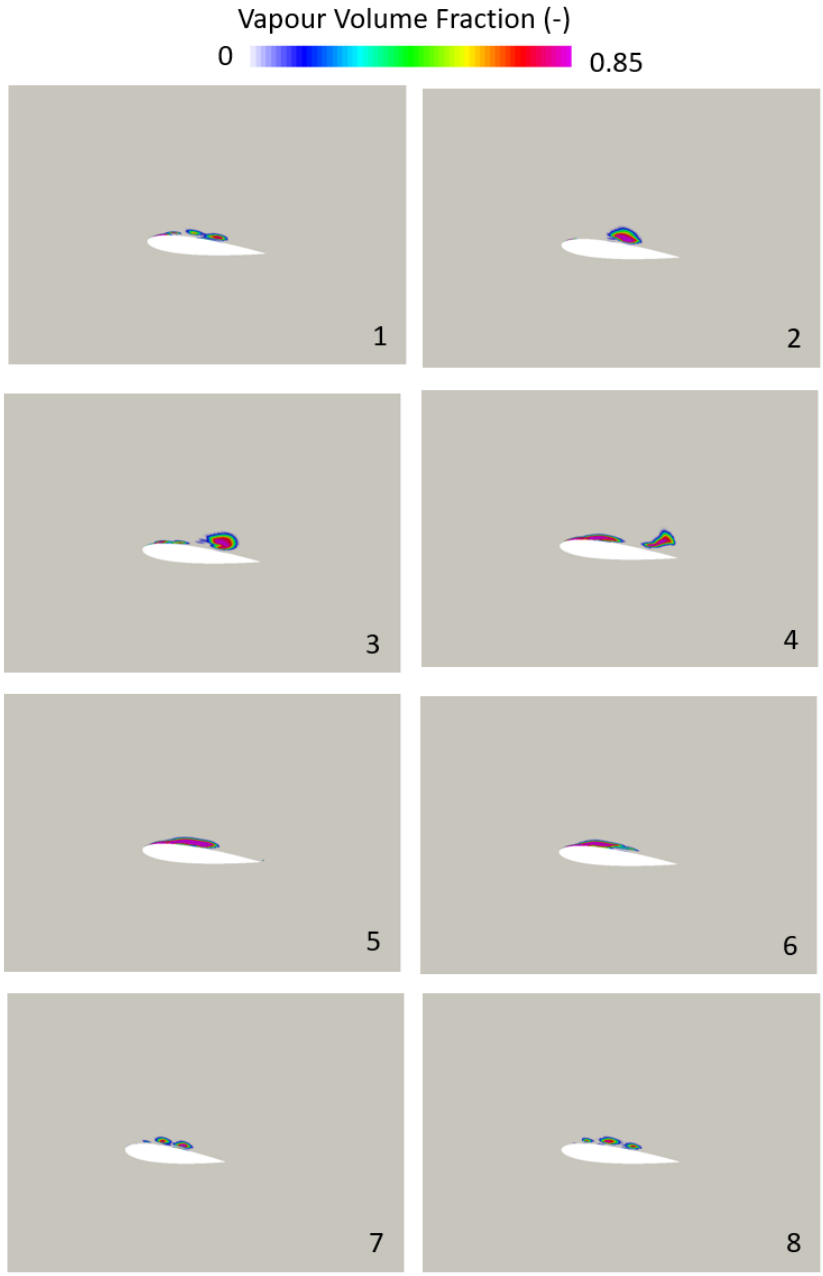

Figure 3.26: Instances of the vapour volume fraction contours for the NACA 0015 hydrofoil.

the collapse is because of the downwards moving shock wave; initially the gaseous bubble and the surrounding liquid share the same temperature and pressure. As soon as the shock wave hits the bubble ($t > 6.6\,\mu s$), the latter starts to shrink, slowly in the beginning ($t = 8, 10, 12\,\mu s$) but rapidly in the later stages of the collapse where a strong jet has been developed on the upper side ($t > 12\,\mu s$). The heart-like shape is distinct from $t = 12.4\,\mu s$ up to $t = 12.8\,\mu s$. At the last two frames ($t = 12.8, 13\,\mu s$) of Fig. 3.29 before the collapse, the jet has been developed and takes its maximum value. At $t = 13.2\,\mu s$ the bubble collapse

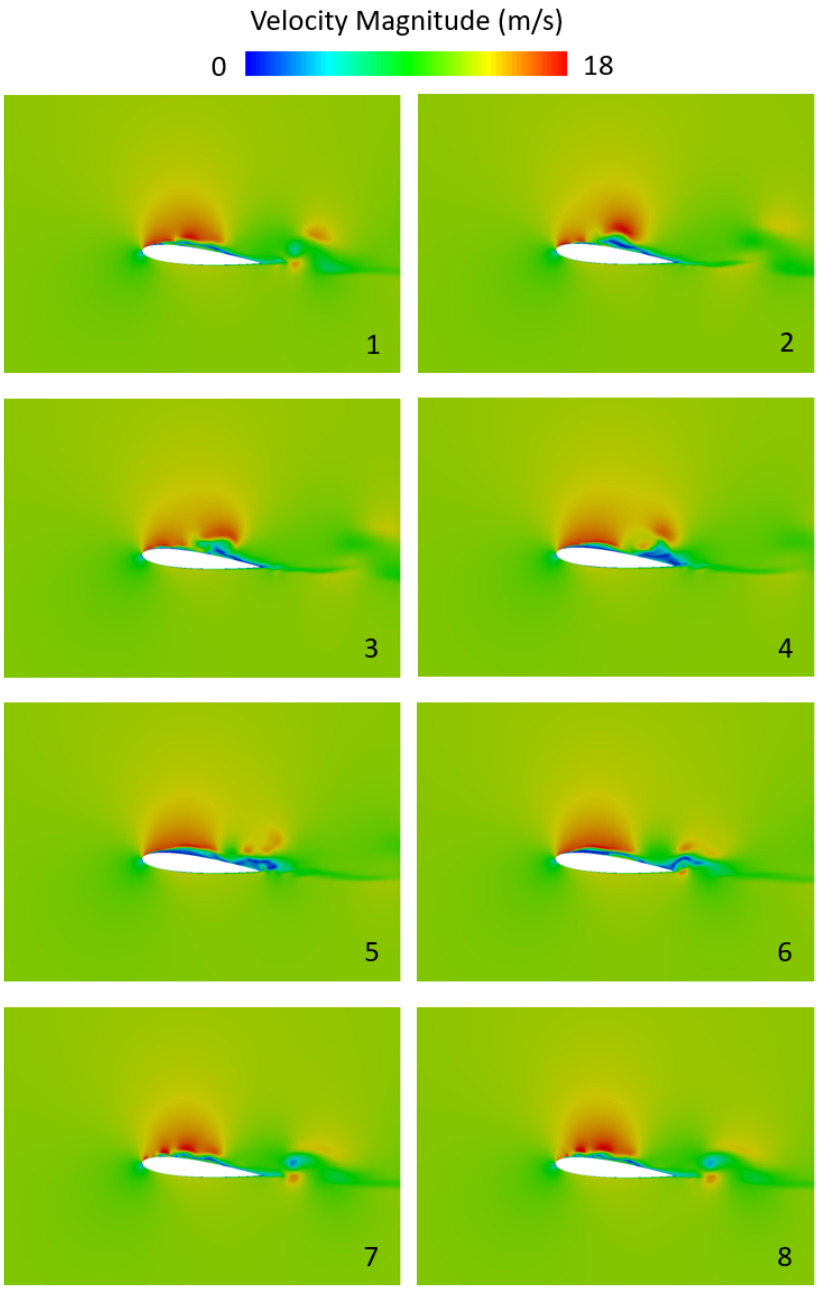

Figure 3.27: Instances of the velocity magnitude contours for the NACA 0015 hydrofoil.

is shown followed by a pressure peak and at times $t = 13.6, 14\,\mu s$ the shock is travelling away from the initial bubble location.

3.7 Droplet impact (3-phase mixture, linear EoS)

The capabilities of the 2-phase solver of section 2.2.1 can be demonstrated in a droplet impact simulation, where gas, liquid and vapour are modelled [226]. A planar 2-D droplet impact case has been selected for qualitative validation

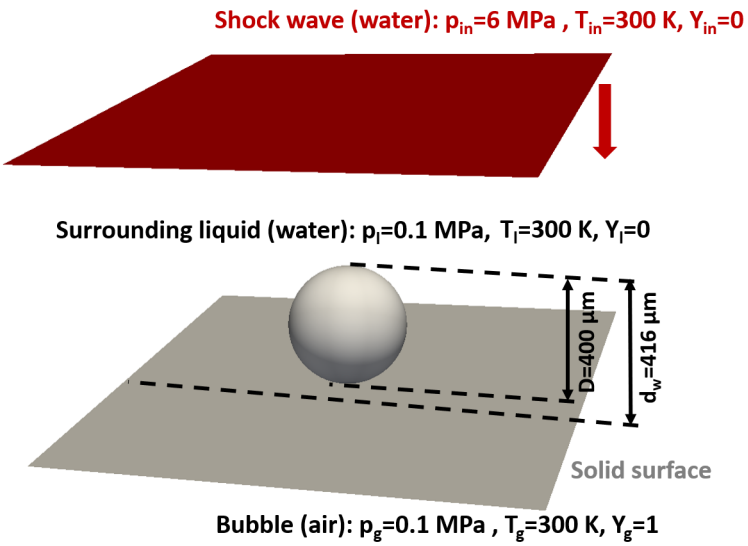

Figure 3.28: Initial configuration of the bubble-shock wave interaction problem.

of the propagating shock and the reflected expansion waves against available experimental data [163]. Then, 2-D axisymmetric droplet impingement on a solid wall is modelled for different impact velocities, in order to investigate the extent of the cavitation zone and how bubble collapse can possibly lead to material erosion. The droplet impact simulations are summarised in Table 3.3, where the Re, We and Fr numbers have been calculated, based on the impact velocity u_{imp} and the droplet diameter D.

Table 3.3: Numbering, description, impact velocity, Reynolds, Weber and Froude numbers of the droplet impact cases which have been simulated. As 2-D axisymmetric are denoted the wedge simulations and no air means that in the initial condition the droplet is attached to the wall, in comparison to the rest of the simulations where the droplet is 3 cells above the wall in the beginning of the simulation.

Name	Description	u_{imp} (m/s)	Re	We	Fr
1	planar 2-D	110	$1.1 \cdot 10^6$	$1.67 \cdot 10^6$	351.2
2	2-D axisymmetric	110	$1.1 \cdot 10^6$	$1.67 \cdot 10^6$	351.2
3	2-D axisymmetric	27.5	$2.75 \cdot 10^5$	$1.05 \cdot 10^5$	87.8
4	2-D axisymmetric	55	$5.5 \cdot 10^5$	$4.19 \cdot 10^5$	175.6
5	2-D axisymmetric	82.5	$8.2 \cdot 10^5$	$9.43 \cdot 10^5$	263.4
6	2-D axisymmetric	220	$2.2 \cdot 10^6$	$6.71 \cdot 10^6$	702.4
7	2-D axisymmetric	550	$5.5 \cdot 10^6$	$4.19 \cdot 10^7$	1756
8	2-D axisymmetric, no air	27.5	$2.75 \cdot 10^5$	$1.05 \cdot 10^5$	87.8

The flow can be considered inviscid (the Reynolds number Re is 10^6 for impact velocity $110\,m/s$ and thus the boundary layer is too thin and the flow

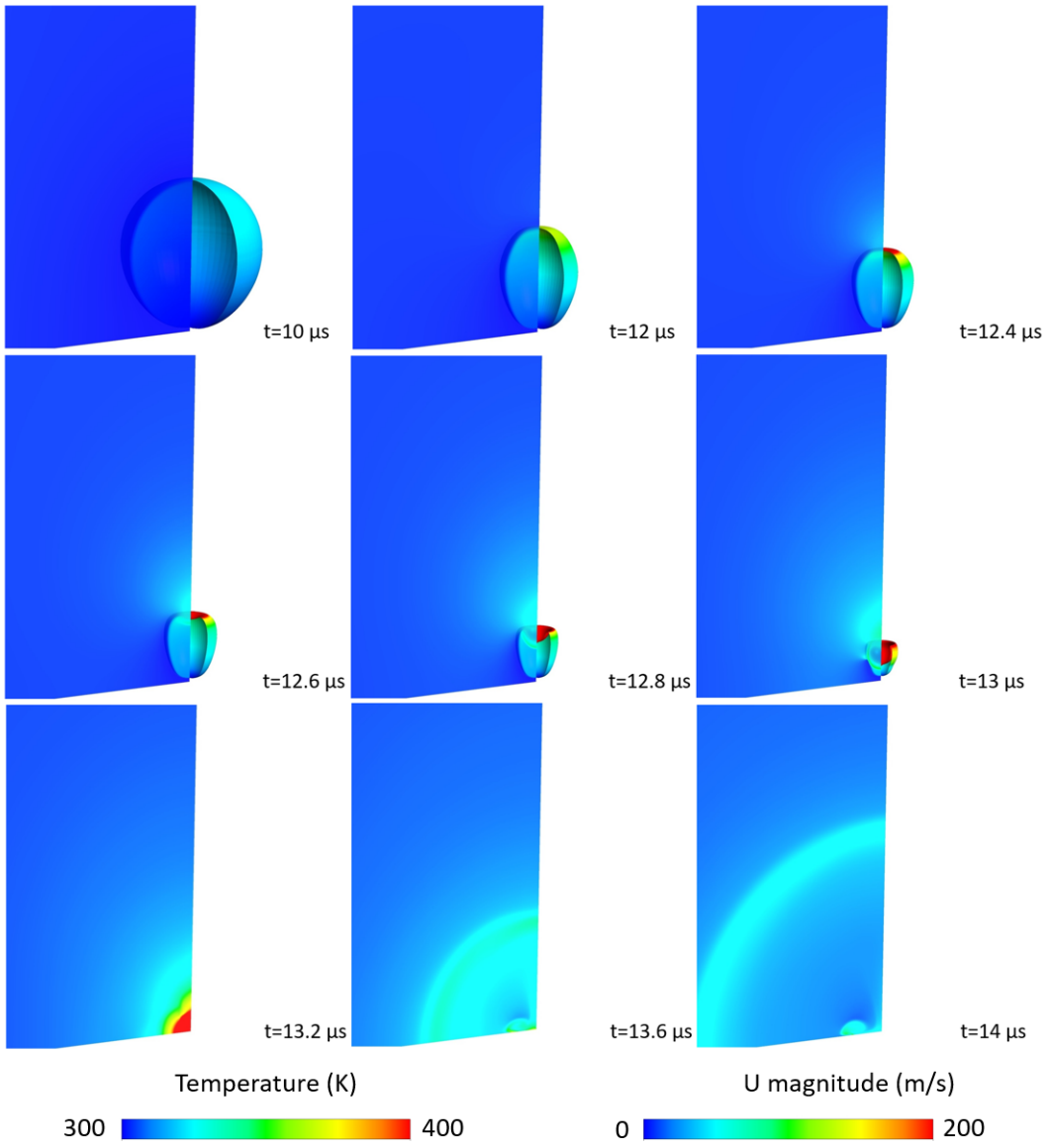

Figure 3.29: Bubble-shock wave interaction contour plots for several time instances. Temperature contours on the left slice, combined with the bubble isosurface for $Y_g = 0.5$, which is coloured by the velocity magnitude.

is inertia driven). Our interest is mainly associated with the initial stages of impact during which cavitation and its subsequent collapse take place; these occur during the early stages of splashing, so inviscid simulations have been performed. The minimum Weber number We in the present droplet impact simulations is calculated to be around 10^5 and thus, surface tension is negligible; the minimum Froude number Fr is 88 and therefore the gravitational forces are insignificant compared to the inertia ones. Due to the high impact velocities which result in high We and therefore neglecting the surface tension, contact angle boundary conditions are not explicitly defined. Zero gradient boundary

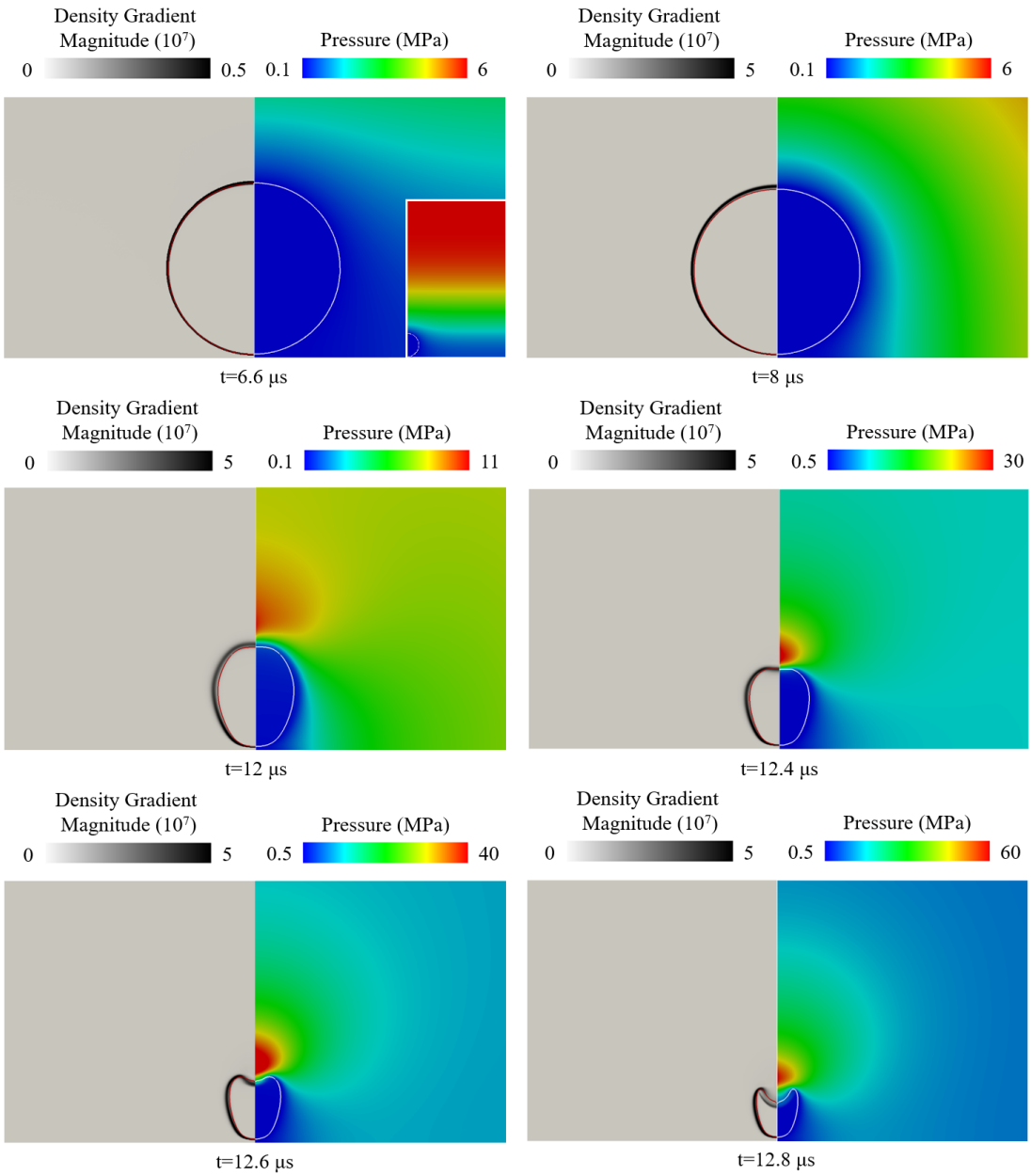

Figure 3.30: Bubble-shock wave interaction contour plots of numerical Schlieren and pressure for several time instances. Density gradient magnitude contours on the left slice, combined with the bubble iso-line for $Y_g = 0.5$ (red) and pressure contours on the right slice, combined with the bubble iso-line for $Y_g = 0.5$ (white). At time $t = 6.6\mu s$ a long shot view of pressure contours is also shown.

condition in the transport equation for the gas mass fraction is used at the wall instead (equivalent to a contact angle of 90°). Surface wettability plays an important role only when a low velocity field is noticed in the lamella and therefore adhesion forces become significant [239]. However, in the present study the lamella velocity is approximately 10 times higher than the $u_{imp} = 110\,m/s$ and therefore such effects are ignored. Although a 3-D simulation would generally

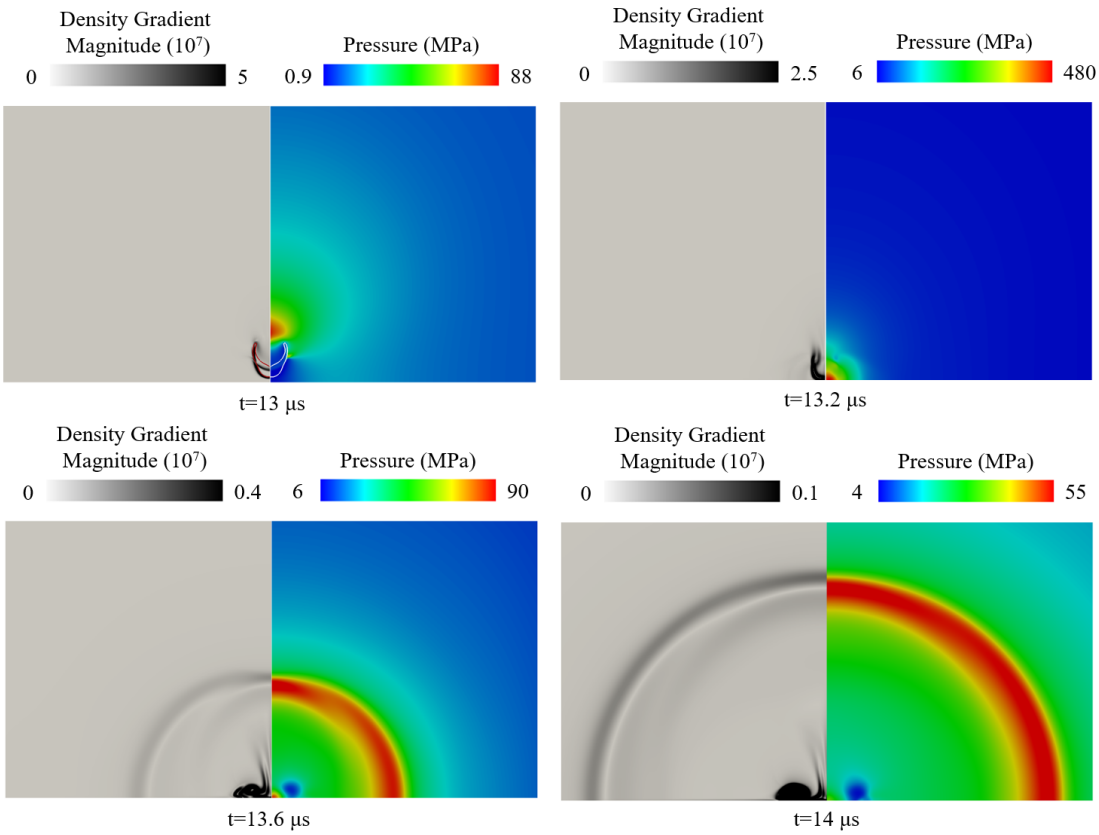

Figure 3.31: Bubble-shock wave interaction contour plots of numerical Schlieren and pressure for several time instances (continued). Density gradient magnitude contours on the left slice, combined with the bubble iso-line for $Y_g = 0.5$ (red) and pressure contours on the right slice, combined with the bubble iso-line for $Y_g = 0.5$ (white).

have captured the interfacial instabilities, a 2-D axisymmetric simulation was preferred instead, in order to reduce the computational cost. In addition, these instabilities are formed at later droplet impact times, which are not simulated here.

In the HEM approach which is followed in the present work, infinite nucleation points and infinite mass transfer are assumed, so thermodynamic equilibrium is achieved instantaneously. This methodology has been demonstrated to accurately predict the Rayleigh collapse of vaporous structures (see [240, 91, 241]). Given the original configuration and the final simulation time, which is before the splashing regime, sharp interface algorithms have not been used in the present study. The droplet is initially placed next to the wall impinging with velocity u_{imp} into stagnant air and as a consequence, there is no droplet motion in the air before the impact. The latter would necessitate sharp interface schemes in order to avoid having a diffusive interface while the droplet is travelling in the air.

In addition, at later stages of splashing, which are not simulated in the present study, sharp interface algorithms are necessary in order to provide a smear-free interface. Concerning temperature effects, they are not taken into account in the present study, since they are negligible. The interested reader is addressed to C, where this assumption is justified.

3.7.1 Planar 2-D droplet impact

The first case examined is a planar droplet impact on a solid wall for which experimental data are available [163]. A 2-D simulation, with second order discretization in space was performed in order to validate the algorithm against the 2-D experimental data of Field at al. [163]. A circular cross-section water column of diameter $D = 10\,mm$ is placed between two transparent plates, separated by a small distance. The impact is modelled by a third plate which is projected with velocity $110\,m/s$ among the two plates. For the numerical simulation, the centre of the droplet was placed at $(x_0, y_0) = (0, 0.00505)$ in the computational domain $(-0.2, 0.2) \times (0, 0.2)$; 150 cells have been placed along the initial droplet radius R (grid size $\sim 33\,\mu m$). The viscous effects are negligible due to the high Re number ($Re = 1.1 \cdot 10^6$) and our interest is mainly associated with the impact and pressure wave dynamics. The same cell size as in the droplet radius has been kept until distance $2R$ in the positive and negative x-direction and until $1.5R$ in the positive y-direction. After that, a stretching ratio of 1.05 has been applied, resulting in a total amount of $380\,k$ cells. A CFL number of 0.5 was chosen for the time step selection ($\Delta t \sim 5 \cdot 10^{-9} s$) in the explicit algorithm. Initially, the pressure of the surrounding air and the water droplet is atmospheric, $p(t = 0) = 101326\,Pa$. In this way, the initial density for the two phases is calculated from the barotropic EoS. Zero gradient boundary conditions have been selected for the right, left and upper faces, whereas the lower face is set as wall. In Fig. 3.32 the experiment [163] (left) and the numerical solution (right) for the droplet impact are compared.

The main mechanisms noticed both in the experimental work [163, 161] and past numerical simulations [181, 180, 182] are jetting, as well as shock and expansion waves; these are also identified in the present study. In frame *(a)* the droplet impacts the wall, whereas in the next frame, a shock wave is forming, as a result of the impact. While the liquid close to the impact point is compressed, the information of the impact has not travelled in the rest of the droplet, which

is still moving with the impact velocity [159]. Those two regions are separated by the shock front (frame *(b)*), which is created by individual wavelets emanating from the contact edge [160, 161]. In the preliminary stages of the impact, the edge velocity is higher than the speed of sound and there is a tendency to decrease. As long as the edge velocity is higher than the shock speed, the shock is attached to the contact edge. When the edge velocity reaches the critical value of the shock speed, the shock wave is detached from the contact line (frame *(c)*) and it is propagating in the rest of the liquid (until frame *(g)*). This mechanism is responsible for the expansion of the liquid and the jetting, which is created in the contact edge (frame *(d)*, denoted as J in the experimental results). In frames *(e)*, *(f)* and *(g)*, the shock wave is reflected normal to the free surface as an expansion wave which focuses in the inner region of the drop. These low pressure areas are potential cavitation regimes and their extent, as well as the volume of the vapour depend on the impact velocity [182]. In frames *(g)*, *(h)*, the shock wave reaches the highest point of the drop and it is then reflected downwards. In the last frames, the jetting is more advanced and the reflected shock is shown in the upper middle of the drop at frames *(i)* and *(j)* (denoted as R in frame *(i)* and focused to point F in frame *(j)* of the experiment).

Comparing the present simulation with previous experimental studies of Field et al. [163], similar wave structures at the same time scale are noticed. The edge pressure in the contact edge is around $0.22\,GPa$ and it exceeds the water hammer pressure [161], which is estimated about $0.16\,GPa$, where the water hammer pressure is defined as $p_{wh} = \rho_l c_l u_{imp}$. The shock wave which is moving upwards and its reflection have been recognized at similar time frames between the experiment and the simulation. Furthermore, the jetting (starting from frame *(d)*) is around ten times the impact speed, or even higher, as it has been mentioned in [161]. Rarefaction waves have been also identified in the later stages of the droplet impact and they follow the same pattern as in the experimental study. The production of vapour in the final stages is evident due to the pressure drop and the areas where vapour is generated are in accordance to the experiment. However, in the experimental study the maximum volume of vapour is in the centre of the droplet, whereas in the present work, vapour is more dominant on the upper sides, perimetrically of the droplet. This is because bulk liquid tension cannot be captured with the present methodology, as negative pressures cannot be predicted by Eq. 2.30 for the given values of c_l, c_m, $\rho_{l,sat}$, p_{sat}.

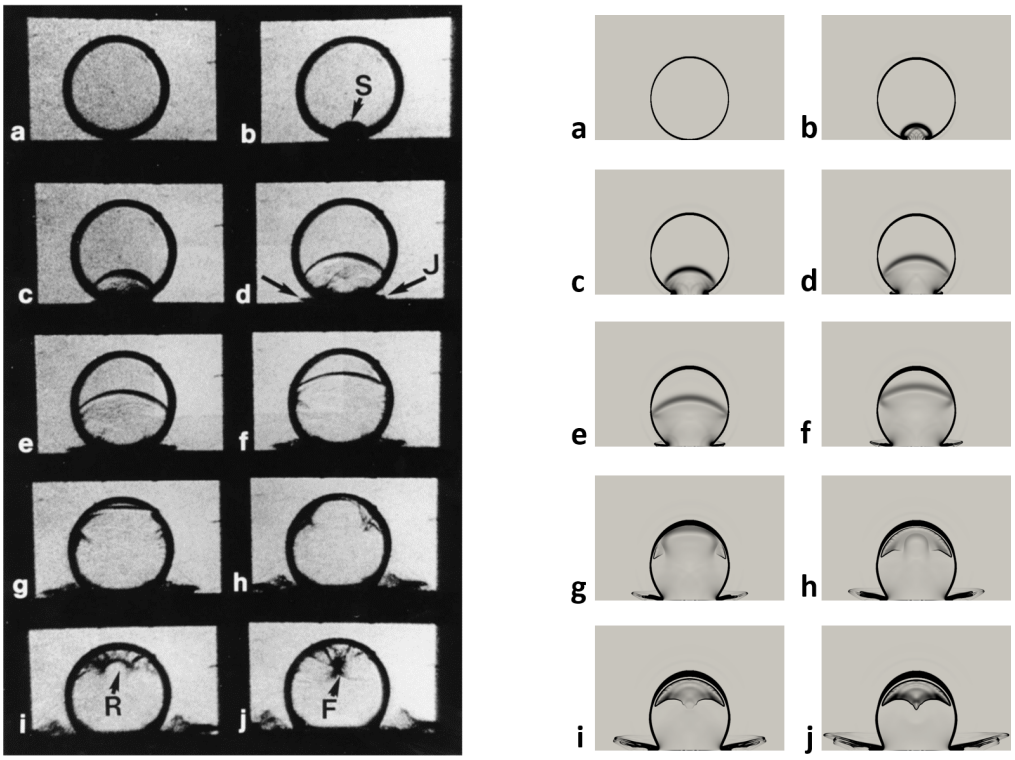

Figure 3.32: Validation of the numerical solution (right) against experiment (left) for a 2-D drop impact on a solid wall with impact velocity $110\,m/s$. The interframe time is $t = 1\,\mu s$. The left figure is taken from Field et. al [163].

3.7.2 2-D axisymmetric droplet impact

The previous simulation is now performed in a 2-D axisymmetric computational domain, in order to model the impact of spherical droplets. Starting from the half of the 2-D meshes of section 3.7.1, a wedge of 5° is created by taking advantage of the axial symmetry (see Fig. 3.33). The same initial and boundary conditions are kept, apart from the wedge faces and the axis of symmetry. At the beginning, a grid independence analysis is performed and then, the effect of the impact velocity's magnitude is investigated for the intermediate grid. Second order accurate spatial discretisation schemes have been used for this simulation and a CFL number of 0.5 was chosen for the time step selection ($\Delta t \sim 3 \cdot 10^{-10}\,s$) in the explicit algorithm. In the following figures, pressure has been non-dimensionalized with the water hammer pressure p_{wh}, velocity with the impact velocity u_{imp} and the dimensionless time is calculated from: $t = \dfrac{T - t_{bimp}}{D/c_l}$, where $t_{bimp} = 0.00005/u_{imp}$ is the time of the impact, based on the initial configuration (in cases where the droplet is not attached to the wall, but there is air between them). This way, the shock wave will be at the same y-position at a given non-dimensional time for all impact velocities.

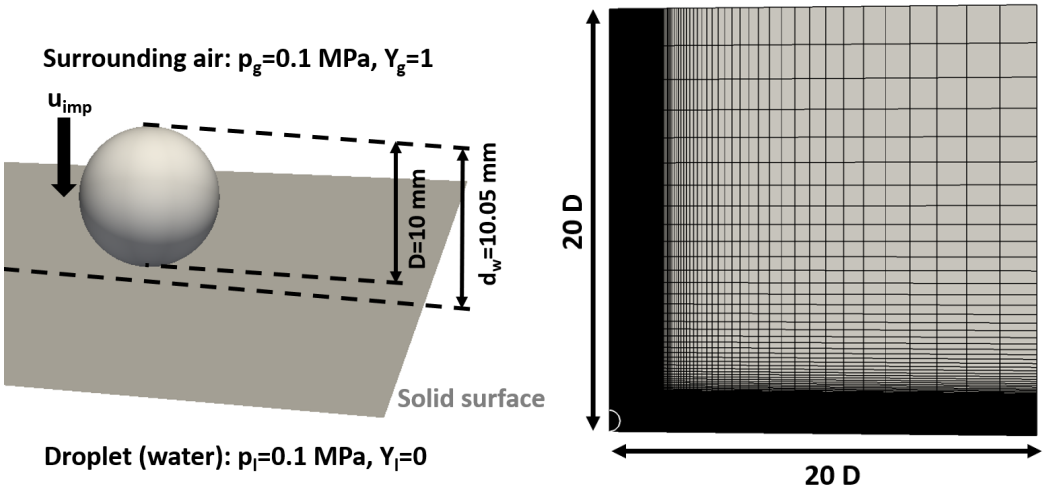

Figure 3.33: Droplet impact configuration (left) and computational grid (right).

In Fig. 3.34 the results of the grid independence study are shown having as impact velocity $110\,m/s$. Three different grids have been utilized, with $117\,k$, $380\,k$ and $1.5\,k$ cells. In the fine area $(0, 2R)\times(0, 1.5R)$ the resolution of 330×225, 660×450 and 1320×900 cells has been used for the coarse, intermediate and the fine grid respectively. On the left-hand side of Fig. 3.34, the maximum wall pressure with respect to time is shown and on the right-hand side the generated volume of vapour at a line parallel to the y axis ($x = 0.6\,mm$) at time $t = 1.19$ is plotted. The maximum wall pressures are similar for all grids and the peak noticed in the vapour volume fraction after $y = 0.8$ is almost identical for all resolutions. It can be concluded from the above study that there is convergence of the solution for the selected grid resolutions. The intermediate grid ($380\,k$ cells), referred as *case 2* from now on, is considered to be accurate enough and it is selected for the rest of the simulations.

In Fig. 3.35 and 3.36 the evolution of the droplet impact is shown for *case 2*. More specifically, in Fig. 3.35 the pressure field (left slice) and the velocity magnitude (right slice) are shown in conjunction with the iso-surface of 0.5 gas mass fraction on the left figures, whereas on the right figures, the numerical Schlieren is depicted by utilizing different scales for the inner and the outer computational domain of the droplet in order to capture the different waves, which are propagating in the liquid water and in the air. In Fig. 3.36 the wall pressure (lower slice) and the vapour volume fraction (upper slice) combined with the iso-surface of 0.5 gas mass fraction are demonstrated for *case 2*. The main mechanisms and the flow pattern in the 2-D axisymmetric simulation (*case 2*)

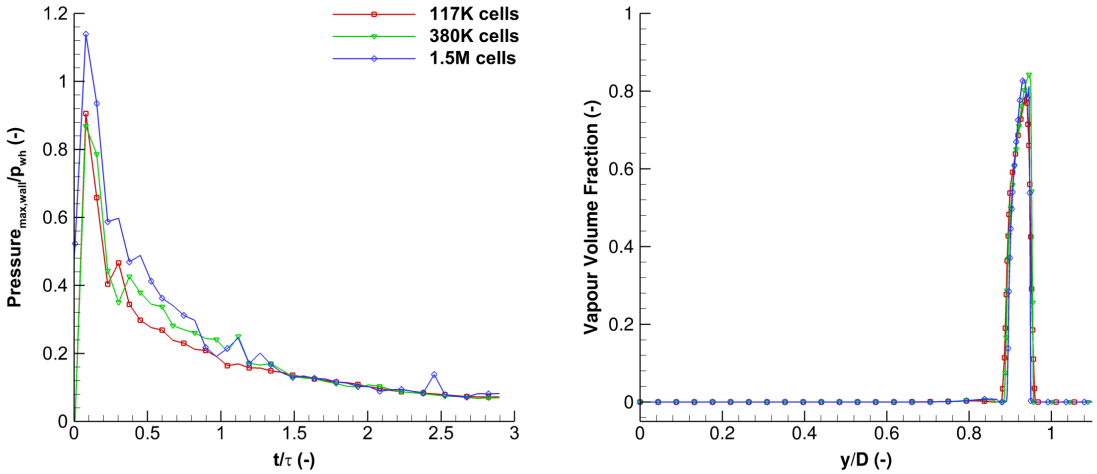

Figure 3.34: Grid independence study for three different grids (coarse, intermediate, fine). Maximum wall pressure with respect to time is shown on the left. The values of the vapour volume fraction on the right figure are exported at a line parallel to the y axis starting from $x = 0.6\,mm, z = 0$ at time $T = 0.083$. Wall pressure is divided by p_{wh}, time is measured from the moment of the impact and it is non-dimensionalized with $\tau = D/c_l$, whereas distance y has been divided by the drop diameter D.

are similar to the planar one (*case 1*) for the same impact velocity ($110\,m/s$). At time $t = 0.44$ the droplet has already impacted the wall and the shock wave is visible in the Sclieren figure. The jetting has started, however it is more evident at time $t = 0.89$ and it is responsible for the non-spherical shape of the droplet. As the shock moves to the upper half of the droplet, it is reflected on the droplet surface and expansion waves, which are moving downwards, are noticed in the Schlieren figures, starting from time $t = 0.89$. Those rarefaction waves create low pressure areas and thus, cavitation is noticed at times $t = 1.19$ and $t = 1.48$ (see also Fig. 3.36). The maximum wall pressure is realised at the moment of the impact and it decreases afterwards (see Fig. 3.41).

The planar and the axisymmetric solutions exhibit many similarities; nevertheless, there is a discrepancy in the pressure field between *case 1* and *case 2*. The maximum pressure is higher in *case 1*, as it can be seen in Fig. 3.37 and has been also noticed in previous studies [161].

At a later stage of the droplet impact (Fig. 3.38), the splashing is more evident than at time $t = 1.48$. In Fig. 3.38 the pressure field (left slice) and the velocity magnitude (right slice) are shown in conjunction with the iso-surface of 0.5 gas mass fraction on the left figures, whereas on the right figures the wall

pressure (lower slice) and the vapour volume fraction (upper slice) combined with the iso-surface of 0.5 gas mass fraction are demonstrated for *case 2*. Several vaporous regions have been created from the rarefaction waves and they start collapsing consecutively. At times $t = 3.19$ and $t = 3.56$ the third and second vaporous regions have just collapsed respectively. A peak in the pressure due to the shock wave created by the collapse is noticed at times $t = 3.56$ and $t = 3.64$, however the location (far away from the wall) and the strength (maximum pressure is $0.09 p_{wh}$) cannot denote erosion. At $t = 3.79$ the beginning of the Richtmyer-Meshkov instability [242] is noticed on the upper side of the droplet, however this issue is not further investigated here, where the main focus is the violent impact dynamics at the early time of the impact, rather than the splashing at later times.

The effect of the impact velocity

In Fig. 3.39, the above results are compared to lower impact velocities, $55\,m/s$ and $27.5\,m/s$ at the same dimensionless time $t = 1.48$. The same configuration as in the left image of Fig. 3.35 is followed here as well. The droplet spreading at lower impact speeds is less dominant and the droplet is closer to the spherical shape, as it can be seen from the droplet iso-surface plots. On the other hand, in *case 2* the transition to splashing is evident, as the jetting area is split to two different regions. Furthermore, the high pressure area and the lamella are larger in *case 2* but the ratio $|\mathbf{u}_{max}|/u_{imp}$ in all cases (*case 2-4*) is between 7.2 and 11, whereas the ratio p_{max}/p_{wh} is around 0.13. Although the above indicate similar non-dimensional maximum pressures and jetting velocities regardless the impact velocity, it is worth pointing out that the maximum pressure and velocity fields are significantly lower in *case 3* and *4*. For example, the jetting velocity is reduced by even one order of magnitude ($\sim$1400 m/s in *case 2* and $\sim$190 m/s in *case 4*).

In order to compare the vapour generated for each impact velocities at the same non dimensional time $t = 1.48$, slices with the vapour volume contour (upper) combined with the same iso-surface are shown in Fig. 3.40 for *case 2, 3* and *4*. For the highest impact velocity (*case 2*) the vapour volume is increased even one order of magnitude compared to the values of lower velocities. It can be concluded that the amount of the vapour and the extent of the cavitation area, which is generated at later stages, monotonically depends on the impact

velocity (this is also evident in Fig. 3.41 where 6 different impact velocities are examined). The wall pressure (bottom) is also depicted in Fig. 3.40; although the maximum is approximately the same for all cases, it extends to a larger area for higher impact velocities.

In Fig. 3.41 a parametric study for six different impact velocities (*case 2-7*) is performed for the intermediate grid resolution, where the maximum wall pressure (left) and the generated volume of vapour (right) with respect to time are plotted. As it has been already discussed in the previous paragraph and in previous studies [182, 168], it is straightforward that higher impact velocities result in higher wall pressures (although the ratio $\frac{p_{max,wall}}{p_{wh}}$ is almost constant regardless of the impact velocity). More production of vapour due to the reflection of a stronger shock developing during the liquid-solid contact is calculated. The cavitation inside the droplet may also contribute to pressure increase on the solid surface at the bubble collapse stage. This is shown on the wall pressure figure, where at higher impact velocities there are small peaks occurring at later times (*case 7*).

The effect of gas in cavitation generation

It is remarkable that the initial configuration can affect the existence or not of cavitation and material erosion close to the wall, even for low impact velocities. As initial condition in *case 8* is now selected the droplet to be attached to the wall (in contrast to *case 1-7*), so there is no air between them. To demonstrate that the impact velocity is not the determining factor here, $u_{imp} = 27.5\, m/s$ was selected. Surprisingly enough, in Fig. 3.42 vapour is created at the impact point and a vaporous region is formed above it due to a rarefaction wave at an early stage of the impact. The maximum vapour volume fraction created is even three times higher than *case 2* at time $t = 1.48$, where the impact velocity is four times larger. Consequently, there is a significant increase in the pressure field due to the collapse, as it can be observed in Fig. 3.43, which results in around 60% higher wall pressure, compared to *case 3*. In practice, the above case can be realised at steam turbine blades, where the rarefied environment implies very low steam density, consequently there is little droplet/vapour interaction.

3.7.3 Conclusions

The comparison against the 2-D planar impact experiment is satisfactory, as similar flow patterns have been identified. Impacts of spherical droplets on a solid surface have been also simulated and the formed cavitation areas have been identified. Due to pressure decrease and vaporisation in the droplets which impact the solid surface, vapour phase has been modelled.

The droplet impact time scale is $t_{impact} = D/u_{imp}$ and in the present configuration for impact velocity $u_{imp} = 110\,m/s$ is calculated to be $t_{impact} \approx 9 \cdot 10^{-5}\,s$, whereas the cavitation collapse time is approximated from the characteristic Rayleigh time $t_{cav} = 0.915 R_{0,vap}\sqrt{\frac{\rho_l}{p_\infty - p_{sat}}}$ and it is calculated to be $t_{cav} \approx 2.2 \cdot 10^{-5}\,s$. The significantly larger time scale of the droplet impact phenomenon in comparison to the characteristic time of the cavitation collapse justifies why the collapse of the vaporous regions inside the droplet don't affect the shape of the droplet and its splashing.

The impact velocity strongly affects the droplet shape and spreading, as well as the jetting velocity and the volume of vapour produced in the upper area of the droplet. Increased impact velocity may result in more damage and possibly material erosion not only because of higher impact pressure, but also due to the collapse of the vaporous bubbles inside the droplet. However, in order to notice significant pressure increase due to the bubble collapse, the impact velocity must be extremely high which is rather difficult to be realised in practical applications such as steam turbines. Apart from that, the initial location of the droplet with respect to the solid surface, which actually means the absence or not of gas around the droplet, can influence the volume of vapour generated at the initial stages of the impact. If there is no gas between the droplet and the solid surface, pressure can get close to its maximum value, which is at the moment of the impact (p_{wh}) and material erosion may take place. It should be clarified here that the above phenomenon can even occur at low impact velocities, $u_{imp} = 27.5\,m/s$.

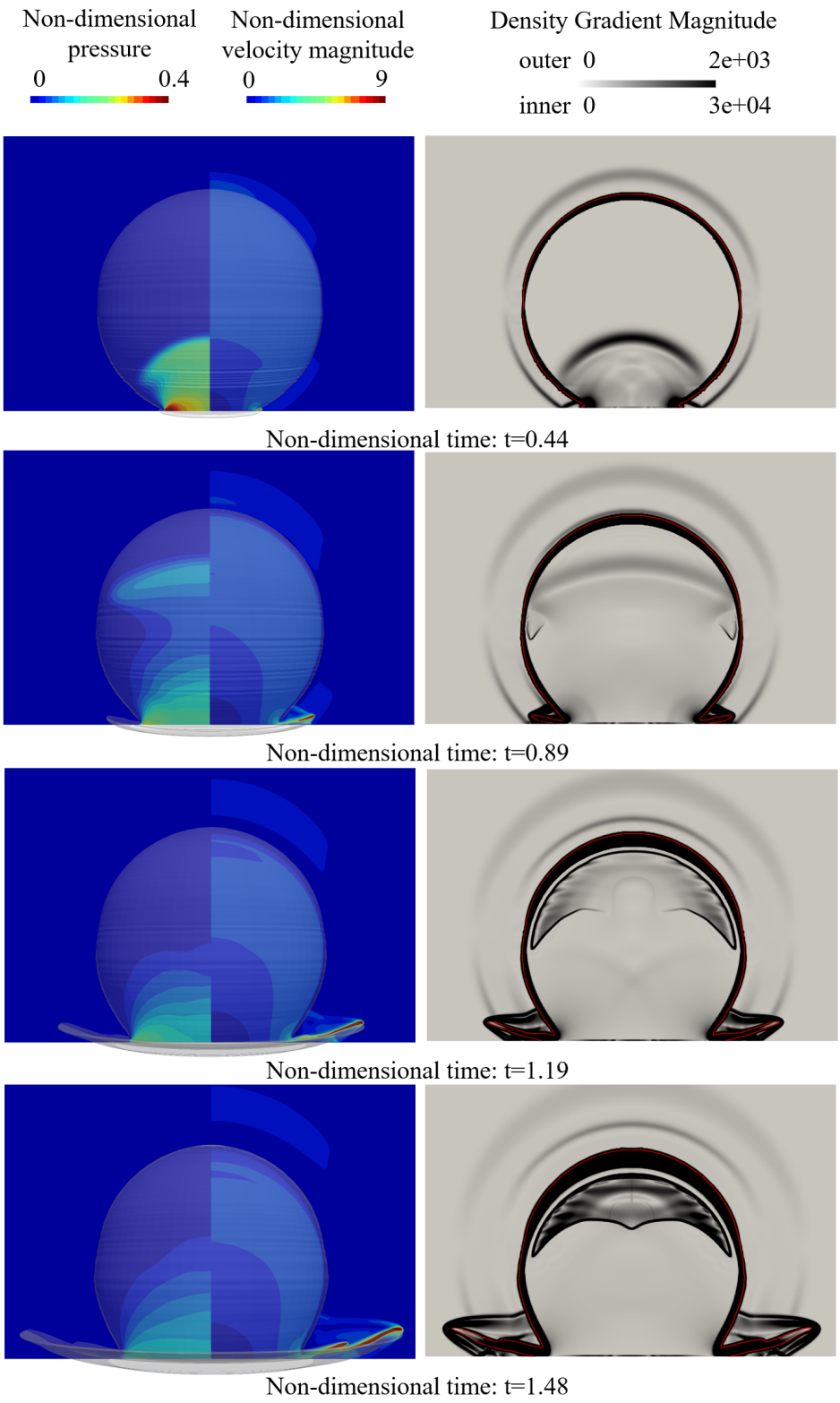

Figure 3.35: Drop impact at velocity $110\,m/s$. Left figure: Iso-surface of liquid mass fraction for $Y_g = 0.5$ combined with pressure (left slice) and velocity magnitude (right slice). Right figure: Density gradient magnitude, different scale for the interior and the exterior of the droplet. Pressure and velocity are divided by p_{wh} and u_{imp} respectively, whereas time is measured from the moment of the impact and it has been non-dimensionalized with D/c_l.

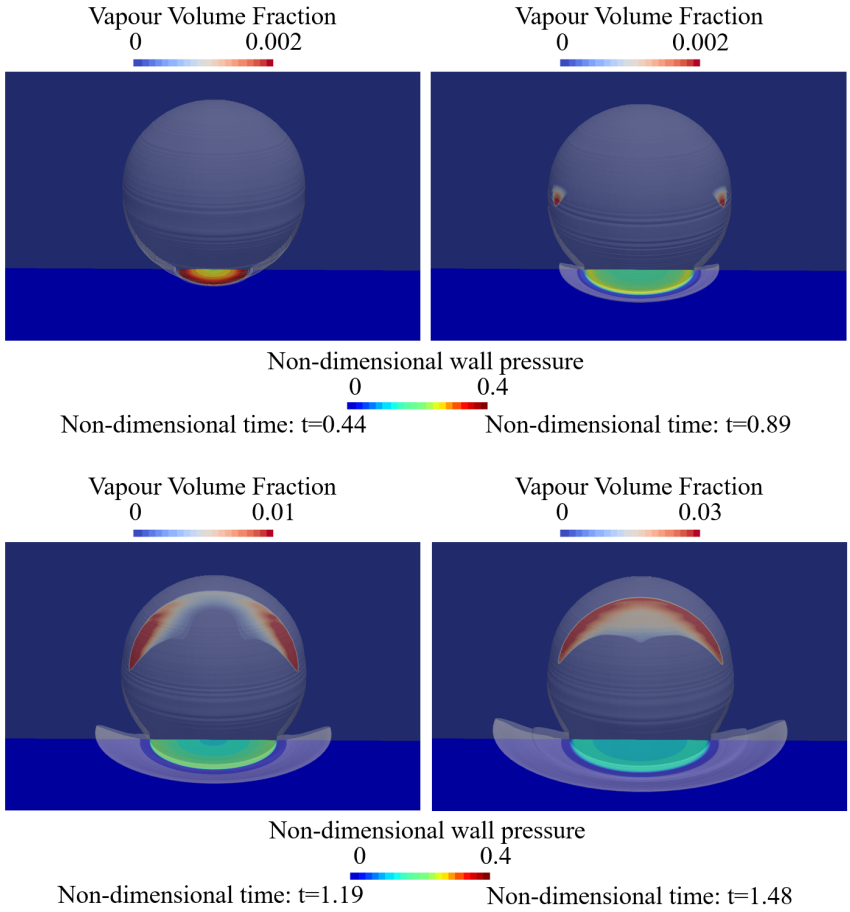

Figure 3.36: Drop impact at velocity $110\,m/s$. Iso-surface of liquid mass fraction for $Y_g = 0.5$ combined with wall pressure (bottom slice) and vapour volume fraction (upper slice). Pressure is divided by p_{wh} and time is measured from the moment of the impact and it has been non-dimensionalized with D/c_l.

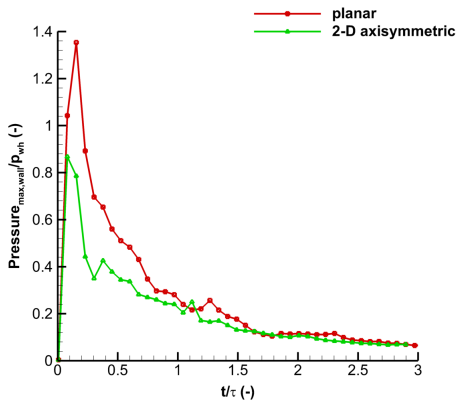

Figure 3.37: Comparison of the maximum wall pressure between a planar 2-D and a 2-D axisymmetric simulation at impact velocity $110\,m/s$. Wall pressure is non-dimensionalized with p_{wh} and time is measured from the moment of the impact and it has been non-dimensionalized with $\tau = D/c_l$.

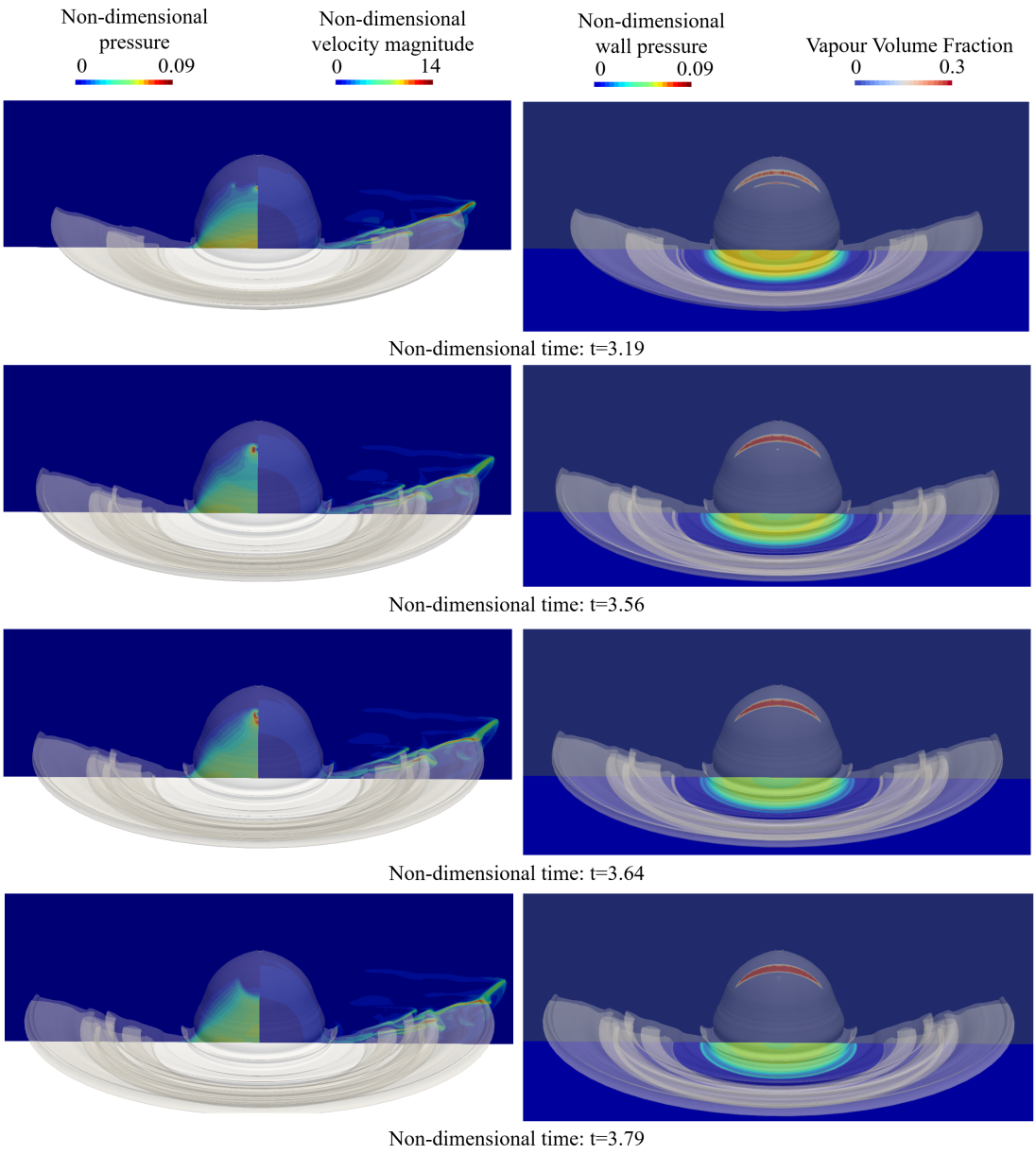

Figure 3.38: Later stage of droplet impact at velocity $110\,m/s$. Left figure: Iso-surface of liquid mass fraction for $Y_g = 0.5$ combined with pressure (left slice) and velocity magnitude (right slice). Right figure: Iso-surface of liquid mass fraction for $Y_g = 0.5$ combined with wall pressure (bottom slice) and vapour volume fraction (upper slice). Pressure and velocity are divided by p_{wh} and u_{imp} respectively, whereas time is measured from the moment of the impact and it has been non-dimensionalized with D/c_l.

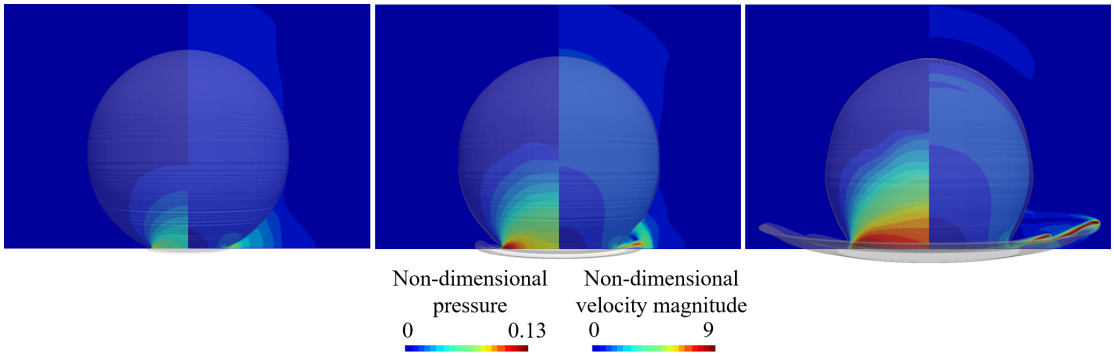

Figure 3.39: Comparison of the pressure (left slice) and the velocity magnitude (right slice) for $u_{imp} = 22.5\,m/s$ (left), $u_{imp} = 55\,m/s$ (middle) and $u_{imp} = 110\,m/s$ (right) at non dimensional time $t = 1.48$. The iso-surface of liquid mass fraction for $Y_g = 0.5$ is also shown. Pressure and velocity are divided by p_{wh} and u_{imp} respectively, whereas time is measured from the moment of the impact and it has been non-dimensionalized with D/c_l.

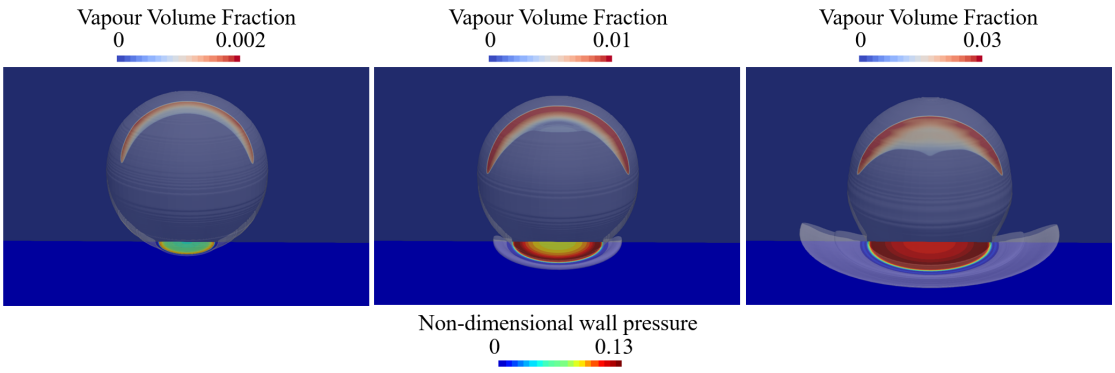

Figure 3.40: Comparison of the vapour volume fraction (upper) and wall pressure (bottom) for $u_{imp} = 22.5\,m/s$ (left), $u_{imp} = 55\,m/s$ (middle) and $u_{imp} = 110\,m/s$ (right) at non dimensional time $t = 1.48$. The iso-surface of liquid mass fraction for $Y_g = 0.5$ is also shown. Pressure is divided by p_{wh} and time is measured from the moment of the impact and it has been non-dimensionalized with D/c_l.

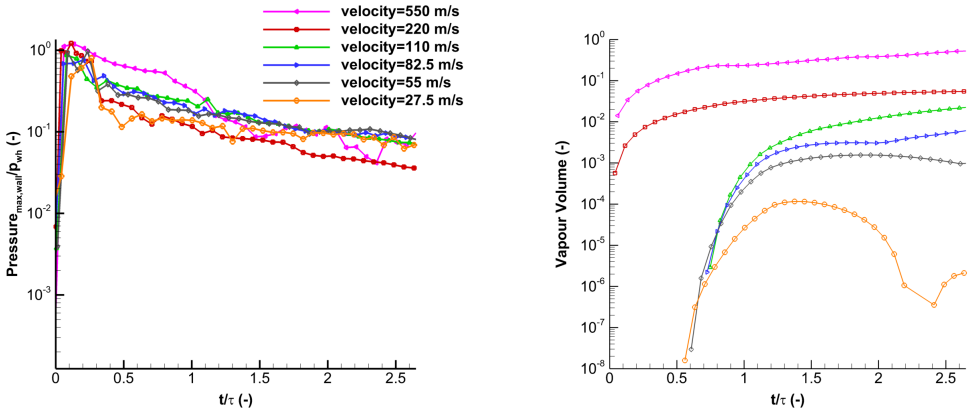

Figure 3.41: Maximum wall pressure (left) and generated vapour volume (right) with respect to time for different impact velocities. Wall pressure is divided by p_{wh}, time is measured from the moment of the impact and it has been non-dimensionalized with $\tau = D/c_l$, whereas vapour volume is divided by the initial droplet volume.

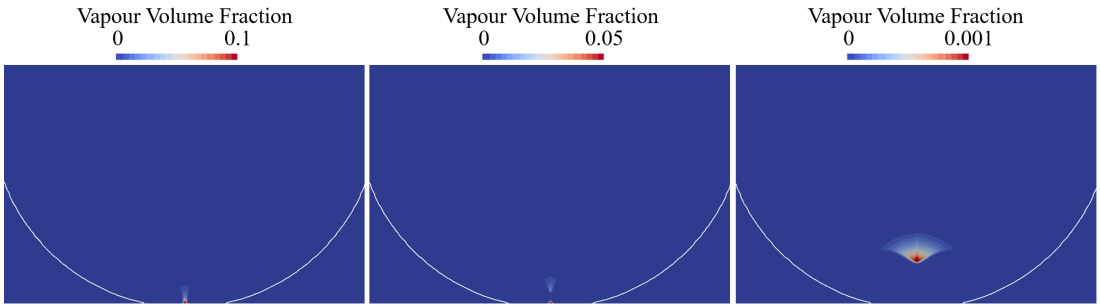

Figure 3.42: Close-up view of *case 8* at non-dimensional times $t = 0.15$ (left), $t = 0.18$ (medium) and $t = 0.25$ (right). Slices of vapour volume fraction combined with iso-line of liquid mass fraction for $Y_g = 0.5$ are shown. Time has been non-dimensionalized with D/c_l.

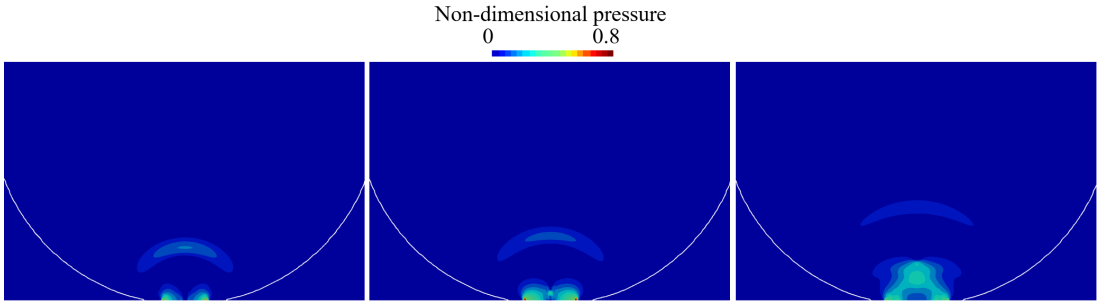

Figure 3.43: Close-up view of *case 8* at non-dimensional times $t = 0.15$ (left), $t = 0.18$ (medium) and $t = 0.25$ (right). Slices of pressure combined with iso-line of liquid mass fraction for $Y_g = 0.5$ are shown. Time has been non-dimensionalized with D/c_l and pressure with p_{wh}.

Chapter 4

Results: Industrial Applications

In this chapter, flows of industrial interest have been studied, such as the flow inside a diesel injector, jet formation in a needle-free device and the cryogenic flow in a converging-diverging nozzle. Diesel injector simulations with a modified barotropic solver in OF have been preformed. Concerning the needle-free device simulation, the cavitation formation inside the nozzle has been modelled for first time, as well as how the jet magnitude and the jet diameter are affected by the meniscus shape of the interface between the liquid and the vapour. In addition, by employing the methodology presented in 2.2.3 for the cryogenic nozzle simulations, a unified treatment for subcritical and supercritical regimes can be modelled, see for example sections 4.3.1 and 4.3.2 respectively.

4.1 Diesel injector simulation (liquid-vapour mixture)

The first case examined in this chapter is the tip of a Diesel injector with 5 holes (see Fig. 4.1 where the main parts of the injector are named). Needle movement is not examined here, the simulations are at a static needle lift of $105\,\mu m$. Given the Re number inside the orifice which is $\sim 30,000$, RANS simulations have been considered by utilizing the k-ϵ model with the Reboud correction. In order to reduce the computational cost and taking advantage of the problem symmetry, one hole of the injector is simulated only, which means 72° of the injector, instead of the 360° (see Fig. 4.1). The resulting grid size is approximately $200k$ cells. Symmetry boundary conditions have been employed on the sides, pressure is specified in the inlet to be $p_{in} = 1800\,bar$, which results

in a cavitation number $C_N = 0.028$. The outlet pressure is set to be $p_{out} = 50\,bar$, whereas no-slip wall boundary conditions have been set on the needle, orifice and the body of the injector. A hemispherical volume is added in the outlet, to avoid influencing the flow in the orifice by the pressure outlet boundary condition. As a consequence of simulating $1/5^{th}$ of the injector nozzle geometry, eccentricity effects which are more dominant during the needle movement, have been omitted and 3-D turbulence phenomena may have been suppressed. Finally, temperature effects have not been considered, since such EoS are less efficient compared to the barotropic approach and may also exceed the applicability range of higher order EoS, for instance of the Helmholtz EoS. The parameters of the barotropic EoS and the kinematic viscosity values for the liquid and the vapour are summarized in Table 4.1.

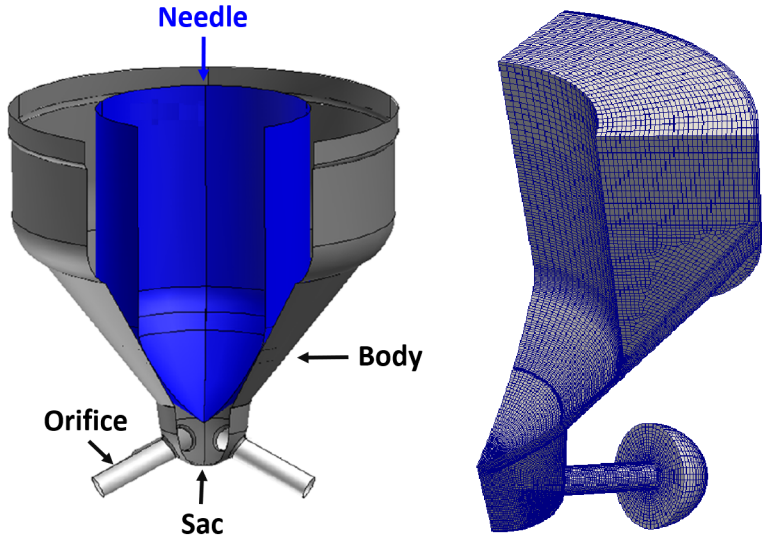

Figure 4.1: 5 hole Diesel injector (left) and computational grid of a 72° domain (right).

In Fig. 4.2 the contour fields of pressure (left), vapour volume fraction (middle) and velocity magnitude (right) are depicted. The flow field inside the nozzle is the expected: the flow accelerates in the narrow passage between the body and the needle, passes through the sac and further accelerates in the orifice, resulting in pressure decrease and cavitation formation on the upper side of the orifice. A steady-state solution is obtained, in other words the cavity on the upper side of the orifice is stationary. Although this steady-state solution contradicts the experimental observations of [243] where cavity shedding and cavitating vortices were noticed, the same cavity pattern has been also predicted in [241]. In the

Table 4.1: Liquid and vapour phase properties utilized in the 5 hole Diesel injector simulation.

Property	ph4 injector
$\rho_{sat,l}\,(kg/m^3)$	747.65
$\rho_{sat,v}\,(kg/m^3)$	6.5
$p_{sat}\,(Pa)$	$1.1 \cdot 10^5$
$B\,(MPa)$	110
$\nu_l\,(10^{-6}m^2/s)$	2.8088
$\nu_v\,(10^{-6}m^2/s)$	1.1538
$n\,(-)$	7.15
$C\,(Pa \cdot kg/m^3)$	1250

latter the incapability of RANS in predicting cavitation inception is reported, as turbulence models fail to accurately resolve the vortex structures in low pressure regions. The purpose of RANS models is to predict the mean flow path by adding turbulent viscosity and therefore, the generation of vortical structures and their connection with cavitation formation is not properly modelled [241]. On the other hand, LES studies accurately predict both the mean velocity profiles and the large eddies responsible for cavitation formation [3, 241].

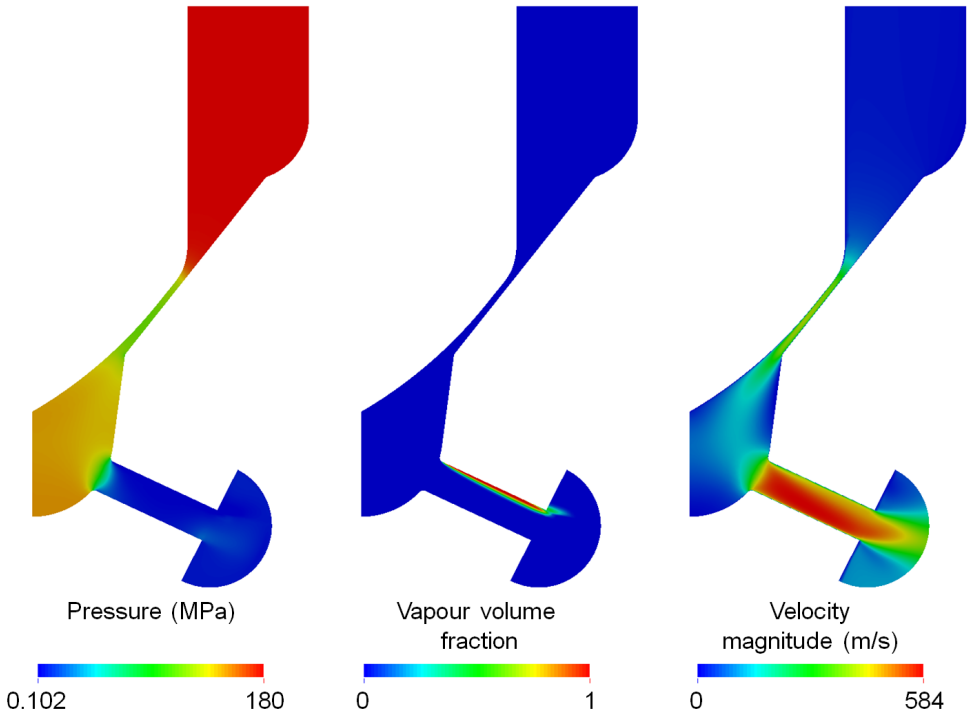

Figure 4.2: Pressure (left), vapour volume fraction (middle) and velocity magnitude (right) contours are shown on $y = 0$ slice for the Diesel injector simulation with k-ϵ turbulence model (Reboud correction).

4.2 Needle-free injection (liquid-vapour-gas mixture, linear EoS)

In this section, numerical simulations of the needle-free device are presented for several different initial conditions, regarding the pressure of the gas bubble and the geometry of the interface between the water and the air [244]. First, results for the conventional meniscus design and comparison with experimental values are shown. Then a parametric study for different values of the bubble pressure is performed as another mean of validating the methodology. In the end, different meniscus geometries have been simulated in order to find a design appropriate for needle-free devices, ensuring focused high speed and focused jets. The different cases examined are summarised in Table 4.2.

Table 4.2: Numbering, meniscus geometry, pressure of the gas bubble, Reynolds and Weber numbers of the needle-free injection cases that have been simulated. The Reynolds and Weber numbers are calculated based on the jet diameter. Trumpet shape is referred to a meniscus geometry, with conical shape close to the axis and hemispherical shape towards the wall (see also Fig. 4.10).

Name	Meniscus geometry	p_{bub} (Pa)	Re	We
case 1	hemispherical	$2 \cdot 10^7$	388	84.3
case 2	hemispherical	$3.7 \cdot 10^7$	459	118
case 3	hemispherical	$5 \cdot 10^7$	704	278
case 4	hemispherical	$7 \cdot 10^7$	839	394
case 5	hemispherical	$1 \cdot 10^8$	1105	683
case 6	hemispherical	$1.35 \cdot 10^8$	1245	866
case 7	hemispherical	$1.5 \cdot 10^8$	1411	1110
case 8	conical	$5 \cdot 10^7$	120	80
case 9	trumpet	$5 \cdot 10^7$	423	1000

The minimum Weber number in the present simulations is calculated to be around $We = 80$ and thus, surface tension has been neglected. However, in order to further justify this argument, the effect of surface tension has been investigated in *case 1* by utilizing Ansys Fluent CFD software. As it can be seen from Fig. 4.3, where the jet velocity is plotted with respect to the distance between the bubble and the jet, the role of surface tension is negligible. The maximum Reynolds number is around $Re = 1411$ and consequently, the flow has been considered to be laminar. Both non-dimensional numbers are based on the jet diameter. It is also worth to mention that the vapour bubble which is created by the focused laser [183, 200], is modelled as a hemisphere of non-condensable gas. It

is impossible to simulate the whole process, as the laser pulse induces transition to plasma state (see [245, 183]), while several chemical reactions take place until finally the vapour bubble is created. Due to lack of available thermodynamic models in order to describe such phenomena, a barotropic approach has been utilized [88]. Additionally, in order to model the heating due to the pulse, the pulse pattern should be known (e.g. the energy deposition over time), since it is not a step function but there is a gradual increase from zero to maximum intensity. Such heating effects have been neglected in the present study. The main focus here is the study of the formation of the primary jet, which is created due to the bursting gas, and to identify the appropriate conditions under which the jet is able to penetrate the skin surface. The vapour bubble collapse and the secondary jet which is created, is out of scope here. Finally, the soft tissue is not modelled here; estimation of the jet penetration into the skin is given based on the water hammer pressure in 4.2.4. Some preliminary simulations modelling the tissue by an additional transport equation are shown in Appendix D, but without modelling the elastic behaviour of the human skin.

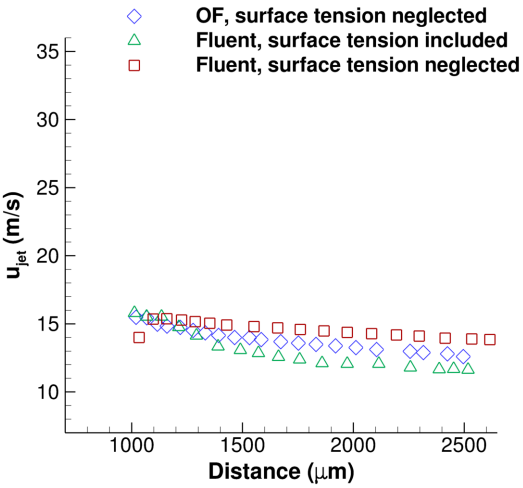

Figure 4.3: Investigation of the surface tension effect on the needle-free injection simulation: plot of the jet velocity with respect to the distance between the bubble and the air-liquid interface($B_g = 0.5$) including (triangles) and neglecting (diamonds) surface tension.

4.2.1 Numerical simulation

The geometry of the device is taken from [183] and can be seen in Fig. 4.4, 4.10. Since the problem is axisymmetric, a structured-mesh wedge of 5° angle is

employed with approximately $90k$ equally spaced cells with $\Delta x = 2.5 \cdot 10^{-6}\, m$ (Fig. 4.4). The upper and the left sides of the wedge have been set as no-slip wall, whereas in the right side, the pressure is specified (atmospheric). Initially, compressed gas (different initial pressure p_{bub} depending on the case examined) is in the hemispherical bubble (gas mass fraction $Y = 1$), which is in the centre of the left wall, while the water ($Y = 0$) and the air ($Y = 1$) are in atmospheric conditions p_{atm}, as it is shown in Fig. 4.4. The liquid phase is left to the meniscus and the gas phase is on the right side of the meniscus. The initial density in each phase is determined from the barotropic EoS.

For the grid independence study, three different meshes have been employed, $22k$ cells (coarse grid), $90k$ cells (intermediate grid) and $356k$ cells (fine grid). In Fig. 4.5 the velocity magnitude (left) and the gas mass fraction (right) values along the x-axis are plotted ($y = 175\,\mu m$) at $t = 10\,\mu s$. While in general the three grids are in good agreement, there are small deviations in the velocity plot. The deviation close to the origin of x axis is due to the more accurate representation of the bubble in higher resolution grids. Concerning the velocity of the jet ($x > 1\,mm$) and how its magnitude depends on the grid resolution, more diffusive solution is obtained with a coarse grid and therefore smaller velocity fluctuations are noticed in velocity plot of Fig. 4.5. The intermediate grid has been selected, since it is in satisfactory agreement with the dense one.

In Fig. 4.6 the pressure ($x - y$ plane) and velocity magnitude ($x - z$ plane) contours are shown, combined with iso-surfaces for the vapour (white) and the air (pink) phases. At time instant $1.5\,\mu s$ the pressure wave has already been reflected at the meniscus resulting in the initialisation of an axisymmetric microjet. Apart from the aforementioned mechanism, the focusing in the nozzle is also responsible for the acceleration of the flow [204, 215] (see also Fig. 4.9). In the next frame ($t = 13.5\,\mu s$), the jet has been formed and a small cavitation regime is barely visible. At time instant $20\,\mu s$ the cavitation area has expanded and the the jet has moved forward.

Comparison with experimental results of Hayasaka et al. [183] is shown in Fig. 4.7. The correspondence between the laser energy in the experiment and the pressure of the hemispherical bubble which has been used as initial condition in the simulation, is achieved by equalising the laser energy with the dynamic energy of the bubble. The dynamic energy of the bubble is calculated from $E_{dyn} = \Delta p V$, where $\Delta p = p_{bub} - p_{liq}$ with p_{bub} and p_{liq} being the pressure of

the bubble and the liquid respectively and V is the volume of the hemisphere. Because of the barotropic EoS, the heat absorbed from the bubble is not taken into account and thus, a calibrating coefficient n is used in order for the dynamic energy of the bubble to match the absorbed laser energy: $E = n\Delta pV$ (in the present study $n = 151$). Overall, the experimental and the numerical values are in satisfactory agreement, as the same pattern is noticed: initially high jet velocities were measured and then an asymptotic decrease of the jet velocity follows. However, in the last points which correspond to the largest available distances, the decrease rate of the jet velocity with respect to distance is slightly smaller in the simulations, compared to the experimental data. This discrepancy in the results is due to the visual approximation of the initial meniscus shape in the simulations, which is roughly replicated from the experiment based on a figure. The jet evolution is strongly affected by the meniscus shape, as it will be shown in section 4.2.3 and hence, even small differences between the approximated shape and the one created in the experiments can cause deviation in the jet velocity. Another reason is the inconsistency between the 0° and 90° experimental data [183], which is more evident for the higher energy experiments. The 0° data have a more abrupt decrease of the jet velocity and significantly larger error bars. The simulation points are either in the range of the 0° experimental points or in the 90° points, while for larger distances the simulation points are slightly above the 90° points.

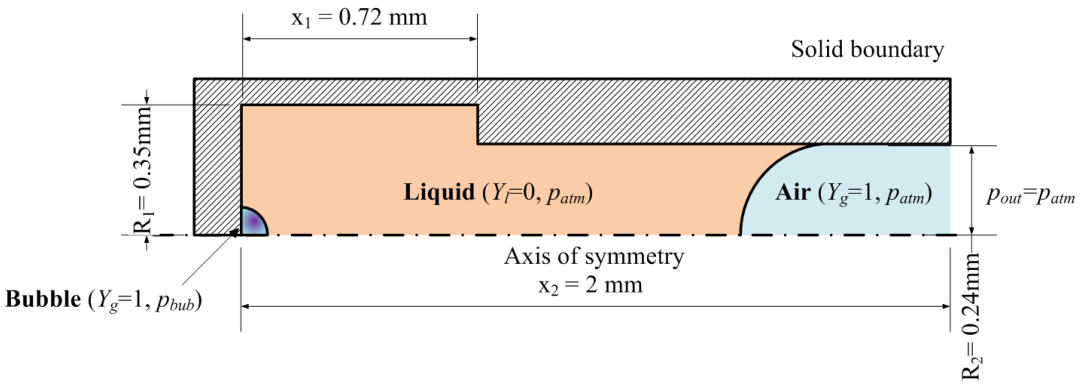

Figure 4.4: Needleless injection configuration for the hemispherical meniscus geometry: the computational domain (liquid, air, bubble), liquid-gas interface (black line), solid boundary (dashed area) and axis of symmetry (dash dot line).

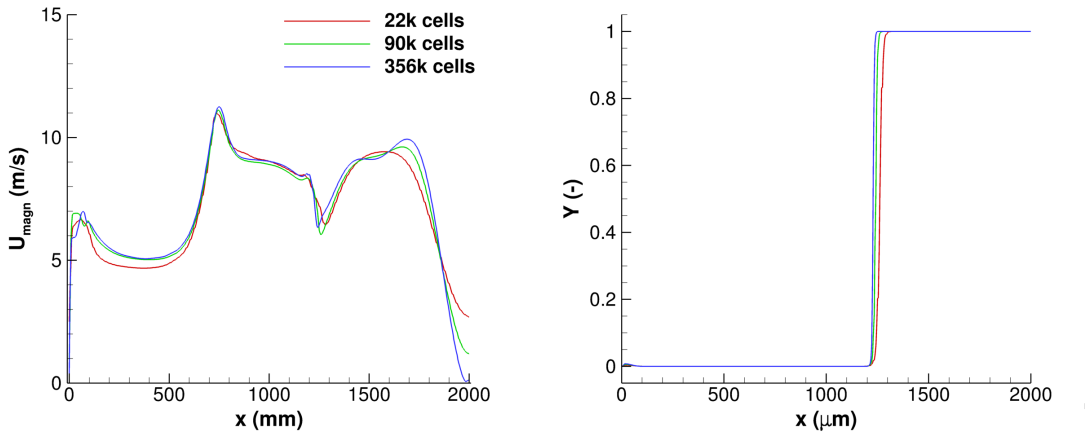

Figure 4.5: Grid independence study for the needle-free device. Plots of velocity magnitude (left) and gas mass fraction(right) along a line parallel to the x-axis ($y = 175\,\mu m$) at $t = 10\,\mu s$.

4.2.2 Dependence on the bubble pressure

Several simulations have been performed for different values of the bubble pressure (*case 1*-*case 7*). In Fig. 4.8 the linear relation between the bubble pressure or the absorbed laser energy and the jet velocity is shown. The laser energy is calculated from the dynamic pressure of the bubble, as explained in 4.2.1. Similar findings have been reported in the experimental work of Tagawa et al. [200] and in the numerical work of Peters et al. [215]. In the latter, they modelled the pressure wave by a pressure pulse on the bubble and they demonstrated the linear correlation between the pressure pulse and the jet velocity. The fact that the linear function is not intercepted at $u_{jet} = 0$, means that a jet is formed even for lower values of absorbed laser energy and there is no threshold heat, in contrary to the previous studies of Tagawa et al. [200] and of Peters et al. [215]. This is due to the energy that has been spent in the experiment in order to heat the fluid before vaporisation [193]. In the simulations of Peters et al. [215], surface tension is responsible for the threshold, whereas in the present work surface tension is not modelled and therefore there is not such a threshold.

In Fig. 4.9 the magnitude of the pressure gradient is shown for *case 3* and *case 7* combined with vapour volume fraction iso-lines of $\alpha = 0.5$ (red). For the first four time instances plotted, the pattern is similar for both cases since the wave emanating from the bubble travels at almost the same wave speed $(u + c)$. In the first time instance plotted ($t = 0.2\,\mu s$), the shock wave, which has been emitted by the bubble, travels in the liquid. At $t = 0.4\,\mu s$ it has already

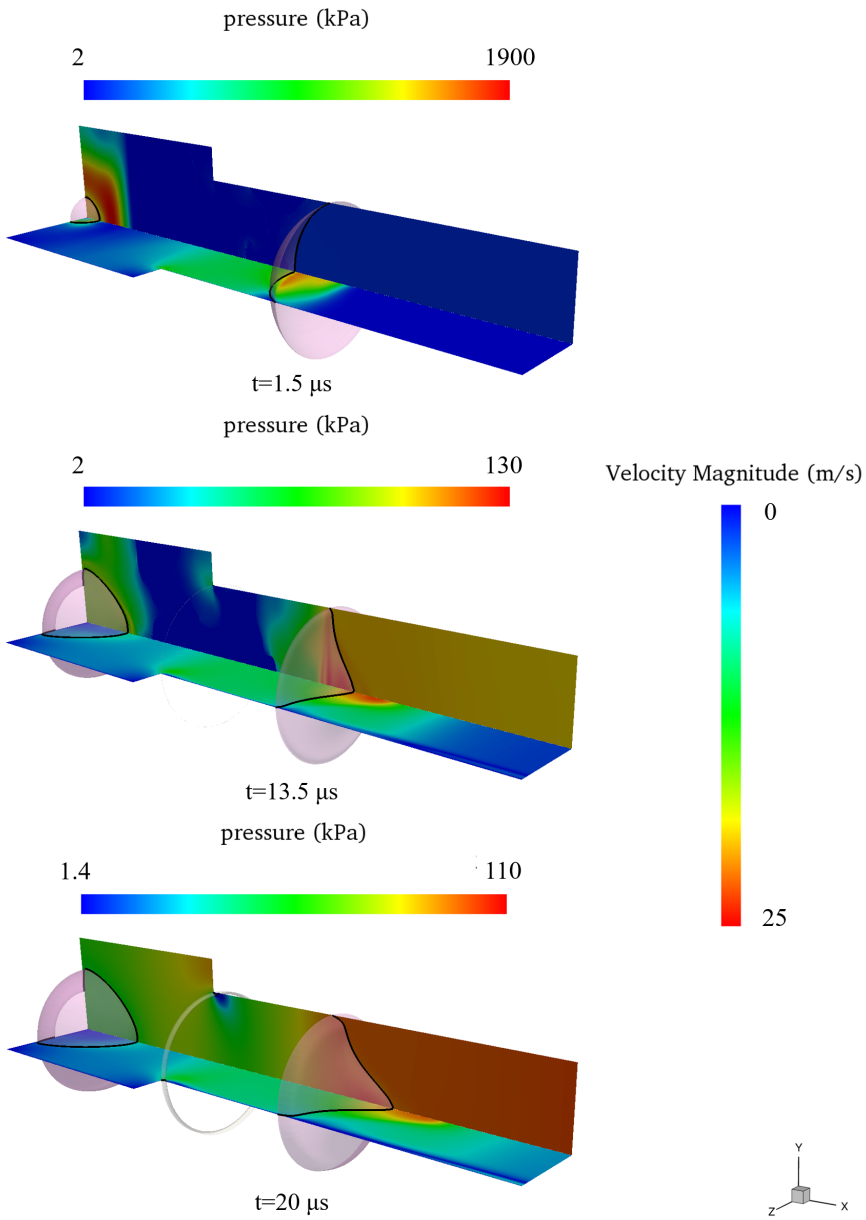

Figure 4.6: 2-D axisymmetric needle-free device simulation for $p_{bub} = 5 \cdot 10^7\, Pa$ and the standard meniscus shape (*case 3*). Pressure field on the $x-y$ plane and velocity magnitude field on the $x-z$ plane are shown, combined with iso-surfaces for vapour volume fraction $\alpha = 0.5$ (white) and iso-surface for gas volume fraction $B_g = 0.5$ (pink).

been reflected from the upper horizontal wall and the reflection of the wave has reached the bubble, while the original wave moves to the positive direction of the x axis. At $t = 0.6\,\mu s$ the superposition of three waves travels in the liquid. The original wave is advancing into the capillary, while its previous reflection has been reflected again from the upper vertical wall and it is moving towards the negative direction of the x axis. Apart from those two waves, another reflection at the bubble moves upwards. At $t = 0.8\,\mu s$ the original wave is reflected at

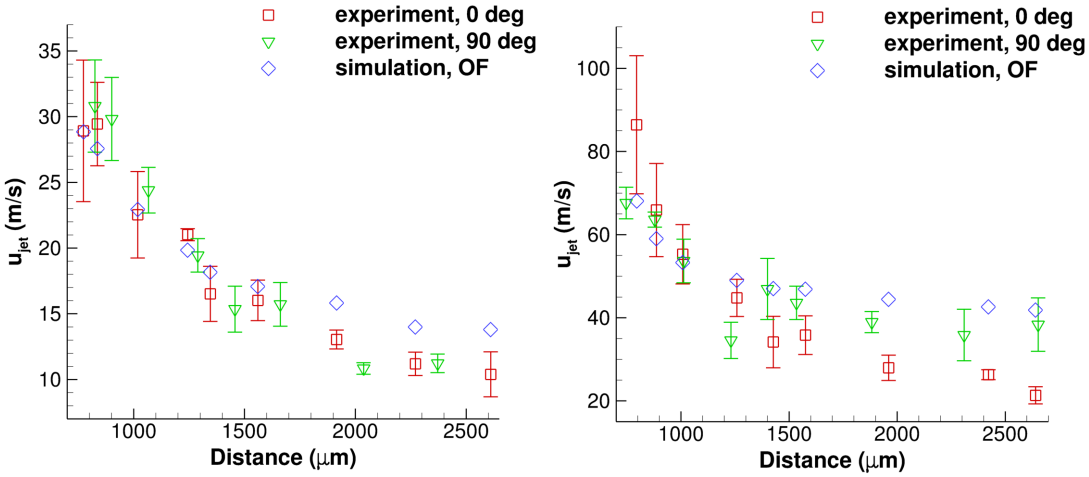

Figure 4.7: Comparison of *case 2* and *case 6* with experimental data of Hayasaka et al. [183]. Jet velocity as a function of the distance between the bubble and the air-liquid interface($B_g = 0.5$) for laser energy $185\,\mu J$ (left) and $650\,\mu J$ (right).

the meniscus and the formation of the jet starts. Due to higher bubble pressure in *case 7*, the jet has travelled a longer distance in the capillary compared to *case 3*, as it can be seen at $t = 9\,\mu s$. In addition, cavitation regions have been formed in the upper wall for both cases; however in *case 7* the vapour phase is much more extended and there is an additional vapour regime close to the axis of symmetry, because of the stronger shock wave. Although a similar low pressure exists in *case 3*, vapour in not generated, as the pressure is slightly above the saturation pressure. In the last time instant plotted ($t = 10.6\,\mu s$), a new shock wave is noticed in *case 7*, emanating from the collapse of the vaporous bubble, something which is not observed in *case 3*.

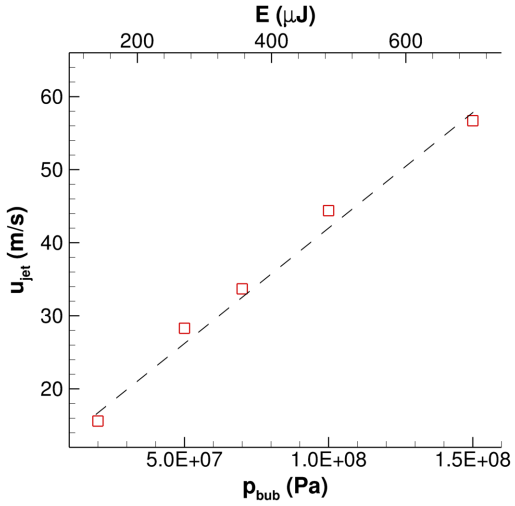

Figure 4.8: The influence of the initial bubble pressure on the jet velocity.

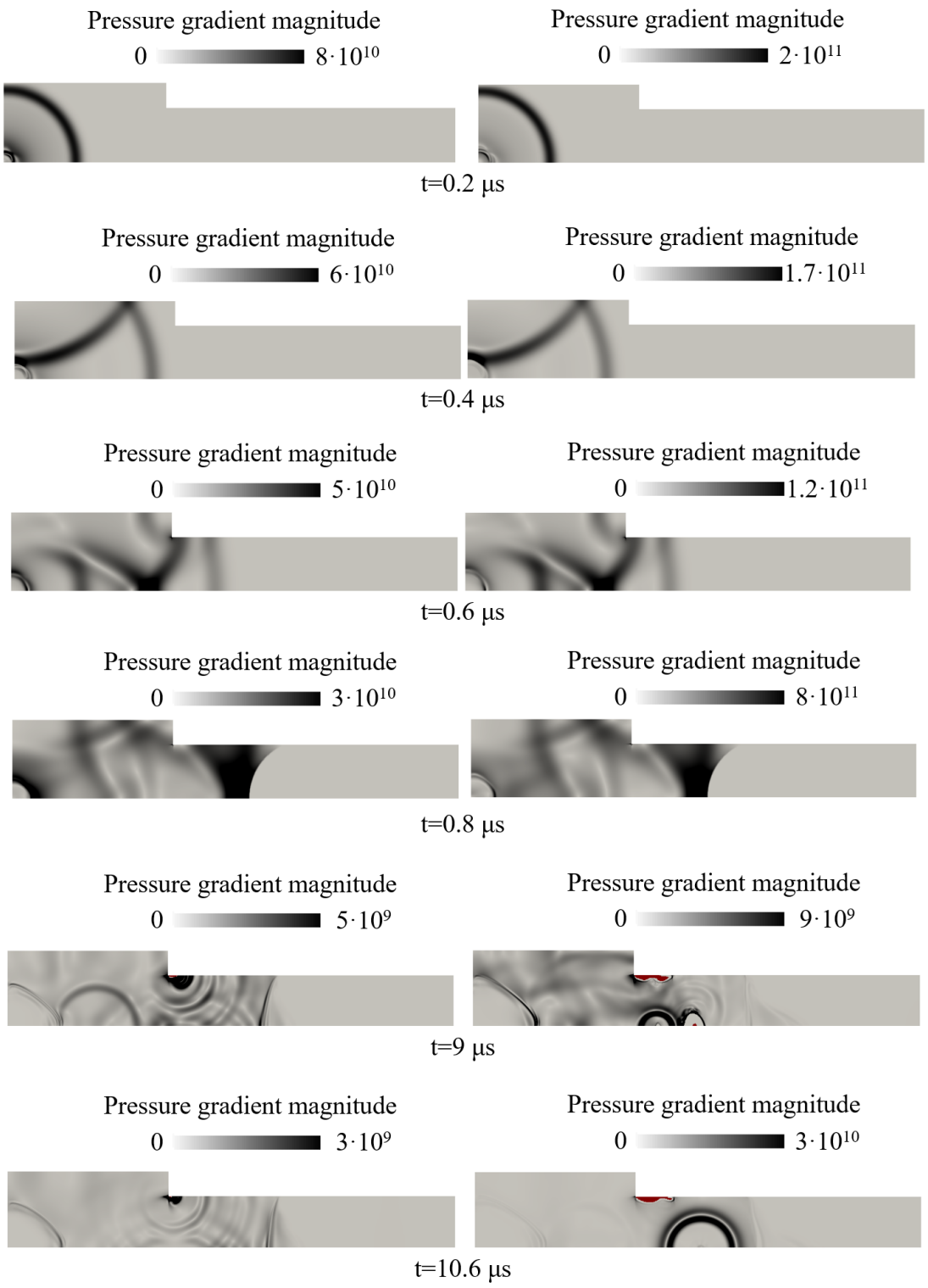

Figure 4.9: Slice on the $x-y$ plane for $z = 0$. Magnitude of the pressure gradient combined with vapour volume fraction iso-lines of $\alpha = 0.5$ (red) for *case 3* (left) and *case 7* (right).

4.2.3 Dependence on the free surface geometry

In this section the sensitivity of the jet velocity to the meniscus geometry is investigated. Based on shaped charge jets, three different geometries for the

free surface have been utilised as initial condition: the hemispherical free surface shape (*case 3*), the conical shape (*case 8*) and the trumpet shape (*case 9*), as they are shown in Fig. 4.10. The hemispherical shape has been also adopted in previous experimental works by dipping the tip of the tube in a hydrophobic solution [200]. In practice, the conical and trumpet shapes of the meniscus can be achieved by placing a gelatin cap on the free surface of the liquid. In Table 4.3 the maximum jet velocity and the jet diameter are summarised. It is evident that by utilising the trumpet shape for the meniscus geometry, jet velocity has the maximum value among the three cases, while at the same time the diameter of the jet remains small. The jet diameter of *case 3* is one order of magnitude smaller than the diameter of the capillary, while the jet diameters of *case 8* and *case 9* are one order of magnitude smaller than *case 3*.

The contact angle between the free surface geometry and the wall determines the focusing of the flow. In the worst case scenario, if the contact angle is 90°, a flat free surface is created, the liquid moves in the tube parallel to the walls and no jet is formed. On the other hand, a contact angle of 0° results in curvature equal to the radius of the capillary. As the contact angle becomes smaller, the focusing is increased, resulting in higher jet velocities [200, 202, 215]. In Fig. 4.11 the vectors on the liquid-gas interface of the capillary are shown, combined with red iso-line of gas volume fraction $B_g = 0.5$ for *case 3*, *case 8* and *case 9*. From the vector field at three frames the increased focusing in the conical and trumpet meniscus is evident, since more liquid volume is on the tip of the interface. On the other hand, in the hemispherical shape the vectors are almost parallel which means reduced focusing. It can be also concluded that the evolution of the jet is much faster in *case 8* and *case 9* and that the jet diameter in *case 3* is much larger compared to the other two cases ($t = 10\,\mu s$). In shaped charges, similar shape for the liner is used with similar effects on the hole diameter and the penetration depth. In general, conical liner results in deeper penetration and a small hole diameter, whereas hemispherical liner create a larger diameter and shallow penetration [246, 247, 248, 249].

In Fig. 4.12 and 4.13 the pressure ($x - y$ plane) and the velocity magnitude ($x - z$ plane) contours are shown combined with iso-surfaces for the vapour (white) and the air (pink) phases. Similar to Fig. 4.6, the first time frame is just after the reflection of the wave at the meniscus interface and the initialisation of the jet is shown. In the second and the third frames, the jet has been formed

and advances in the capillary, while cavitation areas have been identified. The jets with the conical and trumpet initialisation are more focused and have larger velocity magnitude than the hemispherical shape (see also Table 4.3 and Fig. 4.11).

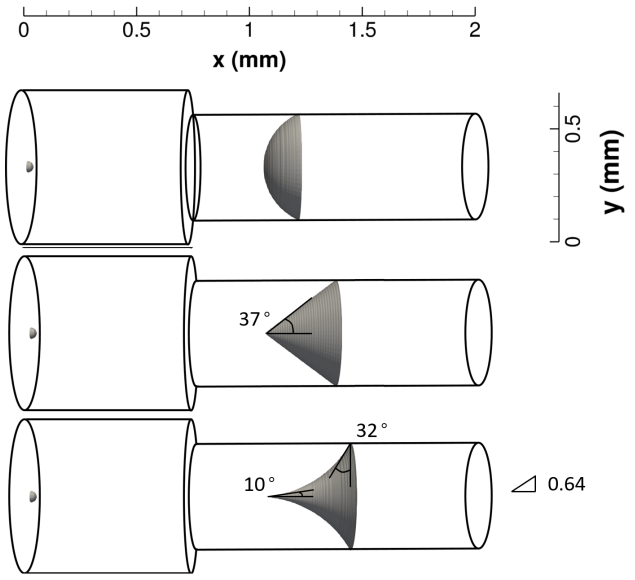

Figure 4.10: Initial condition of the meniscus, from top to bottom: hemispherical initialisation (*case 3*), conic initialisation (*case 8*) and trumpet initialisation (*case 9*). The opening angle of the cone is 37°, the opening angle of the trumpet is 10°, the contact angle between the interface and the y axis is 32° and the aspect ratio is 0.64.

Table 4.3: The effect of the meniscus geometry on the maximum jet velocity and on the jet diameter for $p_{bub} = 5 \cdot 10^7\, Pa$.

Meniscus geometry	u_{jet} (m/s)	D_{jet} (μm)
hemispherical	28.3	25
conical	48	2.5
trumpet	170	2.5

4.2.4 Conclusions

The validity of the results has been assessed by comparison with experimental values, by demonstrating a linear relation between the laser energy (or initial bubble pressure) and the jet velocity and finally, by comparing the results of *case 3* with Ansys Fluent. Then, numerical experiments with different gas-liquid interface shapes, such as hemispherical, conical and trumpet looking shapes are

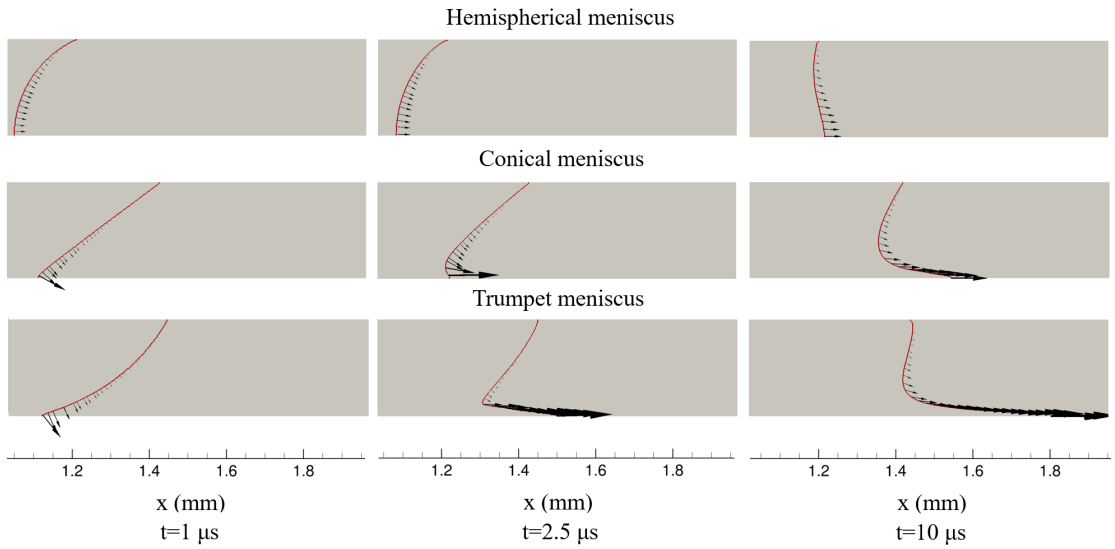

Figure 4.11: Slice on the $x-y$ plane for $z=0$. Vector field on the liquid-gas interface, for gas volume fraction $B_g = 0.5$ (red iso-line). From top to bottom: hemispherical initialization (*case 3*), conic initialization (*case 8*) and trumpet initialization (*case 9*). The magnitude of the vectors is proportional to the velocity magnitude.

performed in order to correlate these shapes with the velocity magnitude and the diameter of the jet. The trumpet shape, which initially resembles to a cone and then takes a spherical shape, was found to give focused microjets, while the velocity magnitude of the jet was the maximum among the cases examined, ensuring skin penetration. The critical jet velocity (u_{cr}) for skin penetration is approximated by equalizing the water hammer pressure (p_{wh}) with the yield stress of the human skin, which has an average value of $15\,MPa$ [250]. In the cases simulated the jet velocity is by far larger than the $u_{cr} = 10\,m/s$ and therefore, the formed jet is strong enough to penetrate the skin. In addition, the jet diameter when using the conical or the trumpet shape in the interface, was found to be one order of magnitude smaller than the jet diameter noticed with the hemispherical meniscus shape. From a practical point of view, the trumpet interface between the medicine and the air can be formed by a soft gel encapsulation machine. In a hypothetical needle-free device, a more focused jet will lead to reduced pain, as less nerve cells will be damaged. Assuming there is a good reproducibility of experiments with the trumpet meniscus shape, such studies can offer insight towards a new needle-free design. However, further investigation from a fluid structure interaction point of view, whether the drug will be successfully delivered or not has to be performed. Preliminary simulations

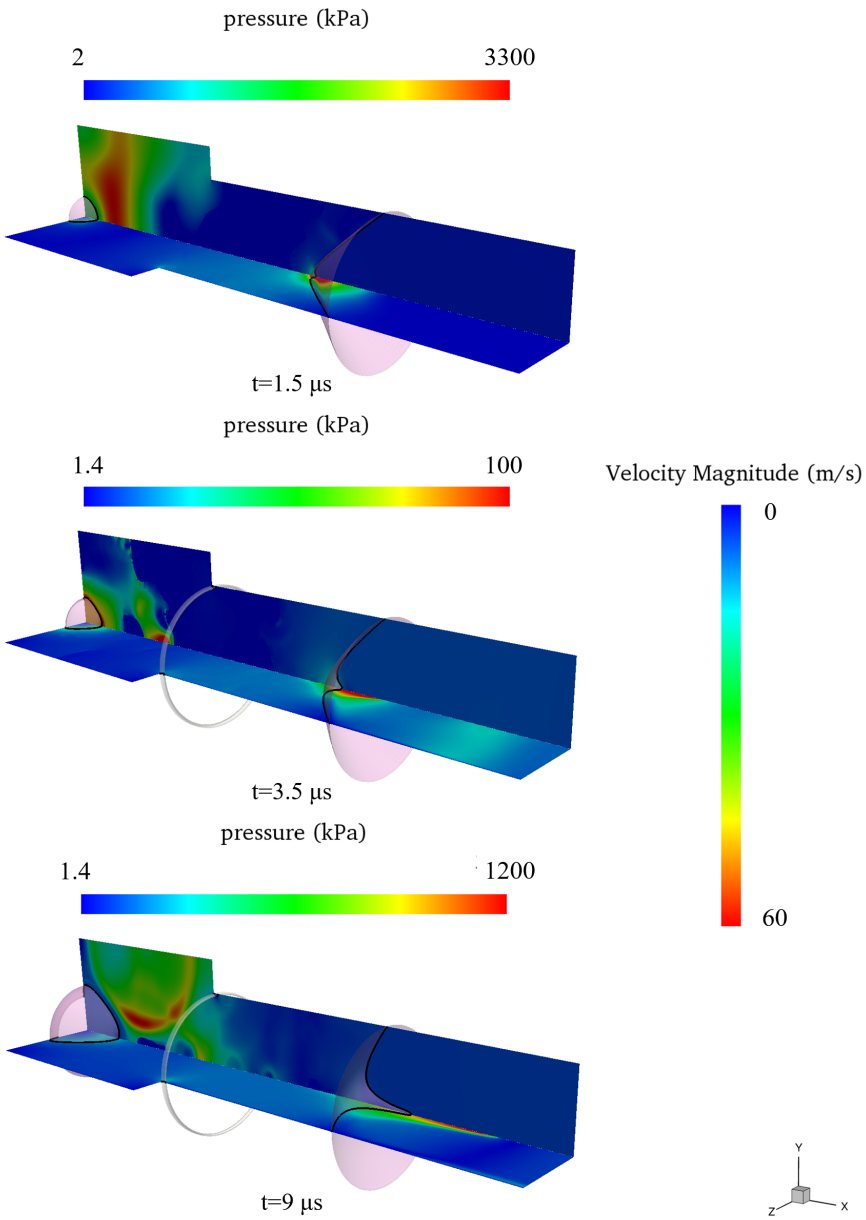

Figure 4.12: 2-D axisymmetric needle-free device simulation for $p_{bub} = 5 \cdot 10^7\, Pa$ and the conical meniscus shape (*case 8*). Pressure field on the $x-y$ plane and velocity magnitude field on the $x-z$ plane are shown, combined with iso-surface for vapour volume fraction $\alpha = 0.5$ (white) and iso-surface for gas volume fraction $B_g = 0.5$ (pink).

are shown in Appendix D. In addition, it must be examined if the drug molecule will be damaged after the interaction with the shock and the penetration. The above are out of scope of the present work, where main focus is placed on the wave dynamics and the modelling of the multiphase flow.

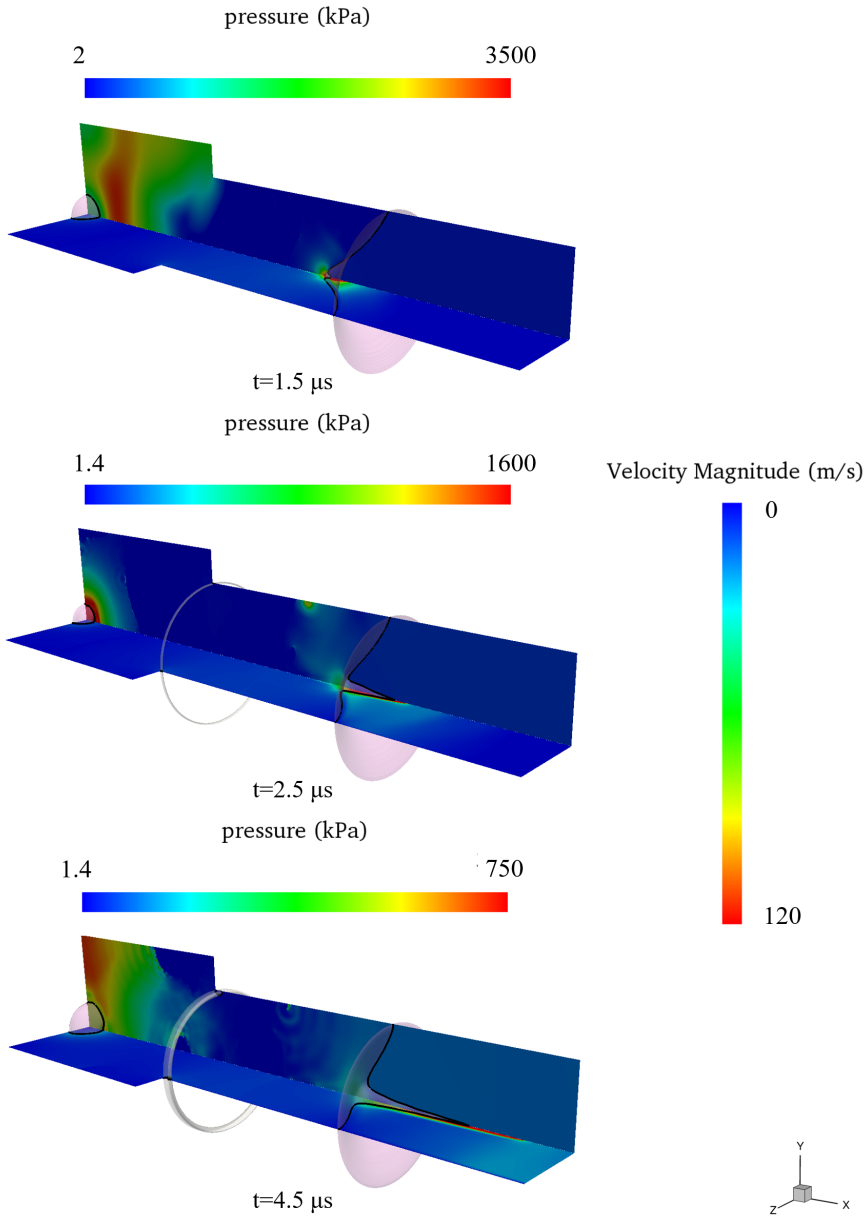

Figure 4.13: 2-D axisymmetric needle-free device simulation for $p_{bub} = 5 \cdot 10^7\ Pa$ and the trumpet meniscus shape (*case 9*). Pressure field on the $x - y$ plane and velocity magnitude field on the $x - z$ plane are shown, combined with iso-surface for vapour volume fraction $\alpha = 0.5$ (white) and iso-surface for gas volume fraction $B_g = 0.5$ (pink).

4.3 Conical converging-diverging nozzle (Helmholtz EoS)

In order to demonstrate the applicability of the tabulated data algorithm in turbulent cryogenic flows, RANS simulations for a conical converging-diverging nozzle are performed. A wedge of 5° is simulated (see Fig. 4.15), taking advantage of the problem symmetry; the nozzle geometry is demonstrated in Fig.

4.14. The $k-\omega$ SST turbulence model with the Reboud correction has been employed and the turbulence variables have been initialized accordingly, based on the Reynolds number in the inflow. The $k-\omega$ SST turbulence model behaves well for moderate and high Reynolds numbers and has been utilised for similar studies, see for example [148].

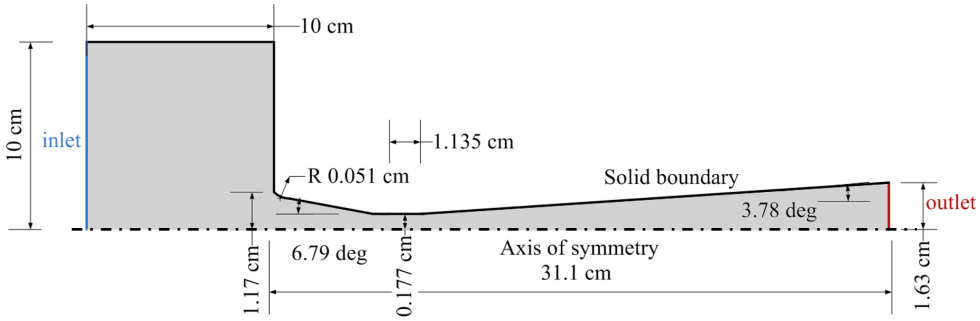

Figure 4.14: Geometry of the conical converging-diverging nozzle [135]. The inflow has been expanded upstream in order to impose the stagnation conditions of the experiment. The grey area denotes the computational domain, whereas inlet and outlet are coloured by blue and red colour respectively.

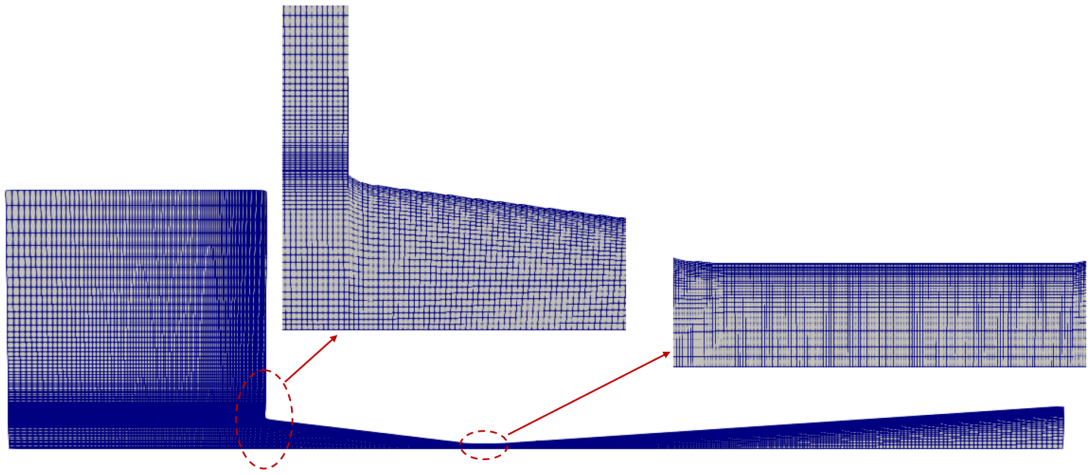

Figure 4.15: Computational grid for the conical nozzle case.

4.3.1 Subcritical conditions

The above geometry is initially tested at subcritical conditions. Validation of the model is performed against the experimental data of Hendricks et al. [135]. Therefore, in the inflow the total pressure is specified $p_{tot,in} = 1.1385\,MPa$ ($Re_{inflow} = 65k$) and the temperature is $T_{in} = 93.6\,K$, whereas in the outlet the static pressure is $p_{out} = 0.26\,MPa$.

In Fig. 4.16 contour fields for the velocity magnitude, temperature and vapour volume fraction are shown. Similar to the previous case, the flow accelerates in the converging part before the throat, due to the subsonic flow conditions. Then a region of supersonic acceleration downstream the throat follows, which is terminated by a normal shock wave. The shock wave produces an instantaneous deceleration of the flow to subsonic speed. The subsonic flow decelerates through the remainder of the diverging section and exhausts as a subsonic jet. The vapour phase generated just after the throat region results in an increased Mach number ($M = 1.2$). The mixture speed of sound here is determined by the Wallis formula [220] under the instantaneous phase change assumption. Almost full liquid vaporization has occurred after the throat, around $x = 0.015$. The discrepancy of this point between the experiment and the simulation is responsible for predicting slightly different location of the shock wave (see also Fig. 4.17).

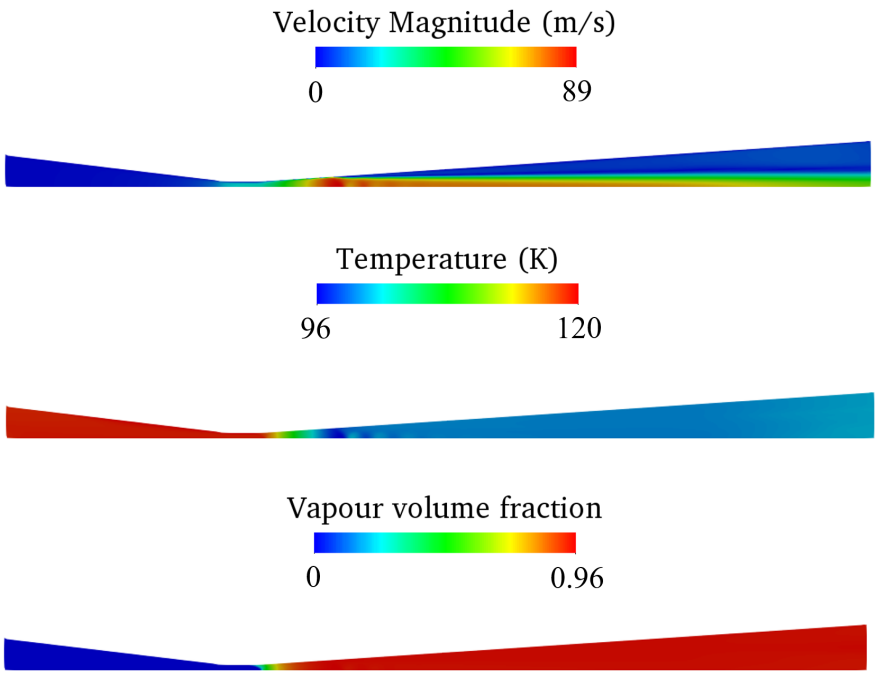

Figure 4.16: Contour fields for the converging-diverging nozzle [135], RANS simulation: velocity magnitude (upper), temperature (middle) and vapour volume fraction (bottom).

In Fig. 4.17 the obtained pressure distribution along x-axis is compared with the experimental results of Hendricks et al. [135]. While admittedly the numerical solutions are in good agreement with the experimental values, there is a small variation in the location of the shock wave between the experiment and

the simulations. Unfortunately, the lack of measurements downstream the nozzle, doesn't allow for further comparison. Compared to the inviscid simulation, the shock wave is suppressed in the RANS simulation and 2 smaller magnitude waves are noticed instead. Furthermore, in the inviscid simulation a pressure step is noticed at the location of the throat, which is not evident in the RANS simulation, due to numerical diffusion which is included from turbulence modelling.

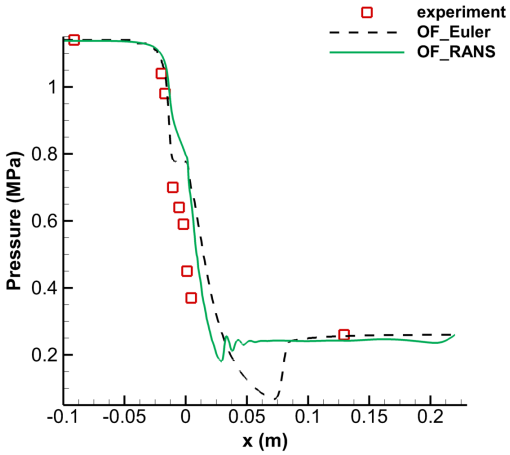

Figure 4.17: Pressure distribution along x-axis for the conical converging-diverging nozzle; comparison between inviscid (dashed black), RANS (green) simulations and the experimental values (red square) [135].

4.3.2 Supercritical conditions

The next case examined is the flow in the same nozzle but at supercritical pressure conditions; the total pressure at the inlet is $p_{tot,in} = 13.3056\,MPa$, the temperature at the inlet is $T_{in} = 93.6\,K$ and the static pressure at the outlet is $p_{out} = 10\,MPa$. Contour fields of velocity magnitude, temperature and pressure are shown in Fig. 4.19. A similar pattern as in 4.3.1 is noticed, however the shock wave at the throat is more abrupt and results in immediate deceleration of the flow, followed by cooling of the liquid. After the steep decrease of pressure in the throat, the pressure field remains constant during the expansion of the nozzle. Since there are not experimental data available for these conditions, comparison against Ansys Fluent CFD package by employing the NIST thermodynamic library is shown in 4.19. As it can be seen, there is a good agreement between the two numerical solutions and the location of the shock wave has been accurately predicted.

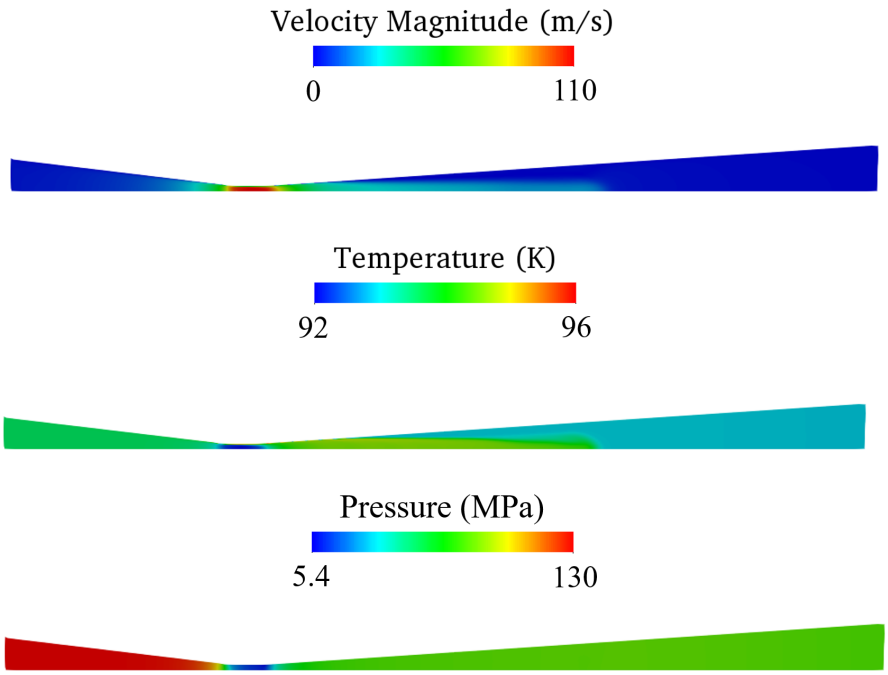

Figure 4.18: Contour fields for the converging-diverging nozzle [135] at supercritical pressure conditions: velocity magnitude (upper), temperature (middle) and vapour volume fraction (bottom).

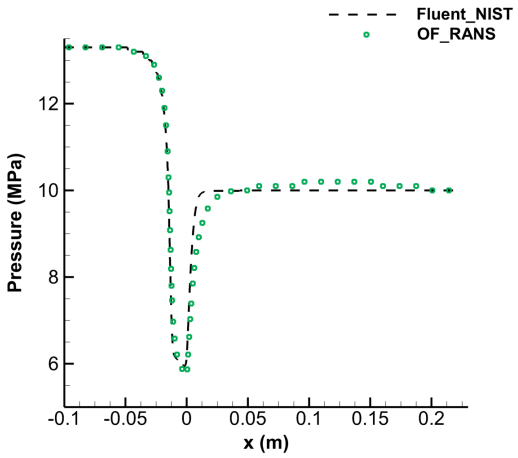

Figure 4.19: Pressure distribution along x-axis for the conical converging-diverging nozzle; comparison between the solutions obtained by OF (dashed black) and Ansys Fluent (green square).

Chapter 5

Conclusions and future work

In conclusion, a FV density based solver, suitable for multiphase applications has been developed and implemented in OF. Several different EoS and their thermodynamic closure have been employed starting from simplified EoS and advancing to real fluid thermodynamics. Apart from modelling phase-change between liquid and vapour, the gas phase has been also simulated by adding a homogeneous transport equation to the NS equations. A Mach number consistent numerical flux is also proposed in order to handle the low Mach number problem, noticed in the liquid regime. Explicit Runge-Kutta schemes have been implemented in OF aiming to accurately model the unsteady cavitation phenomena.

The solver and the different EoS incorporated have been validated against exact solutions for the Riemann problem, the Rayleigh bubble collapse and several other parametric studies of benchmark cases, such as bubble dynamics, droplet impacts, cavitating flow around hydrofoils etc. More specifically, three different thermodynamic models have been utilized and compared for bubble dynamics simulations and non-dimensional bubble collapse studies have been performed for different operating conditions. Regarding the two-phase solver, qualitative and quantitative comparisons have been performed for the 2-D droplet impact and the needleless injection respectively. In addition, the validity of the solver has been assessed by comparison with commercial packages (Ansys Fluent). Finally, the tabulated data algorithm has been tested and compared against experimental data, in-house 1-D numerical tools and Ansys-Fluent for converging-diverging nozzles in cryogenic flow conditions.

Concerning the capabilities of the solver, it is compatible with all the existing turbulence models in OF, as well as with the LES libraries. Therefore, LES studies of injector nozzles are currently being simulated by other researchers

from the author's group using the barotropic approach.

As a future work, the developed methodology can be expanded towards two different directions, either for moving boundary or for Fluid Structure Interaction (FSI) problems. In the former, two different approaches are being followed, IBM and layer addition-removal algorithms, which have been developed in OF by researchers within the same research group. IBM methodologies [55] have been incorporated in the two-phase solver of section 2.2.1 for simulating the impact of a solid body on a liquid jet and for modelling the flow in mechanical heart valves. In addition, layer addition-removal algorithms [126, 127, 128, 129] are being utilized in conjunction with the the barotropic solver of section 2.2.1 for simulating the flow in Diesel injectors with moving needle.

Cavitation is involved in many multi-physics applications, for instance in FSI problems. Starting from the needleless injection system, the human skin can be modelled as an elastic medium [214] by performing a structural analysis. The input in the solid mechanics solver will be the velocity and the pressure fields calculated from the NS equations and as output the deformation of the tissue and possible rupture will be predicted, giving a more accurate estimation whether the liquid jet velocity will penetrate the human skin or not.

Expanding to multi-material applications, such as numerical modelling of the brain and head, the aim here is to model traumatic brain injury (TBI), either due to blast or due to impact and bullet penetration. The formation of the shock wave upon the blast or the impact, as well as the propagation of the wave within the skull and the other structures of the brain can be modelled. In the literature, the properties of the different brain structures, such as the white and grey matter, the cerebral spinal fluid (CSF) and the bone, have been modelled by utilizing several different constitutive models [251, 252, 253, 254, 255, 256, 257]. That way, the cavitating flow solver can be combined with a structural solver for multi-material modelling.

Appendix A

2-D Euler equations in cylindrical coordinates

The 2-D Euler equations in the r-z cylindrical coordinates with a geometric source term for accounting cylindrical symmetry are considered [227]:

$$\mathbf{U}_t + \mathbf{F}(\mathbf{U})_r + \mathbf{G}(\mathbf{U})_z = \mathbf{S}(\mathbf{U}), \tag{A.1}$$

where the t, r, z subscripts indicate differentiation with respect to time, r direction and z direction respectively. $\mathbf{U}$ is the conserved variable vector, $\mathbf{F}(\mathbf{U})$ and $\mathbf{G}(\mathbf{U})$ are the fluxes at the radial (r) and the axial (z) directions respectively, whereas $\mathbf{S}(\mathbf{U})$ is the geometric source term, to take into consideration the axial symmetry.

$$\begin{gathered}\mathbf{U} = \begin{bmatrix} \rho \\ \rho u_r \\ \rho u_z \\ \rho E \end{bmatrix}, \quad \mathbf{F}(\mathbf{U}) = \begin{bmatrix} \rho u_r \\ \rho u_r^2 + p \\ \rho u_r u_z \\ (\rho E + p) u_r \end{bmatrix}, \quad \mathbf{G}(\mathbf{U}) = \begin{bmatrix} \rho u_z \\ \rho u_r u_z \\ \rho u_z^2 + p \\ (\rho E + p) u_z \end{bmatrix}, \\ \mathbf{S}(\mathbf{U}) = -\frac{s}{r} \begin{bmatrix} \rho u_r \\ \rho u_r^2 \\ \rho u_r u_z \\ (\rho E + p) u_r \end{bmatrix}\end{gathered} \tag{A.2}$$

where r is the distance from the axis/point of symmetry and s is unity for cylindrical symmetry and 2 for spherical symmetry. The rest of the variables are the same as in section 2.1.

Appendix B

Analytical Solutions

B.1 Exact Riemann Problem solution for an arbitrary equation of state

In this section, the methodology for finding the exact solution to the Riemann problem for the Euler equations, for an arbitrary equation of state of the form $p = f(\rho, e)$. The equation of state may be provided in closed form, where simplifications as in Toro [227] may be done, or in a general tabular form (The interested reader is also addressed to [258, 259, 260, 261, 262, 263, 224]).

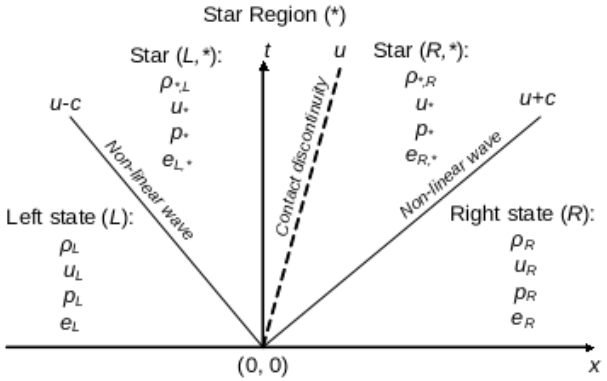

Figure B.1: Wave structure of the Riemann problem for the Euler equations for a general equation of state $p = f(\rho, e)$.

The form of the Riemann problem solved is:

$$\begin{cases} \dfrac{\partial \mathbf{U}}{\partial t} + \dfrac{\partial \mathbf{F}(\mathbf{U})}{\partial x} = 0 \\ \mathbf{U}(x,0) = \begin{cases} \mathbf{U_L}, & x < 0 \\ \mathbf{U_R}, & x \geq 0 \end{cases} \end{cases} \tag{B.1}$$

where $\mathbf{U}(x,t)$ is the vector of conservative variables and $\mathbf{F}(\mathbf{U})$ is the flux vector, as shown below:

$$\mathbf{U} = \begin{bmatrix} \rho \\ \rho u \\ \rho E \end{bmatrix}, \quad \mathbf{F}(\mathbf{U}) = \begin{bmatrix} \rho u \\ \rho u^2 + p \\ u(\rho E + p) \end{bmatrix}, \tag{B.2}$$

where $E = 1/2u^2 + e$, with e being the internal energy. The Jacobian matrix $\mathbf{A}(\mathbf{U})$ is:

$$\mathbf{A}(\mathbf{U}) = \begin{bmatrix} 0 & 1 & 0 \\ \dfrac{\partial p}{\partial \rho} + \dfrac{\frac{\partial p}{\partial e}\left(u^2 - 2e\right) - 2\rho u^2}{2\rho} & u\left(2 - \dfrac{\partial p}{\partial e}\right) & \dfrac{1}{\rho}\dfrac{\partial p}{\partial e} \\ \dfrac{u\left[2p + \frac{\partial p}{\partial e}\left(2e - u^2\right) + \rho\left(u^2 - 2\frac{\partial p}{\partial \rho} + 2e\right)\right]}{2\rho} & \dfrac{\left(\rho - 2\frac{\partial p}{\partial e}\right)u^2 + 2p + 2e\rho}{2\rho} & \dfrac{\left(\frac{\partial p}{\partial e} + \rho\right)u}{\rho} \end{bmatrix} \tag{B.3}$$

and the eigenvalues λ_1, λ_2, λ_3 are:

$$\lambda_1 = u - \sqrt{\frac{\partial p}{\partial \rho} + \frac{\partial p}{\partial e}\frac{p}{\rho^2}} \lambda_2 = u \lambda_3 = u + \sqrt{\frac{\partial p}{\partial \rho} + \frac{\partial p}{\partial e}\frac{p}{\rho^2}} \tag{B.4}$$

The solution of the Euler equations B.1 is self similar, with two genuinely non-linear waves, corresponding to λ_1 and λ_3 eigenvalues, that can be either shock waves or rarefaction waves (Fig. B.1). These waves separate the solution of the Riemann problem to the left state (L), the right state (R) and the star region ($*$). In the star region, pressure and velocity are the same, but density and internal energy are not. The latter also change along the contact discontinuity (corresponding to λ_2). To find the solution to the Riemann problem, one needs to solve a non-linear algebraic equation for pressure:

$$g(p^*) = g_L(p^*) + g_R(p^*) + u_R - u_L = 0 \tag{B.5}$$

Functions g_L and g_R depend on the type of non-linear wave. For shock waves the Rankine-Hugoniot conditions are employed, eventually leading to:

$$g_{K,shock} = \left[\frac{(p^* - p_K)(\rho_K^* - \rho_K)}{\rho_K^* \rho_K}\right]^{1/2}, \tag{B.6}$$

for $K = L$ or R state. Apart from Eq. B.6, energy conservation applies across the shock wave:

$$e_K^* = \frac{1}{2}(p^* + p_K)\left(\frac{\rho_K^* - \rho_K}{\rho_K^* \rho_K}\right) + e_K, \tag{B.7}$$

To solve Eq. B.6 and B.7 an iterative procedure is required; initially one assumes an initial internal energy e_K^* (e.g. equal to e_K) which, combined with pressure p^*, corresponds to a density ρ_K^*. This density can be used to obtain the $g_{K,shock}$ function and the internal energy from the energy balance (Eq. B.7). Since e_K^* from Eq. B.7 and e_K^* are not necessarily the same, due to the guessed value of the latter, e_K^* is corrected and the process is repeated till convergence.

For the rarefaction wave, the calculation is more complicated, since it involves the Riemann invariants across an isentropic path. The Riemann invariants are shown below for the left rarefaction wave:

$$du + \frac{c}{\rho}d\rho = 0, s = s_L \tag{B.8}$$

and the right rarefaction wave:

$$du - \frac{c}{\rho}d\rho = 0, s = s_R \tag{B.9}$$

Integration of these relations is not convenient to be done analytically for a general EoS, which might be expressed in tabular form. It is rather convenient to perform the integration numerically on an isentropic path across the rarefaction wave, as follows for e.g. the left rarefaction wave:

$$u^* - u_L + \int_L^* \left(\frac{c}{\rho}\right)_{s=s_L} d\rho = 0 \tag{B.10}$$

One can split the integral as follows:

$$u^* + \int_{ref}^* \left(\frac{c}{\rho}\right)_{s=s_L} d\rho = u_L + \int_{ref}^L \left(\frac{c}{\rho}\right)_{s=s_L} d\rho, \tag{B.11}$$

where ref is a reference state e.g. at the minimum allowable density of EoS. In

a similar manner one may derive the relation for the right rarefaction wave:

$$u^* - \int_{ref}^{*} \left(\frac{c}{\rho}\right)_{s=s_R} d\rho = u_R + \int_{ref}^{R} \left(\frac{c}{\rho}\right)_{s=s_R} d\rho, \tag{B.12}$$

and eventually, the function

$$g_{K,rarefaction} = \int_{ref}^{*} \left(\frac{c}{\rho}\right)_{s=s_K} d\rho - \int_{ref}^{K} \left(\frac{c}{\rho}\right)_{s=s_R} d\rho, \tag{B.13}$$

Hereafter the integral $\int_{ref}^{K} \left(\frac{c}{\rho}\right)_{s=s_K} d\rho$ will be referred to as $I_K(p_K)$. Calculation of the isentropic integral $I_K(p_K)$ may be done numerically. At first, one needs to calculate the states that have the same entropy s, as the right (R) and left (L) state.

Assuming that the thermodynamic properties are expressed in the form of $f(\rho, e)$, the isentropic path may be calculated as follows:

1. determine the entropy of the K state (K can be either L or R), as $s_K = s(\rho_K, e_K)$.

2. starting from a low reference density, ρ_{ref}, and increasing by intervals $d\rho$, the point that corresponds to s_K is found by iteratively correcting internal energy e, for the given path point i. Internal energy correction may be done with the Newton-Raphson method, till a specified tolerance is reached.

3. after reaching the tolerance, the rest thermodynamic properties (e.g. pressure, speed of sound etc.) for (ρ_i, e_i) may be found. Speed of sound c, is needed to evaluate the term inside the integral I. Pressure is needed in order to express the integral as a function of pressure; this is preferable, because pressure at the whole star region is the same. The integral may be calculated by using the trapezoid rule, or a more accurate Simpson method. Care should be taken in areas of large changes in the speed of sound, as e.g. near saturation lines.

4. the procedure may be done till a high pressure p_{max} which should be greater than the pressure expected to appear in the rest calculations.

Switching between rarefaction and shock wave is done based on pressure:

$$g_K = \begin{cases} g_{K,rarefaction}, & p_K < p^* \\ g_{K,shock}, & p_K \geq p^* \end{cases} \tag{B.14}$$

The solution for the star region can be achieved with the Newton-Raphson method:

$$p_n = p_{n-1} - \frac{g(p_{n-1})}{g'(p_{n-1})} urf \tag{B.15}$$

where n is the number of the iteration, urf is an under-relaxation factor to enhance stability in case of highly non-linear EoS and g' is the derivative of Eq. B.5. Note that for such equations it is preferable to resort to a numerically approximated value of the derivative, as:

$$g' = \frac{g(\rho - \epsilon) - g(\rho)}{\epsilon}, \tag{B.16}$$

where ϵ is a small positive number. For highly non-linear EoS, it might be preferable also to bound the maximum change of pressure from iteration to iteration, in order to prevent overshoots/undershoots and enhance stability, i.e.:

$$p_n = max(min(p_n, p_{max}), p_{min}), \tag{B.17}$$

where p_{max}, p_{min} can be percentage of density during the previous iteration, e.g. 120% and 80% of p_{n-1} respectively. After determining p^* within sufficient tolerance, determining velocity u^* is trivial, through the following equation:

$$u^* = 0.5(u_L + u_R) + 0.5[g_R(p^*) - g_L(p^*)] \tag{B.18}$$

Identification of the type of waves is done depending on pressure at the star region comparing the left and right states: if $p^* > p_K$ then the wave between the $*$ and K region is a shock wave, else it is a rarefaction wave. The type of wave determines the wave speed and the transition between the two states. For a shock wave the transition is sharp and the wave speed is given by: Left shock:

$$S_L = u_L - \frac{Q_L}{\rho_L} \tag{B.19}$$

Right shock:

$$S_R = u_R - \frac{Q_R}{\rho_R} \tag{B.20}$$

with

$$Q_K = \left[\frac{(p^* - p_K)\rho_K^* \rho^*}{\rho_K^* - \rho_K} \right]^{1/2} \tag{B.21}$$

Rarefactions, contrary to shock, are gradual changes in density, pressure and velocity. Thus, they are associated with two speeds, one for the head of the rarefaction and one for the tail: Left rarefaction, head: $S_{LH} = u_L - c_L$ and tail: $S_{LT} = u^* - c_L$ Right rarefaction, head: $S_{RH} = u_R + c_R$ and tail: $S_{RT} = u^* + c_R^*$ In order to find the conditions inside the rarefaction wave, the Riemann invariants shall be used. For a left rarefaction, one has to solve the following equation for the point i inside the rarefaction:

$$\frac{x_i}{t} + c(p_i) + I_L(p_i) = u_L + I_L(p_L) \tag{B.22}$$

Similarly, for the right rarefaction:

$$\frac{x_i}{t} - c(p_i) - I_R(p_i) = u_R - I_R(p_R) \tag{B.23}$$

Solution of Eq. B.22 and B.22 can be done numerically, solving for density, using Newton-Raphson method, applying under-relaxation and taking care during the updating of the density values. Experience has shown that it is better to apply a low under-relaxation factor of even 0.02.

Assuming the n-Dodecane Helmholtz EOS and assuming an initial discontinuity of the form $\rho_L = 752.5 kg/m^3$ and temperature $T_L = 289K$ for $x < 0$, $\rho_R = 717.5 kg/m^3$ and $T_R = 350K$ for $x \geq 0$ (which corresponds to $p_L \sim 44330Pa$ and $p_R \sim 109bar$), one obtains that the solution of the Riemann problem at the star region is: $p^* = 6017572Pa$, $u^* = -5.94 m/s$, $\rho_L^* = 755.86 kg/m^3$, $\rho_R^* = 713.48 kg/m^3$, $T_L^* = 290.02K$, $T_R^* = 349.47K$ With rarefaction wave to the right $S_{TR} = 1125.13 m/s$, $S_{HR} = 1162.62 m/s$ and shock wave to left $S_L = -1336.49 m/s$.

B.2 Exact Riemann Problem for multi-material problems

In this section, the methodology for finding the exact solution to the Riemann problem for the multi-material Euler equations is derived. In the literature there are limited works discussing exact Riemann solvers for multi-material applica-

tions. Mainly, these focus on multiple velocities, pressures and temperature fields, see e.g. [264, 224]. The discussion here will be limited to just two different materials sharing the same velocity, pressure and temperature fields. The materials will be referred to as *material-1* and *material-2*, however the methodology may be extended to any number of materials. For the sake of generality, the discussion will not be limited to an explicit form of equation of state. Instead, the equations of state for the two distinct materials will be assumed to depend on density and internal energy only, i.e. have a form $p = p(\rho)$ or $p = p(\rho, e)$, which may have an explicit formula or be in tabular form as in [89, 95]. Material variation will be tracked using a mass fraction transport equation which will affect the mixture equation of state. Thus, the mixture equation of state that will be examined is of the form $p = p(\rho, Y)$ or $p = p(\rho, e, Y)$, where Y is the mass fraction of *material-2*, defined in Eq. (2.25). Following Toro [227], the form of the Riemann problem solved is:

$$\begin{cases} \dfrac{\partial \mathbf{U}}{\partial t} + \dfrac{\partial \mathbf{F}(\mathbf{U})}{\partial x} = 0 \\ \mathbf{U}(x,0) = \begin{cases} \mathbf{U_L}, & \mathbf{x < 0} \\ \mathbf{U_R}, & \mathbf{x \geq 0} \end{cases} \end{cases} \tag{B.24}$$

The same nomenclature as in the rest of the paper is used.

B.2.1 Pressure is only a function of density and mass fraction

In case the mixture pressure is only a function of density and mass fraction, $p = p(\rho, Y)$ the conservative variables and the flux vector are:

$$\mathbf{U} = \begin{bmatrix} \rho \\ \rho u \\ \rho Y \end{bmatrix}, \quad \mathbf{F}(\mathbf{U}) = \begin{bmatrix} \rho u \\ \rho u^2 + p \\ \rho u Y \end{bmatrix}, \tag{B.25}$$

To derive the Jacobian matrix, it is convenient to recast the $\mathbf{U}$ and $\mathbf{F}(\mathbf{U})$ vectors and equation of state $p = p(\rho, Y)$, as:

$$\mathbf{U} = \begin{bmatrix} u_1 \\ u_2 \\ u_3 \end{bmatrix}, \quad \mathbf{F}(\mathbf{U}) = \begin{bmatrix} u_2 \\ \frac{u_2^2}{u_1} + p\left(u_1, \frac{u_3}{u_1}\right) \\ \frac{u_3 u_2}{u_1} \end{bmatrix}, \quad p = p\left(u_1, \frac{u_3}{u_1}\right), \tag{B.26}$$

The Jacobian matrix is calculated as:

$$\mathbf{A}(\mathbf{U}) = \begin{bmatrix} \frac{\partial f_1}{\partial u_1} & \frac{\partial f_1}{\partial u_2} & \frac{\partial f_1}{\partial u_3} \\ \frac{\partial f_2}{\partial u_1} & \frac{\partial f_2}{\partial u_2} & \frac{\partial f_2}{\partial u_3} \\ \frac{\partial f_3}{\partial u_1} & \frac{\partial f_3}{\partial u_2} & \frac{\partial f_3}{\partial u_3} \end{bmatrix} \tag{B.27}$$

After calculating all terms and replacing back the conservative variables:

$$\mathbf{A}(\mathbf{U}) = \begin{bmatrix} 0 & 1 & 0 \\ \frac{\partial p}{\partial \rho} - u^2 - \frac{\partial p}{\partial Y}\frac{Y}{\rho} & 2u & \frac{1}{\rho}\frac{\partial p}{\partial Y} \\ -uY & Y & u \end{bmatrix} \tag{B.28}$$

The eigenvalue analysis of the Jacobian matrix results to:

$$\begin{aligned} \lambda_1 &= u - c \\ \lambda_2 &= u \\ \lambda_3 &= u + c \end{aligned} \tag{B.29}$$

and right eigenvectors:

$$\mathbf{K_1} = \begin{bmatrix} 1 \\ u - c \\ Y \end{bmatrix}, \quad \mathbf{K_2} = \begin{bmatrix} \frac{\partial p}{\partial Y} \\ u\frac{\partial p}{\partial Y} \\ Y\frac{\partial p}{\partial Y} - \rho\frac{\partial p}{\partial \rho} \end{bmatrix}, \quad \mathbf{K_3} = \begin{bmatrix} 1 \\ u + c \\ Y \end{bmatrix} \tag{B.30}$$

where c is the speed of sound equal to $\sqrt{\frac{\partial p}{\partial \rho}}$. The waves associated with λ_1, λ_3 eigenvalues are non-linear waves (shock waves or rarefaction waves) and the λ_2

eigenvalue is a linearly degenerate wave associated with a contact discontinuity.

B.2.2 Pressure is a function of density, internal energy and mass fraction

In case the mixture pressure is only a function of density, internal energy and mass fraction, $p = p(\rho, e, Y)$ the conservative variables and the flux vector are:

$$\mathbf{U} = \begin{bmatrix} \rho \\ \rho u \\ \rho E \\ \rho Y \end{bmatrix}, \quad \mathbf{F}(\mathbf{U}) = \begin{bmatrix} \rho u \\ \rho u^2 + p \\ u(\rho E + p) \\ \rho u Y \end{bmatrix}, \tag{B.31}$$

where $E = 1/2u^2 + e$, with e being the internal energy. To derive the Jacobian matrix, it is convenient to recast the $\mathbf{U}$ and $\mathbf{F}(\mathbf{U})$ vectors and EoS $p = p(\rho, e, Y)$ as:

$$\mathbf{U} = \begin{bmatrix} u_1 \\ u_2 \\ u_3 \\ u_4 \end{bmatrix}, \quad \mathbf{F}(\mathbf{U}) = \begin{bmatrix} u_2 \\ \dfrac{u_2^2}{u_1} + p\left(u_1, \dfrac{u_3}{u_1} - \dfrac{u_2^2}{2u_1}, \dfrac{u_4}{u_1}\right) \\ \dfrac{u_2}{u_1}\left(u_3 + p\left(u_1, \dfrac{u_3}{u_1} - \dfrac{u_2^2}{2u_1}, \dfrac{u_4}{u_1}\right)\right) \\ \dfrac{u_4 u_2}{u_1} \end{bmatrix}, \tag{B.32}$$

$$p = p\left(u_1, \frac{u_3}{u_1} - \frac{u_2^2}{2u_1}, \frac{u_4}{u_1}\right) \tag{B.33}$$

The Jacobian matrix is:

$$\mathbf{A}(\mathbf{U}) = \begin{bmatrix} 0 & & & \\ \dfrac{2\frac{\partial p}{\partial \rho}\rho + \frac{\partial p}{\partial e}(u^2 - 2e) - 2\left(\rho u^2 + \frac{\partial p}{\partial Y}Y\right)}{2\rho} & & & \\ \dfrac{u\left(-\frac{\partial p}{\partial e}u^2 + \rho u^2 + 2\frac{\partial p}{\partial e}e + 2p - 2\rho\frac{\partial p}{\partial \rho} + 2e\rho + 2Y\frac{\partial p}{\partial Y}\right)}{2\rho} & & & \\ -uY & & & \end{bmatrix}$$
$$\begin{bmatrix} 1 & 0 & 0 \\ \left(2 - \dfrac{\partial p}{\partial e}\dfrac{1}{\rho}\right)u & \dfrac{\partial p}{\partial e}\dfrac{1}{\rho} & \dfrac{\partial p}{\partial Y}\dfrac{1}{\rho} \\ \dfrac{\left(\rho - 2\frac{\partial p}{\partial e}\right)u^2 + 2p + 2e\rho}{2\rho} & \dfrac{u}{\rho}\left(\dfrac{\partial p}{\partial e} + \rho\right) & \dfrac{u}{\rho}\dfrac{\partial p}{\partial Y} \\ Y & 0 & u \end{bmatrix} \tag{B.34}$$

The Jacobian eigenvalues $[\lambda_1, \lambda_2, \lambda_3, \lambda_4]$ are:

$$\begin{aligned} \lambda_1 &= u - c \\ \lambda_2 = \lambda_3 &= u \\ \lambda_4 &= u + c \end{aligned} \tag{B.35}$$

and right eigenvectors:

$$\mathbf{K_1} = \begin{bmatrix} 1 \\ u - c \\ \dfrac{1}{2}\left(u^2 - cu + 2p/\rho + 2e\right) \\ Y \end{bmatrix}, \quad \mathbf{K_2} = \begin{bmatrix} 2\dfrac{1}{X}\dfrac{\partial p}{\partial Y} \\ 2\dfrac{u}{X}\dfrac{\partial p}{\partial Y} \\ 0 \\ 1 \end{bmatrix},$$
$$\mathbf{K_3} = \begin{bmatrix} 2\dfrac{1}{X}\dfrac{\partial p}{\partial e} \\ 2\dfrac{u}{X}\dfrac{\partial p}{\partial e} \\ 1 \\ 0 \end{bmatrix}, \quad \mathbf{K_4} = \begin{bmatrix} 1 \\ u + c \\ \dfrac{1}{2}\left(u^2 + cu + 2p/\rho + 2e\right) \\ Y \end{bmatrix} \tag{B.36}$$

where c is the speed of sound, defined as: $c = \sqrt{\frac{\partial p}{\partial \rho} + \frac{\partial p}{\partial e}\frac{p}{\rho^2}}$ and $X = \frac{\partial p}{\partial e}u^2 + 2\frac{\partial p}{\partial e}e - 2\frac{\partial p}{\partial \rho}\rho + 2\frac{\partial p}{\partial Y}Y$. The waves associated with λ_1, λ_4 eigenvalues are non-linear waves (shock waves or rarefaction waves) and the λ_2, λ_3 eigenvalues are linearly degenerate waves associated with a contact discontinuity.

B.2.3 Exact solver derivation

Despite the difference in the Jacobian matrix structure with respect to the single material, ideal gas Euler equations [227], the eigenstructure is very similar. In both cases (pressure is function of ρ, Y or pressure is a function of ρ, e, Y), the eigenvalues correspond to two non-linear waves and one contract discontinuity wave. In fact, since the material interface will travel at the contact discontinuity, allows to split the original multi-material Riemann problem, to two coupled single-material Riemann problems, as shown in Fig. B.2 and B.3.

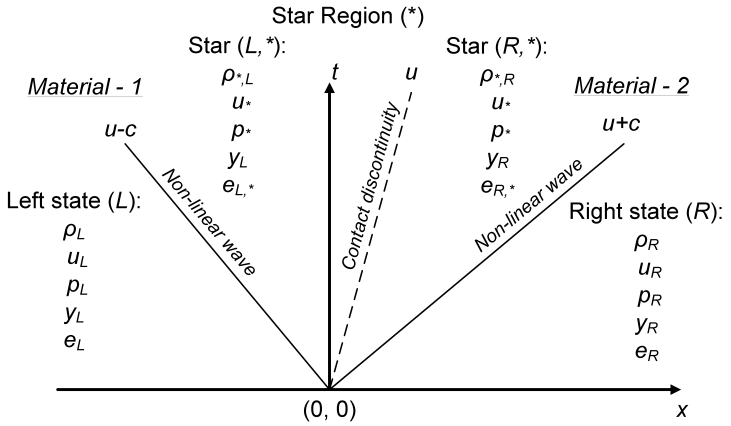

Figure B.2: Wave structure of the Riemann problem for the multi-material Euler equations for a general equation of state $p = f(\rho, e, Y)$.

Consequently, to solve the multi-material Riemann problem exactly, one has to do the following procedure:

1. Assume an initial star region velocity, $u^\star$.

2. Based on this assumed $u^\star$, solve each material separately, with a single material Riemann solver, assuming that the contact discontinuity is a moving wall at velocity $u_{wall} = u^\star$. General Riemann solvers for arbitrary equations of state in the form of $p = p(\rho)$ or $p = p(\rho, e)$ may be found in [95]. The solution of each single-material problem is done assuming wall boundary conditions, i.e. $p_R = p_L$, $\rho_R = \rho_L$, but $u_R = -u_L + 2u_{wall}$. For example,

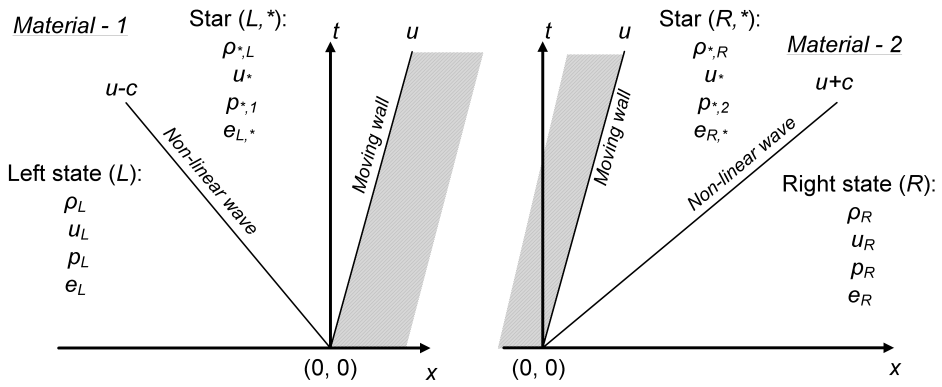

Figure B.3: Equivalent splitting of the multi-material Riemann problem to two coupled single-material Riemann problems.

in Fig. B.3, when solving for *material-1*, the right state conditions are $\mathbf{U} = \begin{bmatrix} \rho_L & \rho_L(2u_{wall} - u_L) & e_L \end{bmatrix}^{\mathbf{T}}$. Similarly for *material-2*, the left state conditions are $\mathbf{U} = \begin{bmatrix} \rho_R & \rho_R(2u_{wall} - u_R) & e_R \end{bmatrix}^{\mathbf{T}}$.

3. After solving the two individual Riemann problems for *material-1* and *material-2*, the calculated star region pressure for the two materials $p_1^\star$ and $p_2^\star$ is not necessarily the same. Thus, the u^* velocity must be corrected iteratively, until $p_1^\star = p_2^\star$.

4. Once $p_1^\star = p_2^\star$ up to a prescribed tolerance, the exact solution of the Riemann problem is the superposition of the two individual problems, i.e. the L and L^* states from *material-1* and R and R^* states from *material-2*. Note that in cases of large disparities in the acoustic impedance of the materials (e.g. liquid/gas interfaces), $p^\star$ will be very sensitive to small variations of $u^\star$ for the stiff phase, thus under-relaxation of the corrected $u^\star$ is advised.

As a demonstration of the aforementioned solver of section 2.6.1, the following cases will be examined and compared with PVRS solvers in literature [227]. The material properties are as follows: *material-1*: Liquid EoS, $p = c_L^2(\rho - \rho_{l,sat}) + p_{sat}$, $c_L = 1482.35\,m/s$, $p_{sat} = 2340\,Pa$, $\rho_{l,sat} = 998.16\,kg/m^3$ *material-2*: Gas EoS, $p = \rho R_g T_{ref}$, $R_g = 287.06\,J/(kgK)$, $T_{ref} = 293\,K$

Case A

The initial configuration of the Riemann problem is shown in Table B.1. The exact solution is $p^\star = 1430.9\,Pa$ and $u^\star = 0.067\,m/s$. The PVRS-solver, using average states between L, R fails to properly predict the star region; in fact, it

predicts $p^\star = 50666.7\,Pa$ (3440.9 % deviation from exact) and $u^\star = 0.11\,m/s$ (66.9 % deviation from exact). On the other hand, the PVRS-solver outlined in section 2.6.1, predicts $p^\star = 1430.9\,Pa$ (practically identical to exact solution) and $u^\star = 0.066\,m/s$ (0.2 % deviation from exact). Note that this is the same case used for validation in section 3.1.2.

Table B.1: Initial configuration for the Riemann problem of B.2.3.

material-1, $x < 0$ (Liquid)	*material-2*, $x \geq 0$ (Gas)
$\rho_L = 998.202\,kg/m^3$	$\rho_R = 0.017\,kg/m^3$
$u_L = 0\,m/s$	$u_R = 0\,m/s$
$p_L = 99902.8\,Pa$	$p_R = 1400\,Pa$

Case B

The second Riemann problem is a much more demanding case, since there is a huge pressure and density variation between the L, R states. The initial configuration of this Riemann problem is shown in Table B.2. The exact solution is $p^\star = 144.4\,Pa$ and $u^\star = 2.73\,m/s$. The PVRS-solver, using average states between L, R again fails to properly predict the star region, due to the averaging; in fact, it predicts $p^\star = 20.2 \cdot 10^5\,Pa$ (1400000 % deviation from exact) and $u^\star = 4.56\,m/s$ (66.7 % deviation from exact). On the other hand, the PVRS-solver outlined in section 2.6.1, predicts $p^\star = 144.4\,Pa$ (practically identical to exact solution) and $u^\star = 2.72\,m/s$ (0.32 % deviation from exact).

Table B.2: Initial configuration for the Riemann problem of B.2.3.

material-1, $x < 0$ (Liquid)	*material-2*, $x \geq 0$ (Gas)
$\rho_L = 1000\,kg/m^3$	$\rho_R = 0.0017\,kg/m^3$
$u_L = 0\,m/s$	$u_R = 0\,m/s$
$p_L = 40.4 \cdot 10^5\,Pa$	$p_R = 143\,Pa$

Case C

In this case, although the pressure and density ratios are much lower than the case in section B.2.3, the challenge is to predict the induced depressurization due to the high gas velocity. The initial configuration of this Riemann problem is shown in Table B.3. The exact solution is $p^\star = 81548\,Pa$ and $u^\star = 2.68\,m/s$. The PVRS-solver, using average states between L, R again fails catastrophically,

predicting a negative $p^\star$; it predicts $p^\star = -154923\,Pa$ (290 % deviation from exact) and $u^\star = 9.46\,m/s$ (250 % deviation from exact). On the other hand, the PVRS-solver outlined in section 2.6.1, predicts $p^\star = 82025\,Pa$ (0.59 % deviation from exact solution) and $u^\star = 2.67\,m/s$ (0.33 % deviation from exact).

Table B.3: Initial configuration for the Riemann problem of B.2.3.

material-1, $x < 0$ (Liquid)	*material-2*, $x \geq 0$ (Gas)
$\rho_L = 1000\,kg/m^3$	$\rho_R = 1\,kg/m^3$
$u_L = 0\,m/s$	$u_R = 10\,m/s$
$p_L = 40.4 \cdot 10^5\,Pa$	$p_R = 84151\,Pa$

Case D

Also, in order to demonstrate the capability in predicting temperature effects and taking into account energy equation, a case examined by Saurel et al. [224] will be discussed. This case involves interaction of vapour and liquid dodecane, modelled as ideal gas and stiffened gas respectively. The properties of the materials are: *material-1*: Liquid, stiffened gas EoS, $p = e(\gamma_L - 1)\rho - \gamma_L p_\infty$, $e = c_{v,L}T + \dfrac{p_\infty}{\rho}$, $c_{v,L} = 1077\,J/(kgK)$, $p_\infty = 4 \cdot 10^8\,Pa$, $\gamma_L = 2.35$ *material-2*: Ideal gas EoS, $p = \rho R_g T_{ref}$, $e = c_{v,G}T$, $R_g = 48.9\,J/(kgK)$, $c_{v,G} = 1956\,J/(kgK)$ The initial discontinuity in this case is described in Table B.4. The exact solution with the described solver is $p^\star = 186835.8\,kg/m^3$, $u^\star = 140.7\,m/s$, $\rho_{\star,L} = 454.9\,kg/m^3$, $\rho_{\star,R} = 3.68\,kg/m^3$ which is identical with the published solution.

Table B.4: Initial configuration for the Riemann problem of B.2.3.

material-1, $x < 0$ (Liquid)	*material-2*, $x \geq 0$ (Gas)
$\rho_L = 500\,kg/m^3$	$\rho_R = 2\,kg/m^3$
$u_L = 0\,m/s$	$u_R = 0\,m/s$
$p_L = 10^8\,Pa$	$p_R = 10^5\,Pa$
$T_L = 688\,k$	$T_R = 1022.3\,K$

Appendix C

Isentropic Compression

In Table C.1, isentropic compression of liquid water starting from saturation conditions ($T = 293\,K$, $p = 2317Pa$) is calculated based on the properties of [265, 223]. The temperature increase is negligible for pressure $2500\,bar$ ($\sim 6\,K$) and even for higher pressures, temperature increase is not significant in comparison to the other phenomena which take place. For example, in the droplet simulations of section 3.7 for impact velocity 110 m/s, the maximum pressure is $1460\,bar$ resulting in temperature increase less than $3.5\,K$. The above justify the barotropic EoS which was selected and the omission of thermal effects.

Table C.1: Temperature difference for isentropic compression of liquid water. Properties are derived from [265].

Pressure (Pa)	Temperature (K)	Temperature Difference (K)
2317.45	293	0
10^7	293.15	0.15
10^8	294.959	1.959
$2.5 \cdot 10^8$	299.109	6.109
$5 \cdot 10^8$	306.905	13.905
10^9	321.933	28.933

Appendix D

Modelling of the skin tissue

In this section, preliminary simulations of the skin tissue are performed by employing Ansys Fluent CFD solver. The validity of the developed model in OF is assessed against Fluent in Fig. 4.3 and therefore it can be concluded that a similar flow field is predicted from the OF solver as well. Regarding the numerical approach in this section, an additional transport equation for modelling the tissue as compressible liquid with large viscosity ($\mu_{tis} = 0.1\, kg/(m \cdot s)$) is added to the equations of section 2.2.1 (see [266, 267]). Therefore, water, air and tissue are treated as immiscible fluids. In Fig. D.1 the initial configuration is shown, whereas in Fig. D.2 pressure (left) and velocity (right) contours combined with the iso-lines of gas volume fraction of $\alpha_g = 0.5$ (gas-liquid interface is denoted by dash line) and tissue volume fraction $\alpha_{tis} = 0.5$ (gas-tissue interface is denoted by solid line) are demonstrated for $p_{bub} = 5 \cdot 10^7\, Pa$. It is elucidated that the developed jet due to the bursting bubble is strong enough to cause skin puncture, which is also in accordance with the estimation given when water hammer pressure was used as criterion for skin penetration. At time $t = 34.3\, \mu s$ the liquid jet is about to impact the skin surface. Due to the compression of the air above the jet, the velocity field of the gas phase is increased, however it does not cause a deformation of the gas-soft tissue interface as it is not focused. On the other hand at time $t = 40.5\, \mu s$ the liquid jet has just reached the soft tissue, whose interface is deformed because of high velocity field of the jet. At later times $t = 53$ and $79.8\, \mu s$ the jet has further travelled into the soft tissue. As the jet further advances, its velocity magnitude is decreasing until a stagnation point is created at the maximum depth.

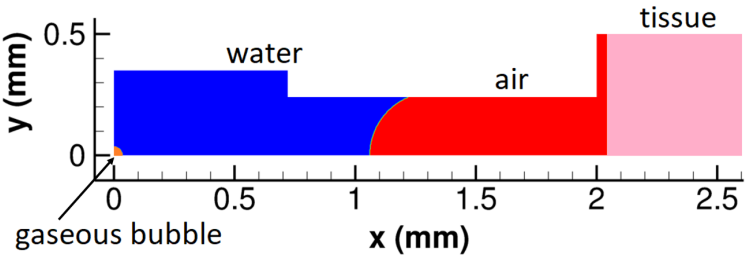

Figure D.1: Initial configuration of the needleless injection with the soft tissue modelled. The gaseous bubble of $p_{bub} = 5 \cdot 10^7$ (orange), the liquid in atmospheric pressure (blue), the air in atmospheric pressure (red) and the soft tissue (pink) are depicted.

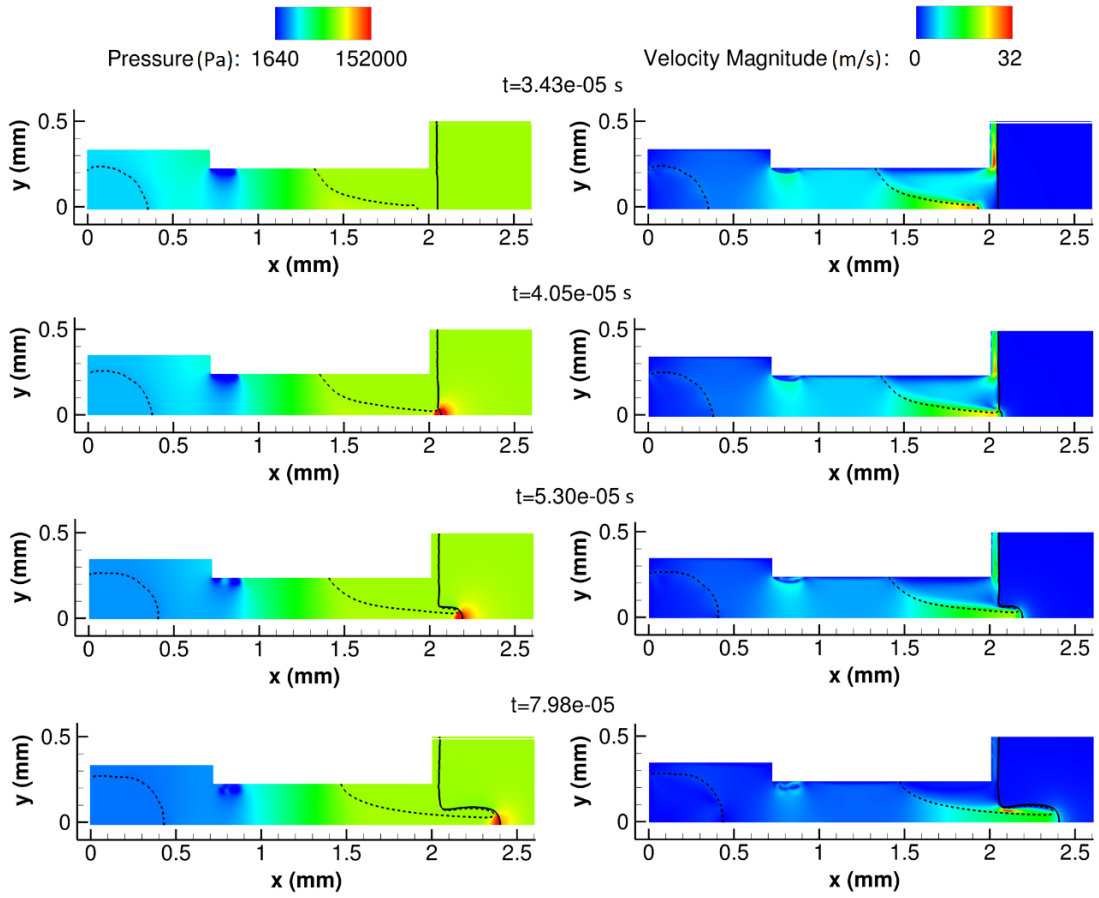

Figure D.2: Contour fields of the needleless injection when considering the additional phase of the soft tissue phase: pressure (left) and velocity contours (right) combined with the iso-lines of gas volume fraction of $\alpha_g = 0.5$ (gas-liquid interface is denoted by dash line) and tissue volume fraction $\alpha_{tis} = 0.5$ (gas-tissue interface is denoted by solid line) at 4 instances during the penetration of the liquid jet into the soft tissue are shown.

Appendix E

Applicability range of Helmholtz EoS

In Tables E.1, E.2 and E.3, the number of the cells where extrapolation was used beyond the applicability range of the Helmholtz EoS is shown for the bubble collapse cases of section 3.3. In addition, the minimum and maximum values of density are also shown in order to get an estimation of how extrapolation affects its value. As it can be seen, a small percentage of the total cells has been calculated beyond the calibration range of the Helmholtz EoS.

Table E.1: Percentage of the cells where the thermodynamic properties have been calculated using the Helmholtz EoS beyond its calibration limit for the bubble collapse of section 3.3 with $d = 416\,\mu m$ (highest postion).

t/τ	Cells beyond calibration	min-max ρ (kg/m^3)
1.04	1.8%	$4 - 826$
1.13	4.2%	$3 - 864$
1.15	3.3%	$5 - 994$
1.18	1.9%	$550 - 916$

Table E.2: Percentage of the cells where the thermodynamic properties have been calculated using the Helmholtz EoS beyond its calibration limit for the bubble collapse of section 3.3 with $d = 140\,\mu m$ (high position).

t/τ	Cells beyond calibration	min-max ρ (kg/m^3)
1.01	0.5%	$4 - 807$
1.09	0.1%	$2 - 890$
1.10	0.1%	$553 - 1014$
1.14	0.9%	$388 - 843$

Table E.3: Percentage of the cells where the thermodynamic properties have been calculated using the Helmholtz EoS beyond its calibration limit for the bubble collapse of section 3.3 with $d = -140\,\mu m$ (low position).

t/τ	Cells beyond calibration	min-max ρ (kg/m^3)
0.72	0%	$4 - 777$
0.75	1.2%	$4 - 852$
0.76	0.7%	$751 - 1011$
0.77	0.5%	$554 - 868$

Publications

Journal publications (newest first)

- I. Karathanassis, **N. Kyriazis**, P. Koukouvinis, T. Lyras, M. Gavaises, On the modelling of liquid oxygen nozzle flows under subcritical and supercritical pressure conditions, Int. J. Heat Mass Transfer, under preparation.
- E. Stavropoulos Vasilakis, **N. Kyriazis**, P. Koukouvinis, M. Farhat, M. Gavaises, Cavitation induction by projectile impacting on a water jet, Int. J. Multiphase Flow, under revision.
- **N. Kyriazis**, P. Koukouvinis and M. Gavaises, Numerical Investigations on bubble-induced jetting and shock wave focusing: application on a needle-free injection, Proc. R. Soc. A: Mathematical, Physical and Engineering Sciences, 475, 2019. doi:10.1098/rspa.2018.0548.
- P. Koukouvinis, **N. Kyriazis** and M. Gavaises, Smoothed particle hydrodynamics simulation of a laser pulse impact onto a liquid metal droplet, PLoS ONE, 13 (9), 2018. doi:10.1371/journal.pone.0204125.
- **N. Kyriazis**, P. Koukouvinis and M. Gavaises, Modelling cavitation during droplet impact on solid surfaces, Adv. Colloid Interface Sci., 260:46-64, 2018. doi:10.1016/j.cis.2018.08.004.
- **N. Kyriazis**, P. Koukouvinis and M. Gavaises, Numerical Investigation of bubble dynamics using tabulated data, Int. J. Multiphase Flow, 93:158-177, 2017. doi:10.1016/j.ijmultiphaseflow.2017.04.004.

Conference publications (newest first)

- **N. Kyriazis**, P. Koukouvinis, I. Karathanassis and M. Gavaises, A tabulated data technique for cryogenic two-phase flows, ECFD2018, Glasgow,

UK, June 2018.

- **N. Kyriazis**, P. Koukouvinis, M. Gavaises, R. Pearson and M. Gold, Heating effects during bubble collapse using tabulated data, CAV2018, Baltimore, US, May 2018.

Bibliography

[1] M. Goud, D. Greif, M. Suffa, E. Winklhofer, and D. Gill. Virtual Erosion Prediction, Design Optimisation and Combustion System Integration of High Pressure Fuel Injector Systems. In *IMechE Conf Fuel Injection Systems for IC Engines*, 2012.

[2] G. Strotos, P. Koukouvinis, A. Theodorakakos, M. Gavaises, and G. Bergeles. Transient heating effects in high pressure diesel injector nozzles. *International Journal of Heat and Fluid Flow*, 51:257 – 267, 2015.

[3] P. Koukouvinis, M. Gavaises, J. Li, and L. Wang. Large Eddy Simulation of Diesel injector including cavitation effects and correlation to erosion damage. *Fuel*, 175:26 – 39, 2016.

[4] C. Arcoumanis, H. Flora, M. Gavaises, and M. Badami. Cavitation in real-size multi-hole diesel injector nozzles. In *SAE Technical Paper*, number 2000-01-1249, 2000.

[5] A. Prosperetti and Y. Hao. Modelling of spherical gas bubble oscillations and sonoluminescence. *Philosophical Transactions of the Royal Society of London A: Mathematical, Physical and Engineering Sciences*, 357(1751):203–223, 1999.

[6] N. I. Kolev. *Multiphase Flow Dynamics 3*. Springer-Verlag Berlin Heidelberg, 1st edition, 2007.

[7] F. Payri, V. Bermúdez, R. Payri, and F. J. Salvador. The influence of cavitation on the internal flow and the spray characteristics in diesel injection nozzles. *Fuel*, 83(4):419 – 431, 2004.

[8] B. Chehroudi, D. Talley, and E. Coy. Visual characteristics and initial growth rates of round cryogenic jets at subcritical and supercritical pressures. *Physics of Fluids*, 14(2):850–861, 2002.

[9] P. Gaillard, C. Le Touze, L. Matuszewski, and A. Murrone. Numerical Simulation of Cryogenic Injection in Rocket Engine Combustion Chambers, AerospaceLab, January 2016.

[10] G. Lamanna, H. Kamoun, B. Weigand, C. Manfletti, A. Rees, J. Sender, M. Oschwald, and J. Steelant. Flashing Behavior of Rocket Engine Propellants. *Atomization and Sprays*, 25:837–856, Aug 2015.

[11] K. Hyunji, K. Hyeongjun, M. Daeho, and K. Chongam. Numerical simulations of cryogenic cavitating flows. *Journal of Physics: Conference Series*, 656(1):012131, 2015.

[12] J. R. Travis, D. P. Koch, and W. Breitung. A homogeneous non-equilibrium two-phase critical flow model. *International Journal of Hydrogen Energy, HySafe 1*, 37(22):17373 – 17379, 2012.

[13] T. R. Kale and M. Momin. Needle free injection technology - an overview. *Innovations in pharmacy*, 5(1):1–8, 2014.

[14] A. D. Ravi, D. Sadhna, D. Nagpaal, and L. Chawla. Needle free injection technology: A complete insight. *International Journal of Pharmaceutical Investigation*, 5(4):192–199, 2015.

[15] S. Mitragotri. Current status and future prospects of needle-free liquid jet injectors. *Nature Reviews Drug Discovery*, 5:543–548, Jul 2006.

[16] J. Canter, K. Mackey, L. S. Good, R. R. Roberto, J. Chin, W. W. Bond, M. J. Alter, and J. M. Horan. An outbreak of hepatitis b associated with jet injections in a weight reduction clinic. *Archives of Internal Medicine*, 150(9):1923–1927, September 1990.

[17] A. Arora, M. R. Prausnitz, and S. Mitragotri. Micro-scale devices for transdermal drug delivery. *International Journal of Pharmaceutics*, 364(2):227 – 236, 2008.

[18] D. R. van der Heul, C. Vuik, and P. Wesseling. Efficient computation of flow with cavitation by compressible pressure correction. In *ECCOMAS*, Barcelona, 2000.

[19] C. D. Munz, S. Roller, R. Klein, and K. J. Geratz. The extension of incompressible flow solvers to the weakly compressible regime. *Computers & Fluids*, 32:173–196, 2003.

[20] H. Guillard and C. Viozat. On the behaviour of upwind schemes in the low Mach number limit. *Computers & Fluids*, 28:63–86, 1999.

[21] A. Meister. Asymptotic Single and Multiple Scale Expansions in the Low Mach Number Limit. *SIAM Journal on Applied Mathematics*, 60:256–271, January 1999.

[22] M.-S. Liou. A sequel to AUSM, Part II: AUSM$^+$-up for all speeds. *Journal of Computational Physics*, 214:137–170, 2006.

[23] S. J. Schmidt, I. H. Sezal, G. H. Schnerr, and M. Talhamer. Riemann Techniques for the Simulation of Compressible Liquid Flows with Phase-Transistion at all Mach Numbers - Shock and Wave Dynamics in Cavitating 3-D Micro and Macro Systems. In *46th AIAA Aerospace Sciences Meeting and Exhibit*, Reno, Nevada, USA, January 2008. DOI: 10.2514/6.2008-1238.

[24] X. Nogueira, L. Ramírez, S. Khelladi, J.-C. Chassaing, and I. Colominas. A high-order density-based finite volume method for the computation of all-speed flows. *Computer Methods in Applied Mechanics and Engineering*, 298:229 – 251, 2016.

[25] D. Fuster and S. Popinet. An all-mach method for the simulation of bubble dynamics problems in the presence of surface tension. *Journal of Computational Physics*, 374:752 – 768, 2018.

[26] A. Prosperetti and G. Tryggvason. *Computational Methods for Multiphase Flow*. Cambridge University Press, 2007.

[27] S. Mirjalili, S. Jain, and M. Dodd. Interface-capturing methods for two-phase flows: An overview and recent developments. *Center for Turbulence Research Annual Research Briefs*, pages 117–135, 12 2017.

[28] A. H. Koop. *Numerical Simulation of Unsteady Three-Dimensional Sheet Cavitation*. PhD thesis, University of Twente, 2008.

[29] H. Huang, M. C. Sukop, and X.-C. Lu. *Multiphase Lattice Boltzmann Methods: Theory and Application*. Wiley-Blackwell, June 2015.

[30] G. R. Liu and M. B. Liu. *Smoothed Particle Hydrodynamics: A Meshfree Particle Method*. World Scientific Publishing Company, January 2003.

[31] L. B. Lucy. Numerical approach to testing of fission hypothesis. *Astron. J.*, 82:1013–1024, 12 1977.

[32] R. A. Gingold and J. Monaghan. Smoothed Particle Hydrodynamics - Theory and Application to Non-Spherical Stars. *Monthly Notices of the Royal Astronomical Society*, 181:375–389, 11 1977.

[33] J.J. Monaghan. Simulating Free Surface Flows with SPH. *Journal of Computational Physics*, 110(2):399 – 406, 1994.

[34] A. Colagrossi and M. Landrini. Numerical simulation of interfacial flows by smoothed particle hydrodynamics. *Journal of Computational Physics*, 191(2):448 – 475, 2003.

[35] N. Grenier, M. Antuono, A. Colagrossi, D. Le Touzé, and B. Alessandrini. An Hamiltonian interface SPH formulation for multi-fluid and free surface flows. *Journal of Computational Physics*, 228(22):8380 – 8393, 2009.

[36] J. P. Vila. On particle weighted methods and smooth particle hydrodynamics. *Mathematical Models and Methods in Applied Sciences*, 09(02):161–209, 1999.

[37] J. C. Marongiu and E. Parkinson. Riemann solvers and efficient boundary treatments: an hybrid SPH-finite volume numerical method. In *Proceedings of the 3rd Spheric workshop*, Lausane, June 2008.

[38] J. C. Marongiu, F. Leboeuf, J. Caro, and E. Parkinson. Low mach number numerical schemes for the SPH-ALE method. application in free surface flow in Pelton turbines. In 4^{th} *Spheric Workshop*, Nantes, France, May 2009.

[39] J. C. Marongiu, E. Parkinson, S. Lais, F. Leboeuf, and J. Leduc. Application of SPH-ALE method to Pelton hydraulic turbines. In 5^{th} *Spheric Workshop*, Manchester, United Kingdom, June 2010.

[40] J. C. Marongiu, F. Leboeuf, J. Caro, and E. Parkinson. Free surface flows simulations in Pelton turbines using an hybrid SPH-ALE method. *Journal of Hydraulic Research*, 48(sup1):40–49, 2010.

[41] A. Crespo, E. Parkinson, J.-C. Marongiu, M. Gómez-Gesteira, and J. M. Domínguez. High Performance of SPH codes: Best approaches for efficient parallelisation on GPU computing. In *4th international SPHERIC workshop*, May 2009.

[42] J. C. Marongiu, J. Leduc, and M. Schaller. GPU implementation of a SPH-ALE fluid dynamics solver. In 6^{th} *international SPHERIC workshop*, Hamburg, Germany, June 2011.

[43] G. B. Wallis. Critical two-phase flow. *International Journal of Multiphase Flow*, 6(1):97 – 112, 1980.

[44] M. R. Baer and J. W. Nunziato. A Two-Phase Mixture Theory for the Deflagration-to-Detonation Transition (DDT) in Reactive Granular Materials. *International Journal of Multiphase Flow*, 12(6):861–889, 1986.

[45] R. Saurel and R. Abgrall. A Multi-Phase Godunov Method for Compressible Multi-Fluid and Multi-Phase Flows. *Journal of Computational Physics*, 150(2):425–467, 1999.

[46] F. H. Harlow. The particle-in-cell method for numerical solution of problems in fluid dynamics. Technical report, United States, 1962.

[47] F. H. Harlow and J. E. Welch. Numerical Calculation of Time–Dependent Viscous Incompressible Flow of Fluid with Free Surface. *The Physics of Fluids*, 8(12):2182–2189, 1965.

[48] M. S. Plesset and R. B. Chapman. Collapse of an initially spherical vapour cavity in the neighbourhood of a solid boundary. *Journal of Fluid Mechanics*, 47:283–290, 1971.

[49] J. Glimm, C. Klingenberg, O. McBryan, B. Plohr, D. Sharp, and S. Yaniv. Front tracking and two-dimensional Riemann problems. *Advances in Applied Mathematics*, 6(3):259–290, September 1985.

[50] S. O. Unverdi and G. Tryggvason. A front-tracking method for viscous, incompressible, multi-fluid flows. *Journal of Computational Physics*, 100:25–37, May 1992.

[51] J. Glimm and O. A. McBryan. A computational model for interfaces. *Advances in Applied Mathematics*, 6(4):422 – 435, 1985.

[52] J. Du, B. Fix, J. Glimm, X. Jia, X. Li, Y. Li, and L. Wu. A simple package for front tracking. *Journal of Computational Physics*, 213(2):613 – 628, 2006.

[53] P. Koukouvinis, N. Kyriazis, and M. Gavaises. SPH simulation of a laser pulse impact onto a liquid metal droplet. *PLoS ONE*, 13(9):e0204125, September 2018.

[54] C. S. Peskin. The immersed boundary method. *Acta Numerica*, 11:479–517, 2002.

[55] F. Örley, V. Pasquariello, S. Hickel, and N. A. Adams. Cut-element based immersed boundary method for moving geometries in compressible liquid flows with cavitation. *Journal of Computational Physics*, 283:1 – 22, 2015.

[56] S. Osher and J. A. Sethian. Fronts propagating with curvature-dependent speed: Algorithms based on hamilton-jacobi formulations. *Journal of Computational Physics*, 79(1):12 – 49, 1988.

[57] S. Osher and R. Fedkiw. *Level set methods and Dynamic Implicit Surfaces.* Springer, 2003.

[58] C. W. Hirt and B. D. Nichols. Volume of fluid (VOF) method for the dynamics of free boundaries. *Journal of Computational Physics*, 39(1):201–225, January 1981.

[59] D. L. Youngs. An interface tracking method for a 3D Eulerian hydrodynamics code. Technical report 44/92/35, AWRE, 1984.

[60] M. Rudman. Volume-tracking methods for interfacial flow calculations. *International Journal for Numerical Methods in Fluids*, 24(7):671–691, 1997.

[61] W. Aniszewski, T. Ménard, and M. Marek. Volume of Fluid (VOF) type advection methods in two-phase flow: A comparative study. *Computers & Fluids*, 97:52 – 73, 2014.

[62] B. J. Parker and D. L. Youngs. Two and three dimensional eulerian simulation of fluid flow with material interfaces. Technical report, UK Atomic Weapons Establishment, Aldermaston, Berkshire, 1992.

[63] R. Scardovelli and S. Zaleski. Direct numerical simulation of free-surface and interfacial flow. *Annual Review of Fluid Mechanics*, 31(1):567–603, 1999.

[64] Y. Kensuke. Efficient implementation of THINC scheme: A simple and practical smoothed VOF algorithm. *Journal of Computational Physics*, 226(2):1985 – 2002, 2007.

[65] M. Marek, W. Aniszewski, and A. Boguslawski. Simplified volume of fluid method (SVOF) for two-phase flows. *TASK Quaterly*, 12(3):255–265, 2008.

[66] F. Xiao, Y. Honma, and T. Kono. A simple algebraic interface capturing scheme using hyperbolic tangent function. *International Journal for Numerical Methods in Fluids*, 48(9):1023–1040, 2005.

[67] D. P. Garrick, W. A. Hagen, and J. D. Regele. An interface capturing scheme for modeling atomization in compressible flows. *Journal of Computational Physics*, 344:260–280, 2017.

[68] F. Xiao, S. Ii, and C. Chen. Revisit to the THINC scheme: A simple algebraic VOF algorithm. *Journal of Computational Physics*, 230(19):7086 – 7092, 2011.

[69] R. K. Shukla, C. Pantano, and J. B. Freund. An interface capturing method for the simulation of multi-phase compressible flows. *Journal of Computational Physics*, 229(19):7411 – 7439, 2010.

[70] M. L. Norman and K.-H. A. Winkler. *2-D Eulerian Hydrodynamics with Fluid Interfaces, Self-Gravity and Rotation*, pages 187–221. Springer Netherlands, Dordrecht, 1986.

[71] E. G. Puckett and J. S. Saltzman. A 3D adaptive mesh refinement algorithm for multimaterial gas dynamics. *Physica D: Nonlinear Phenomena*, 60(1):84 – 93, 1992.

[72] G. H. Miller and E. G. Puckett. A High-Order Godunov Method for Multiple Condensed Phases. *Journal of Computational Physics*, 128(1):134 – 164, 1996.

[73] R. Saurel and R. Abgrall. A Simple Method for Compressible Multifluid Flows. *SIAM Journal on Scientific Computing*, 21(3):1115–1145, 1999.

[74] J. Roenby, H. Bredmose, and H. Jasak. A computational method for sharp interface advection. *Royal Society Open Science*, 3(11), 2016.

[75] T. Marić, H. Marschall, and D. Bothe. voFoam - A geometrical Volume of Fluid algorithm on arbitrary unstructured meshes with local dynamic adaptive mesh refinement using OpenFOAM. (arXiv:1305.3417).

[76] S. Popinet. Gerris: a tree-based adaptive solver for the incompressible euler equations in complex geometries. *Journal of Computational Physics*, 190(2):572 – 600, 2003.

[77] D. Fuster, G. Agbaglah, C. Josserand, S. Popinet, and S. Zaleski. Numerical simulation of droplets, bubbles and waves: state of the art. *Fluid Dynamics Research*, 41(6), 2009.

[78] A. K. Singhal, M. M. Athavale, H. Li, and Y. Jiang. Mathematical Basis and Validation of the Full Cavitation Model. *Journal of Fluids Engineering*, 124(3):617–624, August 2002.

[79] P. J. Zwart. Numerical Modelling of Free Surface Flows and Cavitating Flows. In *Lecture Series-von Karman Institute for Fluid Dynamics*, number 4, page 8, 2005.

[80] P. J. Zwart, A. G. Gerber, and T. Belamri. A Two-Phase Flow Model for Predicting Cavitation Dynamics. In *International Conference on Multiphase Flow (ICMF)*, 2004.

[81] C. L. Merkle, J. Z. Feng, and P. E. O. Buelow. Computational Modeling of the Dynamics of Sheet Cavitation. In *Proceedings of 3rd International*

Symposium on Cavitation, volume 2, pages 307–311, Grenoble, France, 1998.

[82] G. H. Schnerr and J. Sauer. Physical and Numerical Modeling of Unsteady Cavitation Dynamics. In *4th International Conference on Multiphase Flow*, New Orleans, USA, May 2001.

[83] N. A. Adams and S. J. Schmidt. Shocks in Cavitating Flows. In *Bubble Dynamics and Shock Waves*, pages 235–256. Springer Berlin Heidelberg, 2013.

[84] Y. Delannoy and J. L. Kueny. Two-Phase Flow Approach in Unsteady Cavitation Modeling. In *Proceedings of the Spring Meeting of the Fluids Engineering Division*, volume 153-158, 1990.

[85] J. L. Reboud and Y. Delannoy. Two-Phase Flow Modeling of Unsteady Cavitation. In *Proceedings of 2nd International Symposium on Cavitation*, pages 39–44, Tokyo, Japan, 1994.

[86] H. W. M. Hoeijmakers, M. E. Janssens, and W. Kwan. Numerical Simulation of Sheet Cavitation. In *Proceedings 3rd International Symposium on Cavitation*, pages 257–262, Grenoble, France, 1998.

[87] C. P. Egerer, S. Hickel, S. J. Schmidt, and N. A. Adams. Large-eddy simulation of turbulent cavitating flow in a micro channel. *Physics of Fluids*, 26:085102, 2014.

[88] F. Örley, T. Trummler, S. Hickel, M. S. Mihatsch, S. J. Schmidt, and N. A. Adams. Large-eddy simulation of cavitating nozzle flow and primary jet break-up. *Physics of Fluids*, 27(8):086101, 2015.

[89] P. Koukouvinis, M. Gavaises, A. Georgoulas, and M. Marengo. Compressible simulations of bubble dynamics with central-upwind schemes. *International Journal of Computational Fluid Dynamics*, 30:1–12, 2016.

[90] R. Saurel, J. P. Cocchi, and P. B. Butler. A Numerical Study of Cavitation in the Wake of a Hypervelocity Underwater Profile. *Journal of Propulsion and Power*, 15(4):513–522, 1999.

[91] G. H. Schnerr, I. H. Sezal, and S. J. Schmidt. Numerical investigation of three-dimensional cloud cavitation with special emphasis on collapse induced shock dynamics. *Physics of Fluids*, 20:040703, 2008.

[92] I. H. Sezal, S. J. Schmidt, G. H. Schnerr, M. Thalhamer, and M. Förster. Shock and wave dynamics in cavitating compressible liquid flows in injection nozzles. *Shock Waves*, 19(1):49–58, April 2009.

[93] D. Rossinelli, B. Hejazialhosseini, P. Hadjidoukas, C. Bekas, A. Curioni, A. Bertsch, S. Futral, S. J. Schmidt, N. A. Adams, and P. Koumoutsakos. 11 PFLOP/s simulations of cloud cavitation collapse. In *SC '13: Proceedings of the International Conference on High Performance Computing, Networking, Storage and Analysis*, Denver, CO, USA, 2013.

[94] M. Dumbser, U. Iben, and C.-D. Munz. Efficient implementation of high order unstructured WENO schemes for cavitating flows. *Computers & Fluids*, 86:141–168, 2013.

[95] N. Kyriazis, P. Koukouvinis, and M. Gavaises. Numerical investigation of bubble dynamics using tabulated data. *International Journal of Multiphase Flow*, 93:158–177, July 2017.

[96] S. Zhang, J. H. Duncan, and G. L. Chahine. The final stage of the collapse of a cavitation bubble near a rigid wall. *Journal of Fluid Mechanics*, 257:147–181, 1993.

[97] S. Zhang, J. H. Duncan, and G. L. Chahine. The behavior of a cavitation bubble near a rigid wall. In *Bubble Dynamics and Interface Phenomena: Proceedings of an IUTAM Symposium held in Birmingham, U.K.*, pages 429–436. Springer Netherlands, Dordrecht, 1994.

[98] G. Wang, S. Zhang, M. Yu, H. Li, and Y. Kong. Investigation of the shock wave propagation characteristics and cavitation effects of underwater explosion near boundaries. *Applied Ocean Research*, 46:40–53, 2014.

[99] G. L. Chahine. *Modeling of Cavitation Dynamics and Interaction with Material*, pages 123–161. Springer Netherlands, Dordrecht, 2014.

[100] M. S. Mihatsch, S. J. Schmidt, and N. A. Adams. Cavitation erosion prediction based on analysis of flow dynamics and impact load spectra. *Physics of Fluids*, 27(10):103302, 2015.

[101] M. Dular and O. Coutier-Delgosha. Numerical modelling of cavitation erosion. *International Journal for Numerical Methods in Fluids*, 61(12):1388–1410, December 2009.

[102] J. Decaix and E. Goncalvès. Compressible effects modeling in turbulent cavitating flows. *European Journal of Mechanics - B/Fluids*, 39:11–31, May 2013.

[103] P. Koukouvinis and M. Gavaises. Simulation of throttle flow with two phase and single phase homogenous equilibrium model. *Journal of Physics: Conference Series*, 656(1):012086, 2015.

[104] N. A. Hawker and Y. Ventikos. Shock/Gas bubble interactions in infinite and finite volumes of liquid. In *2nd Micro and Nano Flows Conference*, West London, UK, 2009.

[105] N. A. Hawker and Y. Ventikos. Interaction of a strong shockwave with a gas bubble in a liquid medium: a numerical study. *Journal of Fluid Mechanics*, 701:59–97, 2012.

[106] S. Popinet and S. Zaleski. A front-tracking algorithm for accurate representation of surface tension. *Int. J. Numer. Meth. Fluids*, 30(6):775–793, July 1999.

[107] S. Popinet and S. Zaleski. Bubble collapse near a solid boundary: a numerical study of the influence of viscosity. *Journal of Fluid Mechanics*, 464:137–163, 2002.

[108] K. L. Pan and Z. J. Chen. Simulation of bubble dynamics in a microchannel using a front-tracking method. *Computers & Mathematics with Applications*, 67(2):290 – 306, 2014.

[109] B. B. Li, W. Jia, H. C. Zhang, and J. Lu. Investigation on the collapse behavior of a cavitation bubble near a conical rigid boundary. *Shock Waves*, 24:317–324, 2014.

[110] P. Koukouvinis, M. Gavaises, O. Supponen, and M. Farhat. Numerical simulation of a collapsing bubble subject to gravity. *Physics of Fluids*, 28:032110, 2016.

[111] P. Koukouvinis, M. Gavaises, O. Supponen, and M. Farhat. Simulation of bubble expansion and collapse in the vicinity of a free surface. *Physics of Fluids*, 28:052103, 2016.

[112] X. Y. Hu, B. C. Khoo, N. A. Adams, and F. L. Huang. A conservative interface method for compressible flows. *Journal of Computational Physics*, 219:553–578, 2006.

[113] E. Lauer, X. Y. Hu, S. Hickel, and N. A. Adams. Numerical modelling and investigation of symmetric and asymmetric cavitation bubble dynamics. *Computers & Fluids*, 69:1–19, 2012.

[114] S. Nagrath, K. Jansen, R. T. Lahey, and I. Akhatov. Hydrodynamic simulation of air bubble implosion using a level set approach. *Journal of Computational Physics*, 215(1):98 – 132, 2006.

[115] E. W. Lemmon and M. L. Huber. Thermodynamic Properties of n-Dodecane. *Energy & Fuels*, 18:960–967, July 2004.

[116] G. H. Schnerr, S. J. Schmidt, I. H. Sezal, and M. Thalhamer. Schock and Wave Dynamics of Compressible Liquid Flows with Special Emphasis on Unsteady Load on Hydrofoils and on Cavitation in Injection Nozzles. In *Proceedings 6th International Symposium on Cavitation*, Wageningen, Netherlands, 2006.

[117] I. H. Sezal. *Compressible Dynamics of Cavitating 3-D Multi-Phase Flows.* PhD thesis, Technische Universität München, 2009.

[118] F.J. Salvador, J.-V. Romero, M.-D. Roselló, and J. Martínez-López. Validation of a code for modeling cavitation phenomena in diesel injector nozzles. *Mathematical and Computer Modelling*, 52(7):1123 – 1132, 2010.

[119] S. Molina, F. J. Salvador, M. Carreres, and D. Jaramillo. A computational investigation on the influence of the use of elliptical orifices on the inner nozzle flow and cavitation development in diesel injector nozzles. *Energy Conversion and Management*, 79:114–127, 2014.

[120] F.J. Salvador, J. Martínez-López, J.-V. Romero, and M.-D. Roselló. Computational study of the cavitation phenomenon and its interaction with the turbulence developed in diesel injector nozzles by large eddy simulation (LES). *Mathematical and Computer Modelling*, 57(7):1656 – 1662, 2013.

[121] M. Gavaises, D. Papoulias, A. Andriotis, and E. Giannadakis. Link Between Cavitation Development and Erosion Damage in Diesel Injector Nozzles. In *SAE Technical Paper*, volume 2007-01-0246, April 2007.

[122] B. M. Devassy, V. Caika, P. Sampl, W. Edelbauer, and D. Greif. Numerical Investigation of Cavitating Injector Flow Accounting for 3D-Needle Movement and Liquid Compressibility Effects. In *Conference on Fuel Systems for IC Engines*, London, UK, March 2015.

[123] M. Xandra, S. Hoyas, P. Fajardo, and S. Patouna. A moving mesh generation strategy for solving an injector internal flow problem. *Mathematical and Computer Modelling*, 52(7):1143 – 1150, 2010.

[124] Z. He, W. Zhong, Q. Wang, Z. Jiang, and Y. Fu. An investigation of transient nature of the cavitating flow in injector nozzles. *Applied Thermal Engineering*, 54(1):56 – 64, 2013.

[125] M. Battistoni and C. N. Grimaldi. Numerical analysis of injector flow and spray characteristics from diesel injectors using fossil and biodiesel fuels. *Applied Energy*, 97:656 – 666, 2012.

[126] J. Martínez Rubio, F. Piscaglia, A. Montorfano, A. Onorati, and S. M. Aithal. Influence of spatial discretization schemes on accuracy of explicit LES: Canonical problems to engine-like geometries. *Computers & Fluids*, 117:62–78, August 2015.

[127] J. Martínez Rubio, F. Piscaglia, A. Montorfano, A. Onorati, and S. M. Aithal. Influence of momentum interpolation methods on the accuracy and convergence of pressure-velocity coupling algorithms in OpenFOAM. *Journal of Computational and Applied Mathematics*, 309:654–673, 2016.

[128] F. Giussani, A. Montorfano, F. Piscaglia, A. Onorati, J. Helie, and S. M. Aithal. Dynamic VOF Modelling of the Internal Flow in GDI Fuel Injectors. *Energy Procedia*, 101:574–581, 11 2016.

[129] F. Giussani, A. Montorfano, F. Piscaglia, and J. Helie. VOF Simulation of The Cavitating Flow in High Pressure GDI Injectors. In *ILASS Europe 2017, 28th Conference on Liquid Atomization and Spray Systems*, Valencia, Spain, 2017.

[130] Y. Wu, A. Montorfano, F. Piscaglia, and A. Onorati. A Study of the Organized in-Cylinder Motion by a Dynamic Adaptive Scale-Resolving Turbulence Model. *Flow, Turbulence and Combustion*, 100:797–827, December 2018.

[131] F. Piscaglia, A. Montorfano, and A. Onorati. A Scale Adaptive Filtering Technique for Turbulence Modeling of Unsteady Flows in IC Engines. *SAE Int. J. Engines*, 8:426–436, April 2015.

[132] F. Örley, S. Hickel, S. J. Schmidt, and N. A. Adams. Large-eddy simulation of turbulent, cavitating fuel flow inside a 9-hole diesel injector including needle movement. *International Journal of Engine Research*, 18(3):195–211, 2017.

[133] L. Vingert, G. Ordonneau, N. Fdida, and P. Grenard. A Rocket Engine under a Magnifying Glass, January AerospaceLab, 2016.

[134] R. J. Simoneau and R. C. Hendricks. Two-Phase Choked Flow of Cryogenic Fluids in Converging-Diverging Nozzles. NASA Technical Paper 1484, NASA, Lewis Research Center, Cleveland, Ohio 44135, July 1979.

[135] R. C. Hendricks, R. J. Simoneau, and R. F. Barrows. Two-phase choked flow of subcooled Oxygen and Nitrogen. NASA Technical Note D-8169, NASA, Lewis Research Center, Cleveland, Ohio 44135, February 1976.

[136] S. Maksic and D. Mewes. CFD-Calculation of the Flashing Flow in Pipes and Nozzles. In *U.S.-European Fluids Engineering Division Conference*, number FEDSM2002-31033, pages 511–516, 2002.

[137] Y. Liao and D. Lucas. 3D CFD simulation of flashing flows in a converging-diverging nozzle. *Nuclear Engineering and Design*, 292:149 – 163, 2015.

[138] C.A. Marsh and A. P. O'Mahony. Three-dimensional modelling of industrial flashing flows. *Progress in Computational Fluid Dynamics, an International Journal*, 9(6-7):393–398, 2009.

[139] S. Mimouni, M. Boucker, J. Laviéville, A. Guelfi, and D. Bestion. Modelling and computation of cavitation and boiling bubbly flows with the NEPTUNE_CFD code. *Nuclear Engineering and Design*, 238(3):680–692, March 2008.

[140] J. P. Janet, Y. Liao, and D. Lucas. Heterogeneous nucleation in CFD simulation of flashing flows in converging-diverging nozzles. *International Journal of Multiphase Flow*, 74:106 – 117, 2015.

[141] H. Meng and Y. Vigor. A unified treatment of general fluid thermodynamics and its application to a preconditioning scheme. *Journal of Computational Physics*, 189(1):277 – 304, 2003.

[142] N. Zong and V. Yang. Cryogenic fluid dynamics of pressure swirl injectors at supercritical conditions. *Physics of Fluids*, 20(5):056103, 2008.

[143] X. Wang, H. Huo, Y. Wang, L. Zhang, and V. Yang. A three-dimensional analysis of swirl injector flow dynamics at supercritical conditions. In *53rd AIAA Aerospace Sciences Meeting*. American Institute of Aeronautics and Astronautics, January 2015. DOI: 10.2514/6.2015-1827.

[144] Z. Bilicki and J. Kestin. Physical aspects of the relaxation model in two-phase flow. *Proceedings of the Royal Society of London A: Mathematical, Physical and Engineering Sciences*, 428(1875):379–397, 1990.

[145] P. Downar-Zapolski, Z. Bilicki, L. Bolle, and J. Franco. The non-equilibrium relaxation model for one-dimensional flashing liquid flow. *International Journal of Multiphase Flow*, 22(3):473–483, 1996.

[146] D. P. Schmidt, S. Gopalakrishnan, and H. Jasak. Multi-dimensional simulation of thermal non-equilibrium channel flow. *International Journal of Multiphase Flow*, 36(4):284 – 292, 2010.

[147] E. T. Baldwin, R. O. Grover, S. E. Parrish, D. J. Duke, K. E. Matusik, C. F. Powell, A. L. Kastengren, and D. P. Schmidt. String flash-boiling in gasoline direct injection simulations with transient needle motion. *International Journal of Multiphase Flow*, 87:90 – 101, 2016.

[148] I. K. Karathanassis, P. Koukouvinis, and M. Gavaises. Comparative evaluation of phase-change mechanisms for the prediction of flashing flows. *International Journal of Multiphase Flow*, 95:257 – 270, 2017.

[149] T. Ramcke, A. Lampmann, and M. Pfitzner. Simulations of Injection of Liquid Oxygen/Gaseous Methane Under Flashing Conditions. *Journal of Propulsion and Power*, 34(2):395–407, December 2017.

[150] R. Schmehl and J. Steelant. Computational Analysis of the Oxidizer Preflow in an Upper-Stage Rocket Engine. *Journal of Propulsion and Power*, 25(3):771–782, May 2009.

[151] G. Lamanna, H. Kamoun, B. Weigand, and J. Steelant. Towards a unified treatment of fully flashing sprays. *International Journal of Multiphase Flow*, 58:168–184, 2014.

[152] R. B. Stewart, R. T. Jacobsen, and W. Wagner. Thermodynamic Properties of Oxygen from the Triple Point to 300 k with Pressures to 80 Mpa. *Journal of Physical and Chemical Reference Data*, 20:917–1021, September 1991.

[153] M. Rein. Phenomena of liquid drop impact on solid and liquid surfaces. *Fluid Dynamics Research*, 12:61–93, August 1993.

[154] A. L. Yarin. DROP IMPACT DYNAMICS: Splashing, spreading, receding, bouncing... *Annual Review of Fluid Mechanics*, 38(1):159–192, 2006.

[155] R. I. Crane. Droplet deposition in steam turbines. *Proceedings of the Institution of Mechanical Engineers, Part C: Journal of Mechanical Engineering Science*, 218(8):859–870, 2004.

[156] R. Andrade, O. Skurtys, and F. Osorio. Drop impact behavior on food using spray coating: Fundamentals and applications. *Food Research International*, 54(1):397 – 405, 2013.

[157] G. D. Martin, S. D. Hoath, and I. M. Hutchings. Inkjet printing - the physics of manipulating liquid jets and drops. *Journal of Physics: Conference Series*, 105(1):012001, 2008.

[158] Q. Zhou, N. Li, X. Chen, A. Yonezu, T. Xu, S. Hui, and D. Zhang. Water Drop Erosion on Turbine Blades: Numerical Framework and Applications. *Materials Transactions*, 49(7):1606–1615, 2008.

[159] F. J. Heymann. High Speed Impact between a Liquid Drop and a Solid Surface. *Journal of Applied Physics*, 40(13):5113–5122, 1969.

[160] M. B. Lesser. Analytic Solutions of Liquid-Drop Impact Problems. *Proceedings of the Royal Society of London A: Mathematical, Physical and Engineering Sciences*, 377(1770):289–308, 1981.

[161] J. E. Field, M. B. Lesser, and J. P. Dear. Studies of Two-Dimensional Liquid-Wedge Impact and Their Relevance to Liquid-Drop Impact Problems. *Proceedings of the Royal Society of London A: Mathematical, Physical and Engineering Sciences*, 401(1821):225–249, 1985.

[162] J. E. Field, J. P. Dear, and J. E. Ogren. The effects of target compliance on liquid drop impact. *Journal of Applied Physics*, 65(2):533–540, 1989.

[163] J.E. Field, J.-J. Camus, M. Tinguely, D. Obreschkow, and M. Farhat. Cavitation in impacted drops and jets and the effect on erosion damage thresholds. *Wear*, 290–291:154–160, 2012.

[164] F. H. Harlow and J. P. Shannon. The Splash of a Liquid Drop. *Journal of Applied Physics*, 38(10):3855–3866, 1967.

[165] K. Tsurutani, M. Yao, J. Senda, and H. Fujimoto. Numerical Analysis of the Deformation Process of a Droplet Impinging upon a Wall. *JSME international journal. Ser. 2, Fluids engineering, heat transfer, power, combustion, thermophysical properties*, 33(3):555–561, 1990.

[166] N. Hatta, H. Fujimoto, and H. Takuda. Deformation Process of a Water Droplet Impinging on a Solid Surface. *Journal of Fluids Engineering*, 117(3):394–401, September 1995.

[167] Y. Renardy, S. Popinet, L. Duchemin, M. Renardy, S. Zaleski, C. Josserand, M. A. Drumright-Clarke, D. Richard, C. Clanet, and D. Quéré. Pyramidal and toroidal water drops after impact on a solid surface. *Journal of Fluid Mechanics*, 484:69–83, 2003.

[168] J. Fukai, Z. Zhao, D. Poulikakos, C. M. Megaridis, and O. Miyatake. Modeling of the deformation of a liquid droplet impinging upon a flat surface. *Physics of Fluids A: Fluid Dynamics*, 5(11):2588–2599, 1993.

[169] A. V. Chizhov and K. Takayama. The impact of compressible liquid droplet on hot rigid surface. *International Journal of Heat and Mass Transfer*, 47(6–7):1391 – 1401, 2004.

[170] J. M. Waldvogel and D. Poulikakos. Solidification phenomena in picoliter size solder droplet deposition on a composite substrate. *International Journal of Heat and Mass Transfer*, 40(2):295 – 309, 1997.

[171] J. E. Sprittles and Y. D. Shikhmurzaev. The dynamics of liquid drops and their interaction with solids of varying wettabilities. *Physics of Fluids*, 24(8):082001, 2012.

[172] M. R. Davidson. Boundary integral prediction of the spreading of an inviscid drop impacting on a solid surface. *Chemical Engineering Science*, 55(6):1159–1170, 2000.

[173] D. Harvie and D. Fletcher. A hydrodynamic and thermodynamic simulation of droplet impacts on hot surfaces, part ii: validation and applications. *International Journal of Heat and Mass Transfer*, 44(14):2643–2659, 2001.

[174] M. PasandidehFard, Y. M. Qiao, S. Chandra, and J. Mostaghimi. Capillary effects during droplet impact on a solid surface. *Physics of Fluids*, 8(3):650–659, 1996.

[175] M. Rieber and A. Frohn. A numerical study on the mechanism of splashing. *International Journal of Heat and Fluid Flow*, 20(5):455 – 461, 1999.

[176] M. Bussmann, J. Mostaghimi, and S. Chandra. On a three-dimensional volume tracking model of droplet impact. *Physics of Fluids*, 11(6):1406–1417, 1999.

[177] M. PasandidehFard, S. Chandra, and J. Mostaghimi. A three-dimensional model of droplet impact and solidification. *International Journal of Heat and Mass Transfer*, 45(11):2229 – 2242, 2002.

[178] I. Malgarinos, N. Nikolopoulos, M. Marengo, C. Antonini, and M. Gavaises. VOF simulations of the contact angle dynamics during the drop spreading: Standard models and a new wetting force model. *Advances in Colloid and Interface Science*, 212:1 – 20, 2014.

[179] Y. Guo, Y. Lian, and M. Sussman. Investigation of drop impact on dry and wet surfaces with consideration of surrounding air. *Physics of Fluids*, 28(7):073303, 2016.

[180] K. K. Haller, Y. Ventikos, D. Poulikakos, and P. Monkewitz. Computational study of high-speed liquid droplet impact. *Journal of Applied Physics*, 92(5):2821–2828, 2002.

[181] T. Sanada, K. Ando, and T. Colonius. A computational study of high-speed droplet impact. *Fluid Dynamics and Materials Processing*, 7(4):329–340, 2011.

[182] N. Yang-Yao and W. Hong-Wei. Simulations of the shock waves and cavitation bubbles during a three-dimensional high-speed droplet impingement based on a two-fluid model. *Computers & Fluids*, 134–135:196–214, 2016.

[183] K. Hayasaka, A. Kiyama, and Y. Tagawa. Effects of pressure impulse and peak pressure of a shockwave on microjet velocity in a microchannel. *Microfluidics and Nanofluidics*, 21(11):166, 2017.

[184] T. Han and J. J. Yoh. A laser based reusable microjet injector for transdermal drug delivery. *Journal of Applied Physics*, 107(10):103110, 2010.

[185] T. Han, J. Hah, S. Kim, and J. J. Yoh. *Light syringes based on the laser induced shock wave*, volume 2 of *28th International Symposium on Shock Waves*, pages 819–825. Springer, 2012.

[186] M. A. Park, H. J. Jang, F. V. Sirotkin, and J. J. Yoh. Er:YAG laser pulse for small-dose splashback-free microjet transdermal drug delivery. *Opt. Lett.*, 37(18):3894–3896, September 2012.

[187] J. J. Yoh, H. Jang, M. Park, T. Han, and J. Hah. A laser syringe aimed at delivering drug into the outer layer of human skin. *AIP Conference Proceedings*, 1464(1):524–531, 2012.

[188] A. M. Loske. *Medical and Biomedical Applications of Shock Waves*. Shock Wave and High Pressure Phenomena. Springer International Publishing, 2017.

[189] M. S. Longuet-Higgins. Bubbles, breaking waves and hyperbolic jets at a free surface. *Journal of Fluid Mechanics*, 127:103–121, 1983.

[190] M. S. Longuet-Higgins and H. Oguz. Critical microjets in collapsing cavities. *Journal of Fluid Mechanics*, 290:183–201, 1995.

[191] A. Antkowiak, N. Bremond, S. Le Dizès, and E. Villermaux. Short-term dynamics of a density interface following an impact. *Journal of Fluid Mechanics*, 577:241–250, 2007.

[192] J. I. Katz. Jets from collapsing bubbles. *Proceedings of the Royal Society of London A: Mathematical, Physical and Engineering Sciences*, 455(1981):323–328, 1999.

[193] C. Sun, E. Can, R. Dijkink, D. Lohse, and A. Prosperetti. Growth and collapse of a vapour bubble in a microtube: the role of thermal effects. *Journal of Fluid Mechanics*, 632:5–16, 2009.

[194] T. G. Leighton, W. L. Ho, and R. Flaxman. Sonoluminescence from the unstable collapse of a conical bubble. *Ultrasonics*, 35(5):399–405, 1997.

[195] T. G. Leighton, A. D. Phelps, B. T. Cox, and W. L. Ho. Theory and preliminary measurements of the rayleigh-like collapse of a conical bubble. *Acta Acustica united with Acustica*, 84(6):1014–1024 (11), 1998.

[196] T. G. Leighton, B. T. Cox, P. R. Birkin, and T. Bayliss. The Rayleigh-like collapse of a conical bubble: Measurements of meniscus, liquid pressure, and electrochemistry. In *Proceedings of the 137th Meeting of the Acoustical Society of America and the 2nd Convention of the European Acoustics Association*, Berlin, March 1999.

[197] T. G. Leighton, B. T. Cox, and A. D. Phelps. The Rayleigh-like collapse of a conical bubble. *The Journal of the Acoustical Society of America*, 107(1):130–142, 2000.

[198] D. D. Symons. Inertial liquid loading on the nozzle of a needle-free injection device. *Proceedings of the Institution of Mechanical Engineers, Part C: Journal of Mechanical Engineering Science*, 218(2):233–240, 2004.

[199] R. Bergmann, E. de Jong, J.-B. Choimet, D. van der Meer, and D. Lohse. The origin of the tubular jet. *Journal of Fluid Mechanics*, 600:19–43, 2008.

[200] Y. Tagawa, N. Oudalov, C. W. Visser, I. R. Peters, D. van der Meer, C. Sun, A. Prosperetti, and D. Lohse. Highly Focused Supersonic Microjets. *Phys. Rev. X*, 2:031002, July 2012.

[201] Y. Tagawa, N. Oudalov, A. El Ghalbzouri, C. Sun, and D. Lohse. Needle-free injection into skin and soft matter with highly focused microjets. *Lab Chip*, 13:1357–1363, 2013.

[202] G. Morsink. Tubular jet generation by pressure pulse impact. Master thesis, University of Twente, 2011.

[203] C. Berrospe-Rodriguez, C. W. Visser, S. Schlautmann, R. Ramos-Garcia, and D. Fernandez Rivas. Continuous-wave laser generated jets for needle free applications. *Biomicrofluidics*, 10(1):014104, 2016.

[204] S. R. Gonzalez Avila, C. Song, and C.-D. Ohl. Fast transient microjets induced by hemispherical cavitation bubbles. *Journal of Fluid Mechanics*, 767:31–51, 2015.

[205] A. Arora, I. Hakim, J. Baxter, R. Rathnasingham, R. Srinivasan, D. A. Fletcher, and S. Mitragotri. Needle-free delivery of macromolecules across the skin by nanoliter-volume pulsed microjets. *Proceedings of the National Academy of Sciences*, 104(11):4255–4260, 2007.

[206] A. Kiyama, Y. Tagawa, K. Ando, and M. Kameda. Effects of a water hammer and cavitation on jet formation in a test tube. *Journal of Fluid Mechanics*, 787:224–236, 2016.

[207] E. Ory, H. Yuan, A. Prosperetti, S. Popinet, and S. Zaleski. Growth and collapse of a vapor bubble in a narrow tube. *Physics of Fluids*, 12(6):1268–1277, 2000.

[208] M. D. Giavedoni and F. A. Saita. The rear meniscus of a long bubble steadily displacing a newtonian liquid in a capillary tube. *Physics of Fluids*, 11(4):786–794, 1999.

[209] A. López-Villa, A. Medina, and F. J. Higuera. Bubble growth by injection of gas into viscous liquids in cylindrical and conical tubes. *Physics of Fluids*, 23(10):102102, 2011.

[210] L. Duchemin, S. Popinet, C. Josserand, and S. Zaleski. Jet formation in bubbles bursting at a free surface. *Physics of Fluids*, 14(9):3000–3008, 2002.

[211] J. R. Blake, M. C. Hooton, P. B. Robinson, and R. P. Tong. Collapsing cavities, toroidal bubbles and jet impact. *Philosophical Transactions of the Royal Society of London A: Mathematical, Physical and Engineering Sciences*, 355(1724):537–550, 1997.

[212] C. K. Turangan, A. R. Jamaluddin, G. J. Ball, and T. G. Leighton. Free-Lagrange simulations of the expansion and jetting collapse of air bubbles in water. *Journal of Fluid Mechanics*, 598:1–25, 2008.

[213] A. R. Jamaluddin, G. J. Ball, C. K. Turangan, and T. G. Leighton. The collapse of single bubbles and approximation of the far-field acoustic emissions for cavitation induced by shock wave lithotripsy. *Journal of Fluid Mechanics*, 677:305–341, 2011.

[214] C. K. Turangan, G. J. Ball, A. R. Jamaluddin, and T. G. Leighton. Numerical studies of cavitation erosion on an elastic–plastic material caused by shock-induced bubble collapse. *Proceedings of the Royal Society of London A: Mathematical, Physical and Engineering Sciences*, 473(2205), 2017.

[215] I. R. Peters, Y. Tagawa, N. Oudalov, C. Sun, A. Prosperetti, D. Lohse, and D. van der Meer. Highly focused supersonic microjets: numerical simulations. *Journal of Fluid Mechanics*, 719:587–605, 2013.

[216] J.-P. Franc and J.-M. Michel. *Fundamentals of Cavitation*. Kluwer Academic Publishers, 2005.

[217] C. Greenshields. *OpenFOAM - The Open Source CFD Toolbox - User Guide*. OpenFOAM Foundation Ltd., 2.4.0 edition, 21 May 2015.

[218] B. E. Launder. Turbulence Modelling for CFD. by d. c. wilcox. dcw industries inc. *Journal of Fluid Mechanics*, 289:406–407, 1995.

[219] O. Coutier-Delgosha, R. Fortes-Patella, and J. L. Reboud. Evaluation of the turbulence model influence on the numerical simulations of unsteady cavitation. *Journal of Fluids Engineering*, 125(1):38–45, 2003.

[220] C. E. Brennen. *Cavitation and Bubble Dynamics*. Oxford University Press, 1995.

[221] R. E. Bensow and G. Bark. Implicit LES Predictions of the Cavitating Flow on a Propeller. *Journal of Fluids Engineering*, 132(4):041302, 2010.

[222] S. J. Schmidt, I. H. Sezal, G. H. Schnerr, E. Onate P. Wesseling, and J. Periaux. Compressible simulation of high-speed hydrodynamics with phase change. In *European Conference on Computational Fluid Dynamics*, TU Delft, The Netherlands, 2006.

[223] E. Lemmon, M. McLinden, and D. Friend. *NIST Chemistry WebBook, NIST Standard Reference Database Number 69*, chapter Thermophysical properties of fluid systems. 2005.

[224] R. Saurel, F. Petitpas, and R. Abgrall. Modelling phase transition in metastable liquids: application to cavitating and flashing flows. *Journal of Fluid Mechanics*, 607:313–350, 2008.

[225] A. Kurganov and E. Tadmor. New High-Resolution Central Schemes for Nonlinear Conservation Laws and Convection-Diffusion Equations. *Journal of Computational Physics*, 160(1):241 – 282, 2000.

[226] N. Kyriazis, P. Koukouvinis, and M. Gavaises. Modelling cavitation during drop impact on solid surfaces. *Advances in Colloid and Interface Science*, 260:46 – 64, 2018.

[227] E. F. Toro. *Riemann Solvers and Numerical Methods for Fluid Dynamics, A Practical Introduction*. Springer Berlin Heidelberg, 2009.

[228] F. Moukalled, L. Mangani, and M. Darwish. *The Finite Volume Method in Computational Fluid Dynamics, An Advanced Introduction with OpenFOAM and Matlab*, volume 113. Springer International Publishing, 2015.

[229] S. J. Schmidt. Ein Verfahren zur präzisen Berechnung dreidimensionaler, reibungsfreier Idealgasströmungen über dem gesamten Kompressibilitätsbreich. Master's thesis, 2005.

[230] D. Obreschkow, P. Kobel, N. Dorsaz, A. de Bosset, C. Nicollier, and M. Farhat. Cavitation Bubble Dynamics inside Liquid Drops in Microgravity. *Physical Review Letters*, 97:094502, 2006.

[231] D. Obreschkow, M. Tinguely, N. Dorsaz, P. Kobel, A. de Bosset, and M. Farhat. The quest for the most spherical bubble: experimental setup and data overview. *Experiments in Fluids*, 54:1–18, 2013.

[232] C. Pozrikidis. *Fluid Dynamics: Theory, Computation, and Numerical Simulation : Accompanied by the Software Library FDLIB*. Springer Science & Business Media, 2009.

[233] G. Lacaze, A. Misdariis, A. Ruiz, and J. C. Oefelein. Analysis of high-pressure Diesel fuel injection processes using LES with real-fluid thermodynamics and transport. *Proceedings of the Combustion Institute*, 35(2):1603–1611, 2015.

[234] J. Sauer. *Instationär kavitierende Strömungen - Ein neues Modell, basierend auf Front Capturing (VoF) und Blasendynamik*. PhD thesis, Karlsruhe University, 2000.

[235] A. J. Coleman, J. E. Saunders, L. A. Crum, and M. Dyson. Acoustic cavitation generated by an extracorporeal shockwave lithotripter. *Ultrasound in Medicine and Biology*, 13(2):69–76, 1987.

[236] C. C. Church. A theoretical study of cavitation generated by an extracorporeal shock wave lithotripter. *The Journal of the Acoustical Society of America*, 86(1):215–227, 1989.

[237] T. Kodama and K. Takayama. Dynamic behavior of bubbles during extracorporeal shock-wave lithotripsy. *Ultrasound in Medicine and Biology*, 24(5):723–738, 1998.

[238] S. Zhu, F. H. Cocks, G. M. Preminger, and P. Zhong. The role of stress waves and cavitation in stone comminution in shock wave lithotripsy. *Ultrasound in Medicine and Biology*, 28(5):661–671, May 2002.

[239] M. Marengo, C. Antonini, I. V. Roisman, and C. Tropea. Drop collisions with simple and complex surfaces. *Current Opinion in Colloid & Interface Science*, 16(4):292 – 302, 2011.

[240] F. Örley, S. Hickel, S. J. Schmidt, and N. A. Adams. LES of cavitating flow inside a diesel injector including dynamic needle movement. *Journal of Physics: Conference Series*, 656(1):012097, 2015.

[241] P. Koukouvinis, H. Naseri, and M. Gavaises. Performance of turbulence and cavitation models in prediction of incipient and developed cavitation. *International Journal of Engine Research*, 18(4):333–350, 2017.

[242] M. Brouillette. The Richtmyer-Meshkov instability. *Annual Review of Fluid Mechanics*, 34(1):445–468, 2002.

[243] N. Mitroglou, M. McLorn, M. Gavaises, C. Soteriou, and M. Winterbourne. Instantaneous and ensemble average cavitation structures in diesel microchannel flow orifices. *Fuel*, 116:736 – 742, 2014.

[244] N. Kyriazis, P. Koukouvinis, and M. Gavaises. Numerical investigations on bubble-induced jetting and shock wave focusing: application on a needle-free injection. *Proceedings of the Royal Society A: Mathematical, Physical and Engineering Sciences*, 475, February 2019.

[245] Y. Tagawa, S. Yamamoto, K. Hayasaka, and M. Kameda. On pressure impulse of a laser-induced underwater shock wave. *Journal of Fluid Mechanics*, 808:5–18, 2016.

[246] W. H. Lee. *Computer Simulation of Shaped Charge Problems*. World Scientific, 2006.

[247] P. C. Chou, R. D. Ciccarelli, and W. P. Walters. The formation of jets from hemispherical-linear warheads. 7th Int. Symp. on Ballistics, April 1983.

[248] B. Arvidsson and H. G. Ohlsson. Investigation of liners for shaped charges manufactured from cu-powder by x-ray diffraction and ultrasonic techniques. In *8th International Symposium on Ballistics*, October 1984.

[249] D. K. Davison and B. K. Arvidsson. Optimization of a 90 mm Shaped Charge Warhead. In *2nd Symposium on the Interaction of Non-Nuclear Munitions with Structures*, 1985.

[250] C. Edwards and R. Marks. Evaluation of biomechanical properties of human skin. *Clinics in Dermatology*, 13(4):375–380, 1995.

[251] A.I. King, J. S. Ruan, C. Zhou, W. N. Hardy, and T. B. Khalil. Recent advances in biomechanics of brain injury research: a review. *Journal of Neurotrauma*, 12(4), 1995.

[252] L. Voo, S. Kumaresan, F. A. Pintar, N. Yoganandan, and A. Sances. Finite-element models of the human head. *Medical and Biological Engineering and Computing*, 34(5):375–381, September 1996.

[253] X. Yue, L. Wang, and R. Wang. Tissue Modeling and Analyzing with Finite Element Method: A Review for Cranium Brain Imaging. *International Journal of Biomedical Imaging*, page 781603, 2013.

[254] R. K. Gupta and A. Przekwas. Mathematical Models of Blast-induced TBI: Current Status, Challenges, and Prospects. *Frontiers in Neurology*, 4, May 2013.

[255] H. Samaka and F. Tarlochan. Finite Element (FE) Human Head Models / Literature Review. *International Journal of Scientific & Technology Research*, 2(7), 2013.

[256] K. M. Tse, S. Piang Lim, V. B. C. Tan, and H. Lee. A Review of Head Injury and Finite Element Head Models. *American Journal of Engineering, Technology and Society*, 1:28–52, December 2014.

[257] M. A. Meyers. *Dynamic Behavior of Materials*. John Wiley & Sons, Inc., 1994.

[258] R. Menikoff and B. J. Plohr. The Riemann problem for fluid flow of real materials. *Rev. Mod. Phys.*, 61:75–130, January 1989.

[259] O. Le Métayer, J. Massoni, and R. Saurel. Modelling evaporation fronts with reactive Riemann solvers. *Journal of Computational Physics*, 205(2):567–610, May 2005.

[260] S. Müller and A. Voss. The Riemann Problem for the Euler Equations with Nonconvex and Nonsmooth Equation of State: Construction of Wave Curves. *SIAM Journal on Scientific Computing*, 28(2):651–681, January 2006.

[261] S. Müller, M. Bachmann, D. Kröninger, T. Kurz, and P. Helluy. Comparison and validation of compressible flow simulations of laser-induced cavitation bubbles. *Computers & Fluids*, 38(9):1850–1862, October 2009.

[262] F. Petitpas, J. Massoni, R. Saurel, E. Lapebie, and L. Munier. Diffuse interface model for high speed cavitating underwater systems. *International Journal of Multiphase Flow*, 35(8):747–759, August 2009.

[263] R. Saurel and O. Lemetayer. A multiphase model for compressible flows with interfaces, shocks, detonation waves and cavitation. *Journal of Fluid Mechanics*, 431:239–271, 2001.

[264] R. Abgrall and R. Saurel. Discrete equations for physical and numerical compressible multiphase mixtures. *Journal of Computational Physics*, 186(2):361 – 396, 2003.

[265] W. Wagner and A. Pruß. The IAPWS Formulation 1995 for the Thermodynamic Properties of Ordinary Water Substance for General and Scientific Use. *Journal of Physical and Chemical Reference Data*, 31(2):387–535, 2002.

[266] J. B. Freund, R. K. Shukla, and A. P. Evan. Shock-induced bubble jetting into a viscous fluid with application to tissue injury in shock-wave lithotripsy. *The Journal of the Acoustical Society of America*, 126(5):2746–2756, 2009.

[267] V. Coralic and T. Colonius. Shock-induced collapse of a bubble inside a deformable vessel. *European journal of mechanics B Fluids*, 40:64–74, 2013.